Experimental investigation of the ionic conduction and dielectric properties of chitosan based solid biopolymer blend and its nanocomposites for solid-state supercapacitors : EDLC to Hybrid

THESIS SUBMITTED FOR THE DEGREE OF

DOCTOR OF PHILOSOPHY (SCIENCE)
OF
JADAVPUR UNIVERSITY

2022

By

Simantini Majumdar

Department of Physics
Jadavpur University
Jadavpur, Kolkata-700032, India

Experimental investigation of the ionic conduction and dielectric properties of chitosan based solid biopolymer blend and its nanocomposites for solid-state supercapacitors : EDLC to Hybrid

THESIS SUBMITTED FOR THE DEGREE OF

DOCTOR OF PHILOSOPHY (SCIENCE)
OF
JADAVPUR UNIVERSITY

2022

By

Simantini Majumdar

Department of Physics
Jadavpur University
Jadavpur, Kolkata-700032, India

Prof. (Dr.) Ruma Ray
Professor
Department of Physics
Jadavpur University
Kolkata-700032

CERTIFICATE FROM THE SUPERVISOR(S)

This is to certify that the thesis entitled "**Experimental investigation of the ionic conduction and dielectric properties of chitosan based solid biopolymer blend and its nanocomposites for solid-state supercapacitors : EDLC to Hybrid**" submitted by ~~Sri~~/Smt. **Simantini Majumdar**, who got ~~his~~/her name registered on **31/01/2018** for the award of **Ph.D. (Science) degree** of Jadavpur University, is absolutely based upon her own work under the supervision of **Prof. Ruma Ray** in the Department of Physics, Jadavpur University, Jadavpur, Kolkata-700032 and that neither this thesis nor any part of it has been submitted for either any degree / diploma or any other academic award anywhere before.

Ruma Ray 31.01.2022

(Signature of the Supervisor(s), date with official seal)

Dr. Ruma Ray
Professor
Department of Physics
Jadavpur University
Jadavpur, Kolkata-700 032

Dedicated to

my Parents

(Tapaswini Majumdar & Bilash Kumar Majumdar)

&

Elder Sister

(Monoswini Majumdar)

Acknowledgement

As a sense of fulfillment at the completion of this phase of my academic career, I would like to express my happiness and gratitude to my teachers and family members for their constant support and encouragement.

First I wish to express my deepest gratitude towards my supervisor, Prof. (Dr.) Ruma Ray (Department of Physics, Jadavpur University, Kolkata, India) for her continuous support and guidance throughout this research. She has always given me the freedom to choose my own research problems from the first day I had entered her research laboratory. I am thankful to her for being an amazing supervisor to me. She had given her permission and much-needed encouragement to work in the challenging areas of solid state supercapacitor applications. This had been more challenging since this was the first research work on solid-state electrolytes and supercapacitors in our lab. She has always heard all my research-related problems with incomparable patience and provided insightful discussions throughout my whole Ph.d tenure. Thank you Ma’am, for all your guidance, support, encouragement and useful suggestions to make this research work and dissertation possible. Without your strong faith in me, I don’t think I would have been able to come to this stage and write this thesis now.

I would like to express my sincerest gratitude to my research advisor, Dr. Pintu Sen (Physics Group, Material Science Division, Variable Energy Cyclotron Centre, VECC, Kolkata, India) for giving me opportunity to work in his research laboratory and guiding me throughout this research. His countless instructions and valuable advice always helped me to do better. I am thankful to him for being an amazing coach to me throughout my Ph.d tenure. Thank you Sir, for all your guidance and constant support to make this research work on solid-state supercapacitors possible. You have always shown me the right way through stimulating discussions and interactions which helped me a lot in analyzing the problems.

I am also thankful to Prof. (Dr.) Swapan Kumar Bhattacharya (Department of Chemistry, Jadavpur University, Kolkata), a member of my Ph.d Research Advisory Committee (RAC) for his helpful suggestions and useful feedback during my RAC oral presentations.

My sincere gratitude goes to Prof. Shantanu Das (Retired Scientist, Bhabha Atomic Research Centre, BARC, Mumbai, India) for inspiring me to become a good researcher in the initial days of my Ph.d. He was always there to help me whenever I had needed any research-related help or guidance. I consider myself very fortunate to meet this amazing person. I want to thank Prof. Sujata Tarafdar (Condensed Matter Physics Research Centre, CMPRC, Department of Physics, Jadavpur Univerity, Kolkata, India) and Dr. Tapati Dutta (Physics Department, St. Xaviers College, Kolkata, India) for being amazing teachers to me. I am grateful to them for all the guidance they had given me during my initial days of research life at CMPRC.

I wish to thank Prof. Saurav Giri (Department of Solid State Physics, Indian Association for the Cultivation of Science, IACS, Kolkata, India) for allowing me in his research laboratory during few of my experimental measurements in IACS. I would also like to thank Prof. Tapas Ranjan Middya (Retired Professor) and Prof. Argha Deb (Department of Physics, Jadavpur University, Kolkata, India) for the academic help and support during my initial days of research life at Jadavpur Univerity. I am thankful to Prof. Achintya Singha (Bose Institute, Kolkata, India) and Dr. Kaustav Das (Department of Physics, Jadavpur Univerity, Kolkata, India) for giving me opportunity to carry out few of my experimental measurements in his research laboratory.

Special thanks to my senior and junior labmates, Sanchari Sarkar, Archita Mondal, Neepamala Giri, Bohnni Shikha Biswas and Payal Sengupta with whom I had spent a really nice time during my Ph.d journey. I would like to thank Mou Saha, one of my former senior labmate, for her generosity and valuable support during the initial days of my research in this field of solid-state electrolytes. I also want to thank Ashok Banerjee, the lab assistant in my VECC lab, for helping me a lot during the material synthesis and experimental measurements. I specially thank Samir Chattopadhyay and Pradeepta Kumar Ghose (Ph.d scholars, IACS) for their kind help with few of my experimental measurements at IACS. I am thankful to all the faculties and staffs of the Department of Physics, members of research section, Dean office and Ph.D cell in Jadavpur University for various assistance and support. My special thanks goes to VECC, Kolkata for all the assistance and support they had given me to carry out my research work presented in this dissertation.

I thank DST PURSE – II (Ref. No. P-1/RS/18/17) and JU-RUSA 2.0 (Ref. No. R-11/195/2019) for providing me research fellowship.

Finally, I would like to acknowledge the persons who mean the world to me: my mother (Tapaswini Majumdar), my father (Bilash Kumar Majumdar) and my elder sister (Monoswini Majumdar) without whom I would not have made it this far. My mother is my first teacher who had literally taught me everything and provided unconditional love and care. She has sacrificed a lot in her life and has always taken immense care of me and my elder sister since our birth. She fed me whenever I got extremely busy with my research write-ups and had no time to eat with my bare hands. She is my best friend who always hears all of my worries or problems and boost my mental strength. Thank you, Maa for always being my greatest support and teaching me to dream big since my childhood and motivating me to reach greater heights in career. Love you always, Maa. My father is the person who had actually grown my immense interest in science subjects especially Mathematics by teaching it so beautifully. Its always his dream to see both of his daughters as well-educated and well-established individuals. He has truly struggled a lot in bringing us up and giving us proper education from a well-known english medium school in Kolkata. Now when I look back, I understand that his struggle has actually made me a strong individual. Be it for any of my exams or conferences (till now), he always takes me to the venue, as a result of which I never need to worry in searching and reaching the new unknown places in correct time. Thank you, Baba for always taking care and dreaming big for me. Love you always, Baba. My elder sister is my best friend and teacher who taught me Mathematics and Physical Science throughout my school days and she was actually my private tutor as I never had any. Whenever I had any problems in understanding or memorizing a particular topic of any subject, she always taught me the easiest way to understand or remember it. One's parents are always the best but she is the best sister one can have and I love her so much. Because of her, I never had to worry of taking up a job during my Ph.d journey and thus I've thoroughly enjoyed my research life without any worries till date. Thank you, Didi for always supporting me in any career-related decisions of mine. Love you always, Didi. To my parents and elder sister: the amount of love and support you've given me are really worth more than that can be expressed on paper and I'll be forever grateful to you and hoping to fulfill all of your dreams.

Simantini Majumdar
Simantini Majumdar 31.1.2022

Jadavpur University
Kolkata, India
2022

Synopsis

The increasing demands for long-lasting and lightweight portable electronic devices suggest intense research for supercapacitors having higher power density than batteries and conventional capacitors, with solid state electrolytes. Natural polymers such as chitosan has attracted huge attention as solid state electrolytes since the last few decades owing to their low cost, easy availability from shells of shrimps and crabs, principal bio-degradation properties and their ease of fabrication as thin films which are mechanically very strong, though a vast field of investigation is yet to be probed. On the other hand, spinel ferrites, $\boldsymbol{M}\mathrm{Fe_2O_4}$ or $\boldsymbol{M\acute{M}}\mathrm{FeO_4}$ (where $\boldsymbol{M}$ or $\boldsymbol{\acute{M}}$ = Mn, Ni, Zn, Co, etc.) are being considered as fascinating electrode materials in supercapacitor applications for the last several years due to their ability to exhibit different redox states, impressive electrical properties and good electrochemical stability. The objective of this dissertation is to develop a high-performance solid-state supercapacitor by enhancing the ionic conductivity and dielectric properties of an environmental friendly and cost-effective solid polymer electrolyte which involves both faradaic and non-faradaic energy storage mechanisms at the electrode, to reach the increasing power demands in our society.

Here, within the scope of our research work we have focused on plasticized $\mathrm{Li^+}$ ion conducting chitosan (CS) based solid-state electrolytes by blending with other biopolymers [like potato starch (PS) and carboxymethyl cellulose (CMC)] and synthetic polymers [like polyvinylidene fluoride (PVDF) and polymethyl methacrylate (PMMA)] and its composites with carbon based insulating and conducting nanofillers like graphene oxide (GO) and carbon nanotubes (CNT), respectively. The solid-state electrolytes are prepared by probe sonication and solution casting technique. Ionic conduction, dielectric properties, charge carrier relaxation and intra ion diffusion processes in the solid electrolytes are investigated by impedance spectroscopy analysis. The ionic interactions with the host polymers and transport properties are studied using Fourier transform infrared spectroscopy (FTIR) analysis. The thermal properties are investigated by Differential Scanning Calorimetry (DSC) analysis. For the investigation of electrode materials in supercapacitors, we have focused on ternary transition metal spinel ferrite such as manganese cobalt ferrite ($MnCoFeO_4$) nanoparticles and its composite with silver nanoparticles and reduced graphene oxide (rGO). Morphological studies are performed by High Resolution Transmission Electron Microscopy (HR-TEM) and spectroscopic characterization is done by X-ray photoelectron spectroscopy (XPS) to examine the oxidation states of each constituting elements of $MnCoFeO_4$. Types of defects in the rGO nanocomposites are probed by Raman spectroscopy.

A solid polymer electrolyte intended to use in solid-state supercapacitors must have sufficiently high ionic conductivity. Ionic conductivity of the solid electrolytes depends upon the charge carrier concentration which can be changed by doping the biopolymer (CS) with an ionic salt ($LiClO_4$). Firstly, the ionic conductivity of pure chitosan-lithium perchlorate SBE has been investigated which is found to be of the order ~ 10^{-5} S/cm. But the conductivity value is still very low for its implementation in supercapacitor applications. Plasticization and blending with other polymers are done in order to improve the ionic conductivity of the solid electrolytes further. Blending of CS with natural polymers such as PS and CMC improves the conductivity of the solid electrolytes upto an order ~ 10^{-4} S/cm, which is still quite low. Our study reveals that blending CS with PVDF (a synthetic polymer) exhibits the highest conductivity of the solid electrolyte which is of the order ~ 10^{-2} S/cm, whereas blending with another synthetic polymer (PMMA) gives the ionic conductivity value of ~ 10^{-3} S/cm. Dielectric properties of the blended polymers has been tailored by grafting with graphene oxide (GO) and multi-walled carbon nanotube (MWCNT). A significant enhancement of dielectric constant with reduced loss factor is achieved due to the nanocomposite formation. The relaxation function within the solid-state electrolytes is found to be highly non-exponential, suggesting non-Debye relaxation. The intra ion-diffusion processes has been entirely analyzed in the light of anomalous fractional diffusion model which reveals dominating anomalous diffusion behavior of the ions inside the electrolytes.

On the application front, a coin type unique symmetric supercapacitor has been developed respectively with active carbon, $MnCoFeO_4$ and rGO/$MnCoFeO_4$@Ag nanocomposites as electrode materials. We have discussed the poor accessibility of the solid-state electrolyte ions to the active sites in the nanoporous electrode materials unlike liquid electrolytes, thus demanding the evaluation of inter ionic transport properties of the charge carriers in order to determine the effective specific capacitance of the electrode materials. It has been observed that the effective

specific capacitance is increased significantly with $MnCoFeO_4$ compared to that of active carbon. On decorating $MnCoFeO_4$ with silver (Ag) nanoparticles and anchoring them onto graphene sheets enhances the effective specific capacitance remarkably. Our study reveals an enormous enhancement of effective specific capacitance ~ 750 Fg^{-1} which makes our system a promising candidate for future development of safe and cost effective electrochemical hybrid solid state supercapacitors.

Simantini Majumdar
31.1.2022

List of Publications

1. ***Simantini Majumdar***, Pintu Sen and Ruma Ray, High‑performance graphene oxide‑grafted chitosan‑starch solid biopolymer electrolytes for flexible hybrid supercapacitors, Journal of Solid State Electrochemistry (2022), DOI : https://doi.org/10.1007/s10008-021-05093-8

2. ***Simantini Majumdar***, Pintu Sen and Ruma Ray, CNT assisted anomalous Li^+ transport in CS/CMC solid biopolymer nanocomposite: an electrolyte in hybrid solid‑state supercapacitors, Ionics (2021), DOI : https://doi.org/10.1007/s11581-021-04389-z

3. ***Simantini Majumdar***, Ruma Ray and Pintu Sen, Anomalous intra diffusive behavior of chitosan/PVDF solid polymer electrolytes and the enhancement of effective specific capacitance with nanostructured spinel $MnCoFeO_4$ electrode in solid-state supercapacitors, Electrochimica Acta 385 (2021) 138295.

4. ***Simantini Majumdar*** and Ruma Ray, Ionic conduction and charge carrier relaxation in chitosan acetate based solid biopolymer electrolyte embedded with $LiClO_4$, Journal of Polymer Research (2021) 28:157.

5. ***Simantini Majumdar*** and Ruma Ray, γ-irradiation induced dielectric properties of chitosan based solid biopolymer electrolytes, AIP Conference Proceedings 2220, 040001 (2020).

6. ***Simantini Majumdar***, Pintu Sen and Ruma Ray, Ionic interactions and transport properties in chitosan-starch based blend solid biopolymer electrolytes, Materials Today: Proceedings 18, 4913–4920 (2019).

7. ***Simantini Majumdar***, Sanchari Sarkar and Ruma Ray, Dielectric and transport studies of graphene oxide@chitosan based solid biopolymer nanocomposite electrolytes, AIP Conference Proceedings 2115, 030140 (2019).

8. ***Simantini Majumdar***, Pintu Sen and Ruma Ray, Graphene oxide induced high dielectricity in CS/PMMA solid polymer electrolytes and the enhanced specific capacitance with Ag decorated $MnCoFeO_4$ nanoparticles anchored graphene sheets in hybrid solid-state supercapacitors (under review).

PUBLICATIONS (NOT RELATED TO THIS THESIS)

- ***Simantini Majumdar***, Somasri Hazra, Moutushi Dutta Choudhury, Suparna Dutta Sinha, Shantanu Das, Tapas Ranjan Middya, Sujata Tarafdar and Tapati Dutta, A study of the rheological properties of visco-elastic materials using fractional calculus, Colloids and Surfaces A: Physicochem. Eng. Aspects 516 (2017) 181–189.

- A. Mondal, N. Giri, S. Sarkar, ***S. Majumdar*** and R. Ray, Tuning the photocatalytic activity of ZnO by TM (TM = Fe, Co, Ni) doping, Materials Science in Semiconductor Processing 91 (2019) 333–340.

- S. Das, N. Giri, S. Sarkar, A. Mondal, ***S. Majumdar***, S. Giri and R. Ray, Uncompensated grain boundary spin driven exchange bias effect in granular NiO film, Solid State Communications 298 (2019) 113642.

Contents

Chapter 1

Motivation and Arrangement of the Thesis

1.1. Motivation and objectives

The rapid worldwide consumption of fossil resources (such as coal, oil, gas) and the undesirable consequences of environmental pollution are emerging drastically which lead to the development of green, sustainable and highly efficient electrochemical energy storage devices such as batteries and supercapacitors. Supercapacitors have gained its fame over batteries and conventional capacitors due to its extremely high power density, moderate energy density, rapid charge-discharge dynamics and excellent cyclic retention which have potential applications in hybrid power systems such as electric vehicles, memory backup sources, emergency doors etc. But the traditional liquid-state supercapacitors (i.e. liquid electrolyte based supercapacitors) has various drawbacks such as self-discharge and harmful liquid leakage problems along with difficulties in operation under low temperature and designing issues. Therefore, recent researches are being done on solid-state supercapacitors (i.e. solid electrolyte based supercapacitors) which are light in weight, flexible and secure for various applications including powering of miniaturized electronic devices. The main objective of this dissertation is to develop new materials (both solid electrolytes and electrodes) for solid-state supercapacitors having improved performance in comparison with present technology. In this dissertation, I have focused my research on developing environment friendly solid-state supercapacitors with solid electrolytes based on natural polymer (chitosan) and spinel ferrite based electrode materials. The biodegradable property of chitosan and its ease of fabrication in mechanically strong thin film form has motivated us to investigate its electrolytic nature. Conductivity enhancement in the solid electrolytes is an essential criterion for their implementation in solid-state supercapacitors. This thesis is majorly concerned with some interesting properties displayed by chitosan on doping with salt and plasticizer, exposing to gamma irradiation, blending with other compatible polymers and finally grafting with insulating and conducting nanofillers.

1.2. Materials studied

First we report a study on the ionic conduction and charge carrier relaxation in chitosan films with different concentrations of lithium perchlorate ($LiClO_4$) as an ionic salt. The solid biopolymer electrolytes (SBE) have been synthesized by solution casting technique. The dielectric and ion transport properties of the SBE are studied at room temperature (300 K). The shape change of the electric modulus spectra in chitosan based solid electrolytes for different ionic salt concentrations is found to be an effect of the inclusion of high frequency limiting dielectric constant in the modulus definition. The interactions between the biopolymer and $LiClO_4$ salt has been investigated in details with Fourier Transform Infrared Spectroscopy.

Next, we report a study on the effect of high energy gamma irradiation having doses ranging from 0-10 kGy on both plasticized and plasticizer-free chitosan based solid biopolymer electrolytes. The plasticizer used for this study is ethylene carbonate (EC). Gamma irradiation induced dielectric and transport properties of chitosan based SBE are investigated at room temperature (300 K). Theoretical analyses of the permittivity and electric modulus spectra infer that the gamma irradiated SBEs exhibit non-Debye type relaxations.

Further, EC-plasticized chitosan based SBE is doped with different weight fractions of graphene oxide (GO) which are prepared by solution blending and evaporation casting technique. The GO composition dependence of dielectric constant, loss factor and transport parameters are investigated at room temperature (300 K). Enhancement of conductivity, mobility and dielectric constant along with reduction of loss factor makes graphene oxide@chitosan based solid nanocomposite electrolytes attractive for energy storage applications.

In our next work, a highly conducting solid polymer electrolyte based on chitosan (CS) and polyvinylidene difluoride (PVDF) blend is prepared with $LiClO_4$ as an ionic salt and glycerol as a plasticizer. High dielectric constant with low loss factor demands its intensive capacitive nature. In order to understand the mechanism of the conductivity of the solid polymer electrolytes, a fractional diffusive model has been adopted. Ion transport parameters have been evaluated by FTIR spectra through deconvolution technique. Finally, an innovative coin type hybrid solid-state supercapacitor has been developed with nano crystallites of manganese cobalt ferrite ($MnCoFeO_4$) as electrode material and CS/PVDF blended polymers as solid polymer electrolyte. A unique model has been approached to evaluate the inter ionic transport properties of the charge carriers in order to determine the effective specific capacitance of the electrode materials. An effective specific capacitance of 750 Fg^{-1} has been achieved with this new hybrid solid-state supercapacitor which is ~ 24 times enhanced compared to that achieved with the electrical double layer supercapacitor (EDLC) containing the same solid electrolyte.

Next, a conducting biodegradable solid polymer nanocomposite electrolyte comprising the blend of chitosan (CS) and carboxymethyl cellulose (CMC), plasticized with glycerol, lithium perchlorate ($LiClO_4$) as dopant salt and carbon nanotube (CNT) as nanofiller has been prepared. The ion dynamics and charge carrier relaxation properties in CNT incorporated solid biopolymer nanocomposite electrolytes (SBNE) are studied. The scaling of the conductivity and permittivity spectra are performed to study the effect of dopant composition on the relaxation mechanism. A symmetric hybrid solid-state supercapacitor has been fabricated with active carbon and nano crystallites of manganese cobalt ferrite ($MnCoFeO_4$) as electrode materials and CNT incorporated CS/CMC blended biopolymers as solid state nanocomposite electrolyte, obtaining a fairly good effective specific capacitance of ~ 94 Fg^{-1}.

In our next work, we report a study on the charge carrier relaxation and transport properties of graphene oxide (GO) grafted blended solid biopolymer electrolytes comprising of chitosan (CS) and potato starch (PS) with $LiClO_4$ as a charge carriers and glycerol as a plasticizer. The ion-diffusion processes in the GO grafted SBNE has been analyzed based on anomalous fractional diffusion model. The effect of GO in the CS/PS blended SBNE are investigated from the molecular point of view. A hybrid solid-state supercapacitor has been fabricated based on manganese cobalt ferrite ($MnCoFeO_4$) nanocrystallites as electrode and GO grafted CS/PS SBNE. This demonstates a high effective specific capacitance of ~ 288 Fg^{-1} with 9 wt. % GO grafted blended nanocomposite electrolyte which is ~ 31 times enhanced compared to that achieved with GO-free CS/PS solid electrolyte.

Lastly, a new hybrid solid-state supercapacitor based on silver decorated manganese cobalt ferrite ($MnCoFeO_4$) nanoparticles anchored graphene sheets as advanced electrode material and graphene oxide (GO) grafted chitosan (CS) / polymethyl methacrylate (PMMA) blend as solid polymer electrolytes is developed. Dielectric and thermal properties of the GO grafted CS/PMMA solid polymer nanocomposite electrolytes (SPNE) are studied. The low frequency dispersion in the AC conductivity spectra is analyzed considering the fractal nature of the interfacial region of the electrode and SPNE. An effective specific capacitance of ~ 294 F g^{-1} is obtained with Ag decorated $MnCoFeO_4$ nanoparticles anchored onto rGO electrode which is ~2.5 times enhanced compared to that with $MnCoFeO_4$ electrode.

1.3. Outline

The thesis is organized as follows:

Chapter 1 presents the research motivation and outline of the thesis.

Chapter 2 gives an introduction to the background of our research and the scope of this study.

Chapter 3 describes the experimental procedures and principles applied in this work.

Chapter 4 presents the ionic conduction and charge carrier relaxation in chitosan acetate based solid biopolymer electrolytes embedded with $LiClO_4$.

Chapter 5 presents the conductivity and dielectric studies of plasticizer-free and plasticized chitosan based solid biopolymer electrolytes exposed to gamma irradiation.

Chapter 6 provides the synthesis, dielectric and transport studies of graphene oxide@chitosan based solid nanocomposite electrolytes and explores its dielectric properties.

Chapter 7 presents the anomalous intra diffusive behavior of CS/PVDF blend solid polymer ekectrolytes and the enhancement of effective specific capacitance with nanostructured spinel $MnCoFeO_4$ electrode in solid-state supercapacitors.

Chapter 8 provides CNT assisted anomalous Li^+ transport in CS/CMC solid biopolymer nanocomposite electrolyte and presents its application in hybrid solid-state supercapacitors.

Chapter 9 presents the high-performance energy storage of graphene oxide grafted chitosan-starch solid biopolymer electrolytes in hybrid solid-state supercapacitors and reveals its charge carrier relaxation, dielectric and transport properties.

Chapter 10 presents graphene oxide induced high dielectricity in CS/PMMA solid polymer electrolytes and the enhanced specific capacitance with Ag decorated $MnCoFeO_4$ nanoparticles anchored graphene sheets in hybrid solid-state supercapacitors.

Chapter 11 presents general conclusions.

Chapter 2

Introduction

2.1. Solid electrolytes

Solid electrolytes represent a class of solid materials that have exceptionally high ionic conductivity ($10^{-5} - 10^{-1}$ S/cm) at room temperature, comparable to that of common liquid electrolytes. These are also termed as "*superionic solids*" or "*fast ion conductors*". In 1834, English physicist and chemist Michael Faraday had introduced the term "*ion*" by discovering their motion in liquid and solid electrolytes. The word "ion" is originated from the Greek term *ion* or *ienai* which means "to go" or "moving". *Solid state* ionics is an emerging area of materials science which involves the study of the fast ion conductors (solid electrolytes). The term "Solid State Ionics" was coined by Takehiko Takahashi of Japan in 1970. Since then it has been the field of interest among the researchers, as these materials have technological applications in various energy storage and energy conversion devices (such as batteries, supercapacitors, dye-sensitized solar cells, etc.). Depending on the concentration of the defects present, ionic solids are classified into two categories: one is "low concentration type defects" in which the concentration of defects is very low ($< 10^{18}$ cm^{-3}) and the other is "high concentration type defects" in which the defect concentration is very high ($> 10^{20}$ cm^{-3}). An ionic solid having high defect concentration is called superionic solid. The ionic conductivity of a superionic solid depends on various physical properties such as its crystal structure, degree of lattice disorder, size and concentration of the mobile ions, ion-ion interactions, bonding characteristics, availability of conducting pathways etc. [1,2]. A superionic solid (solid electrolyte) possess the following characteristics:

- Ions are the principal charge carriers.
- Ionic transference number is close to unity ($t_{ion} \sim 1$).
- Ionic conductivity is high of the order of $10^{-5} - 10^{-1}$ S/cm.
- Electronic conductivity is negligible.
- Activation energy is low (0.1 eV – 1 eV).
- Highly disordered, layered or channeled internal structure.

The most common solid electrolyte is Yttria-stabilized Zirconia (YSZ). Major breakthrough in the field of solid state ionics occurred in 1937 with the development of the first solid oxide fuel cell with YSZ solid electrolyte by Baur and Preis [3]. The discovery of fast sodium ion conduction in Beta-alumina solid electrolyte (BASE) by the researchers, Y. Yao, J.T. Kummer and N. Weber at Ford Motor Company and silver ion conduction in rubidium silver iodide ($RbAg_4I_5$) had further enriched the field of solid state ionics. Thereafter a huge number of superionic solids have been discovered which have shown their potential applications in solid-state electrochemical device applications. Superionic solids can be divided into different classes based on their morphology, phase and composition which is shown in Fig. 2.1.

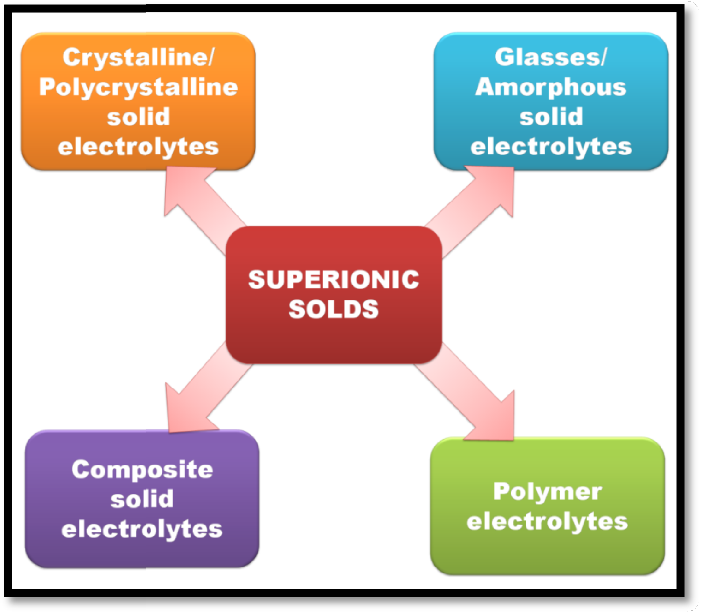

Fig. 2.1. Classification of superionic solids.

Crystalline or *polycrystalline solid electrolytes* are those materials in which ions migrate within a rigid crystalline framework. These materials are further divided into two subcategories, one is soft framework crystal and the other is hard framework crystal. Soft framework crystals are characterized by high polarizability of ions, ionic bonding, low Debye temperature and a sharp order-disorder phase transition between high and low conducting phases, whereas covalent bonding, high Debye temperature, low polarizability of mobile ions and a less sharp order-disorder phase transition are the characteristic feature of hard framework crystals. Silver iodide (AgI) and Beta-alumina solid electrolyte (BASE) are the two most studied materials belonging to the soft and hard framework crystal categories, respectively [4,5]. *Ion conducting glasses*, also known as *amorphous solid electrolytes* are highly disordered materials having high isotropic ionic conduction and are prepared by quenching molten mixture of a glass former, a glass network modifier (usually a metal oxide) and a dopant salt (usually a metal halide). In 1973, Kunze *et al* [6] reported the first Ag^+ ion conducting glass, AgI-Ag_2SeO_4 which was completely amorphous in nature. Conductivity up to 10^{-2} S/cm was obtained by varying the concentration of glass former, modifier and dopant salt. *Composite solid electrolytes* are two-phase solid systems in which submicron or nano-sized filler particles such as SiO_2, Al_2O_3 etc. are dispersed in different ionic salts (like AgCl, KCl, AgBr etc.) in order to tune the material properties such as ionic conductivity at room temperature, physical and mechanical properties. In 1973, a significant enhancement in conductivity (1.2×10^{-5}) in LiI- Al_2O_3 system has been reported by Liang *et al* [7]. The last class of superionic solids are *polymer electrolytes* which have garnered huge attention among the researchers worldwide in the recent years since they have high potential to replace classical (liquid) electrolytes in the electrochemical energy storage devices. Fenton *et al* [8] discovered the first polymer electrolyte in 1973 by doping alkali salts in polyethylene oxide (PEO). Polymer electrolytes have several advantages over other superionic solids and liquid electrolytes which include their better mechanical properties, excellent thermal stability, wide electrochemical window, ease of fabrication in thin film form, good flexibility, intimate contact between electrode and electrolyte, free from issues of leakage, high safety, cost effective, light weight etc. This class of superionic solids is the topic of research interest in the present dissertation and hence are discussed in great details.

2.2. Polymer Electrolytes

Polymer electrolyte is an essential component in electrochemical devices such as rechargeable batteries, supercapacitors, etc. The term ‘polymer’ was derived from the Greek words *poly* means ‘many’ and *meros* means ‘parts’. A polymer is a very large molecule (macromolecule) composed of many small individual repeating units called monomers which are connected by covalent bonds. The chemical process through which the structural units (monomers) are united together to form a complex polymer molecule is called “polymerization” [9-11]. The polymer molecules which essentially consist of carbon atoms in their backbone chain are called organic polymers. There are two types of organic polymers: (1) natural and (2) synthetic. Common examples of natural organic polymers are starch, cellulose, chitosan, etc. whereas polyethylene oxide (PEO), polyvinyl alcohol (PVA), etc. are few examples of synthetic organic polymers. Inorganic polymers, on the other hand, are polymer materials that contain no carbon atoms in the primary backbone. The most common example of inorganic polymer is polydimethylsiloxane (PDMS) which is also known as silicone rubber. Polymers, in general, are semi-crystalline i.e. both crystalline and amorphous domains are present (schematic representation shown in Fig. 2.2).

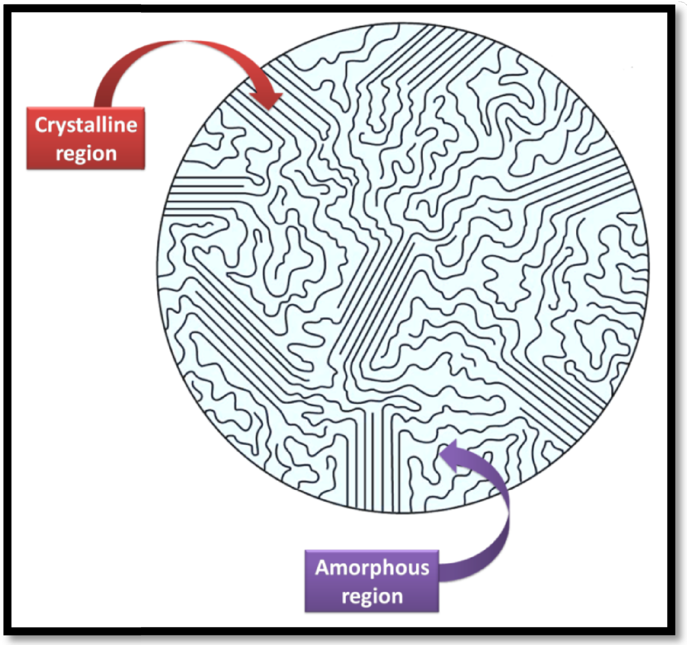

Fig. 2.2. Schematic representation of crystalline and amorphous regions of a polymer.

A polymer can be electron conducting (termed as "conducting polymers") and/or ion conducting (termed as "polymer electrolytes"). Polymer electrolytes are macromolecular systems capable of ion conduction on doping with ionic salts into it. In 1979, Armand *et al* [12] first proposed the use of polyether-alkali-metal based salt complexes (polymer electrolytes) in electrochemical devices. The polymer electrolytes for their application in solid-state supercapacitors and batteries must satisfy the following criteria:

- Ionic conductivity of the order of 10^{-3} S/cm or higher is desirable at room temperature.
- Must have low electronic conductivity.
- High thermal stability is desirable since charge/discharge may release heat which might result in degradation of the supercapacitor.
- High mechanical strength and stability are important.
- Ease of fabrication and low in cost are very important for commercial purposes.
- Must have good compatibility with the electrode material.
- High electrochemical stability is important.

On the basis of composition, preparation routes and morphology, polymer electrolytes can be divided into the following categories as shown in Fig. 2.3.

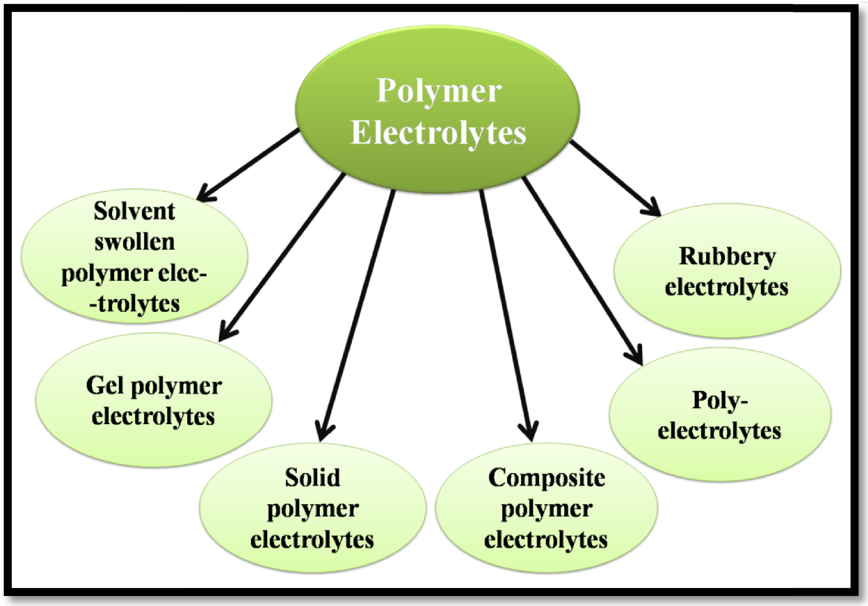

Fig. 2.3. Classification of polymer electrolytes.

2.2.1. Solvent swollen polymer electrolyte

In solvent swollen polymer electrolytes, solvents (aqueous or non-aqueous) swell the polymer host matrix [such as polyvinyl alcohol (PVA), polyvinylpyrrolidone (PVP) etc.] to dope the ionic solute like H_3PO_4 in the swollen polymer matrix and allow the motion of ions in solvent rich region of polymer host. In this case, conduction is significant when a continuous network is formed throughout the polymer matrix. Conductivity of this kind of polymer electrolytes depends on temperature, concentration and pretreatment history of the polymers, which leads to the instability in the material.

2.2.2. Gel polymer electrolyte (GPE)

Gel polymer electrolyte (GPE) was first introduced by Feuillade and Perche in 1975 [13]. GPE can be prepared by mixing an organic liquid solvent with a salt followed by addition of polymer material to provide the mechanical stability. In short, a GPE is defined as a system consisting of a polymer network swollen with solvent, therefore possessing both the diffusive transport properties of liquids and the cohesive properties of solids. An alkali metal salt is usually used to prepare GPE and the polymers used are PMMA (Polymethyl methacrylate), PEO (Polyethylene dioxide), PVDF (Polyvinylidene difluoride) etc. The solvents commonly used to prepare GPE are liquid plasticizers, hence they are also known as “plasticized polymer electrolyte”. The commonly used liquid plasticizers are dimethylformamide (DMF), glycerol, mixture of ethylene carbonate (EC) and propylene carbonate (PC), etc. In recent years, a new solvent has been introduced to prepare GPEs which is ionic liquid (IL). Ionic liquids (ILs) are a special group of molten salts possessing high values of ionic conductivity, non-inflammable, better thermal and electrochemical stability and wider liquid phase temperature range [14,15]. Both ionic liquid and liquid plasticizers act as lubricants by reducing polymer chain rigidity [16,17]. A GPE usually exhibits ionic conductivity of the order of $10^{-5} - 10^{-2}$ S/cm [18-25]. In 1994, Telcordia Technologies (former Bellcore Company) introduced the first commercial GPE based lithium ion battery based on PVDF-HFP (polyvinylidene fluoride-hexofluoropropylene) polymer [26,27]. However, GPEs have certain drawbacks such as their poor mechanical properties, soft morphology and appreciable viscosity which may be the cause of internal short-circuits and thereby giving rise to safety issues which hamper their use in wider practical applications [28].

2.2.3. Solvent free polymer-salt complex or solid polymer electrolyte (SPE)

The ionic motion in the absence of a solvent inside the polymer matrix is a new phenomenon. Solid polymer electrolyte or dry SPE is a solvent free high molecular weight polar polymer host having ion conducting phase formed by dissolving monovalent alkali metal / ammonium salts. In order to form a stable SPE, the lattice energy of the salt should be low so that the dissolution of salt in the host polymer matrix is facilitated. The macromolecule itself acts as a solvent for the salt in a polymer matrix which becomes partially dissociated in the matrix and is responsible for the electrolytic behavior as conductivity comes due to the molecular motion in the structure. A SPE is prepared by solution casting technique in which salt is dissolved in polymer solution and poured in glass or polypropylene petri dishes and allowed to dry at room temperature or in a vacuum oven to form free-standing solid thin films. The distinct characteristics of SPE compared to other solid electrolytes are as follows:

- ♠ Easy processing technique.
- ♠ Capability to form flexible free-standing thin films.
- ♠ High ionic conductivity
- ♠ Light weight.

Solid polymer electrolytes (SPEs) are therefore promising materials for fabricating flexible and light-weight solid-state electrochemical energy storage devices. First solvent free polymer-salt complex or SPE investigated was polyethylene oxide (PEO) based system [29]. The most significant property of any SPE is its ionic conductivity which is due to the local relaxation and segmental motion of the polymer chains that continuously creates dynamic coordination sites along which the migration of ions take place. Ion transport is characterized by intra- and inter-chain ion hopping between the coordination sites. The schematic representation of this ion hopping motion assisted by polymer chain segmental motion in a SPE is shown in Fig. 2.4. Ionic conduction essentially takes place in the amorphous regions of the polymers due to their less well-formed structures which are more flexible and contain more mobile chains [30-34]. In other words, SPE works in such a region where crystallinity is low and segmental motion is high.

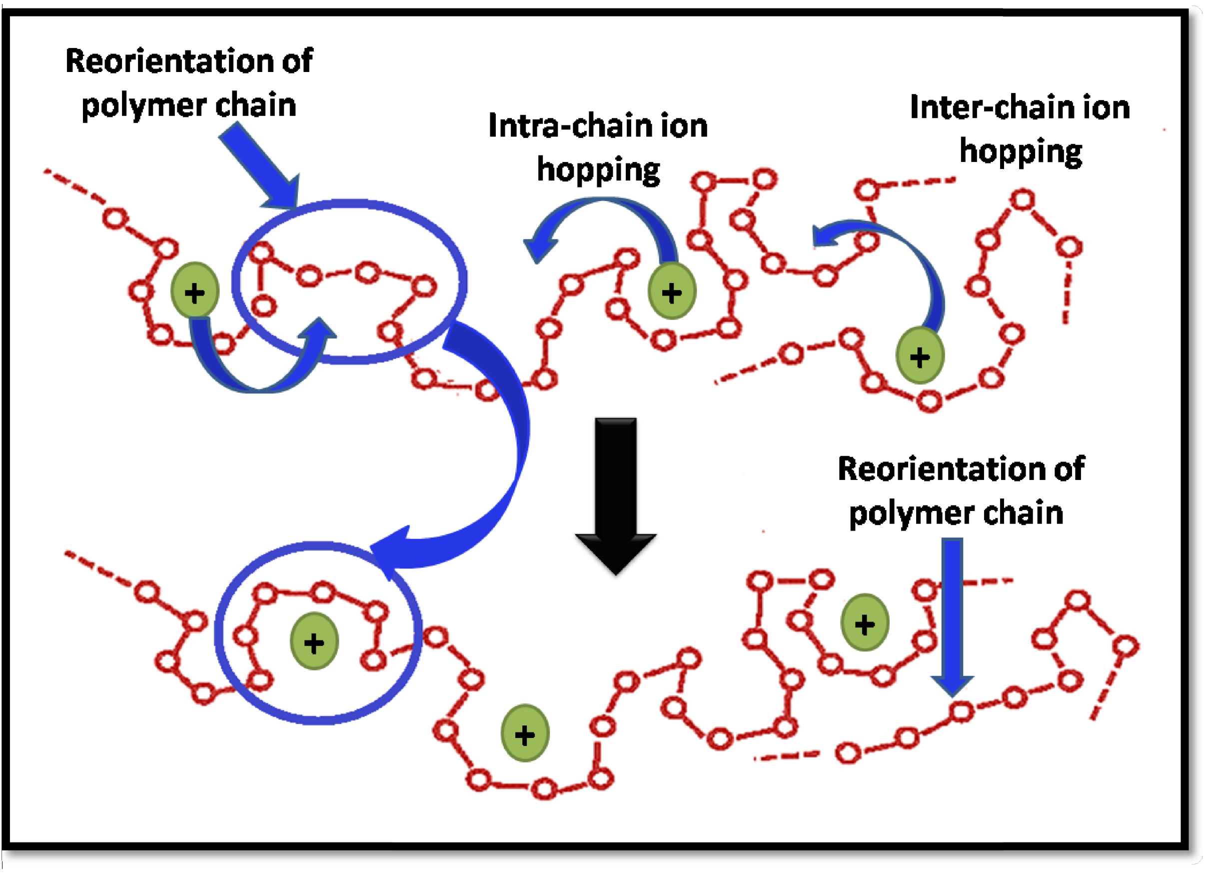

Fig. 2.4. Schematic representation of cationic motion in a solid polymer electrolyte assisted by segmental motion of the polymer chain.

The polymer segmental motion is ceased below the glass transition temperature (T_g) of a polymer. There is significant segmental motion of the polymer chains between T_g (glass transition temperature) and T_m (melting temperature). There are several factors which affect the ionic transport in the SPEs such as degree of dissociation of salt and its concentration, degree of aggregation of charge carriers, dielectric constant of host polymer and polymer chain mobility

[35,36]. Conductivity values of few solvent free polymer-salt complexes or dry SPEs are listed in Table 2.1.

Table 2.1. Some important solvent free polymer-salt complexes or solid polymer electrolytes (SPE) along with their conductivity values.

Solid Polymer Electrolytes	DC conductivity (S/cm)	Temperature (^{0}C)	References
PEO + NH_4NO_3	5.00×10^{-7}	RT	[37]
PEO + NH_4ClO_4	1.0×10^{-5}	30	[38]
PEO + $LiPF_6$	1.5×10^{-5}	RT	[39]
PEO + $LiCF_3SO_3$	1.3×10^{-6}	RT	[40]
PAN + NH_4SCN	5.79×10^{-3}	RT	[41]
PVDF + $LiPF_6$	2.3×10^{-6}	120	[42]
Chitosan + NH_4I	3.73×10^{-7}	RT	[43]
Rice starch + LiI	4.68×10^{-5}	RT	[44]
Potato starch + NH_4I	2.40×10^{-4}	RT	[45]
CMC + NH_4F	2.68×10^{-7}	RT	[46]
Corn starch + $LiClO_4$	1.28×10^{-4}	80	[47]
Gelatin + $LiClO_4$	$\sim 10^{-4}$	RT	[48]
PAN + LiBOB	$\sim 10^{-5}$	RT	[49]
CMC + $(NH_4)_2CO_3$	7.71×10^{-6}	RT	[50]

2.2.4. Composite polymer electrolyte (CPE)

Composite polymer electrolyte (CPE) is defined as a system in which a small fraction of nano / micro-sized inorganic (ceramic) or organic filler particles are dispersed in the polymer electrolyte matrix. These are basically two-phase composite solid polymer electrolyte systems. SPEs serve as phase I, while the filler materials serve as phase II. The filler particles are used to modify the electrical, mechanical and optical properties of the SPE matrix. The incorporation of inert ceramic filler particles (such as alumina or Al_2O_3) in the PEO based SPE was first introduced by Weston *et al* [51]. It has been observed that the filler remarkably improved the mechanical strength of the CPE. Since then, CPEs incorporated with different types of filler materials such as TiO_2, SiO_2, ZnO, etc. were investigated by various researchers [52-55]. Generally, it has been observed that nano / micro-sized filler particles have a positive effect on the CPE, especially enhancing the ionic conductivity of the system by few orders of magnitude compared to the undispersed system. Incorporation of fillers in the polymer electrolytes generally increase the amorphous region of the polymer and provide a new ion conducting path through polymer-filler interactions [55]. The shape, size, surface area and volume fraction of the filler particles play active roles in improving the electrical properties of a CPE [56-59]. Weiczorek *et al* [56,57] reported a significant increase in conductivity in Al_2O_3 incorporated PEO based CPE when the size of the Al_2O_3 particles was smaller than 4 µm. It was suggested that the surface groups of ceramic filler particles play a very significant role in promoting local structural modifications. Scrosati *et al* [55] and Croce *et al* [58] reported significant enhancement in conductivity by dispersing submicron particles of TiO_2 and SiO_2 in PEO based CPE. Weiczorek *et al* [56] applied the Lewis acid-base theory to understand the mechanism of ion transport in CPE complexed with alkali metal salts. Enhancement in ionic conductivity and electrochemical properties have also been reported with ferroelectric fillers (such as $BaTiO_3$, $PbTiO_3$, etc.) incorporated into the PEO based CPE [60,61]. Ferroelectric fillers result in a more stable system compared to other filler materials. Few examples of composite polymer electrolytes along with their conductivity values at room temperature are listed in Table 2.2.

Table 2.2. Some important composite polymer electrolytes (CPE) along with their conductivity values.

Composite Polymer Electrolytes	DC conductivity (S/cm)	Temperature (^{0}C)	References
PEO + $LiClO_4$ + α-Al_2O_3	1×10^{-5}	25	[62]
PEO + NH_4I + Al_2O_3	8×10^{-4}	70	[63]
PEO + LiI + Al_2O_3	1×10^{-4}	RT	[64]
PEO + $LiClO_4$ + SiO_2	1×10^{-5}	RT	[55]
PVdF-HFP + $LiClO_4$ + ZnO	1.043×10^{-3}	RT	[54]
PEO + $LiClO_4$ + $BaTiO_3$	1×10^{-3}	70	[61]

2.2.5. Polyelectrolyte

Polyelectrolytes are characterized by self generating ion groups that are covalently bonded with the main chain of the polymers. There exists a counter-ion firmly bonded to the oppositely charged fixed ions on the polymer chain by the coulombic force of attraction in dry conditions to maintain the electro-neutrality [65,66]. After the uptake of high dielectric constant solvent (water), these solvated counter ions are free to migrate within the polymeric system. The unattached counter ions are responsible for its mobility and provide higher ionic conductivity to the system. The unique feature of polyelectrolytes is the single ion transport in the bulk systems. Ionic conductivity is a function of solvent (mostly water) content which makes these electrolytes suitable for humidity sensor applications. Some important examples are poly-sulphonic acid based polyelectrolytes such as NAFION, Polystyrene sulphate etc. NAFION is a good H^+ ion conductor which is commercially used in H_2 / O_2 fuel cells [67].

.

2.2.6. Polymer-in-salt or Rubbery electrolyte

Rubbery electrolytes were first introduced by Angell *et al* [68]. They are synthesized by dissolving a small amount of high molecular weight polymer in a low temperature molten salt mixture in order to form a rubbery material having low glass transition temperature, below room temperature [69]. The most commonly used polymers for this system are polyethylene oxide (PEO), polypropylene oxide (PPO) etc. Since a large amount of salt is mixed with a low amount of polymer in rubbery electrolytes, they are also referred as “polymer in salt” system. The conductivities of these electrolytes are higher than that of conventional polymer electrolytes. However, the dissolved salts have the tendency to crystallize at lower temperatures which affects the electrochemical stability of the electrolytes and hence, obstruct their use in practical electrochemical device applications.

2.3. Natural biopolymer versus synthetic polymer hosts

The preparation of polymer electrolytes require at least one polymer host which can be classified into two broad categories that are natural and synthetic polymers. Most of the literature reports in the past years are based on synthetic polymer based polymer electrolytes which are derived from petrochemicals. Synthetic polymers have poor degradability and therefore, these polymers will end up as wastes in the ground and oceans and thus their widespread use can cause serious environmental pollution. Few examples of synthetic host polymers are polyethylene oxide (PEO), polyvinylidene fluoride (PVDF), polymethyl methacrylate (PMMA), polyacrylonitrile (PAN), etc. Natural or bio-based polymers (biodegradable polymers) have been emerged as the possible substitute to these non-biodegradable synthetic polymers and are expected to play a significant role in a society moving towards a sustainable and environment friendly materials. Natural biopolymers are non-toxic, reusable and recyclable, hence the use of these materials can contribute in minimizing the environmental waste, thereby lowering the cost of the energy storage and energy conversion devices. Examples of some natural host biopolymers are starch, cellulose, gelatin, chitosan, dextran etc. The categories of polymers and their relevant examples along with the generalized structures are summarized in Fig. 2.5.

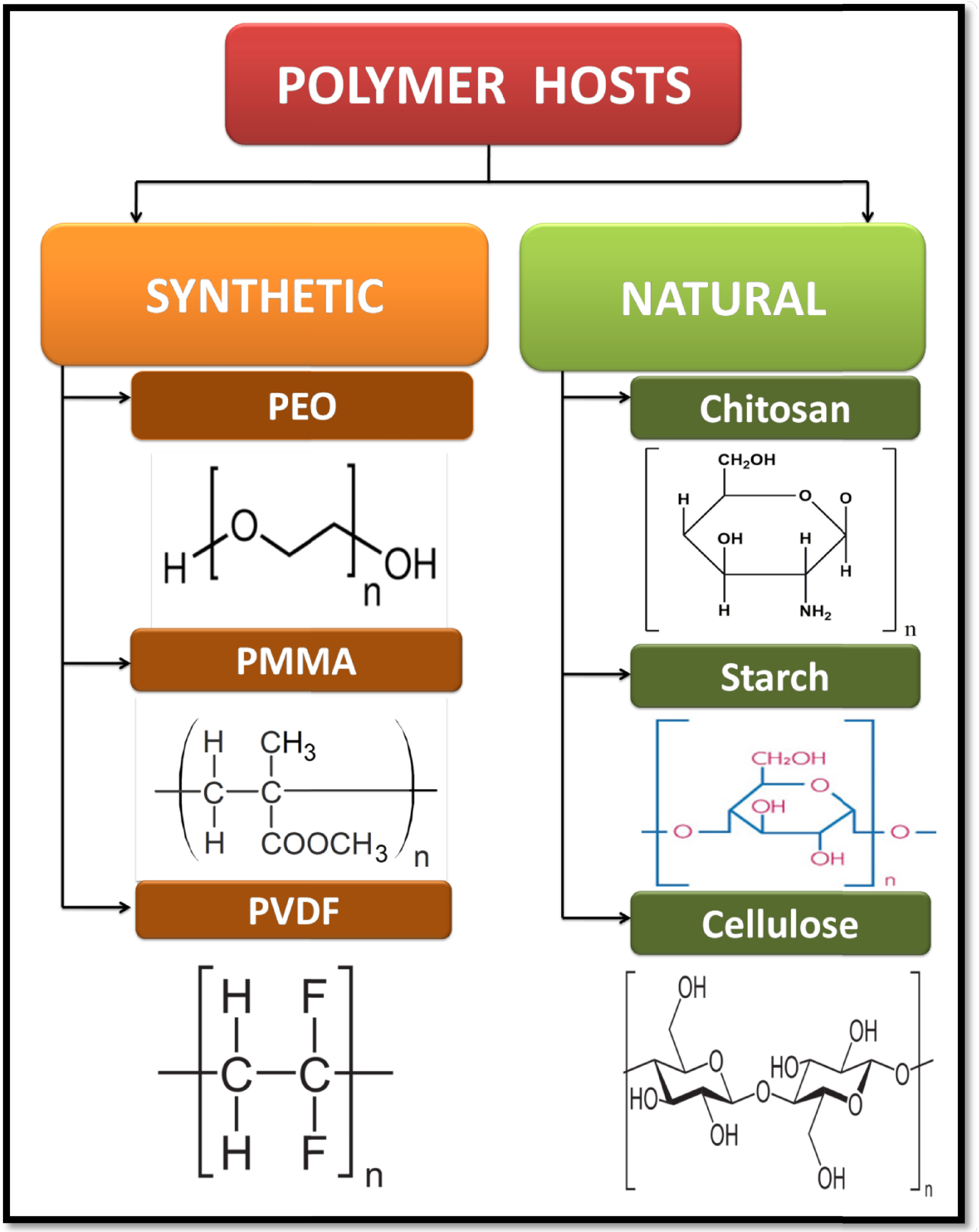

Fig. 2.5. Few examples of synthetic and natural polymers along with their generalized structures.

To develop a better solid polymer electrolyte (SPE), the host polymer need to possess some important characteristics in order to target higher conductivity values, as suggested by Park *et al* [70]. The host polymer matrix requires the presence of polar groups, mainly containing nitrogen, oxygen and sulphur which are important in salt complexation and solvation [71]. Among all the natural biopolymer hosts, chitosan which is composed of two main groups i.e. glucosamine and *N*-acetyl glucosamine units linked by β-1,4-glycosidic bonds, has attracted considerable attention of researchers in the development of SPE since the past few decades [71]. The presence of polar functional groups in chitosan such as hydroxyl and amine can give the material a dipole moment that affects the dielectric polarization. Hence, intermolecular interactions are created between these polar groups of chitosan and alkali metal salt ions, leading to the solvation of salt [71]. Also chitosan has some other outstanding features such as its abundant availability, low cost of extraction, non-toxicity, biodegradability, biocompatibility and excellent mechanical strength [72,73]. Hence, chitosan can be considered as a fascinating polymer host for developing SPE and thus it has potential applications in the energy industry.

2.4. Chitosan based solid biopolymer electrolytes

Chitosan is a semi-crystalline polymer produced by the partial deacetylation of chitin. It is the second most abundant natural biopolymer available in the nature. The major sources of chitin are shells of crabs, lobsters, shrimps and scale of fish. Generally, if the degree of deacetylation (DD) of chitin is more than 70 % after the process of deacetylation, it is considered as chitosan. The DD of commercially available chitosan is in the range of 70 – 90 %. In recent decades, several electrolytes have been developed using chitosan which demonstrated high conductivity, good mechanical strength and stability over a wider potential and temperature range which made them attractive for energy storage applications [72]. The electrical properties of solid biopolymer electrolytes based on chitosan doped with various lithium and proton donor salts such as $LiCF_3SO_3$ [74], lithium acetate [75], NH_4I [43], NH_4Cl [76] have been reported in the literature by various researchers.

2.4.1. Proton-conducting solid biopolymer electrolytes

Proton-conducting solid polymer electrolytes have attracted much attention of researchers owing to the smaller size and higher conductivity of the proton, which facilitates conduction in the SPE [77]. The proton can be provided in two ways. The addition of inorganic acids is one way to donate protons to the polymer host, but they can cause serious problems such as chemical degradation and corrosion [72,77]. Another way is to add proton donor salts such as ammonium salts that produce protons by dissociation. Therefore, ammonium salts are being chosen by most researchers due to their high thermal stability and low lattice energy in comparison to other salts [78]. In the past years, various chitosan-based solid biopolymer electrolytes have been developed by doping with ammonium salts [43,76]. However, pristine chitosan has very low conductivity which is one of the major challenges in developing high-performance chitosan based solid biopolymer electrolytes [72]. This issue has been tackled by doping salts in polymer matrix synthesized by blending chitosan with other polymers which has been discussed in detail in the subsequent section 2.6.1. Polyethylene oxide (PEO) is one of the most widely used polymers for preparing solid polymer electrolytes since they have good conductivity at room temperature owing to the presence of lone pair electrons in the polyether groups in its structure [79]. These free electron pairs make a coordination complex with the salt cations. According to the previous reports, a maximum amorphous structure is obtained by blending chitosan and PEO at 3:2 ratio [79]. It is well documented that the amorphous portion is principally responsible for ion conduction. Hence, a polymer blend of chitosan and PEO has been doped with NH_4NO_3 which exhibited a maximum conductivity of 1.02×10^{-4} S/cm at room temperature [79]. Another proton-conducting SPE with NH_4SCN as proton donor salt in the chitosan–PEO polymer host was reported in the literature, which exhibited a maximum conductivity of 2.11×10^{-4} S/cm [77]. These results reveal a remarkable increase in the conductivity compared to that of pure chitosan.

2.4.2. Li^+ conducting solid biopolymer electrolytes

Lithium ion (Li^+) conducting solid polymer electrolytes have gained immense popularity owing to their various suitable properties including lightness in comparison to other metals and they provide electrochemical stability up to 4 V which for a proton-conducting SPE is up to 1-2 V [80]. According to previous literature reports, various lithium salts such as $LiBF_4$, LiTFSI, $LiClO_4$ etc. have been incorporated in the polymer matrix for developing Li^+ conducting chitosan based solid biopolymer electrolytes [81-83]. The lithium salts can be easily dissolved in the chitosan biopolymer matrix due to the coordination interaction between the polar functional groups of the host biopolymer and Li^+ cations [73]. Conductivity of the order of ~ 10^{-6} S/cm was reported with a polymer blend of chitosan and methyl cellulose doped with $LiBF_4$ salt [81]. The salt $LiBF_4$ has low lattice energy compared to other lithium salts [81]. In another report, a polymer blend of chitosan and PEO incorporated with LiTFSI salt demonstrated an ionic conductivity of the order of 10^{-6} S/cm at room temperature [82]. The bulky structure of LiTFSI enhances the electrochemical stability. Also LiTFSI dissociates well in low dielectric solvents and exhibits excellent thermal stability [73,84]. Another report suggests a SPE material developed by incorporating $LiClO_4$ in the host polymer matrix made of the chitosan-polyethylene glycol blend with ethylene carbonate and propylene carbonate as the plasticizers [83]. This SPE exhibits a maximum conductivity of ~ 10^{-4} S/cm at room temperature [83]. The significance of incorporation of plasticizers in the polymer matrix will be discussed in detail in the subsequent section 2.6.3. $LiClO_4$ possesses high dissociation energy and composed of a small-sized cation and a large-sized anion which makes it highly preferable and compatible as a dopant salt for developing solid polymer electrolytes [85]. Another Li^+ conducting SPE with $LiClO_4$ salt in chitosan-dextran blended biopolymer host was reported in the literature, which exhibits a maximum conductivity of ~ 10^{-3} S/cm with a high electrochemical stability of ~ 2.3 V [86]. Hence, these preliminary studies suggest the suitability of chitosan for developing Li^+ conducting SPE materials.

2.5. Diffusion processes inside solid polymer electrolytes

Solid polymer electrolytes are comprised of fractal structures in macroscopic as well as in microscopic scales where anomalous diffusion of the charge carriers mainly governs their ionic conductivity [87]. Anomalous diffusion is a diffusion process with scaling different to that of normal diffusion. Mean squared displacement ($\boldsymbol{r}$) of the diffusing ions grows in time as $\langle \boldsymbol{r}^2(\boldsymbol{t}) \rangle$ ~ t^γ for the case of normal diffusion. The parameter γ is the anomalous exponent. For normal Fickian diffusion, $\gamma = 1$. When the diffusion is sub-diffusive, the value of γ lies between 0 and 1. Solid polymer electrolytes are generally sub-diffusive systems having a complex microstructure with dynamic disorder present in these materials. This leads to non-Debye relaxation phenomenon inside the solid polymer electrolytes. The conductivity behavior of solid polymer electrolytes is correlated to the diffusion rate of the mobile charge carriers in the electrolyte. Impedance spectroscopy provides a detailed picture of the diffusive behavior of ions inside the solid polymer electrolytes, when analyzed through a realistic model.

In 2009, Lenzi *et al* [88] reported that the fractional diffusion equation is the most convenient framework to describe the frequency behavior of an electrolytic cell. They had presented an approach to determine the impedance of the cell by taking into account the anomalous diffusion phenomenon. The influence of the ions on the electrochemical impedance of a cell had been calculated in the framework of a model in which the fractional drift-diffusion problem is analytically solved and the resulting distribution of the electric field inside the sample is determined by solving Poisson's equation. Furthermore, the diffusive process is considered in a general formalism represented by the fractional diffusion equation for which anomalous diffusion can be found which infers that the diffusion of the ions follows a nonconventional behavior in the sample. They had studied this behavior inside liquid electrolytes. Later, Basu *et al* [48] applied the same theory for the case solid polymer electrolytes. The ion-conduction mechanism inside non-crystalline solid electrolytes is very similar to that in liquid electrolytes, especially for the polymer samples above the glass transition where dynamic disorder is present [48]. These materials are characterized by segmental motion, with parts of the macromolecular chain in incessant motion on very small spatial and temporal scales [48]. The ions inside the bulk solid polymer electrolytes obey normal integer order diffusion equation at larger time scales and fractional order diffusion equation at smaller time scales. In order to achieve a complete description of the diffusion phenomenon inside the electrolytes, a fractional derivative of distributed order has been invoked on the diffusion equation which infers that the diffusive process occurring inside the sample is not characterized by a unique regime and can be better explained when one considers the presence of both normal and anomalous diffusion regimes for the ions inside the solid electrolytes.

2.6. Different approaches for improving the performance of solid polymer electrolytes (SPE)

High ionic conductivity is an essential requirement of high-performance solid polymer electrolyte (SPE), where SPE suffers profoundly. Various approaches have been implemented by scientific communities worldwide in order to tune the properties and performance of the SPE material such as polymer blending, exposing to high energy gamma irradiation, incorporation of plasticizers and nanofillers [59,83,89].

2.6.1. Polymer blending

Polymer blending is the most feasible technique among the various approaches adopted to tailor the polymer-salt complex or SPE. It is defined as a process of physical mixing of two polymers with or without any chemical bonding between them [73]. The mixing of a polymer blend is dependent on the miscibility of the two polymers in one another which in turn depends on the nature and amount of the individual polymers in the blend. Charge transfer interactions, hydrogen bonding and dipole-dipole interaction forms the basis for miscibility of any polymer blend. Polymer blending synergizes the advantageous aspects of two polymers and is helpful in achieving enhanced properties of SPE that are superior to those of the component polymers. One of the main advantages of polymer blending approach is that it provides materials with desired mechanical, chemical and electrical properties. Buraidah *et al* [90] reported a maximum conductivity of 1.77×10^{-6} S/cm with chitosan/PVA polymer blend containing NH_4I as dopant salt which is one order of magnitude higher compared to that of unblended system (3.73×10^{-7} S/cm). The existence of strong hydrogen bonding between the hydroxyl functional groups of chitosan and PVA due to blending provided better mechanical properties [90].

2.6.2. Gamma irradiation

The study of the effect of radiation on solid polymer electrolytes has started gaining interest among the researchers in order to boost their ionic conductivities. Gamma irradiation is a unique approach to modify the chemical, structural, mechanical and electrical properties of the polymer by producing irreversible changes in their macromolecular structure [91]. Gamma rays are high energy photons that are emitted by radioactive nuclei through a process called gamma decay. The radioactive isotopes, ^{60}Co and ^{137}Cs are used as the main sources of gamma radiation. The electronics sectors require speciality polymer materials that undergo radiation induced scission or crosslinking for resist applications, while aerospace sectors require highly radiation stable materials. The changes in the polymer macromolecular structure occur as a result of radiation-induced chemical reactions which can be classified as:

- **Chain-crosslinking** : The cross-linking process results in formation of chemical bonds between two adjacent polymer molecules. This reaction increases the molecular weight of the material. The material becomes more rigid as a result of crosslinking.
- **Chain-scission** : Irradiation of polymers results in bond scission which gives rise to small molecular products. This reaction decreases the molecular weight and substantially changes the properties of a polymer material by decreasing its strength.

The effect of radiation on solid polymer electrolytes has great importance since it may help in improving the ionic conductivities of the SPEs. Different physical and electrical properties of SPE materials are greatly influenced through cross-linking and/or scission of the long polymer chains. In the past few decades, various efforts had been devoted to study the effect of gamma radiation on different SPE materials. Rahaman *et al* [92] reported irradiation effect on polyvinylidene difluoride (PVDF) - lithium bis(oxalato)borate (LiBOB) SPE which exhibited an increased ionic conductivity of ~ 10^{-4} S/cm compared to that of pristine SPE. Another report suggests an increase in dielectric constant in PVDF-$LiPF_6$ SPE with increasing doses of γ-irradiation [93]. Maccallum *et al* [94] reported a small decrease in conductivity in γ-irradiated PEO-$LiClO_4$ SPE due to crosslinking which resulted in restricted backbone segmental motion. Hence, the effect of gamma irradiation depends on the nature of a particular polymer which may be beneficial or detrimental for a definite application. However, controlled gamma irradiation may help in improving the various properties of the SPE materials.

2.6.3. Addition of plasticizers

The ionic conductivity of solid polymer electrolytes can be effectively improved by adding high dielectric constant and low molecular weight organic molecules such as glycerol, ethylene carbonate (EC), polyethylene glycol (PEG) in the polymer electrolyte matrix [95]. This technique is called plasticization. The addition of plasticizers in SPE has the following advantages [96] :

- Increases the amorphous phase content.
- Decreases the degree of crystallinity.
- Lowers the glass transition temperature (T_g).
- Dissociates ion aggregates.
- Increases the polymer chain segmental motion and flexibility.

For better transport of ions in the SPE material, plasticizers need to have low viscocity. Although plasticization results in a prominent increase in conductivity, its major drawback is that it reduces the mechanical property of the plasticized SPE material. In 1973, Fenton and co-workers first developed a plasticized SPE based on PEO [8]. According to a previous report, a biopolymer blend of chitosan and starch incorporated with NH_4Cl as dopant salt and glycerol as a plasticizer, exhibited a maximum conductivity of ~ 10^{-4} S/cm which is three orders of magnitude higher compared to that of the unplasticized SPE [80]. Another report suggests an increase in ionic conductivity (~10^{-3} S/cm) by two orders in magnitude in NH_4Br doped chitosan-starch blended SPE plasticized by ethylene carbonate, as compared to that of the same SPE without plasticizer [97].

2.6.4. Addition of nanofillers

Embedding various types of nanoparticles (popularly termed as “nanofillers”) into the solid polymer electrolytes is an area of rapidly increasing interest. It is one of the popular approach in boosting the ionic conductivities of the solid polymer electrolytes. Nanofiller incorporated SPE materials (popularly known as “solid polymer nanocomposite electrolytes” or SPNE) have several other advantages such as improved mechanical strength, better thermal stability, electrochemical and interfacial stability in contact with various electrode materials [73]. Also nanofillers reduce the crystallinity and hence enhances the degree of amorphicity that leads to better ionic conductivity of the SPNE material [73]. Inert nanoparticles such SiO_2, TiO_2 and Al_2O_3 are frequently used as filler materials in developing SPNE. In 1999, Capiglia *et al* [98] reported nano-sized silica (SiO_2) embedded into the PEO-$LiClO_4$ SPE system which exhibited ionic conductivity of the order of ~ 10^{-5} S/cm, two orders in magnitude higher than that of the same SPE without nanofiller. Another report by Xiong *et al* [99] suggests that nanosized SiO_2 incorporated starch-based solid biopolymer electrolyte improved the mechanical properties and reduce the crystallinity of the developed SPNE material. A SPNE based on PEO-PEG-$LiCF_3SO_3$ incorporated with TiO_2 nanoparticles exhibited an ionic conductivity of the order of ~ 10^{-4} S/cm, as reported by Ali *et al* [100]. The ionic conductivity of a SPNE depends strongly on the specific surface area and Lewis acid and surface chemistry characteristics of the nanofillers [101].These nanofillers interact with the polymer and the lithium based salt by Lewis acid-base interactions through surface functional groups that promote the salt dissociation which aids in conductivity enhancement of the SPNE [102,103]. Moreover, incorporation of these nanofillers also reinforces mechanical stability to the SPNE material [103].

2.6.4.1. Carbon based nanofillers

Recently carbon based nanofillers such as graphene oxide and carbon nanotubes are emerging as suitable dispersoids in developing solid polymer electrolytes [REF]. Two-dimensional nanosheet of graphene oxide (GO) is emerging as a promising filler candidate for solid polymer electrolytes owing to their ultra-large surface area, excellent mechanical strength, highly oxygenated functional groups [103]. As GO possesses various oxygen containing functional groups on its edges and basal planes (shown in Fig. 2.6), it can increase the ionic conductivity of the SPNE material due to the interactions between the functional groups of GO and Li^+ cations which possibly can enhance the dissociation of the lithium based salt.

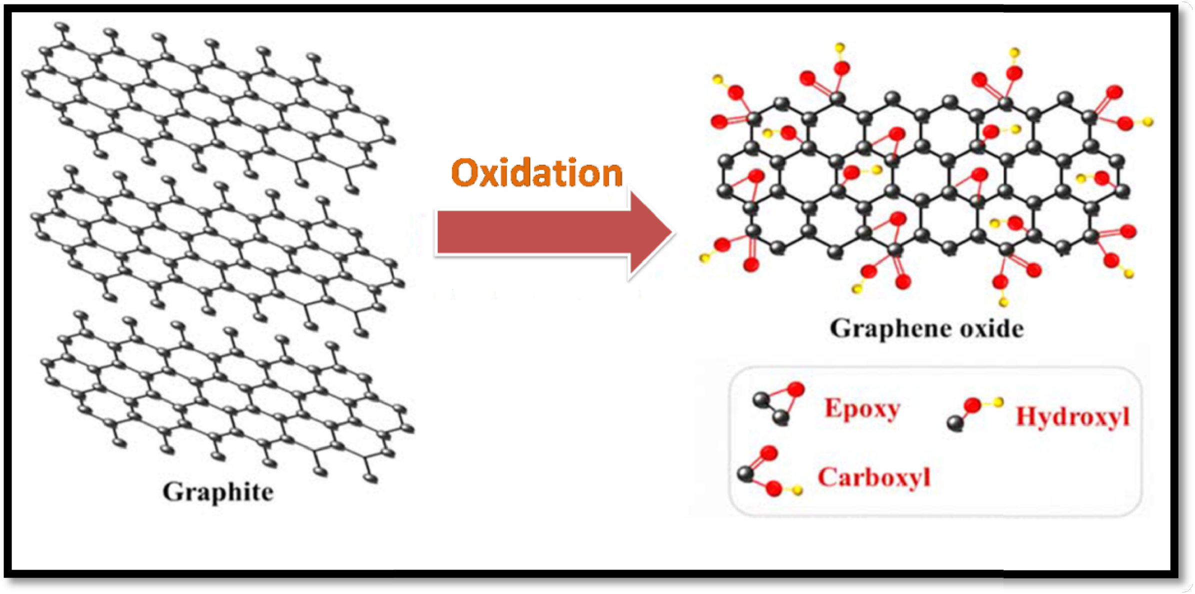

Fig. 2.6. Schematic representation of graphene oxide (GO).

Due to the excellent mechanical strength of GO, the mechanical stability of the SPNE material can be increased by incorporating GO into the polymer matrix. Shim *et al* [103] had developed graphene oxide (GO) incorporated PEG based SPE with excellent ionic conductivity of ~ 10^{-4} S/cm and superior thermal and mechanical stabilities. Yuan *et al* [104] reported nearly two orders of magnitude improvement in ionic conductivity in PEO-$LiClO_4$ SPE dispersed with GO.

Apart from graphene oxide (GO), carbon nanotubes (CNT) have also received considerable attention of researchers as potential filler materials for developing solid polymer electrolytes. In comparison to other allotropes of carbon, CNT has low electrical resistance, high aspect ratio, more mechanical and chemical stability which makes them a promising reinforcing filler material for SPEs [105,106]. However, there remains a risk of electrical shorting due to the high conductivity of CNTs which have limited their applications in the development of solid polymer electrolytes. The incorporation of carbon fillers in polymer electrolytes was proposed by Appetecchi and Passerini in order to improve the conductivity of the solid electrolyte [107]. Since then, various research works were done with CNT as filler materials in polymer matrices which had shown improved electrical and mechanical properties of the composite material [108-110]. Agrawal *et al* [106] reported an improvement in the ionic conductivity of the order of ~ 10^{-4} S/cm on incorporating CNT in PVA-NH_4SCN SPE. The covalent linkage between the polymer and CNT can lead to improved interfacial interaction [111]. Banitaba *et al* [112] reported an order of magnitude improvement in ionic conductivity in PEO–EC–$LiClO_4$ SPE dispersed with CNT. The strong affinity between the rich electron cloud of CNT and lithium cations facilitates dissociation of lithium based salt and hence improves the ion transport through the SPNE [113]. Moreover, previous reports suggest that the Li^+ cations can potentially find low-energy conducting pathways along the carbon based filler / polymer matrix interface [103]. Hence, incorporation of carbon based nanofillers in the polymer matrix can be a promising approach for developing high-performance solid polymer electrolytes.

2.7. Energy storage

Since the last century, there is a rapid growth observed in the global energy demands which are mostly meet by the fossil fuels (oil, coal, natural gas) and renewable resources (solar energy, wind energy, etc.). The rising consumption of fossil fuels is the major reason behind the global climate change as they are the remarkable contributors of greenhouse gases such CO_2, methane, etc. The global energy-related emission of CO_2 has grown by 48 % in the duration of 1998-2018 which need to reduce at the same rate over the next 20 years to coordinate with the international climate goals. Besides that, petroleum is becoming significantly expensive and scarce which may cause energy crisis in the next few decades. On the other hand, the biggest hurdle with renewable energy sources is their expensive technology and dependency on the condition of weather which limits their usage. Thus, developing green, cost-effective and highly efficient energy storage devices have been the focusing area of research since the last few decades. Batteries and supercapacitors are such energy storage technologies which are being used in our daily lives to run different portable electronic devices and are also required for the renewable energy production. Nowadays, almost all the new electronic devices from smart phones to sensors have variable power requirements and consumers are asking for fast charging solutions to their devices. While the lithium ion batteries are progressively occupying the market of energy storage technology, they can never compete with supercapacitors which offer an exclusive combination of high power density and moderate energy density, highly reversible charge-discharge features and long cycle life, thereby bridging the gap between traditional capacitors and batteries. Solid-state supercapacitors are emerging supercapacitor technology that has the ability to capture the market of future energy storage.

2.7.1. Solid-state supercapacitors

"Supercapacitor" was a brand-name coined by a Japanese corporation, Nippon Electric Company (NEC) in 1971 for their energy storage device in computer memory backup. A conventional capacitor is basically a charge storage device which stores charge electrostatically in an electric field. Capacitor consists of two parallel conducting plates (electrodes) which are separated by an insulating (dielectric) layer (viz. mica, plastic film, paper etc.). The schematic diagram showing the structure of a conventional capacitor is shown in Fig. 2.7a. The measure of a device's ability to store electrical charge at a given voltage is measured by its capacitance "C" which is a function of the spacing "d" between the plates and area "A" of the plates. The capacitance "C" can be increased by maximizing "A" and minimizing "d". The conventional capacitors used in electronic circuits can store only minuscule amount of charge (capacitance on the order of picofarads, nanofarads and microfarads). Thus supercapacitors came into the limelight as it can store thousands, millions or even billions times more charge (capacitance on the order of Farads) than a regular capacitor. A traditional supercapacitor has two conducting metal plates soaked in a liquid electrolyte which is rich in ions and the metal plates are coated with a porous material (typically carbon-based materials which are electrically conductive) which provides a larger surface area (on the order of ~ 10^3 m^2/g for activated carbon) for storing more charge (schematic diagram shown in Fig. 2.7b). There is a separator (generally an ion-permeable membrane) used in between the two porous electrodes in a traditional supercapacitor to prevent the device from electrical short circuits and transport of ions during charging/discharging processes. When voltage is applied between the two electrodes of a supercapacitor, the ions from the liquid electrolyte diffuse to the pores of the electrode of opposite charge. The solvated ions form two charged layers at the interface between the electrode and the electrolyte, known as "electrical double layer" having thickness on the order of nm. The key differences between a conventional capacitor and a traditional supercapacitor are tabulated in Table 2.3.

Table 2.3. Comparisons of conventional capacitor and traditional supercapacitor.

Characteristics	Conventional Capacitor	Traditional Supercapacitor
Charging Time	10^{-6} - 10^{-3} seconds	s to min
Discharging Time	10^{-6} - 10^{-3} seconds	s to min
Specific Energy (Wh/ kg)	< 0.1	1-10
Cycle life	> 5,00,000	1 million
Operating temperature	-20 to 65 °C	-40 to 65 °C

But the traditional supercapacitors have several disadvantages like leakage of liquid electrolyte, heavy weight and self-discharge problems. In marked contrast, solid-state supercapacitors have no such issues since they are made of solid polymer electrolytes which act as a dielectric material between the two porous electrodes (schematic diagram shown in Fig. 2.7c) and thus are flexible, light weight and secure for powering different electronic gadgets.

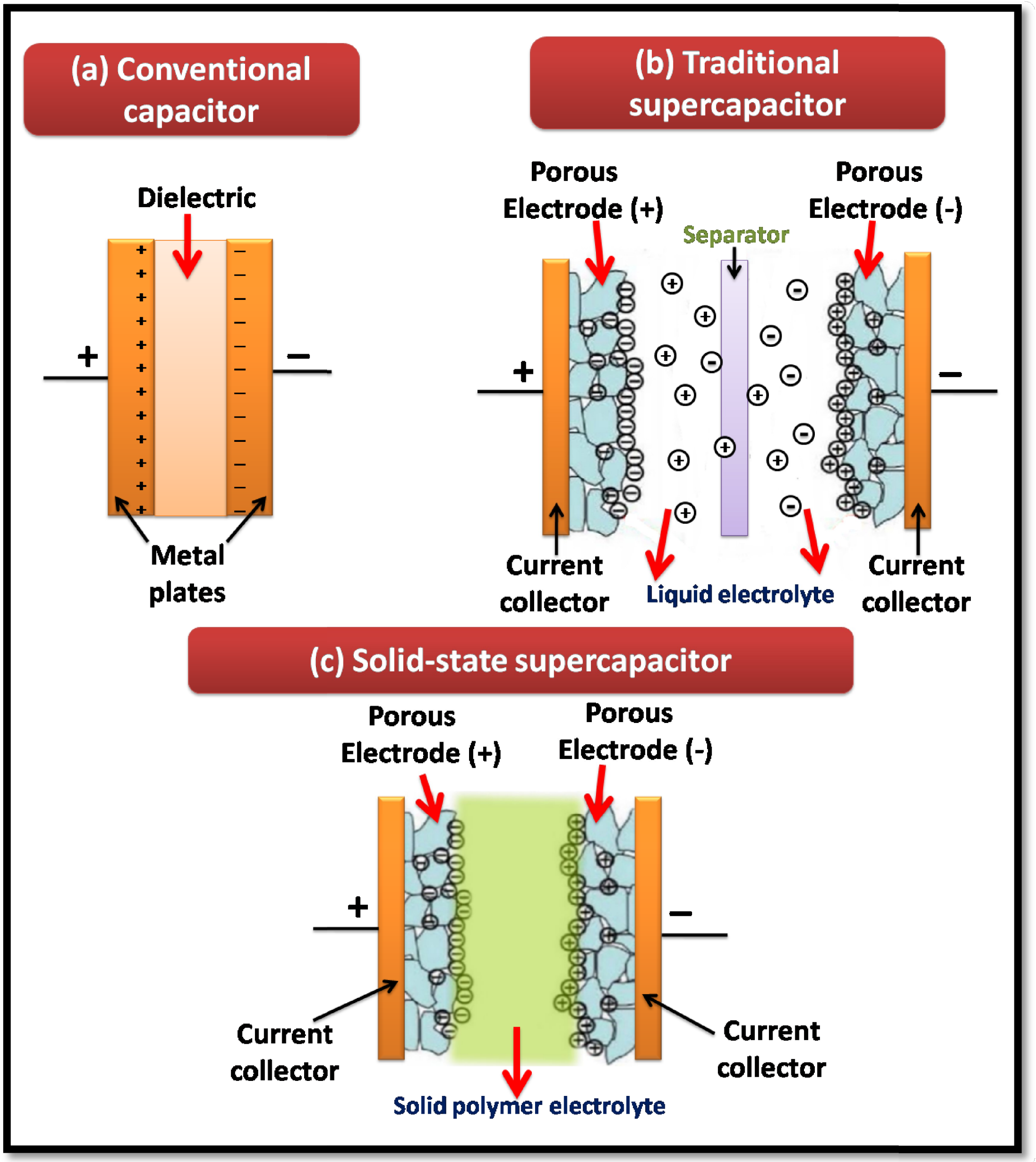

Fig. 2.7. Schematic diagram showing the structure of (a) conventional capacitor, (b) traditional supercapacitor and (c) solid-state supercapacitor.

2.7.2. Supercapacitors versus batteries

Energy density and power density are generally used to describe the characteristics of any energy storage device. Suppose the energy storage device is being considered to use in an electric vehicle, its energy density shows how long it can run on a single charge and its power density shows how fast it can go [114]. Batteries store large amounts of energy but they charge and discharge very slowly, similar to the behavior of the big water jar as shown in Fig. 2.8. On the other hand, supercapacitors store relatively small amounts of energy compared to batteries, but the speed at which the power is discharged is very high for supercapacitors, similar to the bucket in Fig. 2.8. Generally, a supercapacitor can sustain a million of charge and discharge cycles, while a battery can handle a maximum of ~ 1000 cycles. Also a supercapacitor can be charged within seconds compared to that of batteries which usually take hours to charge up. While a supercapacitor can be operated at temperatures as low as −40 °C, a battery can't work properly at such low temperatures.

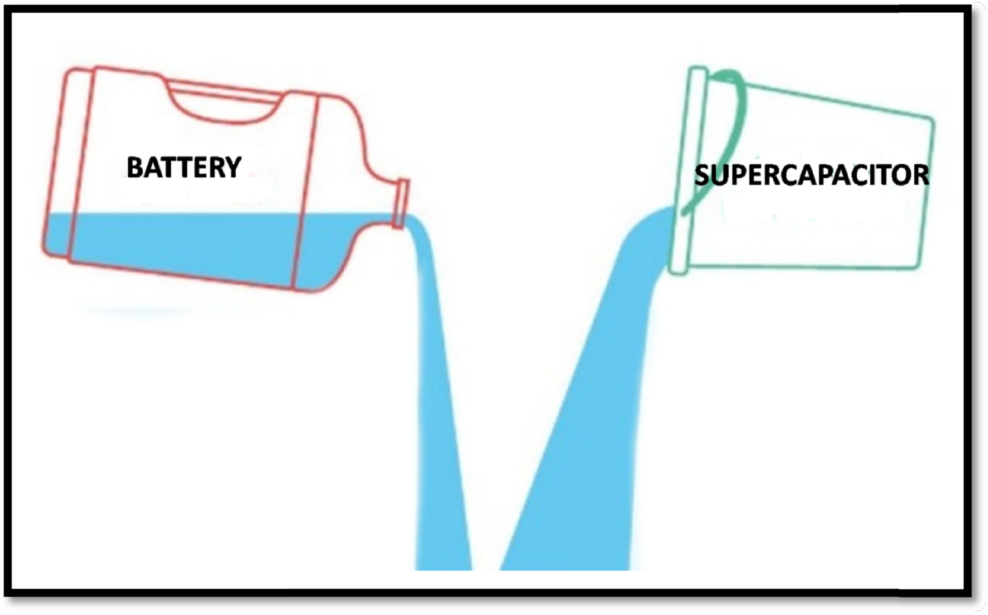

Fig. 2.8. Energy density and power density comparison between a battery and a supercapacitor.

One of the major advantages with supercapacitors is that they does not degrade over time. This means a 2.7 V supercapacitor today will remain a 2.7 V supercapacitor in the next 15 years, whereas a battery's performance gradually diminishes with time. Though the power density of a battery pales against supercapacitors, the major drawback of a supercapacitor is its low energy density (~ 1-10 Wh/kg) which is generally very high (~ 20-200 Wh/kg) for batteries. In short, a battery can store 20 times the energy of a supercapacitor for a given weight and size (Fig. 2.9). Hence, there is a growing interest among the researchers to develop new materials for supercapacitors with increased energy density and power density in order to meet the increasing demands of power-hungry gadgets as a progress towards making the ultimate energy storage device.

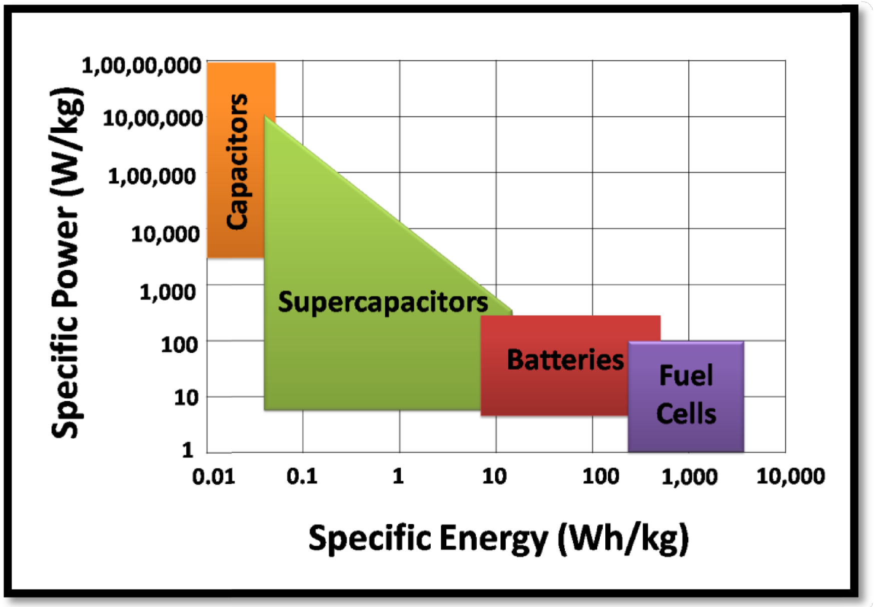

Fig. 2.9. Ragone plot of specific power versus specific energy for various energy storage devices.

2.7.3. Classification of supercapacitors based on capacitive energy storage mechanisms

Depending on the charge storage mechanism, supercapacitors can be classified into three broad categories: electric double layer capacitors (EDLC), pseudocapacitors (PC) and hybrid supercapacitors as shown in Fig. 2.10.

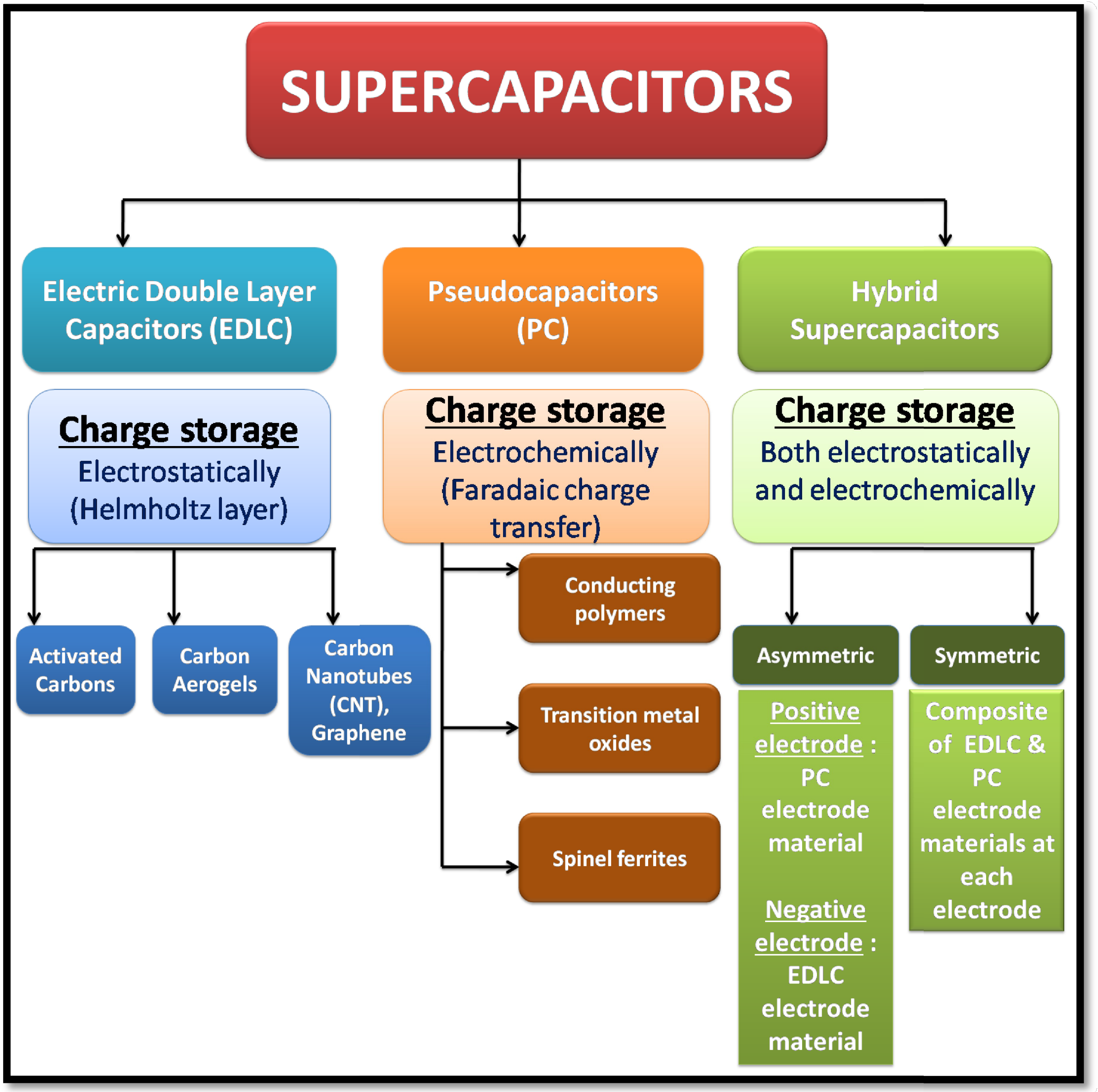

Fig. 2.10. Classification of supercapacitors and their corresponding electrode materials.

Electric double layer capacitors (EDLC) have gained immense popularity worldwide among the researchers since no redox (electron transfer) reactions are involved and thus the energy storage system is non-faradic in nature. Energy is stored electrostatically as a result of the reversible adsorption of electrolyte ions onto the surface of the electrode [72,115]. The materials for EDLC store charge mainly in an electrochemical double-layer formed at the electrode-electrolyte interface instead of storing them in the bulk of the capacitive material. The double layer capacitance is produced as a consequence of charge separation, occurring due to polarization at the electrode–electrolyte interface. The capacitance depends on the electrode surface area accessible to the electrolyte ions. The significant factors that influence its electrochemical performance are specific surface area, electrical conductivity, pore-size distribution, pore shape and structure, etc [116]. The electrodes for EDLC are fabricated usually with carbon due to its abundance in nature, stability (good corrosion resistance and ability to withstand high temperature), high conductivity, inexhaustibility and high electrochemical surface area. Recently highly conductive carbons such as activated carbon, carbon aerogels, carbon foams, carbon fibers, carbon nanotubes (CNTs) and graphene are being considered as electrode materials to increase its electrochemical surface area [117-121].

A supercapacitor that undergoes Faradaic process at its electrode is known as a *pseudocapacitor* (PC). Pseudocapacitors store charge mainly via speedy and reversible redox (Faradaic) reactions happening at or near the surface of the electrode [72,122]. In 1971, Trasatti *et al* [123] developed the first pseudocapacitor using RuO_2 which was a new electrode material exhibiting high specific capacitance and low internal resistance. In recent years, the composites of conducting polymers (such as polyaniline, polypyrrole etc.) and transition metal oxides (such as NiO, Co_3O_4, MnO_2, etc) are commonly used for the fabrication of electrodes for PC [124-128]. Various types of faradic processes occurring in the electrodes of PC are [129-131]: (a) reversible adsorption or desorption of hydrogen on the electrode surface, (b) redox reactions related to oxidation state change when transition metal oxides are used as the active electrode materials and (c) reversible processes of electrochemical doping (oxidation) and de-doping (reduction) in electrodes based on conductive polymers. The charge storage performance of the pseudocapacitors has been drastically increased with the introduction of the redox reactions in the electrode [114,132]. Since the storage is based on the redox reactions, pseudocapacitor has similarities to a battery in its behavior to some extent. Typically, pseudocapacitors (PC) can increase the value of capacitance by an order of magnitude, compared to that of EDLCs. However, pseudocapacitors have poor cycling stability due to the nature of the redox reactions.

The concept of *hybrid supercapacitors* came into existence as an attractive alternative to conventional supercapacitors by combining the characteristics of both EDLC and PC in order to achieve better performance, including high energy density and power supplying capability. The formation of hybrid supercapacitors is done by coupling different EDLC and redox materials such activated carbon, graphene, carbon nanotubes, transition metal oxides, conducting polymers etc [133-135]. This offers higher working potential and higher capacitance which is at least two to three times more than that of EDLC and PC [136]. Hybrid supercapacitors can be either symmetric or asymmetric which depends on the configuration of the assembly. Symmetric hybrid supercapacitor is the assembly of two similar electrodes comprising of EDLC and PC components whereas the assembly of two dissimilar electrodes leads to the formation of an asymmetric hybrid supercapacitor [136]. Most of the commercially available hybrid supercapacitors are asymmetric. In contrast to PC, hybrid supercapacitors maintain the cycling stability and provide higher values of specific capacitance.

2.7.4. Classification of the electrode materials based on their applications in supercapacitors

Electrode materials are one of the most significant parts of a supercapacitor as the energy stored largely depends on the specific capacitance, which is determined by the electrochemically active surface area of the electrodes. *Carbon* is the most frequently used electrode material for supercapacitors. They have low cost, high surface area, adaptable porosity, environmental friendly and can be attained in different forms such as powders, fibers, foams, aerogels. A supercapacitor having specific capacitance of 76 F/g was reported with carbon aerogel as the active electrode material [137]. Among various carbon-based materials, activated carbon, graphene and carbon nanotube (CNT) are most extensively utilized for manufacturing electrodes. Activated carbon is the most widely used material in the majority of supercapacitors currently available in the market owing to its excellent surface area, lower cost, chemical stability, easy processing and manufacturing and favorable electronic characteristics. A solid-state supercapacitor demonstrating high specific capacitance of ~ 133 F/g was reported with activated carbon as electrode material and a solid biopolymer blend as electrolyte material [138]. However, activated carbon is limited by its relatively effective pore area and the low ion transport rate through its microporous structure [139]. CNT has garnered a lot of attention as an electrode material due to its outstanding electrical conductivity, good mechanical and thermal stability and high surface area. Graphene with its two-dimensional sheet-like structure has gained huge popularity during the past few years due to its high conductivity and large open specific surface area that is readily accessible to electrolyte with a small diffusion barrier. It exhibits an internal surface area of 2630 m^2/g. Hence, its high surface area promises extremely high energy density and specific capacitance of graphene based supercapacitors. Various c*onducting polymers* such as polypyrrole (PPy), polyaniline (PANI), poly(3,4-ethylenedioxythiopene) (PEDOT), polythiophenes, etc. have been suggested by several authors as electrode materials for fabrication of supercapacitors [124,125,140,141]. Supercapacitors with polypyrrole hydrogel based electrodes show a high specific capacitance of ~380 F/g [142]. PANI displays higher specific capacitance values and its ease to prepare along with better electrical conductivity and environmental stability [136,143]. PANI prepared by chemical method shows specific capacitance of ~ 200 F/g while that prepared by electrochemical method displays specific capacitance of ~ 1500 F/g [144]. *Conducting transition metal oxide* such as RuO_2 was the most favorable electrode material in early supercapacitors used for space or military applications. RuO_2 offers some unique characteristics such as extensive potential window, large redox reversibility and high stability [72]. Its specific capacitance was reported to be as high as ~ 750 F/g with the H_2SO_4 electrolyte at low temperature [145-147]. But these supercapacitors, however, turned out to be too expensive and are only suitable for aqueous electrolytes. Researches are being done to develop supercapacitors having high specific capacitance and good cycling stability at a much reduced cost with different transition metal oxides such as MnO_2, NiO, SnO_2, Fe_3O_4 [126,148-150]. Recently, spinel ferrites have emerged as potential electrode materials for supercapacitor applications and they are being explored by researchers owing to their various redox states, reasonable cost, high and tunable electrochemical activity, favorable electrical properties and high specific capacitance [151]. Moreover, spinel ferrites are easy to synthesize and can be prepared by simple chemical synthesis methods from widely-available precursor materials at relatively low temperatures with simple apparatus [151].

2.7.4.1. Spinel ferrites as electrode materials

In general, ferrites adopt a spinel crystal structure that has alternating tetrahedral and octahedral layers as shown in Fig. 2.11. Spinel ferrites having the unit formula of MFe_2O_4, are a family of spinel oxides based on Fe^{3+} as the major trivalent metal ion and M^{2+} as a doping divalent metal cation (M: Mn, Co, Ni, Mg, Zn) that are distributed between octahedral and tetrahedral interstitial sites.

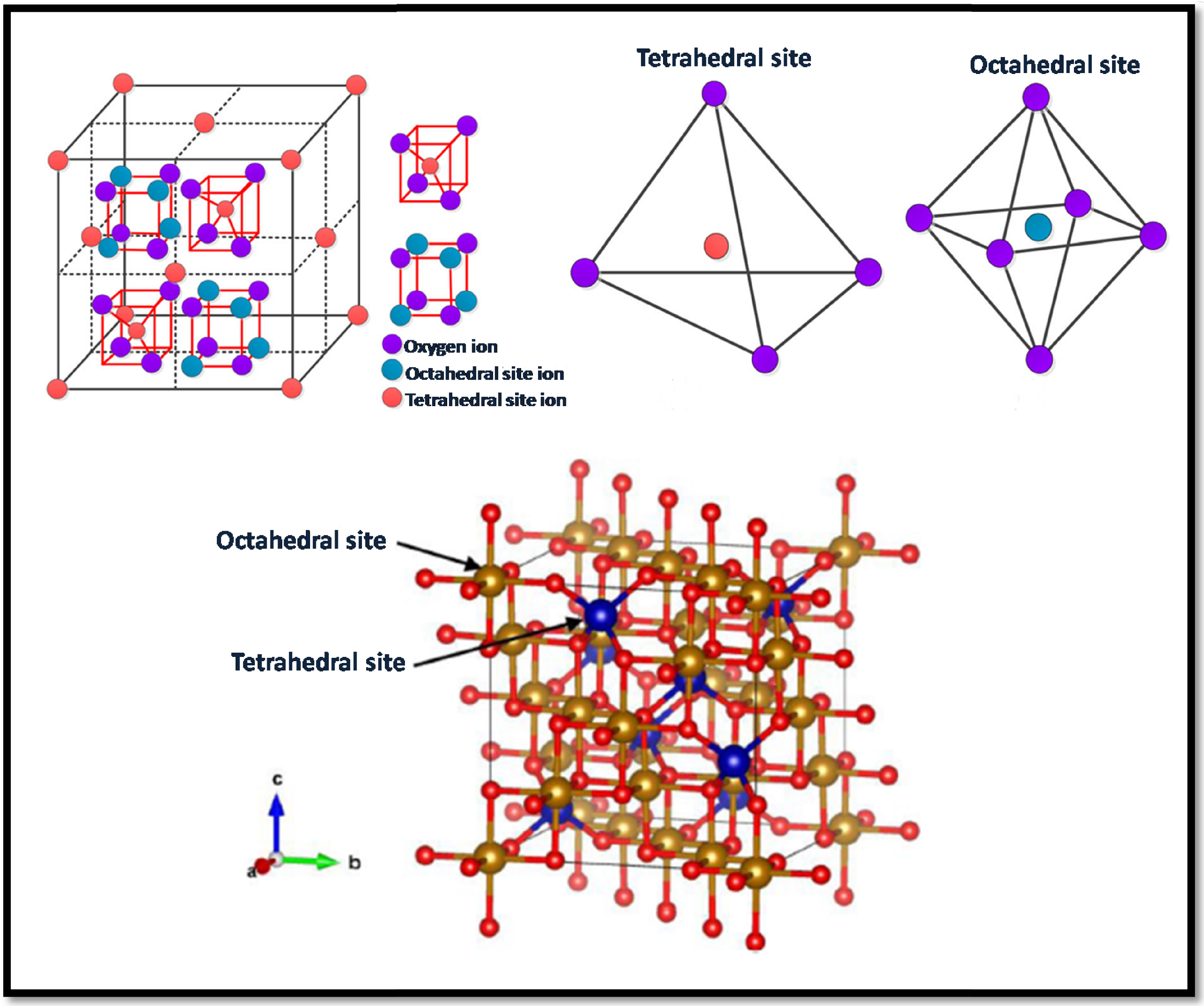

Fig. 2.11. The crystal structure of spinel ferrite.

In a unit cell of spinel lattice, there are 64 tetrahedral and 32 octahedral interstitial sites. These two interstitial positions experience different crystal fields exerted by the O^{2-} anions that can determine the site occupation by either M^{2+} or Fe^{3+} cations. The occupancy at the interstitial sites also depend on the cation radii, cation charges and electrostatic contribution to the lattice energy. A spinel ferrite structure can be classified into three groups based on the positions of M^{2+} and Fe^{3+} cations such as normal, inverse and mixed. In a normal spinel ferrite structure (Fig. 2.12), M^{2+} cations occupy the tetrahedral sites, while Fe^{3+} cations occupy the octahedral sites (i.e. $[M^{2+}]^{tet}[Fe^{3+}]^{oct}{}_2O_4$), while for an inverse spinel structure (Fig. 2.12), M^{2+} cations occupy the octahedral sites and Fe^{3+} cations are equally distributed between tetrahedral and octahedral sites (i.e. $[Fe^{3+}]^{tet}[M^{2+}Fe^{3+}]^{oct}{}_2O_4$). And in a mixed spinel structure, M^{2+} and Fe^{3+} cations randomly occupy both the sites. An example of a normal spinel ferrite is $ZnFe_2O_4$, while $CoFe_2O_4$ is an example of inverse spinel ferrite.

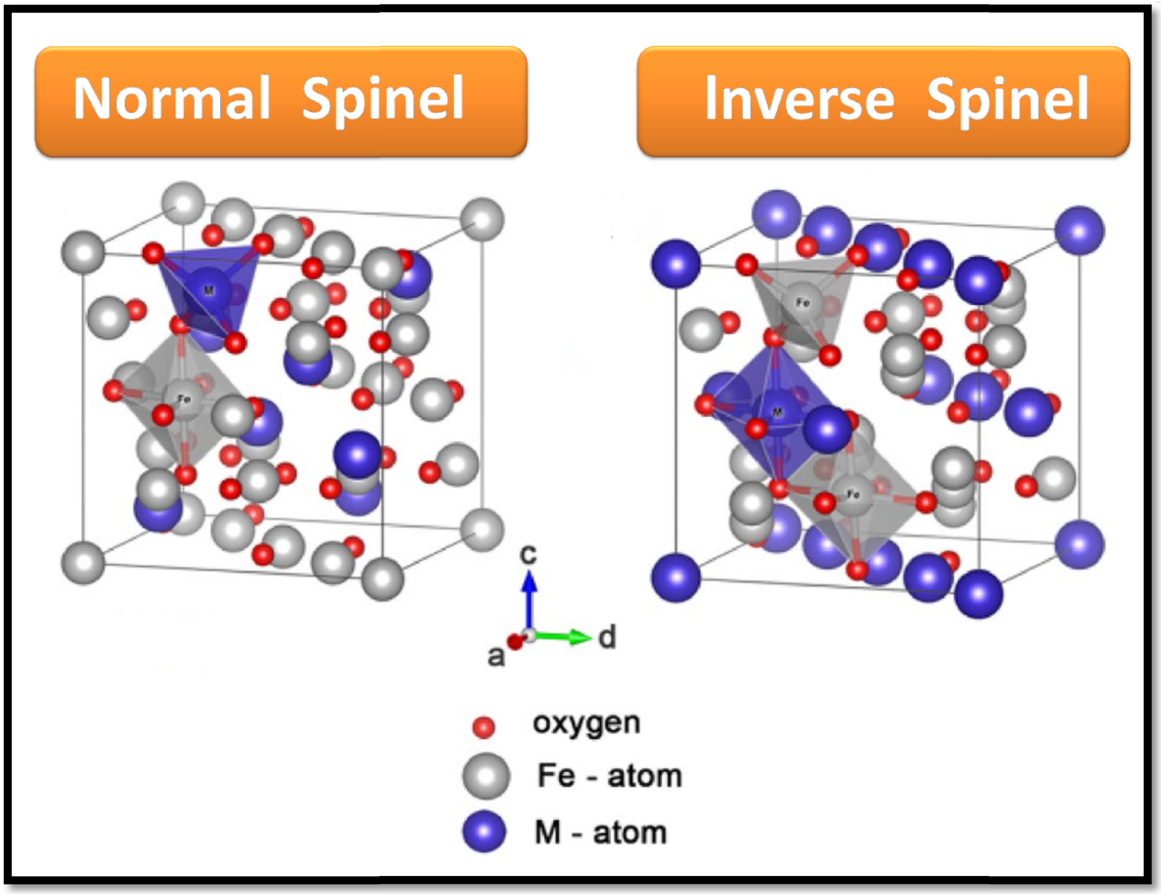

Fig. 2.12. Crystal structures of normal and inversel spinel ferrites.

Among all the spinel ferrites, cobalt ferrite ($CoFe_2O_4$) which is a binary transition metal (TM) ferrite, has received considerable attention among the researchers for developing high-performance supercapacitors owing to their rich redox chemistry, high chemical and structural stability [152]. Kumbhar *et al* [153] synthesized $CoFe_2O_4$ nanoflakes and reported specific capacitance of 366 F/g at a scan rate of 5 mV/s. Gao *et al* [154] reported high specific capacitance of 503 F/g at a current density of 2 A/g with porous $CoFe_2O_4$ nanosheets on Ni foam. Another binary TM ferrite, manganese ferrite exhibits a high specific capacitance value of 190 F/g at a scan rate of 2 mV/s [155], while nickel ferrite ($NiFe_2O_4$) nanospheres shows specific capacitance of 137 F/g at a current density of 1 A/g [156]. In the recent years, different research works have been done with ternary TM ferrites as the electrode materials for developing supercapacitors. A high specific capacitance of 397 F/g was reported with $CuCoFe_2O_4$, while $NiCoFe_2O_4$ exhibits a specific capacitance value of 50 F/g [157,158]. Mesoporous $MnZnFe_2O_4$ exhibits a specific capacitance value of 550 F/g at a current density of 0.8 A/g [159]. Recent trend of research involves development of high-performance hybrid supercapacitors using composite electrodes made from activated carbon, carbon nanotubes, graphene, transition metal oxide, conducting polymers, spinel ferrites etc. in order to take full advantage of different EDLC and PC electrode materials. According to a previous report, a high specific capacitance of ~ 261 F/g at a current density of 2A/g was obtained with $CoFe_2O_4$/rGO nanocomposite [160]. A nanocomposite of polypyrrole/graphene/$MnFe_2O_4$ was reported to have a specific capacitance value of 147 F/g at a scan rate of 10 mV/s [161]. Xiong *et al* [162] reported high specific capacitance of ~ 1133 F/g at a scan rate of 1 mV/s with $CoFe_2O_4$/graphene/polyaniline nanocomposite electrode material.

Chapter 3

Experimental and Methodology

3.1. Introduction

This chapter will encompass different experimental methodologies which have been used in my Ph.D. research work. It is divided into three parts. The first part consists of a brief description of the processes of sample preparation whereas the second part describes the experimental techniques used for proper characterization of the samples and their properties studied. The method used to fabricate electric double layer capacitor (EDLC) and hybrid supercapacitors and the electrochemical characterization techniques are covered in the last part of this chapter.

Chitosan based solid biopolymer blend and its nanocomposites as solid-state electrolytes are prepared by solution casting method. Pure graphene oxide (GO) is prepared using modified Hummers method. Electrode materials such as $MnCoFeO_4$ (manganese cobalt ferrite) and its rGO (reduced graphene oxide) based nanocomposite are prepared using chemical precipitation and reduction methods. Solid-state electrolytes are characterized by Impedance Spectroscopy (IS), Fourier transform infrared spectroscopy (FTIR), Field emission scanning electron microscopy (FESEM), DC polarization method and Differential Scanning Calorimetry (DSC). Electrode materials are characterized by X-ray powdered diffraction (XRD), High resolution tunneling electron microscopy (HR-TEM), X-ray photoelectron spectroscopy (XPS) and Raman

Spectroscopy. The electrochemical performance of the fabricated EDLC and hybrid solid-state supercapacitors are characterized using Cyclic Voltammetry (CV), Galvanostatic charge-discharge (GCD) and Electrochemical impedance spectroscopy (EIS).

3.2. Sample synthesis techniques

3.2.1. Synthesis of solid-state electrolyte materials

Solid polymer electrolytes (SPE) are prepared by solution casting method. This is the easiest and most cost effective method to develop films of solid polymer electrolytes with uniform distribution and different thickness as per experimental requirement. The solvent used in this process plays the most important role. The basic criteria for selecting the most suitable solvent is that it must not react with any of the chemical constituents used in the material preparation and the polymer must be completely soluble in such solvent followed by the addition of dopant salt and plasticizer. The solution is stirred at room temperature for few hours until a homogeneous solution is obtained. Then the resultant solution is poured into polypropylene petri dishes and allowed to dry at room temperature or in a vacuum oven at 40 ^{o}C to form a free-standing SPE film. The host biopolymer, dopant salt and plasticizers chosen to develop SPEs for this dissertation are chitosan (CS), lithium perchlorate ($LiClO_4$) and ethylene carbonate / glycerol, respectively.

This same method is applied to prepare blended solid polymer electrolytes and solid polymer nanocomposite electrolytes (SPNE). To prepare a SPNE, different weight percentages of a nanofiller are dispersed individually in a suitable solvent and sonicated in a ultrasonic bath sonicator or probe sonicated in an ultrasonic processor UP400S (400 Watts, Hielscher, Fig. 3.1a) until a uniform mixture is obtained. Then it is blended with the polymer solution in order to develop thin films of SPNE. The polymers chosen to blend with chitosan (CS) in this thesis are potato starch (PS), carboxymethyl cellulose (CMC), polyvinylidene fluoride (PVDF) and polymethyl methacrylate (PMMA), whereas the nanofillers chosen to prepare SPNE are graphene oxide (GO) and carbon nanotubes (CNT). A typical film of chitosan based SPE prepared from this method of solution casting is shown in Fig. 3.1b.

3.2.2. Synthesis of graphene oxide (GO)

Graphene oxide (GO) has been prepared following modified Hummers' method. This method has been taken up by many researchers and chemists who are interested in the use of GO for various purposes since it is the fastest conventional method of producing large quantities of graphene oxide. 2 g of graphite powder is vigorously stirred with 1 g sodium nitrate and 50 ml concentrated sulphuric acid in an ice bath. 6 g $KMnO_4$ is added slowly keeping the temperature of the solution below 10 ^oC. Then the solution is brought to 80 ^oC with adding some warm water. After 1 hour, H_2O_2 (30%) is added which created huge inflammation. The bright yellow solution is centrifuged in speed 6000 r.p.m. for 10 minutes after adding some HCl to eliminate the metallic impurities. Product is washed with distilled water and dried at 50 ^oC to form graphene oxide (GO).

3.2.3. Synthesis of electrode materials

In this dissertation, $MnCoFeO_4$ (a spinel ferrite) has been chosen as the electrode material for the fabrication of solid-state supercapacitors. The spinel ferrite nanoparticles have been prepared using the following procedure: At first, $MnCl_2.4H_2O$, $CoCl_2.6H_2O$ and anhydrous $FeCl_3$ taken in stoichiometric ratio are dissolved in deionised water. Then we add 100 ml of 0.8 M NaOH solution dropwise in the mixed solution with continuous stirring until a black precipitate was formed. This precipitate was washed several times with deionised water and ethanol via centrifugation and dried at 100 ℃. Finally, the product was calcined at 600 *℃* for 3 hours and the desired ferrite nanoparticles are formed.

These nanoparticles are further used in the synthesis of silver decorated spinel ferrite@rGO nanocomposite with required weight fraction of spinel ferrite. The GO powder (synthesized using modified Hummers' method), silver nitrate and the prepared ferrite nanoparticles in deionised water are sonicated in the ultrasonic processor UP400S (400 Watts) for 30 minutes. Then the solution is heated at 100 ℃ and few ml of Hydrazine Hydrate solution (99-100 %) is added dropwise for reduction of both silver (Ag^+) ions and GO. Stirring at 100 *℃*

is then done initially for 4 hours, after which stirring is continued at room temperature for the next 20 hours which is followed by centrifuging and washing the whole solution repeatedly by ethanol and distilled water. The precipitate collected is dried at 100 ℃ and the desired silver decorated spinel ferrite@rGO nanocomposite is formed which has been used as an electrode material for the development of hybrid solid-state supercapacitors in the present dissertation.

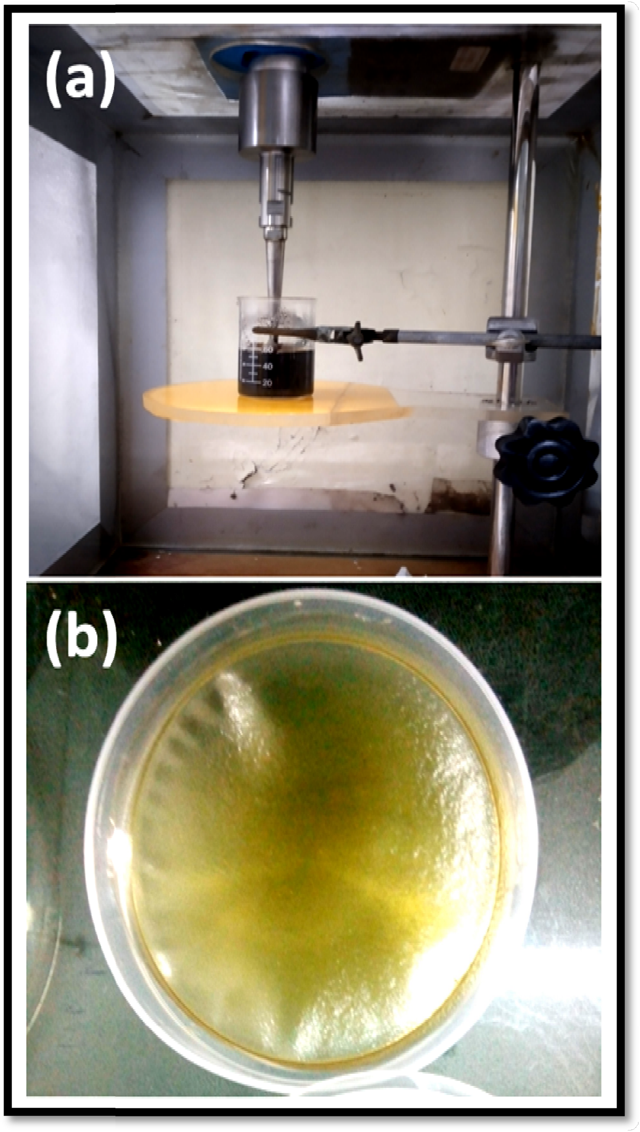

Fig. 3.1. (a) Nanofiller dispersed in a suitable solvent probe sonicated in an ultrasonic processor UP400S (400 Watts, Hielscher), (b) a typical film of chitosan based solid polymer electrolyte prepared using the method of solution casting.

3.3. Characterization techniques, measurements and studies

3.3.1. X-Ray Diffraction (XRD)

X-ray diffraction (XRD) is a rapid analytical technique primarily used for the identification of the crystalline structure and identification of different phases in a sample. Max von Laue, in 1912, discovered that crystalline substances act as three-dimensional diffraction gratings for X-ray wavelengths similar to the spacing of planes in a crystal lattice. XRD is now a common technique to measure the average spacings between layers or rows of atoms and the size, shape and internal stress of small crystalline regions.

A cathode ray tube is used to generate the X-rays. X-rays are short-wavelength and high-energy beams of electromagnetic radiation. X-rays are produced when a metal target is excited using an electron beam which causes inner shell electrons to be ejected and replaced by electrons from an outer shell. As a result, energy is released by emitting an X-ray with a specific wavelength or photons with specific energy. Then they are filtered to produce monochromatic radiation and then collimated to concentrate before directing towards the sample.

In X-ray diffraction, a goniometer is used to rotate the sample in the path of the incident beam at an angle θ. An arm-mounted X-ray detector is maintained at an angle of 2θ. The schematic representation of X-ray optical system of goniometer is shown in Fig. 3.2. When X-rays fall upon the material surface, scattered rays are emitted in all possible directions. In a few particular directions they interfere constructively, which are determined by Bragg's law:

$$2\mathrm{d}\sin\theta = \mathrm{n}\lambda \tag{3.1}$$

where, λ is the wavelength of the incident X-rays (CuKα is used as a source), d is the spacing between the atomic arrays, θ is the Bragg angle and n is the order of diffraction (Fig. 3.3).

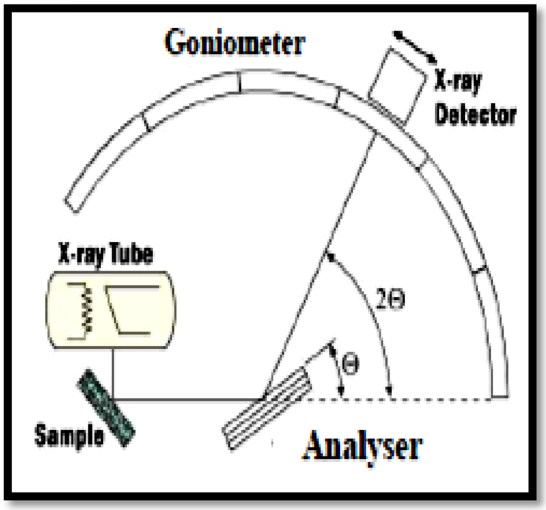

Fig. 3.2. An X-ray spectrograph consists of a high voltage power supply (~ 50kV or 100kV), a broad band X-ray tube, a specimen holder, an analyzing crystal, a goniometer and an X-ray detector device.

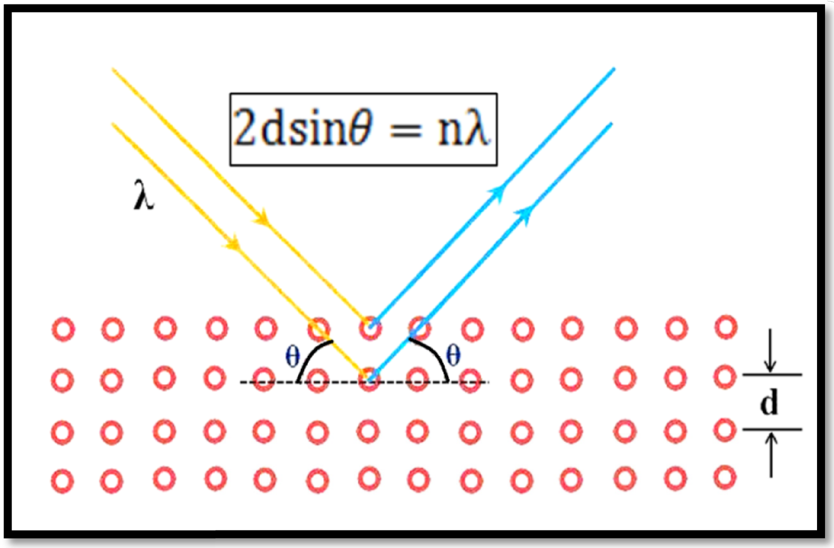

Fig. 3.3. Schematic diagram of X-Ray diffraction.

It is possible to create a three-dimensional picture of the density of electrons within the crystal by measuring the angles and the intensities of the diffracted beams. The mean positions of the atoms, chemical bonds, bond angles, crystallographic disorder and several other informations can be obtained from this electron density. It is important to note that the grain size is one of the main factors for the formation of the diffraction pattern. Larger the grain size, sharper and higher is the intensity peaks and vice versa. The crystallite size can be determined using well known Scherrer's formula. Scherrer showed that the average dimension of the crystallites that compose a crystalline powder is given by,

$$D = \frac{0.89\lambda}{\beta \cos\theta} \tag{3.2}$$

where, λ the wave length of the X-ray, D the size of the crystallite in the direction perpendicular to the reflecting planes and β the FWHM of the peak in radian. Williamson and Hall proposed a modified version of Scherrer's formula which is given as,

$$\beta \cos\theta = \frac{0.89\lambda}{D} + 2\varepsilon \sin\theta \tag{3.3}$$

where, ε is the microstrain.

For a single crystal having very small dimension, there are various other methods of X-ray diffraction available such as powder diffraction, fiber diffraction and small-angle X-ray scattering (SAXS). In our work, all our XRD has been carried out in X-ray powder diffractometer BRUKER D-8 ADVANCE (Germany, Fig. 3.4).

Fig. 3.4. X-ray powder diffractometer BRUKER D-8 ADVANCE (Department of Physics, Jadavpur University).

3.3.2. Transmission Electron Microscopy (TEM)

High resolution transmission Electron Microscopy (HR-TEM) is a microscopy technique used to get high resolution image of a particular sample and helps in determining the particle size, shape and morphology of that sample. In this technique, a beam of high-energy electrons is transmitted through a very thin specimen. As the electron beam strikes the specimen, it interacts with the atoms and parts of it are transmitted. This transmitted beam of electrons carry all the informations regarding the structure of the specimen which is thus analyzed to get an image of the whole sample. The image is magnified and focused in an imaging device to get the final image. Due to the smaller de Broglie wavelength of the electrons, transmission electron microscopes are capable of imaging at a significantly higher resolution than light microscopes. HR-TEM is also used to study dislocation, defects, interface, inter-planar spacing etc. The sample is well dispersed in ethyl alcohol and then put dropwise on a carbon coated copper grid before taking its image. Not more than one or two drops are allowed as excess sample refrain the electron beam from transmitting through the specimen. The grid is then dried in air before using it under microscope. In our research work, all the images are recorded using the microscope, JEOL (model: JEM, 2100F, Indian Association for the Cultivation of Science, IACS).

3.3.3. Field Emission Scanning Electron Microscopy (FESEM)

Field Emission Scanning Electron Microscopy (FESEM) is a high resolution (resolution as low as ~1 nm) microscopy technique by which the surface morphology of a sample can be imaged. A focused beam of high-energy electrons is used which is directed at the surface of a sample and scans a selected area. Electron beam is produced from a field emission source and accelerated through field gradient under vacuum. The electrons interact with the atoms at various depths within the sample and generate signals which reveal information about the sample along with surface topography and composition. Various types of signals are produced which includes back-scattered electrons (BSE) and secondary electrons (SE). When high energy electrons strikes the surface of a sample, the back-scattered electrons (BSE) are produced by elastic scattering and secondary electrons (SE) are produced by inelastic scattering. BSE are incident electrons that are scattered by atoms in the sample while SE are electrons that are ejected from atoms in the sample. BSE are typically deflected at large angles and retain 60–80% of the energy of the incident electrons. In contrast, SE are typically deflected from the sample at small angles and have low energy. Back-scattered electrons are useful for the formation of elemental composition contrast, while the secondary electrons are useful for achieving topographic contrast. The sample has to be made highly conducting by coating it with very thin layer (1.5 - 3.0 nm) of gold before taking the images. In our research work, we have used scanning electron microscope JEOL (Model: JSM-7610F, Fig. 3.5).

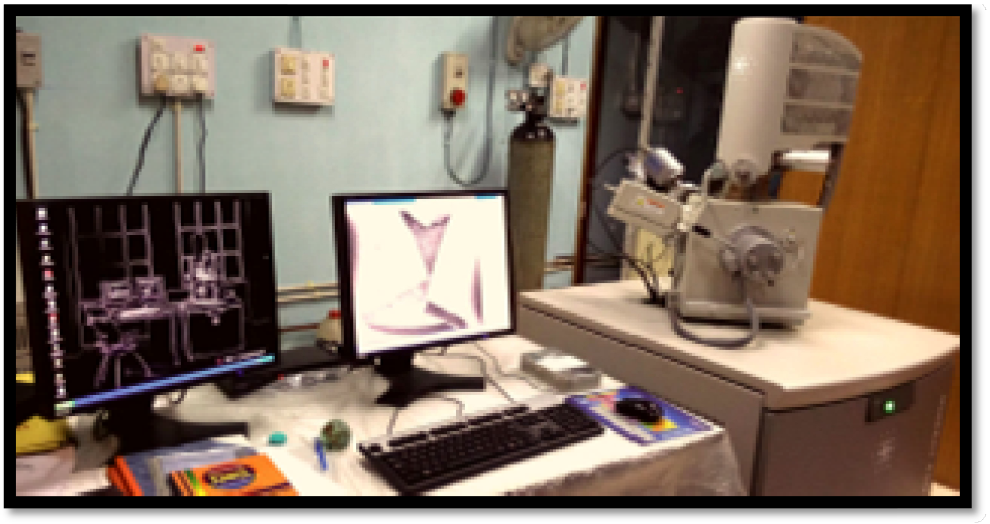

Fig. 3.5. Scanning electron microscope, Model: JSM-7610F, JEOL (Department of Physics, Jadavpur University).

3.3.4. X-ray Photoelectron Spectroscopy (XPS)

X-ray Photoelectron Spectroscopy (XPS) is a spectroscopic technique developed on the theory of photoelectric effect proposed by Einstein in 1905. This technique is used to obtain informations regarding the elemental compositions in the material and their chemical states. In 1981, Kai Siegbahn was awarded the Nobel Prize in Physics for his work in XPS. Photoelectric effect is the emission of electrons when photons of sufficient energy incident on the surface of a sample and the electrons which are emitted from the sample surface in this manner are termed as photoelectrons. XPS is typically done by exciting the sample surface with monochromatic or unfiltered Al K_α X-rays causing emission of photoelectrons from its surface (Fig. 3.6). An electron energy analyzer is used to determine the energy of the emitted photoelectrons which in turn give rise to several photoelectron peaks. The energy peaks are characteristic for a particular element and hence the valance state and quantity of a detected element can be determined from the binding energy and intensity of a photoelectron peak. An atom when bonded with other atoms in a material may be in different energy state or valance state and thus alters the binding energy (BE) of a photoelectron which causes change in measured kinetic energy (KE). The relation by which BE is related to KE is as follows, BE = hν – KE, where hν is the photon (X-ray) energy. The bonding information can be derived from these chemical shifts. XPS can sense all other elements apart from hydrogen or helium and the measurement must be carried out in ultra-high vacuum conditions. In our research work, XPS measurement is carried out using OMICRON-0571 system (Indian Association for the Cultivation of Science, IACS).

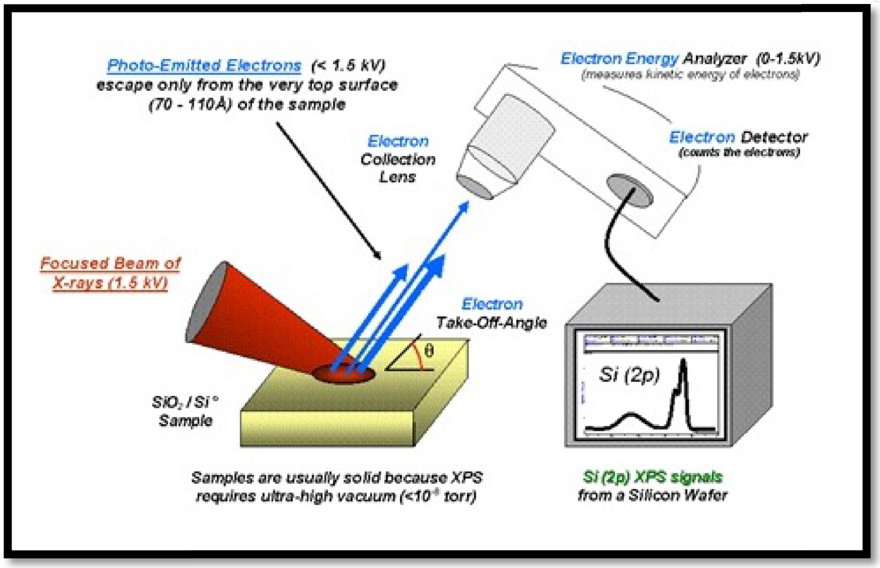

Fig. 3.6. Schematic diagram of X-ray Photoelectron Spectroscopy.

3.3.5. Raman Spectroscopy

Raman spectroscopy is a vibrational spectroscopic technique which provides detailed information about molecular vibrations that can be used for identification of a sample. It is the most convenient tool to probe the defects as well as the properties of graphene, and is also able to identify graphene from graphite and few-layers graphene. This technique involves irradiating the sample by an intense laser beam in the UV-visible region (υ_0) and detecting the scattered light that is observed in the direction perpendicular to the incident beam. The scattered light are of two types: one is called Rayleigh scattering which is strong and has the same frequency as the incident beam (υ_0), and the other, called Raman scattering which is very weak (~ 10^{-5} of the incident beam) and has frequencies $\upsilon_0 \pm \upsilon_m$, where υ_m is a vibrational frequency of a molecule. The $\upsilon_0 - \upsilon_m$ and $\upsilon_0 + \upsilon_m$ lines are called the Stokes and anti-Stokes lines, respectively. Thus, we measure the vibrational frequency (υ_m) as a shift from the incident beam frequency (υ_0) in Raman spectroscopy. Raman shifts are typically reported in wavenumbers, which has units of inverse length, as this value is directly related to energy. These shifts provide informations about the vibrational modes in the system. It is necessary to separate out the weak inelastically scattered Raman signal from the intense elastically scattered Rayleigh signal and reflected laser signal for collecting high quality Raman spectra. Notch filters are used for that purpose. Raman scattered light is typically collected and dispersed by a spectrograph (Fig. 3.7). Raman spectroscopy of our sample is performed in backscattering geometry using LabRAM HR (Jobin Yvon) spectrometer equipped with a Peltier-cooled charge-coupled-device (CCD) detector (Bose Institute).

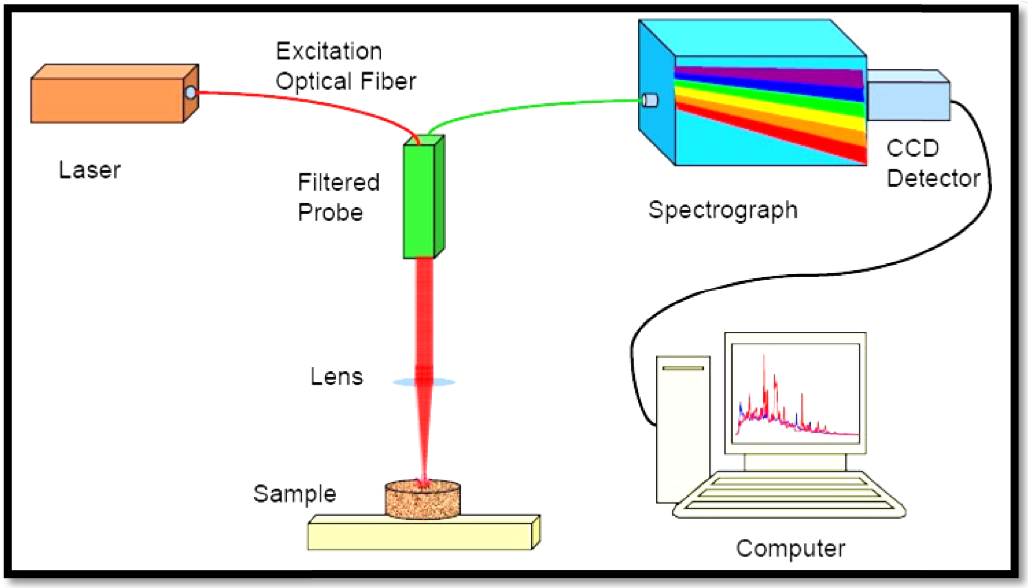

Fig. 3.7. Schematic diagram of Raman Spectroscopy.

3.3.6. Fourier Transform Infrared Spectroscopy (FTIR) and ion transport studies

Fourier transform infrared (FTIR) spectroscopy is a powerful technique for identifying different chemical compositions such as the presence of certain functional groups in a molecule by producing an infrared absorption spectrum as a molecular "fingerprint". In this technique, a beam of infrared light is passed through the sample and the absorption of the infrared light by the sample is measured which is plotted against wavenumber of the infrared radiation. The basic principle is that a specific molecule absorbs light energy at a specific frequency which is called as resonance frequency. The absorption of energy (quanta) leads to the increase in vibrational energy of atoms. A molecular bond vibrates at several specific frequencies which corresponds to ground state or any of higher excited state. To increase the frequency of a molecular vibration one has to excite the bond by facilitating the absorption of light energy. If E_0 is the energy of ground state and E_1 is the energy of first excited state, $E_1 – E_0 = hc/\lambda$, where λ is the wavelength of light, c is the speed of light, h is Planck's constant. A vibration is said to be IR-active if the dipole moment is changed during the vibration. FTIR spectroscopy provides information regarding the chemical bonding or molecular structure of samples. The term “Fourier transform infrared spectroscopy” originates from the fact that a Fourier transform is required to convert the raw data into the actual spectrum.

The basic mechanism of a Fourier transform spectrometer is very simple. It uses an interferometer to modulate the wavelength from a broadband infrared source. The intensity of the transmitted or reflected light is measured by a detector and it provides a signal which is nothing but an interferogram that is analyzed by a computer by transforming it to a single-beam infrared spectrum. FTIR spectrometer works by taking a very small quantity of a sample and introducing it to the infrared cell when is then subjected to an infrared light source and scanned usually from 4000 cm^{-1} to 400 cm^{-1}. The intensity of transmitted light is measured at each wave number. This is known is the infrared spectrum of the sample. In our research work, Fourier transform infrared spectroscopy (FTIR) was performed using Perkin Elmer FT-IR Spectrum 2 spectrometer having resolution of 4 cm^{-1} (Variable Energy Cyclotron Centre, VECC, Fig. 3.8)

The transport properties of the solid polymer electrolytes can be determined by deconvoluting the FTIR spectrum for which one usually apply the Gaussian-Lorentz fitting functions in Origin software. In FTIR deconvolution technique, the region of interest must be converted into the absorbance mode before proceeding to the deconvolution analysis. The transport parameters such as number density (n) of free mobile ions, ionic mobility (μ) and diffusion coefficient (D) of the free charge carriers are calculated using the following equations,

$$n = \frac{M \times N_{\mathrm{A}}}{V_{\mathrm{total}}} \times P_{\mathrm{f}} \tag{3.4}$$

$$\mu = \frac{\sigma_{\mathrm{DC}}}{ne} \tag{3.5}$$

$$D = \frac{\mu K_{\mathrm{B}} T}{e} \tag{3.6}$$

where, P_{f} represent the percentage of free ions, σ_{DC} denotes the DC conductivity of the solid polymer electrolyte, M is the number of moles of ionic salt in each sample, N_{A} is the Avogadro's number and V_{total} is the total volume of the solid polymer electrolyte. The percentage of free ions ($\mathrm{P_f}$) in the solid polymer electrolyte can be directly estimated from the deconvolution analysis using the following equation,

$$\mathrm{P_f} = \frac{\mathrm{A_f}}{\mathrm{A_f} + \mathrm{A_c}} \times 100\ \% \tag{3.7}$$

where, $\mathrm{A_f}$ is the area under the peak representing the free ions and $\mathrm{A_c}$ is the area under the peak representing the contact ion pairs.

Fig. 3.8. FTIR spectrometer, Model : Perkin Elmer FT-IR Spectrum 2 spectrometer (Variable Energy Cyclotron Centre, VECC).

3.3.7. Impedance Spectroscopy (IS): Ionic conductivity and dielectric properties studies

A solid polymer electrolyte intended for use in energy storage device must have adequate ionic conductivity for the intended purpose along with negligible electronic conductivity. AC Impedance spectroscopy is a powerful technique for characterizing the electrical properties of solid polymer electrolytes and their interfaces with electronically conducting electrodes in a broad range of frequencies at a given applied AC potential of small amplitude. In our research works, we have used computer interfaced impedance analyzers : (1) Solartron SI 1260 Impedance Analyzer (Variable Energy Cyclotron Centre, VECC) and Agilent 4294A-Precision Impedance Analyzer (Department of Physics, Jadavpur University) in the frequency range between 40 Hz and 100 KHz at room temperature (300 K) for impedance spectroscopy (IS) measurement of our samples. The solid polymer electrolyte material is usually sandwiched between two gold electrodes which act as blocking electrodes for the electrolyte ions. At each frequency, the complex impedance (Z*), real impedance (Z') and imaginary impedance (Z") values were obtained. The relationship between Z*, Z' and Z" is $Z^* = Z' - jZ''$. The complex impedance plots are termed as “Cole-Cole” or “Nyquist” plots, having imaginary impedance component (Z") plotted against the real impedance component (Z') at each frequency. The bulk resistance value (R_b) is determined from the high frequency intercept on the Z’ axis of the Cole-Cole plot which is a very important component used to calculate the DC ionic conductivity. The DC ionic conductivity (σ_{DC}) of the solid polymer electrolyte is calculated using the following relation,

$$\sigma_{DC} = \frac{L}{R_b A} \tag{3.8}$$

where, L is the sample thickness, A is the effective contact area of the electrode and the electrolyte surface and R_b is the bulk resistance of solid electrolyte.

The electrical behavior of a solid polymer electrolyte sandwiched between two blocking electrodes under an applied electrical signal in the simplest case can be described by an equivalent circuit and the schematic representation of a sample cell is shown in Fig. 3.9. The well known Helmholtz double layer is formed when positive and negative charges are accumulated at the relevant interfaces of the blocking electrodes on application of an electrical signal to the sample cell having angular frequency ω (shown in Fig. 3.9). These double layers result in electrode polarization and they behave as two capacitors with capacitance (C_e). The geometrical capacitance (C) of the capacitor is formed by the two electrodes (without considering double layer capacitance) and the solid electrolyte. The parallel combination of R and C is correlated with the bulk property whereas the capacitive behavior of electrode/electrolyte polarization is represented by the straight line. In real situations, the semi-circle is a depressed one and the spike is tilted. Such type of behavior is associated with leaky capacitor which is also known as "Constant Phase Element" (CPE). The angle of depression of the semicircle and the angle of inclination of the straight line are due to the distributed microscopic material properties (a typical Cole-Cole or Nyquist plot is shown in Fig. 3.10). Analyzing the depressed impedance semicircle provide the bulk resistance of the material.

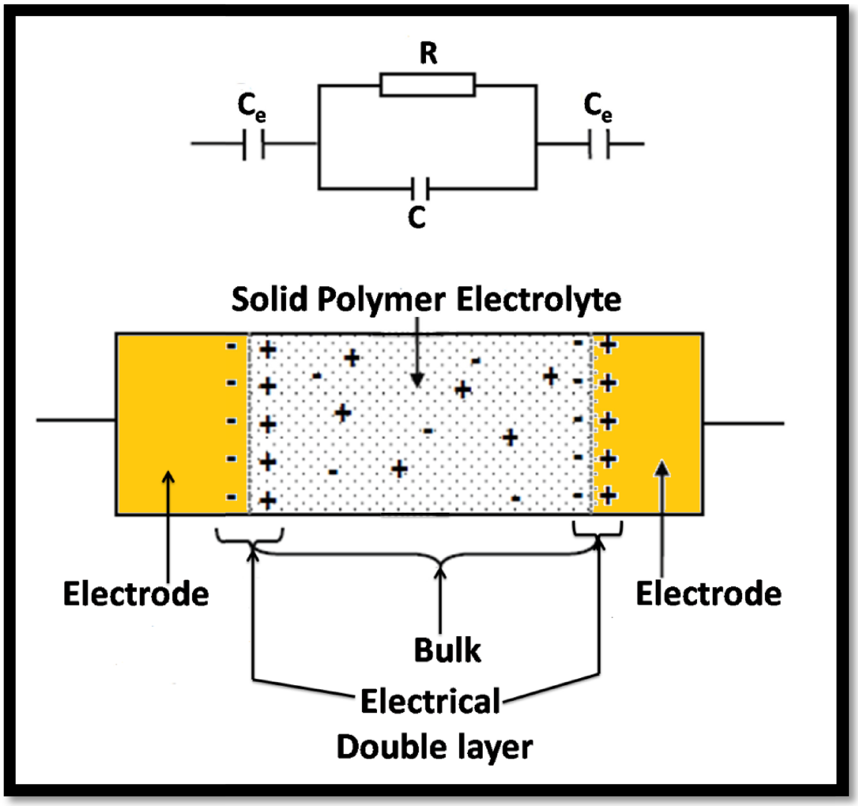

Fig. 3.9. Schematic diagram showing polarization in a sample cell and equivalent circuit for a solid polymer electrolyte sandwiched between two blocking electrodes.

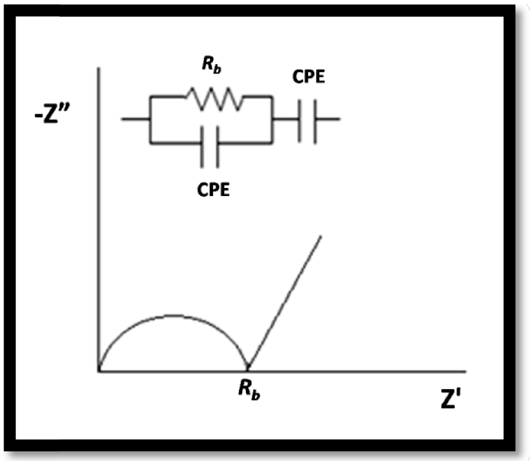

Fig. 3.10. Impedance spectra i.e. a typical Nyquist (Cole-Cole) plot and its corresponding equivalent circuit.

Dielectric property of any material is associated with the polarization phenomenon the inside the material and the interface of electrode and material of the measuring cell. Complex permittivity of a system is defined by, $\varepsilon^* = \varepsilon_r - j\varepsilon_i$ where, ε_r and ε_i are the real and imaginary parts of complex permittivity. The real part of complex permittivity is the dielectric constant which is a measure of polarization of the material. The imaginary part is the dielectric loss which is a measure of the energy loss due to the movement of ions and alignment of dipoles when the polarity of the electric field reverses. The values of dielectric constant (ε_r) and dielectric loss (ε_i) can be calculated from the impedance data using the following equations :

$$\varepsilon_r = \frac{|Z''|}{\omega C_0 (Z'^2 + Z''^2)} \tag{3.9}$$

$$\varepsilon_i = \frac{|Z'|}{\omega C_0 (Z'^2 + Z''^2)} \tag{3.10}$$

where, Z' and Z'' are the mod values of real and imaginary parts of impedance, ω is angular frequency and C_0 is the capacitance of the empty cell which is given by,

$$C_0 = \frac{\varepsilon_0 A}{L} \tag{3.11}$$

where, ε_0 is the vacuum permittivity (8.854×10^{-14} F/cm), A and L are the electrode area and their separation distance respectively. The loss tangent (tan δ) is a measure of the ratio of electrical energy loss to electrical energy stored ($\varepsilon_i/\varepsilon_r$) in periodic field. The loss tangent varies with frequency and appears maximum at a certain frequency (ω_{peak}) corresponding to the characteristic dielectric relaxation time (τ), satisfying the equation, $\omega_{\text{peak}}\tau = 1$. Many materials exhibit a non-Debye dielectric nature with a broader asymmetric loss peak.

Electric modulus (M*) formalism is used to investigate the conductivity relaxation phenomena. It suppresses the electrode polarization effects in the low frequency regime and results in a better picture of the existing electrical relaxation processes. The frequency dependent complex electric modulus (M^*) is given as follows,

$$M^*(\omega) = \frac{1}{\varepsilon^*(\omega)} = M' + j\,M'' = \frac{\varepsilon_{\mathrm{r}}}{\varepsilon_{\mathrm{r}}^2+\varepsilon_{\mathrm{i}}^2} + j\,\frac{\varepsilon_{\mathrm{i}}}{\varepsilon_{\mathrm{r}}^2+\varepsilon_{\mathrm{i}}^2} \qquad (3.12)$$

where, $M'$and M''denotes the real and imaginary parts of M^*, respectively.

3.3.8. Differential Scanning Calorimetry (DSC)

Differential scanning calorimetry (DSC) is a thermoanalytical technique in which a sample is exposed to a controlled temperature program and we measure the heat flow into or out of a sample as a function of temperature. This technique was developed by Watson and O'Neill in 1962. DSC is generally used to evaluate the crystallinity, melting and glass transition temperatures of a solid polymer electrolyte material. The DSC set up consists of a computer and measurement chamber. Two pans are heated in the measurement chamber. The sample pan contains the material under investigation whereas, the second pan, which is typically empty, is used as a reference. The computer monitors the temperature and regulates the rate at which the temperature of the pans changes. The heat capacity (C_p) of a system is the amount of heat required to raise its temperature by 1 ^{0}C. It is usually given in units of *Joule*/*K* and can be determined from the heat flow and heating rate. The heat flow is the amount of heat supplied (Q) per unit time and the heating rate is the time rate change of temperature. Hence, heat capacity is given as, C_p = Heat flow / Heating rate = Q / ΔT, where ΔT is the change in temperature. If a polymer in its molten state is cooled, at some point it will reach its glass transition temperature (T_g). When the polymer is cooled below T_g, it becomes hard and brittle. The polymer undergoes a change in heat capacity (C_p) before and after the glass transition temperature. The melting process results in an endothermic peak in the DSC curve and the melting temperature and enthalpy can be determined. In our research work, Differential Scanning Calorimetry (DSC) measurement was done using DSCQ 2000 TA Instrument (Waters India) (Indian Association for the Cultivation of Science, IACS).

3.3.9. DC Polarization method and transference number measurement

DC polarization method is a significant mechanism to observe the macroscopic ion transportation process and to understand the ion transport behavior in the solid polymer electrolytes. It is the most useful technique to estimate the ionic or electronic contribution to the total conductivity in ionic or mixed conductors. In this technique, the sample is placed between the two blocking electrodes and a DC potential (~ 1 or 2 Volt) is applied across it which drives the mobile ionic species to move towards the respective electrodes. The schematic diagram of experimental set up for DC polarization is shown in Fig. 3.11 using which the ionic transference number can be estimated.

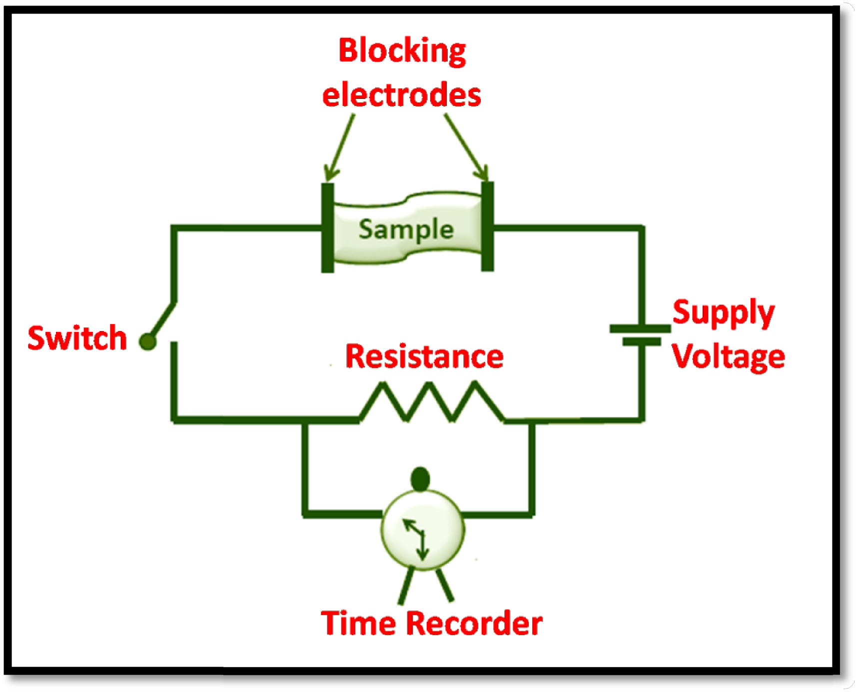

Fig. 3.11. Schematic diagram of experimental set up for measurement of ionic transference number.

In our research work, Keithley 2450 source meter (Department of Physics, Jadavpur University) is used to measure the ionic transference number. A fixed dc voltage of 1 V was applied to the sample and the current was measured as a function of time. The DC current decreases with time and becomes almost constant as polarization develops. In current versus time plot, $I_{initial}$ is the initial current which is sum of ionic and electronic current. The residual current I_{final} is contributed by the electrons. We can calculate the ionic transference number (t_{ion}) using the following equation,

$$t_{ion} = \frac{I_{initial}-I_{final}}{I_{initial}} \tag{3.13}$$

3.4. Electrochemical applications

3.4.1. Fabrication of the symmetric supercapcitor

The electrodes are fabricated by using a paste of a homogeneous mixture made of acetylene black (AB) and polytetrafluoroethylene (PTFE) for the case of symmetric electric double layer capacitor (EDLC) and spinel ferrite nanoparticles / silver decorated spinel ferrite@rGO nanocomposite, acetylene black (AB) and polytetrafluoroethylene (PTFE) taken in the wt. % ratio of 50:45:5 for the case of symmetric hybrid supercapacitors. The paste is then compacted into a thin sheet using mortar and pestle and compressed on a stainless steel mesh having the surface area of 1 cm^2. The prepared electrode was heated at 60 ℃ for 6 h under vacuum to evaporate the solvent completely. The total weight of the active material in the electrode is usually ~10-20 mg. A coin type unique symmetric supercapacitor has been developed with the prepared electrode material which is used as both cathode and anode for the cell and a solid polymer electrolyte material is sandwiched between those two electrodes (shown in Fig. 3.12).

3.4. 2. Electrochemical characterization

The electrochemical behavior of the fabricated supercapacitor is investigated with AUTOLAB-30 potentiostat/galvanostat (Fig. 3.12c, Variable Energy Cyclotron Centre, VECC) which is used to study cyclic voltammetry (CV), galvanostatic charge-discharge (GCD) and electrochemical impedance spectroscopy (EIS) performances of the developed cell.

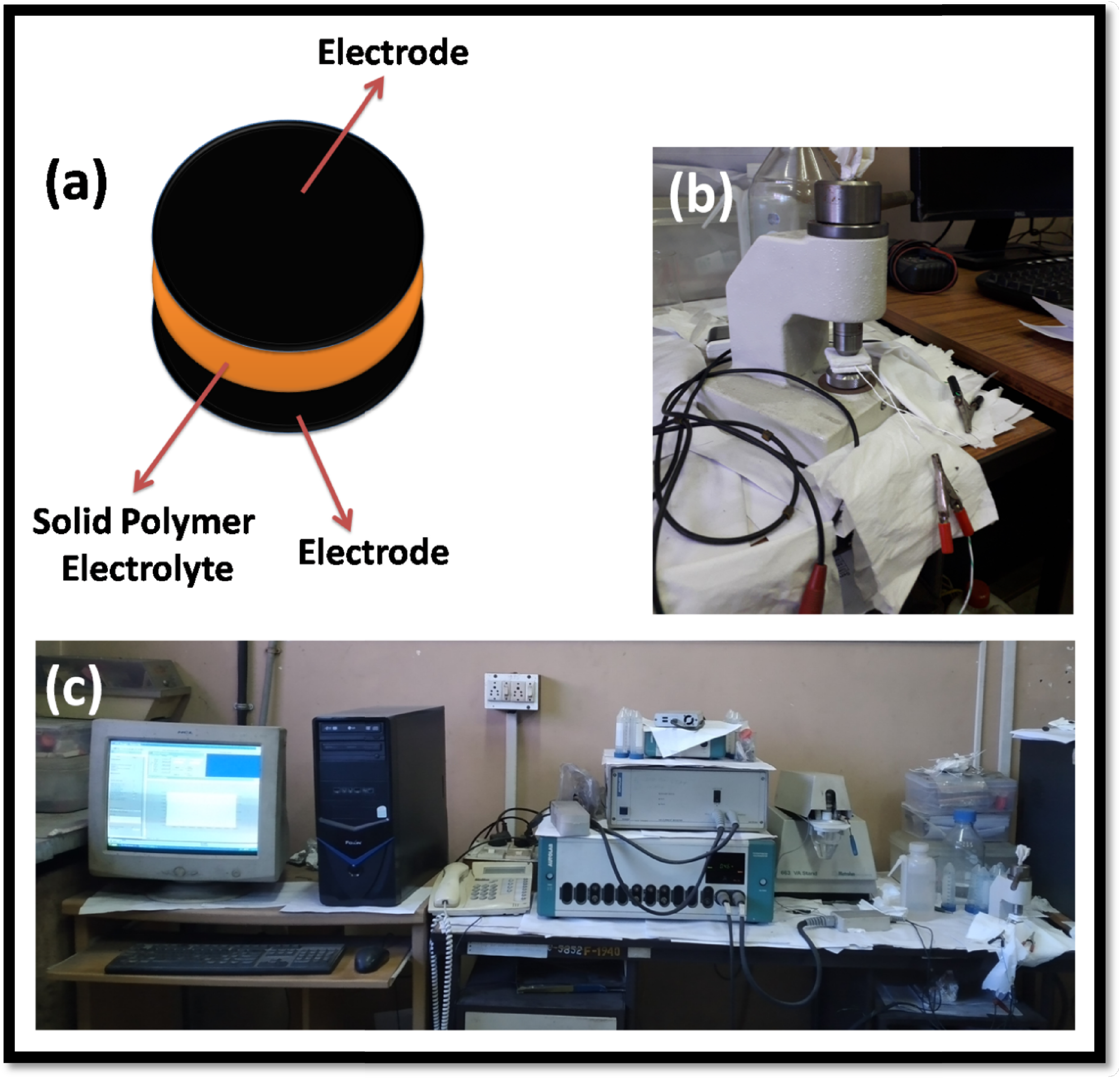

Fig. 3.12. (a,b) Schematic diagram and original picture of the fabricated coin type symmetric supercapacitor cell, (c) AUTOLAB-30 potentiostat/galvanostat for electrochemical measurement of the fabricated supercapacitor.

3.4. 2.1. Cyclic Voltammetry (CV)

Cyclic voltammetry (CV) is a widely used technique to test the performance of a supercapacitor. In CV method, the potential of the supercapacitor is scanned linearly between two potential limits (V_1 and V_2) using a triangular waveform as shown in Fig. 3.13a. During the potential scan, the potentiostat measures the current resulting from the applied potential. The current versus potential is represented by a cyclic voltammogram (a typical curve of a symmetric EDLC is shown in Fig. 3.13b). This gives insight into the capacitive and pseudocapacitive behavior of the electrochemical cell. The current is independent of potential and shows a rectangular plot for an ideal double layer capacitor. However, the rectangular shape is distorted if redox reactions occur displaying oxidation and reduction peaks. The anodic peak exists at a higher potential, while the cathodic peak exists at a lower potential.

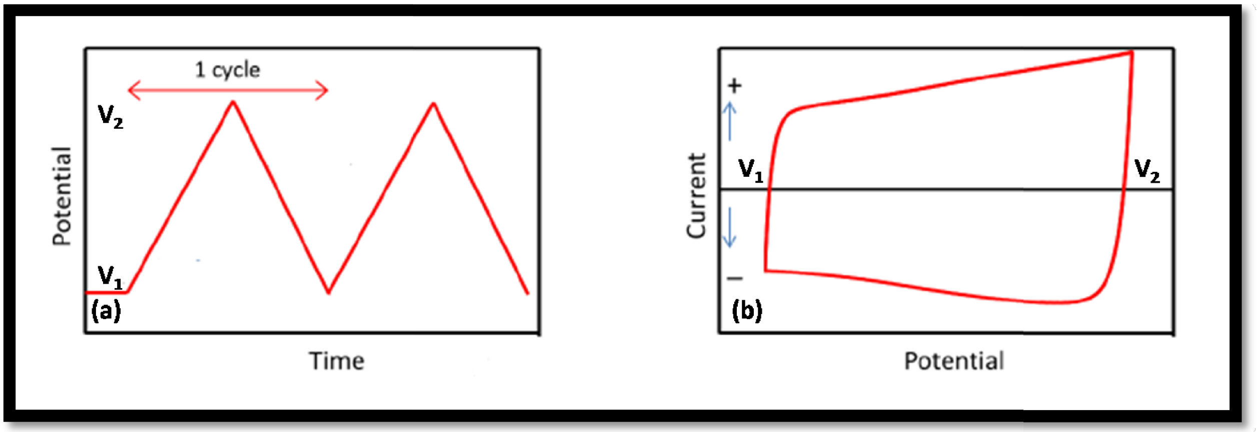

Fig. 3.13. (a) The supercapacitor potential is scanned linearly between two potential limits (V_1 and V_2) using a triangular waveform, (b) a typical cyclic voltammogram curve of a symmetric EDLC.

3.4.2.2. Galvanostatic charge-discharge (GCD)

The applicability and performance analysis of a supercapacitor is evaluated through galvanostatic charge-discharge (GCD) technique. In GCD method, the supercapacitor is charged and discharged under constant current or galvanostatic conditions and the voltage (V) is recorded as a function of time (t). First, the supercapacitor is charged at a constant current until the voltage changes from the discharged state (V_1) to its maximum operating voltage (V_2). Then the current is reversed to discharge the supercapacitor back to the discharged state (V_1) as shown in Fig. 3.14. A typical charge-discharge curve of a symmetric EDLC is shown in Fig. 3.14. The specific capacitance (C_{sp}) can be evaluated from the charge-discharge curve using the following equation,

$$C_{sp} = \frac{2I}{\left(\frac{\Delta V}{\Delta t}\right) \times m} \tag{3.9}$$

where, I is the charging current, ΔV is the potential window, Δt is the discharging time and m is the mass of the active material per electrode.

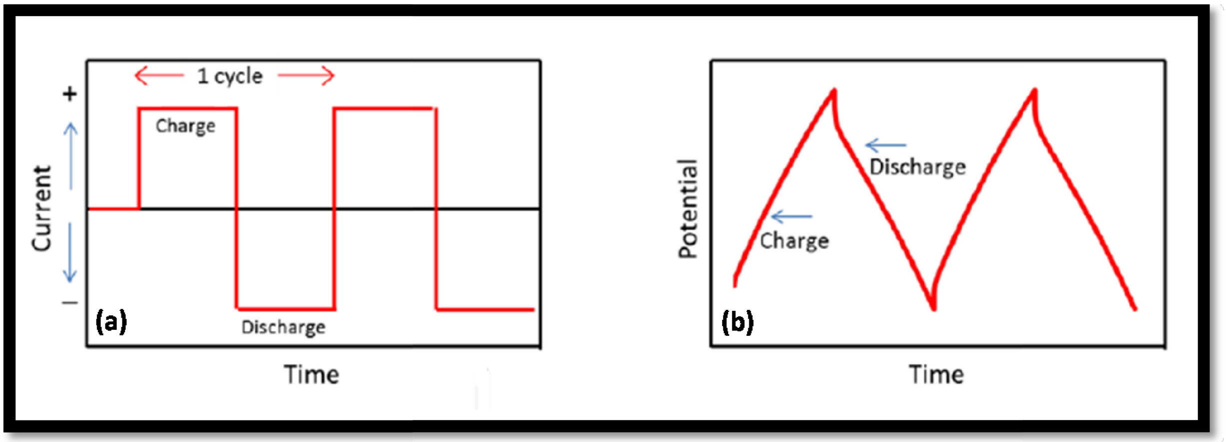

Fig. 3.14. (a) A constant current to charge and discharge a supercarpacitor , (b) a typical charge-discharge curve of a symmetric EDLC.

Generally, the charge-discharge curve consists of two parts: capacitive and resistive as shown in Fig. 3.15. The capacitive part represents the voltage change during the discharge of the capacitor, while the resistive part represents the voltage drop due to the equivalent series resistance (ESR or R_s) of the supercapacitor. Energy density (E_D) and power density (P_D) are two important parameters to evaluate of the electrochemical performance of any supercapacitor. These parameters can be estimated from the following relations,

$$E_D = \frac{1}{2}\left[\frac{C_{sp}\Delta V^2}{3.6}\right] \mathrm{Wh/kg} \tag{3.10}$$

$$P_D = \left[\frac{E_D}{t_d}\right] \times 3600 \ \mathrm{W/kg} \tag{3.11}$$

where, t_d is the discharging time.

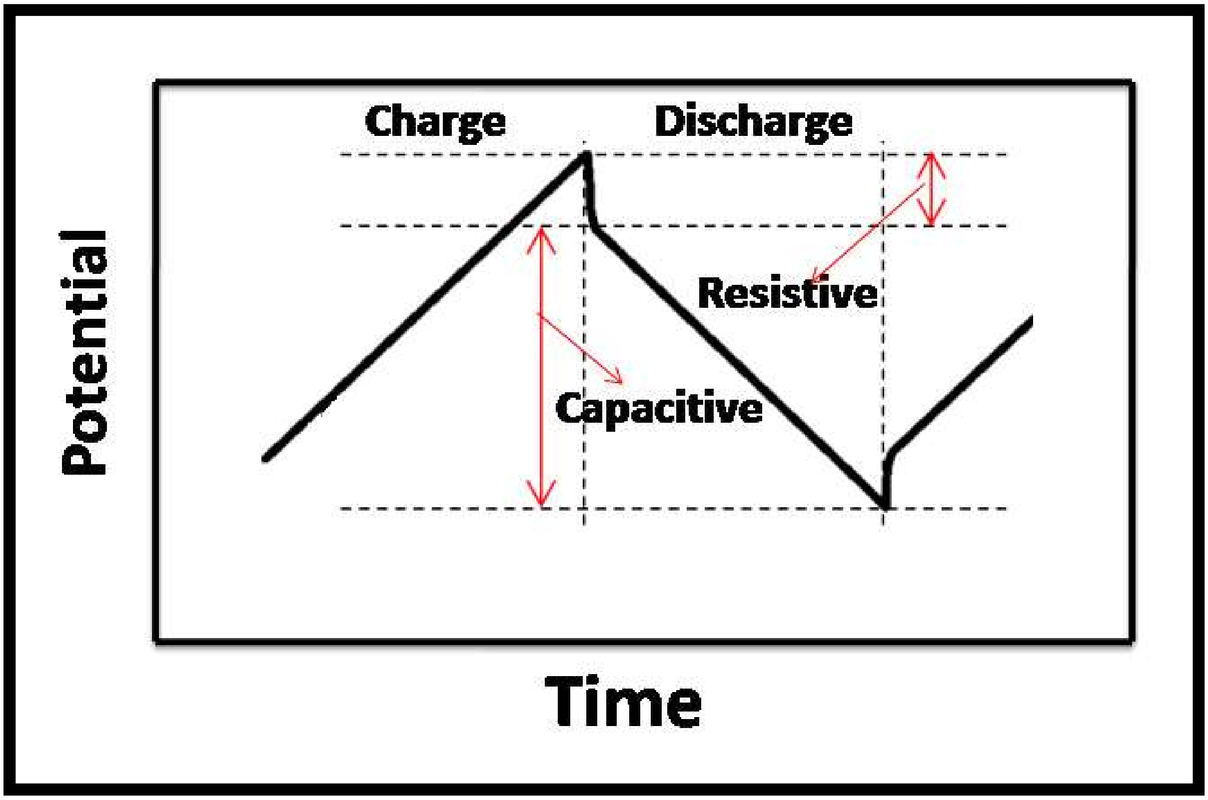

Fig. 3.15. Constant current charge-discharge curve showing resistive and capacitive parts.

3.4.2.3. Electrochemical impedance spectroscopy (EIS)

Electrochemical impedance spectroscopy (EIS) is a widely used technique to measure the impedance of a supercapacitor by applying a sinusoidal voltage perturbation to the system, in the frequency domain. The equivalence series resistance (ESR or R_s), charge transfer resistance (R_{ct}) and Warburg factor of the device (a typical Nyquist plot for a EDLC is illustrated in Fig. 3.16a) can be determined using this technique. The impedance spectra is usually analyzed based on Randles equivalent circuit as shown in Fig. 3.16b. The ESR arises from the electronic resistance of the electrode material, interfacial resistance between the current-collector and the electrode and that with the electrode and electrolyte. The value of R_{ct} must be low to assure better diffusion of ions at the electrode-electrolyte interface. The diffusion process of the electrolyte ions inside the electrode pores is described as the Warburg factor.

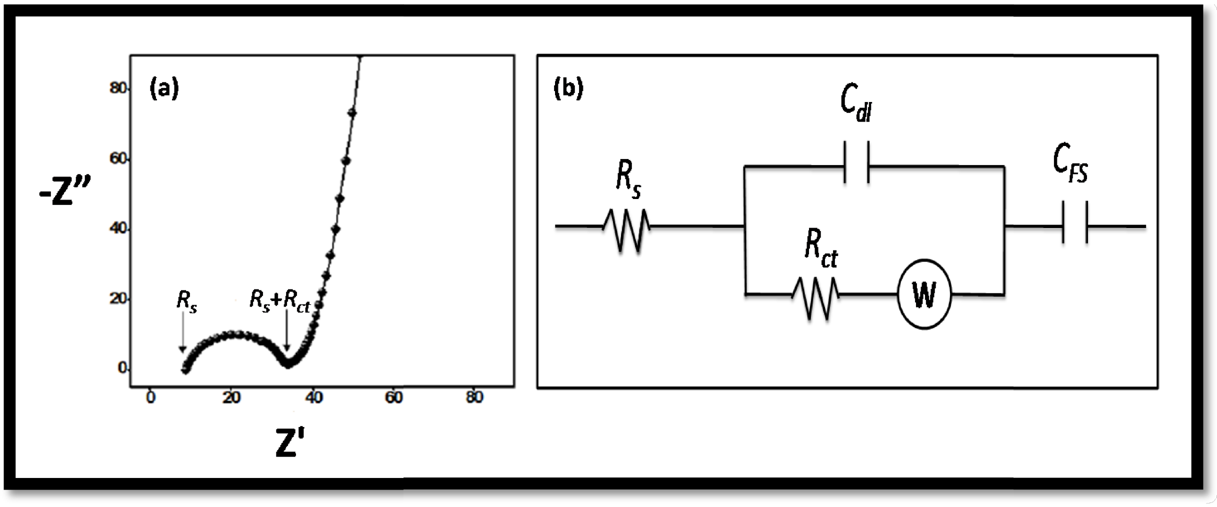

Fig. 3.16. (a) A typical Nyquist plot for a EDLC, (b) Randles equivalent circuit used to analyze the impedance spectra of a supercapacitor.

In the Randles equivalent circuit (Fig. 3.16b), C_{dl} represents the electric double layer capacitance and C_{FS} represents the pseudocapacitance which accounts for the faradaic reactions inside the electrode.

Chapter 4

Ionic conduction and charge carrier relaxation in chitosan acetate based solid biopolymer electrolyte embedded with $LiClO_4$

4.1. Introduction

Solid biopolymer electrolytes (SBE) have been extensively studied for the last few decades owing to their potential applications in electrochemical energy storage and energy conversion devices such as dye-sensitized solar cells (DSSC) [1,2], batteries [3,4] and supercapacitors [5,6]. These materials are emerging as promising alternatives to liquid electrolytes which involve risk of leakage. Recently, the biopolymers such as starch, cellulose, gelatin, chitosan etc. attract more attention as they are biodegradable, environmental friendly, low cost and non-toxic and thus becoming highly favorable over synthetic polymers [7-10]. The commercial chitosan, derivable from the shell of shrimps and crabs, has amine and hydroxyl groups in its structure. These chemical groups enable it to get modified which is crucial for several applications [11-13]. On the contrary, chitosan has low conductivity like other biopolymers. This conductivity can be tuned by using ionic salts and suitable plasticizers as dopant materials of the host polymer [5]. The most common and popular salt used for introducing charge carriers in the polymer host is lithium perchlorate ($LiClO_4$) [14], although different ammonium, sodium and zinc salts are also used [10,15,16]. Impedance spectroscopy is a widely used technique to study the ionic conduction and charge carrier relaxation processes in the solid polymer electrolytes, while the Fourier transform infrared spectroscopy is used to study the complexation and ionic interactions of the salt with the polymer material. The ion transport mechanism in solid polymer electrolytes is very complex owing to the inherent complexity of the polymer microstructure [17]. The study of ionic transport in solid polymer electrolytes is controlled by ionic motion coupled with the polymer segmental motion [18]. The relaxation dynamics can be understood through dielectric permittivity and modulus formalisms [19]. In the low frequency region, the complex permittivity data are concealed by electrode polarization effects as a result of which the relaxation processes are not well observed, while using electric modulus formalism, the relaxation phenomenon becomes distinct by suppressing the effects of electrode polarization.

In this work, the ionic conductivity, dielectric and transport properties of the chitosan acetate based solid biopolymer electrolytes (SBE) containing different weight fractions of dopant salt ($LiClO_4$) are studied using impedance spectroscopy analysis at room temperature (300 K). The frequency dependence of the conductivity spectra is studied in order to understand the ion dynamics. The relaxation behavior of the charge carriers in the SBE material is studied for different salt concentrations using electric modulus spectra analysis. Further, FTIR spectroscopy analysis is done to understand the interactions between the host biopolymer and the dopant salt.

4.2. Experimental

4.2.1. Sample Preparation

Chitosan acetate films (CA) with lithium perchlorate ($LiClO_4$) as a source of charge carriers were synthesized by the solution casting technique. 500 mg of commercial chitosan powder was dissolved in acetic acid and then doped with ($16.67 - 44.44$ wt.%) amount of $LiClO_4$. The mixtures were magnetically stirred until homogenous solutions were obtained. All the resulting solutions were cast in separate polypropylene petri dishes and allowed to dry at room temperature for the thin polymer films to form. The formed transparent films (thickness $43 - 188\ \mu$m) were then stored in dessicator to prevent from moisture contamination.

4.2.2. Characterization

Impedance measurement of the solid biopolymer electrolyte films (SBE) was done by using computer interfaced impedance analyzer (Agilent 4294A-Precision Impedance Analyzer) in the frequency range between 40 Hz and 2 MHz at room temperature (30℃). For the electrical impedance measurement, the SBEs were cut into suitable sizes and sandwiched between two gold blocking electrodes, each of diameter 1 cm. Fourier transform infrared spectroscopy (FTIR) of the SBE was performed on a Perkin Elmer Frontier FTIR spectrometer and the FTIR absorption spectra were collected in the wavenumber ranging between 600 and 4000 cm^{-1} at room temperature (30 °C) with a resolution of 4 cm^{-1}.

4.3. Results and Discussion

4.3.1. Electrochemical Impedance Spectroscopy (EIS)

4.3.1.1. Ionic conductivity studies of the biopolymer composites

Impedance spectroscopy studies have been investigated to probe the conductivity and ion transport properties of the solid biopolymer electrolyte material (SBE). The ionic conductivity for various compositions of lithium perchlorate ($LiClO_4$) incorporated in chitosan acetate (CA) biopolymer films are studied using impedance spectroscopy. Fig. 4.1a represent the Nyquist plots of CA and $LiClO_4$ composite films (henceforth noted as LC@CA) for different weight percentages of lithium perchlorate (w_{LC}) in the range $0 \leq w_{LC} \leq 44.44$ at ambient temperature (300 K). The Nyquist plot has two well defined regions: a semi-circular arc in the high frequency range which is attributed to the conduction process in the SBE bulk material and a tilted spike representing the electrical double layer (EDL) part between electrode-electrolyte interface. All the results are analyzed based on an equivalent circuit consisting of combinations of resistor and constant phase element (CPE) as shown in Fig. 4.1b and the bulk resistance (R_b) of the SBE is calculated. The R_b for all the LC@CA SBEs decreases with increase in $LiClO_4$ concentration (w_{LC}). The dc conductivity (σ_{DC}) of the SBE is calculated using the relation,

$$\sigma_{DC} = \frac{L}{R_b A} \tag{4.1}$$

where, L is the sample thickness and A is the effective contact area of the gold blocking electrode and the SBE surface.

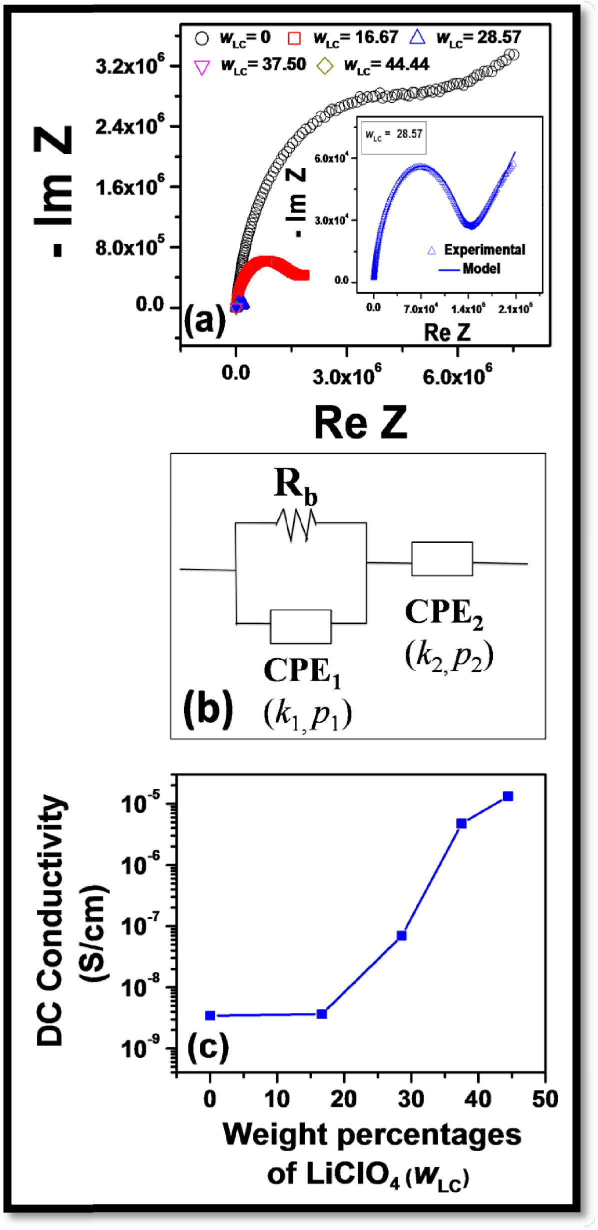

Fig. 4.1. (a) Nyquist plots at room temperature (300 K) with varying composition of $LiClO_4$ in LC@CA SBE material and the inset diagram shows the Nyquist plot fitting of the experimental data based on Eq. 4.2 for LC@CS SBE material with $w_{LC} = 28.57$, (b) The equivalent circuit used to model the Nyquist plots for LC@CS SBE material, (c) DC conductivity (σ_{DC}) shown as a function of salt concentrations (w_{LC}) at room temperature.

The variation of σ_{DC} of LC@CA biopolymer composites for different w_{LC} as illustrated in Fig. 4.1c, shows an increasing trend of room temperature ionic conductivity with increase in $LiClO_4$ concentration. This gradual increment of ionic conductivity can be correlated with increase in number density (n) or mobility (μ) of the free charge carrier ions or both [20-22]. The room temperature ionic conductivity has increased by four orders in magnitude (from ~ 10^{-9} to ~10^{-5} S/cm) on the incorporation of salt ($w_{LC} = 44.44$) in chitosan acetate (CA).This enhancement in ionic conductivity with $LiClO_4$ concentration may be due to the transition from a semi-crystalline to an amorphous phase of the biopolymer complex resulting more free space which facilitates ion migration. Moreover with increase in w_{LC}, the segmental mobility of the biopolymer chains might have increased which being coupled with the mobile ions result in an increase in ionic conductivity. Increasing $LiClO_4$ concentrations beyond $w_{LC} = 44.44$ makes the CA films brittle making it unsuitable for further study.

The constant phase element (CPE) used in the equivalent circuit as shown in Fig. 4.1b is a "leaky capacitor". In real systems, there is always some energy dissipation and thus the experimental results can only be reproduced by an equivalent circuit involving leaky capacitors instead of ideal capacitors. The impedance of the CPE is given by, $Z_{\mathrm{CPE}} = k\,(j\omega)^{-p}$, where k is the CPE coefficient and p is some fractional parameter ($0 < p < 1$). When $p = 1$, the CPE would become identical to an ideal capacitor having its impedance given by, $Z_{\mathrm{C}} = (j\omega C)^{-1}$,with inverse of k corresponding to the capacitance. On the other hand, CPE would behave like a resistor for $p = 0$ where k corresponds to the resistance. For $0 < p < 1$, CPE behaves like a leaky capacitor. The impedance of the equivalent circuit as shown in Fig. 4.1b is given as,

$$Z^{*} = \frac{R_b}{1+R_b k_1^{-1}(j\omega)^{p_1}} + k_2(j\omega)^{-p_2} \tag{4.2}$$

where, k_1^{-1} and k_2^{-1} represent the bulk geometrical capacitance of the polymer electrolyte and the capacitance of EDL part between electrode-electrolyte interface, respectively. The Nyquist plot along with the best fit curve using Eq. 4.2 is shown in the inset of Fig. 4.1a as a representative curve for $w_{LC} = 28.57$. It is important to note here that the value of the exponent (p_2) associated with CPE_2 decreases from ~ 0.77 to ~ 0.60 with increase in $LiClO_4$ concentrations. This indicates that the salt ($LiClO_4$) creates stronger disorder in the biopolymer structure.

4.3.1.2. AC conductivity study

The frequency dependence of the conductivity for different $LiClO_4$ salt concentrations is studied in order to understand the ion dynamics in LC@CA SBE material. The AC conductivity is calculated using the following relation, $\sigma(\omega) = \omega\varepsilon_0\varepsilon_{im}$ where, ε_0 is the permittivity of vacuum and ε_{im} is the dielectric loss. Fig. 4.2a represents the frequency dependent AC conductivity spectra at room temperature (300 K) for $16.67 \leq w_{LC} \leq 44.44$. It is observed that the AC conductivity spectra show an almost frequency independent plateau region at lower frequencies and a dispersive region at higher frequencies for lower salt concentrations ($w_{LC} = 16.67$ and 28.57). As the materials exhibit significantly large ionic conductivity for higher salt concentrations ($w_{LC} = 37.50$ and 44.44), a low frequency dispersive region is observed which is due to the accumulation of charge carriers at the electrode-electrolyte interface followed by an almost frequency independent conductivity region corresponding to the DC conductivity. The frequency independent plateau region characterizes the ionic conduction in SBE material related to the hopping motion of the mobile Li^+ ions.

According to Almond-West (AW) formalism, the ac conductivity can be explained in terms of ion-hopping frequency (ω_p) which is given as follows [23,24],

$$\sigma(\omega) = \sigma_{DC}\left[1 + \left(\frac{\omega}{\omega_p}\right)^n\right] \tag{4.3}$$

where, n is the AW power law exponent and σ_{DC} is the DC conductivity of the SBE material. The carrier concentration term (K) for the SBE material can be calculated from ion-hopping frequency (ω_p) which is given as [25],

$$K = \frac{\sigma_{DC}T}{\omega_p} \tag{4.4}$$

where, T is the ambient temperature. The best fit of the AC conductivity spectra based on Eq. 4.3 for $16.67 \leq w_{LC} \leq 44.44$areshown in Fig. 4.2a. However, it is to be mentioned here that Eq. 4.3 is unable to reproduce the experimental AC conductivity results at lower frequencies for composites having large salt concentrations ($w_{LC} = 37.50$ and 44.44). It should be noted here that the value of n is ~ 0.7 which confirms that LC@CA SBE system is principally an ionic conductor. An ion successfully hops from one site to another neighbouring vacant site in the biopolymer matrix when the frequency is lower than the ion-hopping frequency (ω_p), thus contributing to the DC conductivity. With increasing LiClO$_4$ concentrations, the ion-hopping frequency shifts towards higher frequencies as shown in Fig. 4.2b. This transition from the frequency independent region to the high frequency dispersion region indicates the onset of the conductivity relaxation process. The relaxation at high frequencies above ω_p arises from the motion of the biopolymer chains. At higher frequencies, there may happen two competing relaxation processes: (A) unsuccessful hopping (i.e. ion hopping back to its initial site) and (B) successful hopping (i.e. neighbourhood ions relax with respect to the ion's position). When the ratio of successful to unsuccessful hopping increases, conductivity becomes more dispersive at higher frequencies [26]. It is observed that the higher DC ionic conductivity is associated to increased ion hopping rate. With increase in w_{LC}, the carrier concentration term (K)increases which indicates the increased free Li$^+$ ion concentration (Fig. 4.2b), resulting in an enhanced ionic conductivity.

Since the AW formalism is not applicable in the low frequency regime where electrode polarization in dominant, the fractal nature of the electrode-SBE interface has been considered and thus the frequency dependent complex AC conductivity is given as [27, 28],

$$\sigma(\omega) = \sigma_0 + \frac{\sigma_{\mathrm{DC}} - \sigma_0}{1 + (i\omega\tau_j)^{-\alpha}} + i\omega\varepsilon_0[\varepsilon_{relax}(\omega) - \varepsilon_\infty] \tag{4.5}$$

where, σ_{DC} is the DC conductivity of the SBE material, σ_0 is the conductivity at constant electric field, ε_0 is the vacuum permittivity, $\varepsilon_{relax}(\omega)$ determines the contribution of the dielectric relaxation part, ε_∞ is the high frequency limiting value of dielectric permittivity, τ_j is the characteristic relaxation time and α is a constant determining the fractal dimension of the space-time ensemble in the space-charge region having its value lies between 0 and 1. The complex AC conductivity in the intermediate and high frequency regimes is analyzed using Dyre's random free-energy barrier model (RBM) where the ionic conduction is considered to take place through hopping motion of the charge carrier ions, which are subjected to spatially random varying energy barriers and is given as [29],

$$\sigma(\omega) = \sigma_{\mathrm{DC}}\left[\frac{i\omega/\omega_e}{\ln(1 + i\omega/\omega_e)}\right] \tag{4.6}$$

where, $\omega_e = 1/\tau_e$ is the attempt frequency to overcome the free energy barrier determining the DC conductivity. The real part of the experimental frequency dependent AC conductivity spectra for the SBE material with $w_{LC} = 37.50$ and 44.44 along with the best fit using Eqs. 4.5 and 4.6 are shown in Fig. 4.2c. The best fit parameters are listed in Table 4.1. It is noted here that the values of σ_{DC} and σ_0 do not coincide due to the effects of electrode polarization and the value of σ_0 is less than that of σ_{DC}. The values of α are less than unity, indicating fractal dimension of the electrode-SBE interface. Thus, the complete AC conductivity spectra for the SBE material at higher salt concentrations can be analyzed using the RBM model by combining the contribution of the electrode polarization effects.

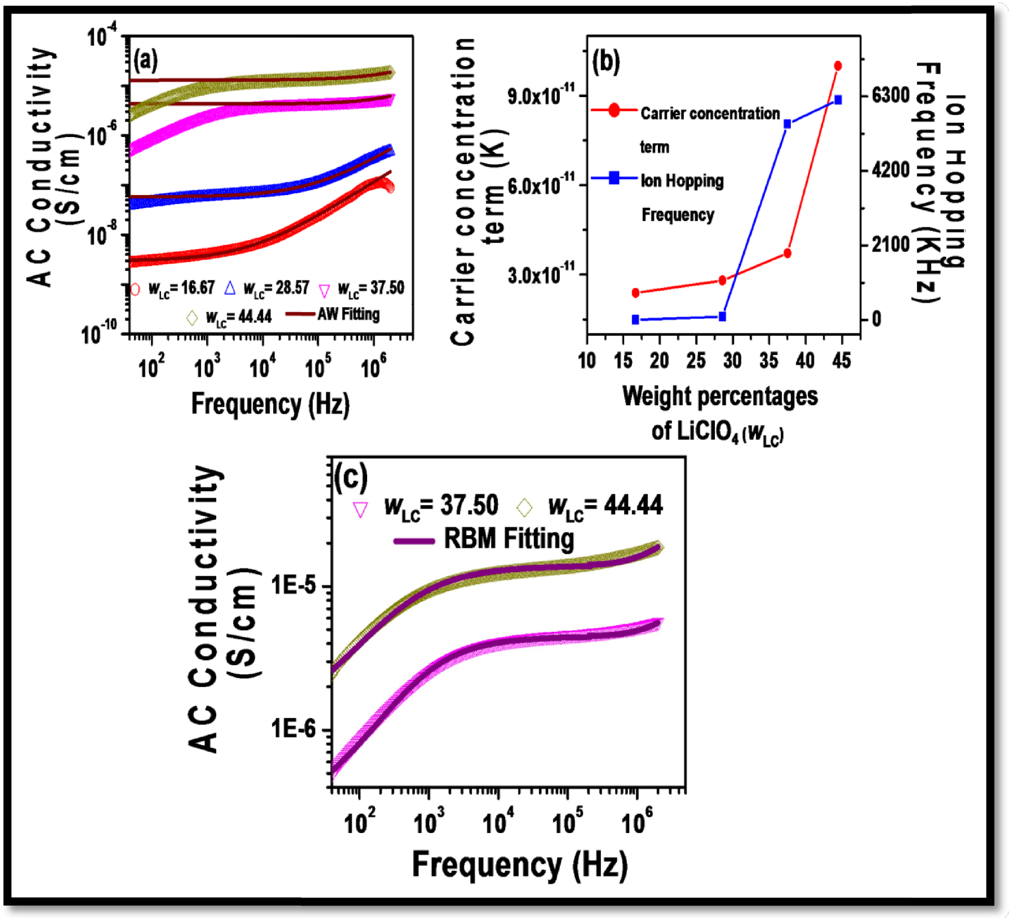

Fig. 4.2 (a) AC conductivity spectra at different w_{LC} in LC@CA SBE material. Solid lines are the fits of the experimental data to Eq. 4.3, (b) Variation of ion hopping frequency and mobile carrier concentration factor with w_{LC}, (c) AC conductivity spectra at w_{LC}= 37.50 and 44.44 in LC@CA SBE material where solid lines are the fits of the experimental data to Eqs. 4.5 and 4.6.

Table 4.1. Values of the fitting parameters σ_{DC}, σ_0, τ_j, α and τ_e for LC@CA SBE material.

Solid biopolymer electrolytes	σ_{DC} (S/cm)	σ_0(S/cm)	τ_j (s)	α	τ_e (s)
$w_{LC} = 37.50$	4.5×10^{-6}	0.2×10^{-6}	0.20×10^{-3}	0.67	2.0×10^{-7}
$w_{LC} = 44.44$	1.4×10^{-5}	0.8×10^{-6}	0.36×10^{-3}	0.62	2.7×10^{-7}

4.3.1.3. Dielectric relaxation study

The dielectric permittivity spectra are studied in order to understand the dielectric relaxation process and conductivity behavior of the LC@CA SBE material. The frequency dependent complex dielectric permittivity (ε^*) is given by, $\varepsilon^*(\omega) = \varepsilon_r(\omega) - j\varepsilon_{im}(\omega)$ where ε_r and ε_{im} are the real and imaginary parts of the complex dielectric permittivity. The real part of permittivity known as the dielectric constant and imaginary part known as the dielectric loss quantifies the amount of energy stored and energy dissipated in the material, respectively during each cycle of the applied AC electric field. The frequency dependent dielectric constant and dielectric loss are shown in Figs. 4.3a and 4.3c respectively for different w_{LC} in LC@CA SBE at room temperature. The dielectric permittivity dispersion of the SBE material with frequency is attributed to the electrode polarization (EP) and ionic polarization processes [30]. It is observed that both the values of ε_r and ε_{im} increases gradually with decreasing frequency. This is due to the space charge polarization near electrode-SBE interface at low frequencies. But in the high frequency regime, the dipoles are incapable to synchronize with the fast periodic reversal of the electric field leading to a frequency lag between the oscillating dipole and the applied AC electric field, and thus the polarization due to charge accumulation decreases. At high frequencies of the applied AC electric field, the ionic polarization process is associated with the short range ionic motion. The dielectric loss (ε_{im}) shows a sudden increase in magnitude at lower frequencies with increasing salt concentrations. This is related to the motion of the free carrier ions in the bulk of the LC@CA SBE material. This indicates that the chitosan biopolymer segments become more flexible with increase in w_{LC}, thereby promoting better ion mobility.

Fig. 4.3b shows the variation of dielectric constant (ε_r) with different w_{LC}in LC@CA SBE material at different frequencies viz. 40 Hz, 10 KHz, 100 KHz and 2 MHz. It is observed that the values of ε_r at low frequency (40 Hz) are four orders of magnitude high compared to its high frequency (2 MHz) limiting ε_r value for $w_{LC} = 44.44$, indicating the dominant contribution of EP process in the low frequency regime. Also the value of ε_r at low frequency (40 Hz) changes enormously from ~ 10^2 ($w_{LC} = 0$) to ~ 10^5 ($w_{LC} = 44.44$) with increase in salt concentrations. This trend of ε_r variation is similar to that of DC conductivity variation with w_{LC}. The higher ionic conductivity with increasing w_{LC} might be due to more localization of charge carriers along with the mobile ions [31,32].

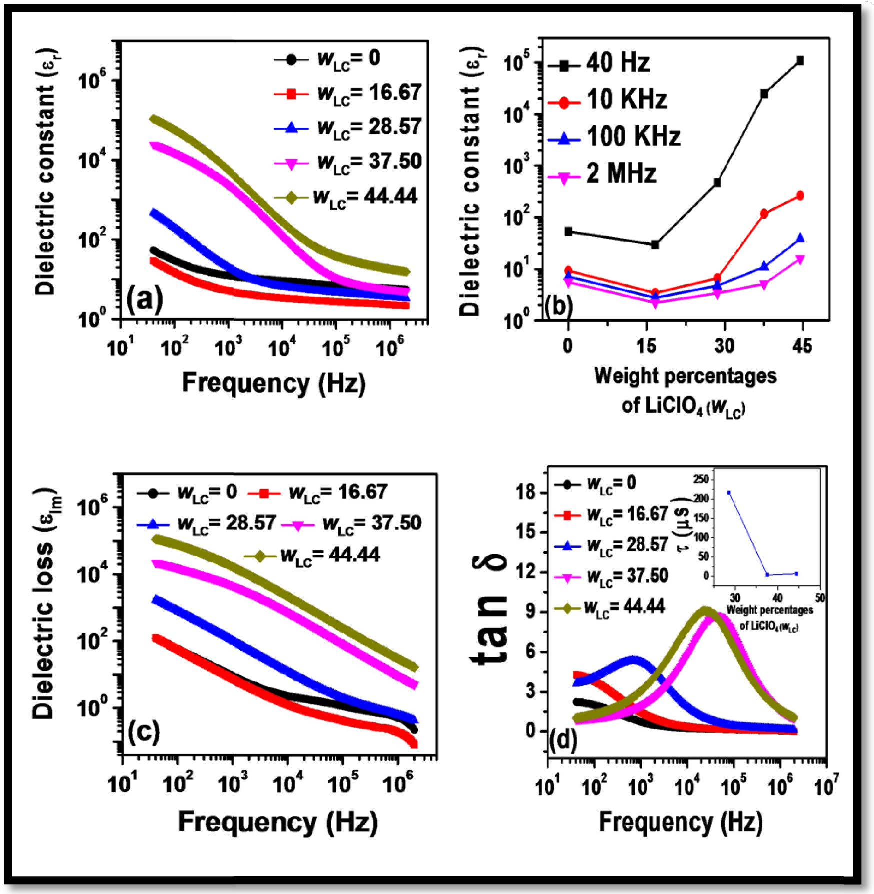

Fig. 4.3. Frequency dependence of (a) dielectric constant (ε_r) and (c) dielectric loss (ε_{im}) for different w_{LC} in LC@ CA SBE material at room temperature, (b) Variation of $\varepsilon_r$as a function of w_{LC} at different frequencies (40 Hz, 10 KHz, 100 KHz and 2 MHz), (d) Variation of tan δ with frequency at room temperature for different w_{LC} in LC@CA SBEs, the inset figure shows the variation of dielectric relaxation time with w_{LC}.

The loss tangent (tan δ) is defined as the ratio of energy loss to energy stored ($\varepsilon_{im}/\varepsilon_r$) in an applied AC electric field. The frequency dependence of the loss tangent appears maximum at a certain frequency (ω_{peak}) corresponding to the characteristic dielectric relaxation time (τ), satisfying the equation, $\omega_{peak}\tau = 1$. Fig. 4.3d shows the variation of tan δ with frequency for different w_{LC} in LC@CA SBE material at 300 K. No significant relaxation peaks is observed for pure CA film ($w_{LC} = 0$) in the frequency range under investigation. But it appears along with the inclusion of LiClO$_4$ ($w_{LC} > 16.67$) in the composite. Fig. 4.3d illustrates that the peak shifts towards higher frequency side with increase in LiClO$_4$ concentrations. Dielectric relaxation time thus decreases with increase ofw_{LC}as shown in the inset of Fig. 4.3d. This infers that an increase in the amorphous content of the SBEs with increase in w_{LC} speeds up the segmental motion of the biopolymer chains or segments by promoting motion of the mobile ions. The large width of the loss peak suggests that there is a distribution of relaxation times which support non-Debye relaxation.

4.3.1.4. Electric field Decay Function

Electric modulus formalism has been used to analyze the conductivity relaxation processes in the LC@CA SBE material by suppressing the electrode polarization (EP) effects which is dominant in the low frequency region. The frequency dependent complex electric modulus (M*) is given as follows,

$$\mathrm{M}^*(\omega) = \frac{1}{\varepsilon^*(\omega)} = \mathrm{M}' + j\,\mathrm{M}'' = \frac{\varepsilon_r}{\varepsilon_r^2+\varepsilon_{im}^2} + j\,\frac{\varepsilon_{im}}{\varepsilon_r^2+\varepsilon_{im}^2} \tag{4.7}$$

where, M$'$ and M$''$ are real and imaginary parts of complex electric modulus, respectively. The frequency dependence of M$''$ for different w_{LC} are shown in Fig. 4.4a at 300 K. The imaginary modulus (M$''$) shows a distinct relaxation peak along with a shoulder at high frequency in the composites having low w_{LC}. The frequency of the peak of M$''$ spectra is attributed to the conductivity relaxation frequency (ω_c). The conductivity relaxation time (τ_c) is obtained from the relation, $\omega_c\tau_c = 1$. The value of τ_c (7.5×10^{-6} s) for LC@CA SBE material with $w_{LC} = 28.57$ is two orders of magnitude smaller than that obtained for $w_{LC} = 0$ (2.7×10^{-4} s). Below ω_c, conducting mobile ions exhibit long-range hopping motion, while above ω_c, ions exhibit short-range localized motion. The conductivity relaxation time (τ_c) decreases with the increase of salt concentration (w_{LC}). This indicates the increase in long-range hopping motion of the Li$^+$ ions along the chitosan biopolymer chains. This also suggests that the ionic motion is coupled with the biopolymer segmental mobility which results in the shifting of the M$''$ peak towards high frequency with the increase in w_{LC}.

The electric modulus spectra are analyzed using Havriliak-Negami (HN) function [33,34] given by,

$$\mathrm{M}^* = \mathrm{M}_\infty + \frac{\mathrm{M}_s - \mathrm{M}_\infty}{[1+(j\omega\tau_c)^{\alpha_{HN}}]^{\gamma_{HN}}} \tag{4.8}$$

where, M_∞ and M_s are the high frequency and low frequency limiting values of the electric modulus spectra, respectively, α_{HN} and γ_{HN} are the shape parameters with $0 < \alpha_{HN} \le 1$ and $0 < \gamma_{HN} \le 1$. For Debye relaxation, both the shape parameter values should be unity. Fig. 4.4a shows the best fit of the experimental M$''$ spectra according to Eq. 4.8. The shape parameters obtained from the best fits for different w_{LC} are listed in Table 4.2 and their values are found to be less than unity, indicating the nature of the relaxation phenomenon is of non-Debye type.

For a quantitative analysis of the modulus data in the time domain, the relaxation function or the decay function, $\varphi\ (t)$ giving the time evolution of the electric field $[E(t) = E(0)\varphi\ (t)]$ within the LC@CA SBE material is studied. The complex electric modulus, $\mathrm{M}^*(\omega)$ is expressed in terms of Fourier transform of the relaxation function $\varphi\ (t)$ given as [34],

$$\mathrm{M}^*(\omega) = \mathrm{M}_\infty\left[1 - \int_0^\infty e^{-j\omega t}\left(-\frac{\partial\varphi(t)}{\partial t}\right)dt\right] \tag{4.9}$$

where, M_∞ is the high frequency limiting value of the electric modulus. The relaxation function can be calculated in the time domain using the inverse transform of Eq. 4.9 is given as [35],

$$\varphi(t) = \frac{2}{\pi}\int_0^\infty \frac{\mathrm{M}''}{\omega \mathrm{M}_\infty}\cos(\omega t)d\omega \tag{4.10}$$

The inverse transform is carried out for different w_{LC} using the modulus of HN equation (Eq. 4.8) keeping the parameters same as obtained from the fitting of the experimental M$''$ spectra and the resulting decay curves obtained from Eq. 4.10 are shown in Fig. 4.4b for different salt concentrations in LC@CA SBE material. The relaxation function is exponential for

Debye-type nature of relaxation phenomenon, but for non-Debye type relaxations, the relaxation function is approximated by the KWW or stretched exponential decay function [36,37] given by,

$$\varphi(t) \approx exp\left[-\left(\frac{t}{\tau_{KWW}}\right)^{\beta_{KWW}}\right] \tag{4.11}$$

where, β_{KWW} is the stretched exponent lying between 0 and 1. It is observed that the decay function calculated using HN function matches well with the KWW function as shown in Fig. 4.4b for LC@CA SBE with different w_{LC} over a particular time domain.The values of β_{KWW} for different w_{LC} as obtained from the best fits are tabulated in Table 4.2.

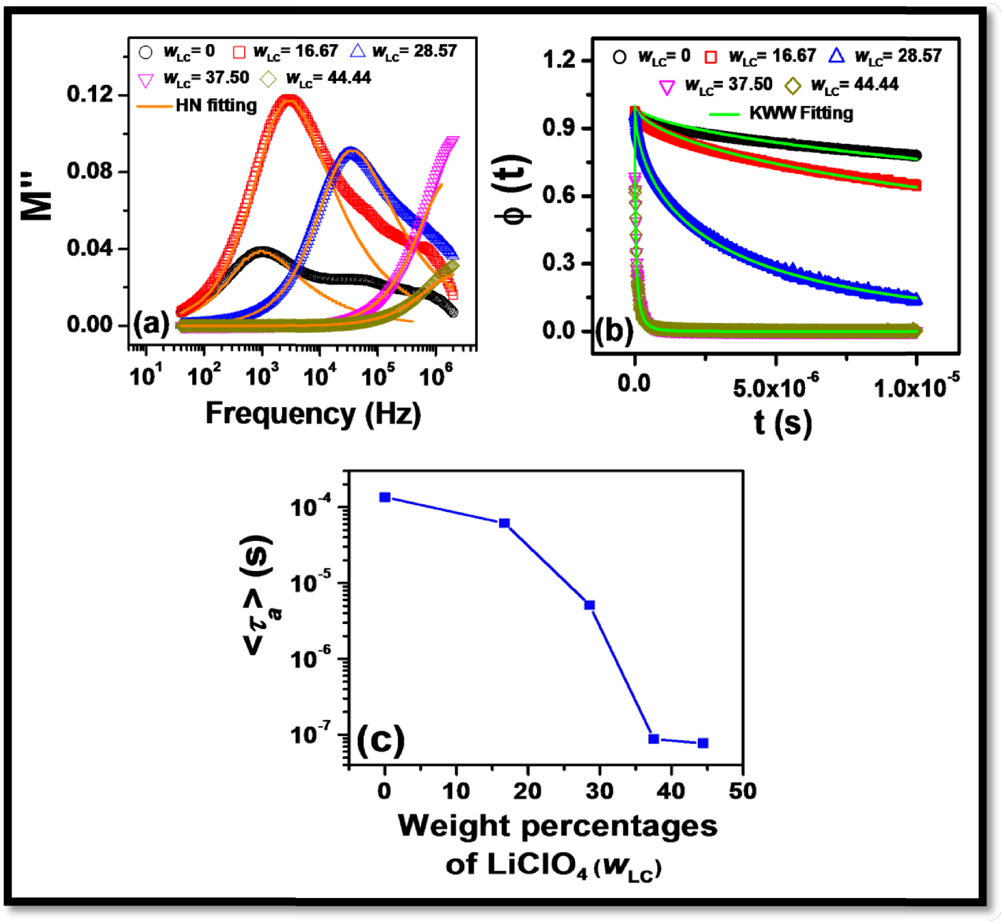

Fig. 4.4. Frequency dependence of (a) imaginary part (M″) of electric modulus (M*) for different w_{LC} in LC@CA SBE material at room temperature. The solid lines are fits of the experimental data to Eq. 4.8, (b) Relaxation function, $\varphi(t)$ shown as a function of time in LC@CA SBE material. The solid lines are fits of the calculated HN relaxation function with the stretched exponential KWW decay function (Eq. 4.11), (c) Variation of average relaxation time ($< \tau_a >$) of charge carriers with different w_{LC} in the SBE material.

Both the HN and KWW approaches are considered to have same physical significance if the HN and KWW fitting parameters follow the relation [38], $\beta_{KWW} = (\alpha_{HN}\gamma_{HN})^{\frac{1}{1.23}}$. It is found that the fitting parameters for LC@CA SBE material as listed in Table 4.2 obey the above relation successfully. The small values of β_{KWW} (< 1) signify that the relaxation behavior is highly non-exponential for LC@CA SBE material, suggesting co-operative biopolymer chain segmental motion resulting from the long-range ion-ion interactions [39] in the material. The average relaxation time, $< \tau_a >$ associated with the stretched exponential KWW decay function [35] is given as,

$$< \tau_a > = \frac{\tau_{KWW}}{\beta_{KWW}}\left[\Gamma\left(\frac{1}{\beta_{KWW}}\right)\right] \tag{4.12}$$

where, Γ is the gamma function. The variation of average relaxation time of the charge carriers for different w_{LC} in LC@CA SBE is shown in Fig. 4.4c. It is clear that the average relaxation time for the LC@CA SBE material with $w_{LC} = 44.44$ (7.68×10^{-8} s) is four orders of magnitude smaller than $w_{LC} = 0$ (1.8×10^{-4} s).

It is important to note here that the shape of the imaginary modulus, M″ spectra changes with increase in ionic salt concentrations (w_{LC}) where, β_{KWW} value is found to decrease from 0.6 to 0.51, while the shape of the AC conductivity spectra are independent of w_{LC} in which the AW power law exponent *n* is ~ 0.7. As reported by Sidebottom et al. [40], the shape of the M″spectra is very sensitive to high frequency limiting dielectric constant, $\varepsilon_r(\omega \to \infty)$. It is shown in Fig. 4.5a that the M″ (ω) curve for each w_{LC} in LC@CA SBE material cannot be scaled into a common curve by using $\varepsilon_r(\omega \to \infty)$as a scaling parameter for the M″ (ω) axis. As $\varepsilon_r(\omega \to \infty)$ is not directly related to the hopping dynamics of the mobile carrier ions, a hopping modulus, $M^*_{hop}(\omega) = 1/[\varepsilon^*(\omega) - \varepsilon_r(\omega \to \infty)]$ is defined containing only hopping motion contribution of the charge carriers and its imaginary part is given as [40],

$$M''_{hop}(\omega) = \frac{1}{\Delta\varepsilon_r} H\left(\frac{\omega}{\omega_p}\right) \tag{4.13}$$

where, $\Delta\varepsilon_r = [\varepsilon_r(\omega \to 0) - \varepsilon_r(\omega \to \infty)]$ which is exclusively dependent on the hopping motion of the mobile charge carriers and $H\left(\frac{\omega}{\omega_p}\right) = \frac{\sigma(\omega)/\left[2\pi\left(\frac{\omega}{\omega_p}\right)\sigma_{\mathrm{DC}}\right]}{[(\varepsilon_r(\omega)-\varepsilon_r(\omega\to\infty))/\Delta\varepsilon_r]^2+\left[\sigma(\omega)/\left(2\pi\left(\frac{\omega}{\omega_p}\right)\sigma_{\mathrm{DC}}\right)\right]^2}$

with ω_p being the ion-hopping frequency obtained from AW formalism for each w_{LC} in LC@CA SBE material. It is observed from Fig. 4.5b that the $\mathrm{M}''_{\mathrm{hop}}(\omega)$ curves for each w_{LC} can now be scaled into a common curve taking $\Delta\varepsilon_r$ as a scaling parameter for the $\mathrm{M}''_{\mathrm{hop}}(\omega)$ axis with no characteristic peaks for lower w_{LC} unlike $\mathrm{M}''(\omega)$ curves (Fig. 4.5a). Thus it can be concluded that the shape of $\mathrm{M}''_{\mathrm{hop}}(\omega)$ is virtually independent of w_{LC} and the peaked shape characteristic of $\mathrm{M}''(\omega)$ for different w_{LC} is actually an effect of the inclusion of $\varepsilon_r(\omega \to \infty)$ in the electric modulus definition.

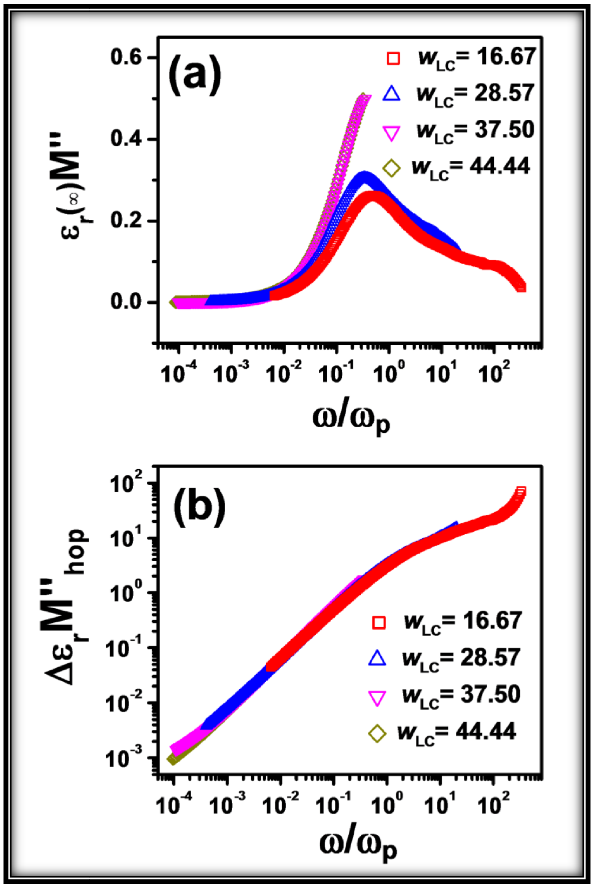

Fig. 4.5.Variation of (a) $\varepsilon_r(\infty)\mathrm{M}''(\omega)$ and (b) $\Delta\varepsilon_r\mathrm{M}''_{\mathrm{hop}}$with $\boldsymbol{\omega}/\boldsymbol{\omega}_{\mathrm{p}}$ for each w_{LC} in LC@CA SBE material.

Table 4.2.Values of the fitting parameters k_2, α_{HN}, γ_{HN} and β_{KWW} for LC@CA SBE material.

Solid biopolymer electrolytes	k_2 (F^{-1})	α_{HN}	γ_{HN}	β_{KWW}
$w_{LC} = 0$	13×10^7	0.95	0.56	0.60
$w_{LC} = 16.67$	6×10^6	0.90	0.58	0.59
$w_{LC} = 28.57$	9.7×10^5	0.92	0.55	0.574
$w_{LC} = 37.50$	4×10^5	0.93	0.50	0.54
$w_{LC} = 44.44$	2.2×10^5	0.89	0.49	0.51

4.3.1.5. Ion transport properties

The diffusion coefficient (D) of the free charge carriers in LC@CA SBE material are calculated based on Bandara - Mellander (BM) method which is given as [21,41],

$$\mathrm{D} = \frac{\lambda^2}{\tau} = \frac{(k_2\varepsilon_r\varepsilon_0 A)^2}{\tau} \qquad (4.14)$$

where, τ and ε_r are the dielectric relaxation time and dielectric constant for each SBE, λ is the thickness of each electrical double layer which is of the order of Debye length, A is the effective contact area of the electrode and the SBE surface, ε_0 is the vacuum permittivity (8.854×10^{-14} F/cm) and $k_2^{-1} = C_e = \frac{\varepsilon_r\varepsilon_0 A}{\lambda}$ is the electrical double layer capacitance. The values of k_2 as obtained from the Nyquist plot equivalent circuit fitting for the individual samples are listed in Table 4.2. Mobility (μ) of the free charge carriers has been determined from Nernst-Einstein relation,

$$\mu = \frac{e\mathrm{D}}{K_B T} = \frac{e\,(k_2\varepsilon_r\varepsilon_0 A)^2}{\tau K_B T} \qquad (4.15)$$

where, K_B is the Boltzmann constant, T is the ambient temperature (300 K) and e is the electron charge. Eqs. 4.14 and 4.15 are used to calculate the transport parameters of the LC@CA SBE material and their values are listed in Table 4.3. It reveals that both D and μ follow the DC ionic conductivity trend with different w_{LC} in the LC@CA SBE material. The mobility of the free charge carriers for $w_{LC} = 44.44$ (3.38×10^{-7} cm^{2}V^{-1}s^{-1}) is remarkably increased by two orders of magnitude compared to that for $w_{LC} = 16.67$ (8.27×10^{-9} cm^{2}V^{-1}s^{-1}). Here, the mobility for $w_{LC} \leq 16.67$ is overestimated as the relaxation time has been calculated by considering the lowest available frequency i.e. 40 Hz even though it is much greater as clear from Fig. 4.3d. The increase in mobility of the free charge carriers with $LiClO_4$ concentrations is attributed to fast ionic transport through the chitosan biopolymer matrix. Thus the amorphous content of the SBE material must be increased on increasing the salt content in the composite. Also the polymer segmental motion is enhanced with w_{LC} which being coupled with the mobile ions increased the transport properties on incorporation of salt. It is known that the free lithium (Li^+) cations have greater mobility than free perchlorate (ClO_4^-) anions [42]. Thus the polar amide group ($R\text{-}CONH_2$) present in chitosan acetate which will act as dipoles on applying an electric field, interacts with the Li^+ cations due to Coulombic force. This interaction of the amide band with the Li^+ cations aids in their transport by inter-chain and intra-chain ion hopping [43] during chitosan biopolymer segmental motion, as a result of which ionic conductivity increases with addition of salt in LC@CA SBE material. This interaction of the Li^+ cations with the amide band of chitosan acetate will be discussed in detail in the subsequent section 4.3.2 (Fourier Transform Infrared Spectroscopy).

Table 4.3. Values of the transport parameters D and μ for LC@CA SBE material.

Solid biopolymer electrolytes	D (cm^{2}s^{-1})	μ (cm^{2}V^{-1}s^{-1})
$w_{LC} = 16.67$	2.14×10^{-10}	8.27×10^{-9}
$w_{LC} = 28.57$	2.42×10^{-10}	9.35×10^{-9}
$w_{LC} = 37.50$	6.08×10^{-9}	2.35×10^{-7}
$w_{LC} = 44.44$	8.75×10^{-9}	3.38×10^{-7}

4.3.2. Fourier Transform Infrared Spectroscopy (FTIR)

FTIR spectroscopy is done to study the complexation and interactions between the biopolymer and $LiClO_4$ salt which can induce changes in the vibrational modes of the biopolymer molecules in the LC@CA SBE material. Figure 4.6 shows the FTIR transmission spectra for the SBEs over the range of 600 and 4000 cm^{-1}. The band around 1375 cm^{-1} is assigned to the symmetric angular deformation of CH_3 [44]. The band due to C-N stretching coupled with N-H plane deformation appears at 1410 cm^{-1} [45]. The doublet peaks at 2875 cm^{-1} and 2930 cm^{-1} are assigned to the asymmetric and symmetric stretching vibrations of C-H, respectively [44,46]. The FTIR transmission spectra of LC@CA SBE material is divided into four regions (as shown in Fig. 4.7) in order to analyze the interactions of $LiClO_4$ salt with chitosan acetate in specific vibrational bands with increase in salt content.

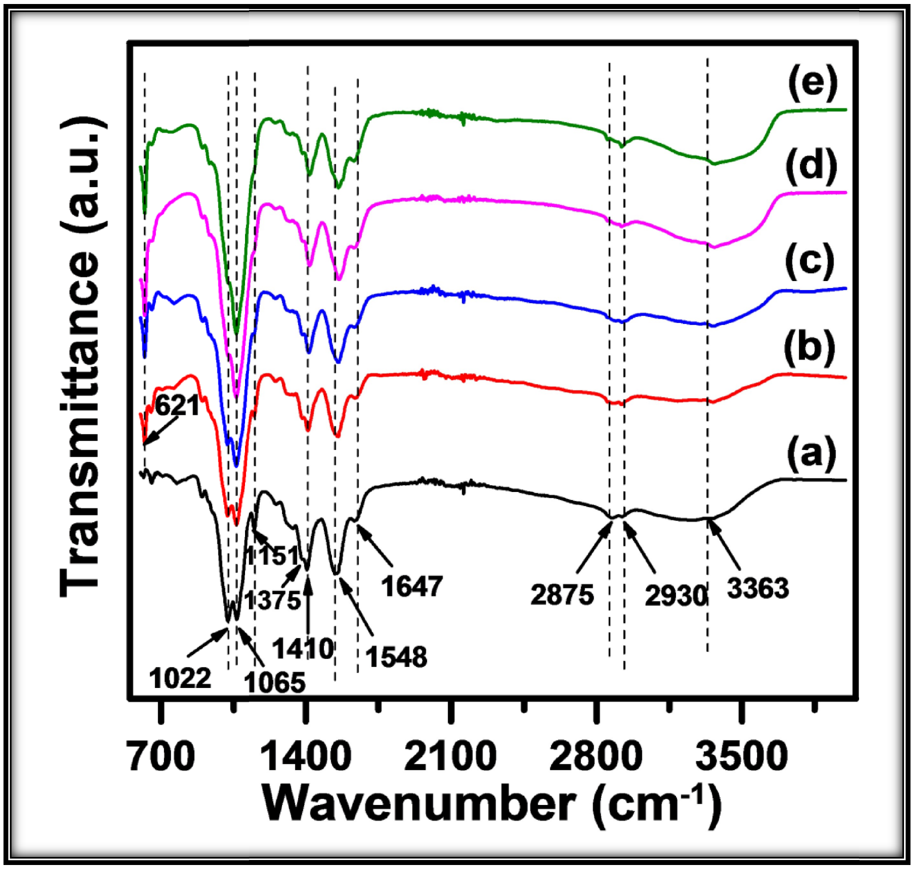

Fig. 4.6. FTIR transmission spectra over the range of 600 and 4000 cm^{-1} for LC@CA SBE material with (a) $w_{LC} = 0$, (b) $w_{LC} = 16.67$, (c) $w_{LC} = 28.57$, (d) $w_{LC} = 37.50$ and (e) $w_{LC} = 44.44$.

Region 1: 600-650 cm^{-1}

Figure 4.7A shows the FTIR transmission spectra in the region of 600-650 cm^{-1} for different w_{LC} in LC@CA SBE material. The band around 621 cm^{-1} is associated with the free ClO_4^- ions [47]. It can be observed that with increasing $LiClO_4$ content from $w_{LC} = 16.67$ to 44.44, the intensity of the $\upsilon(ClO_4^-)$ absorption peak is increased significantly and shifted slightly to higher wave number by ~ 1 cm^{-1} as shown in Fig. 4.8A. This suggests an increase in the number of free ions which results in higher ionic conductivity with increase in w_{LC}.

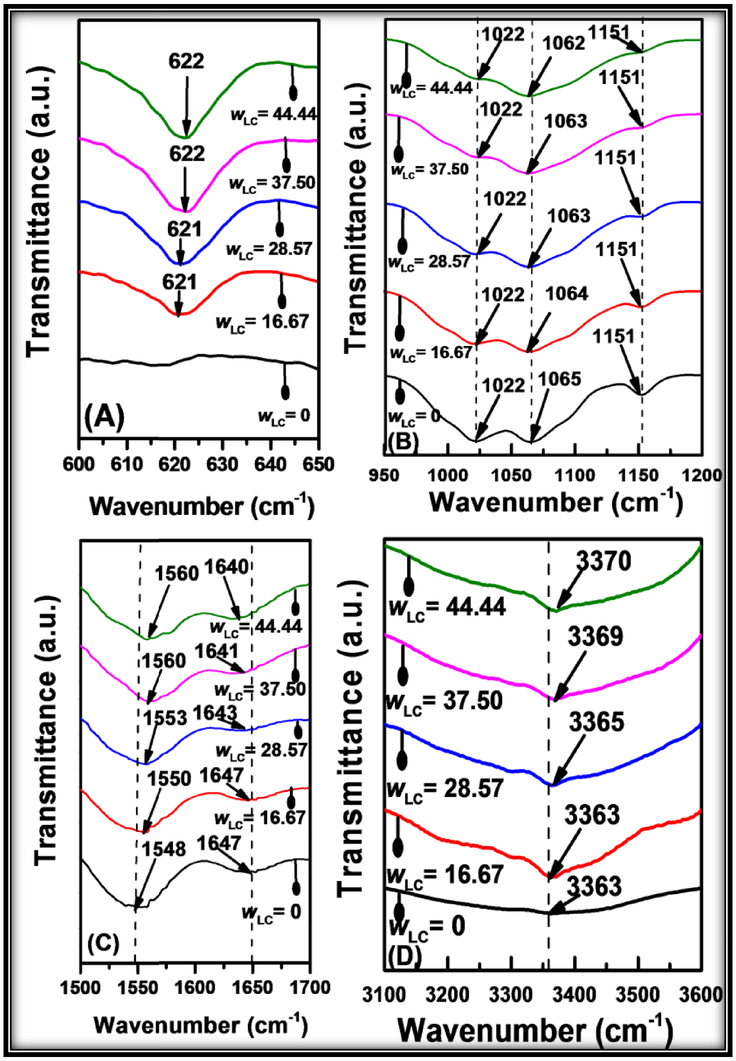

Fig. 4.7. FTIR transmission spectra in the four regions, (A) 600 cm^{-1} to 650 cm^{-1}, (B) 950 cm^{-1} to 1200 cm^{-1}, (C) 1500 cm^{-1}to 1700 cm^{-1} and (D) 3100 cm^{-1}to 3600 cm^{-1}for LC@CA SBE material with different w_{LC}.

Region 2: 950-1200 cm^{-1}

Figure 4.7B shows the FTIR transmission spectra in the region of 950-1200 cm^{-1} for different w_{LC} in LC@CA SBE material. The triplet peaks centered at 1022 cm^{-1}, 1065 cm^{-1} and 1151 cm^{-1} are attributed to the stretching vibrations of C-O-C of chitosan biopolymer [44,46]. It can be observed that with increase in salt content (w_{LC}), the symmetric stretching vibrational band of C-O-C centered at 1065 cm^{-1} is shifted to lower wave numbers by ~ 1-3 cm^{-1} with significant enhancement in intensities of the υ(C-O-C) absorption peaks as shown in Fig. 4.8B. This red shiftof the υ_s(C-O-C) mode clearly indicates the Li$^+$ ion interaction with the C-O-C band of chitosan. The increase in the vibrational C-O-C band intensity with increase in salt content can be associated with the local conformational change in the biopolymer structure upon complexation with $LiClO_4$.

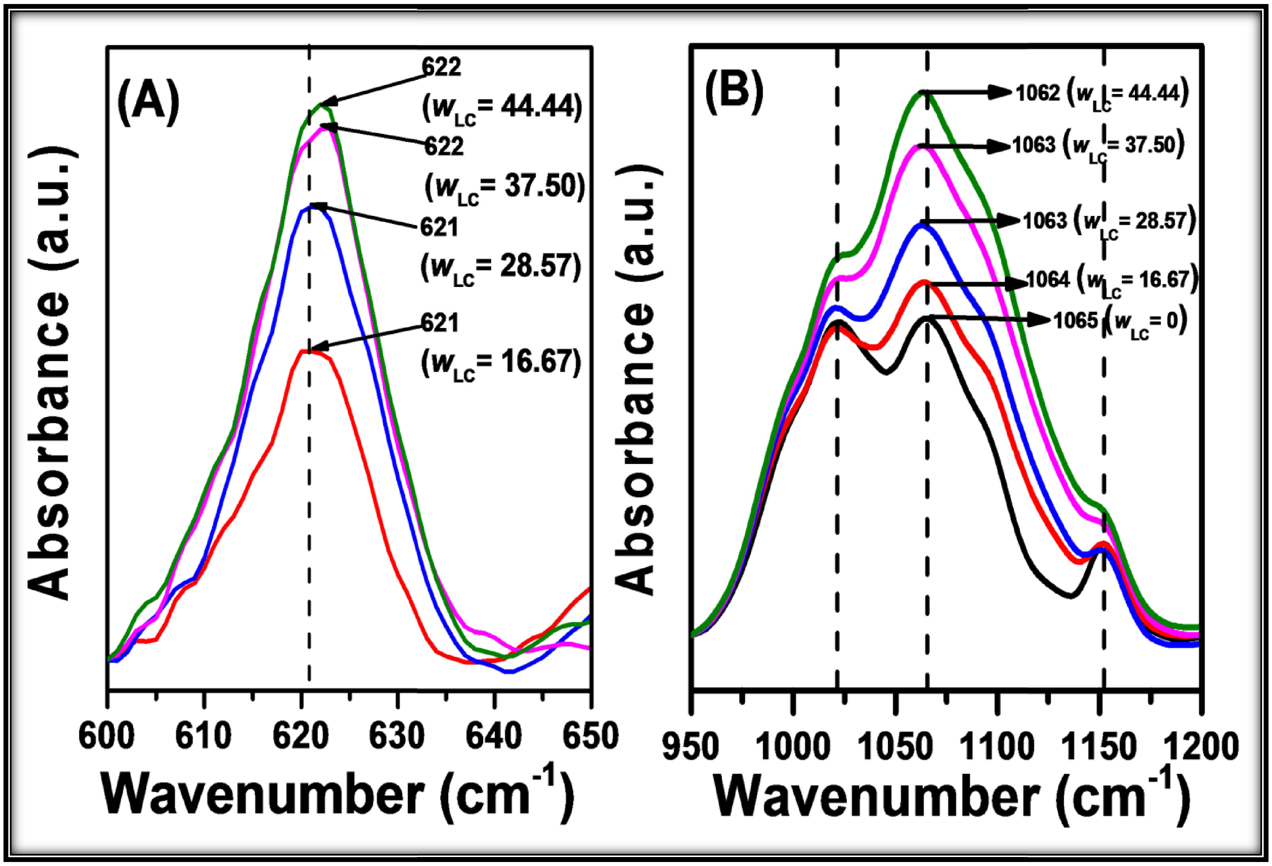

Fig. 4.8. FTIR absorption spectra in (A) 600 cm^{-1} to 650 cm^{-1} and (B) 950 cm^{-1} to 1200 cm^{-1} for LC@CA SBE material with different w_{LC}.

Region 3: 1500-1700 cm^{-1}

The FTIR transmission spectra in the region of 1500-1700 cm^{-1} for different w_{LC} in the LC@CA SBE material are shown in Fig. 4.7C. The doublet peaks centered around 1548 cm^{-1} and 1647 cm^{-1} are assigned to amine (R-NH$_2$) and secondary amide (R-CONH$_2$) of chitosan in the LC@CA SBE material, respectively [48-50]. A quantitative analysis has been done by deconvoluting the FTIR absorption spectra for different w_{LC} in the SBE material in the region of 1500-1700 cm^{-1} based on Gaussian fitting function as shown in Figs. 4.9a-e. There is a shift of the absorption peak of amine (R-NH$_2$) and secondary amide (R-CONH$_2$) of chitosan are observed from 1590 cm^{-1} to 1548 cm^{-1} and 1667 cm^{-1} to 1647 cm^{-1} respectively for $w_{LC} = 0$ i.e. pure chitosan acetate (CA) film [49]. This indicates the interaction of the nitrogen donors of chitosan biopolymer with the acetic acid [49,50], resulting a shift of amine and amide bands in pure CA film.

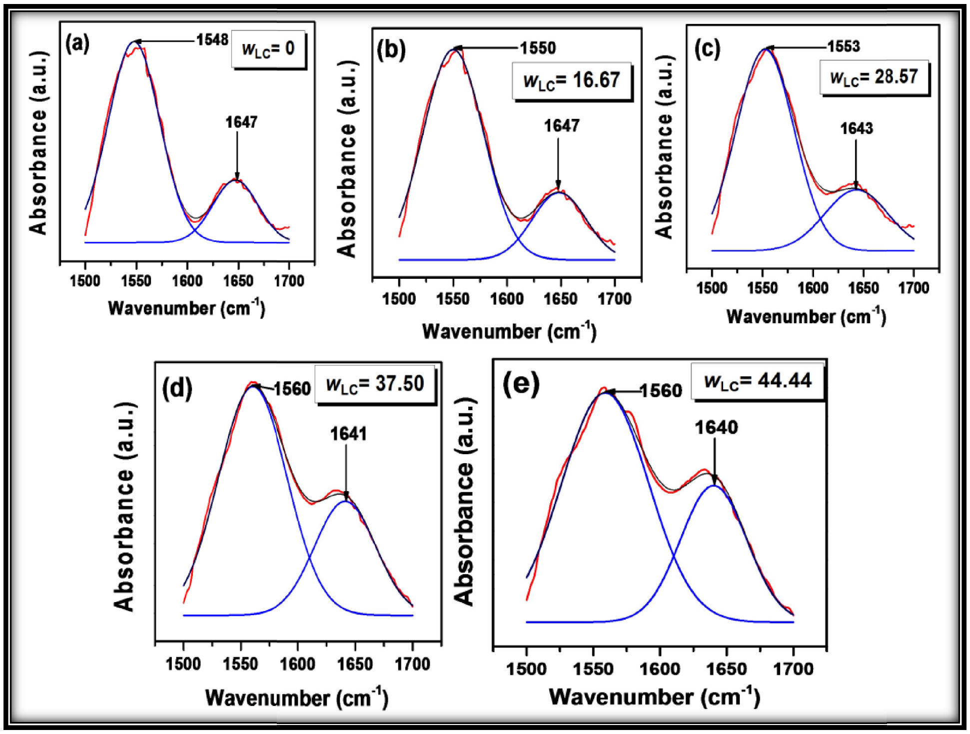

Fig. 4.9. Deconvolution of the FTIR absorption spectra in the region of 1500-1700 cm^{-1} based on Gaussian fitting function for LC@CA SBE material with (a) $w_{LC} = 0$, (b) $w_{LC} = 16.67$, (c) $w_{LC} = 28.57$, (d) $w_{LC} = 37.50$ and (e) $w_{LC} = 44.44$.

On addition of salt, the amine band undergoes a blue shift by ~ 2-12 cm^{-1} and the amide band undergoes a red shift by ~ 4-7 cm^{-1}. The area under the absorption peak of amine(R-NH$_2$) is plotted as a function of w_{LC} as shown in Fig. 4.10, where peak area decreases with increase in salt content. On the other hand, the area under the absorption peak of amide (R-CONH$_2$) increases significantly with increase of w_{LC}, as shown in Fig. 4.10. This may be attributed to the more interaction of Li$^+$ ion with the secondary amide (R-CONH$_2$) compared to amine (R-NH$_2$).

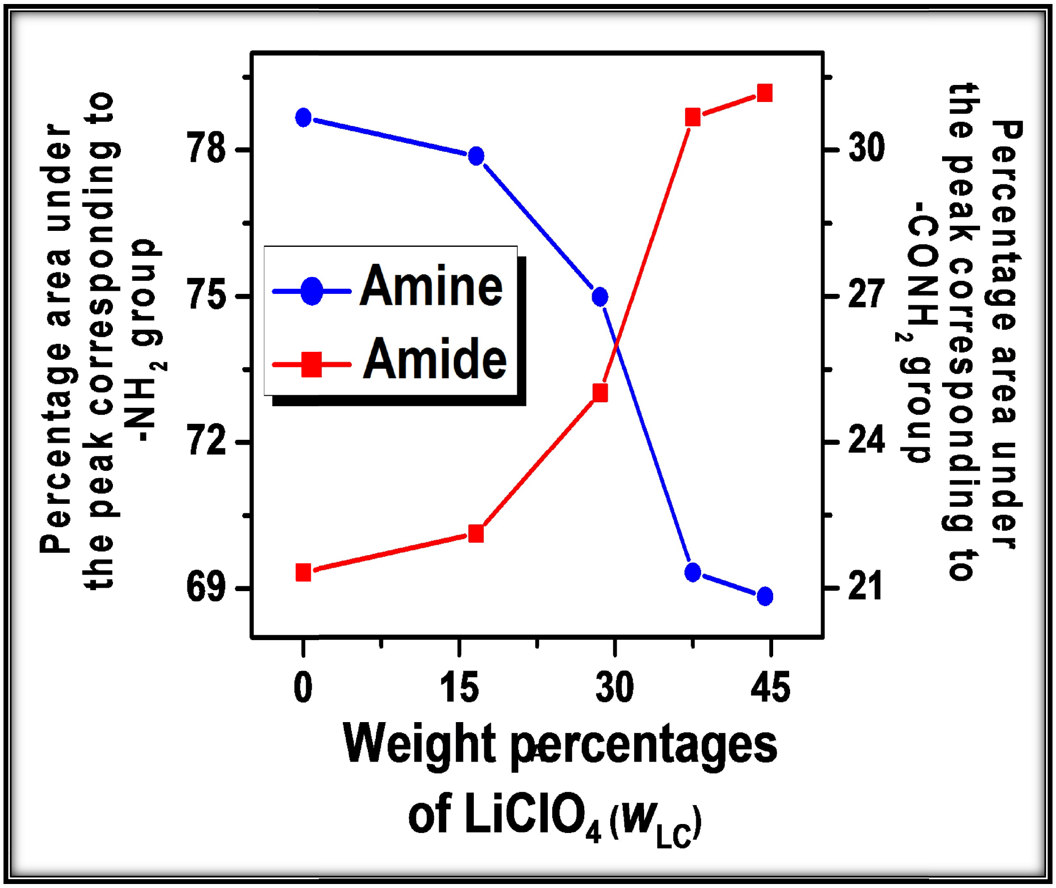

Fig. 4.10. Percentage areas under the peaks corresponding to amine and amidegroupsare shown as a function of w_{LC}.

Region 4: 3100-3600 cm^{-1}

Figure 4.7D shows the FTIR transmission spectra in the region of 3100-3600 cm^{-1} for different w_{LC} in LC@CA SBE material. The peak around 3363 cm^{-1} is assigned to the hydroxyl band of chitosan [50] which is shifted to higher wave numbers by ~ 2-7 cm^{-1} on addition of LiClO$_4$ salt. This infers interaction of salt with the biopolymer at the hydroxyl band. The hydrogen bonding between ClO_4^- anions and hydroxyl groups of the biopolymer may result in blue shift of the υ(O-H) band with increase in salt content (w_{LC}).

4.4. Conclusions

The ionic conductivity and relaxation behavior of LC@CA solid biopolymer electrolytes (SBE) have been investigated. Introduction of $LiClO_4$ salt improves the ionic conductivity of chitosan acetate from ~ 10^{-9} S/cm to ~ 10^{-5} S/cm at 300 K. The transport properties of the SBE material are studied using Bandara – Mellander method of equivalent circuit modeling of Nyquist plot obtained from impedance spectroscopy, which indicates enhancement in ionic mobilityby two orders of magnitude on addition of salt. The frequency dependence of the conductivity spectra are analyzed based on Almond – West formalism. This suggests an increase in charge carrier hopping rate and carrier concentration with increase in salt concentrations.The conductivity spectrum in the low frequency regime has been analyzed based on a model considering the fractal nature of the electrode-SBE interface. An enhancement in dielectric constant of ~ 10^5 at 40 Hz is achieved with 44.44 wt. % $LiClO_4$ concentrations in the SBE material. The electric modulus spectra of the SBE material are analyzed using HN approach inferring non-Debye type of relaxation. The highly non-exponential behavior of the relaxation function also supports non-Debye relaxation phenomenon within the SBE material. The change in shape of the electric modulus spectra for different ionic salt concentrations is actually a consequence of the inclusion of high frequency limiting dielectric constant $\varepsilon_r(\omega \rightarrow \infty)$ in the modulus definition. The shape of the hopping modulus $M''_{\mathrm{hop}}(\omega)$ containing only hopping motion contributions of the mobile charge carriers has been found to be virtually independent of ionic concentrations**.** FTIR spectroscopy results suggest the interaction of $LiClO_4$ salt with chitosan acetate as evidenced from the shift of amine, secondary amide and hydroxyl bands. In the conduction mechanism, the role of polar amide dominates over amine as revealed from FTIR spectra.

Chapter 5

γ-irradiation induced dielectric properties of chitosan based solid biopolymer electrolytes

5.1. Introduction

Solid polymer electrolytes (SPE) have attracted huge interest for their applications in electrochemical devices with high potential to replace liquid electrolytes which have harmful leakage problems. Recently due to the increasing demand of renewable energy sources, SPE using biodegradable polymers such as chitosan is being considered due to their easy availability, low cost and their ease of fabrication in the form of thin films which is mechanically strong [1]. The low ionic conductivity of SPEs demands the development of lots of techniques to improve their conductivities. High energy gamma irradiation is one such unique technique to modify the structural, mechanical and electrical properties of the polymer by producing irreversible changes in their macromolecular structure [2,3]. The irradiation on chitosan lead to the scission of polymer chains which can improve the molecular mobility [4]. In this work, we investigate the effect of gamma irradiation on the dielectric and transport properties of chitosan based solid biopolymer electrolytes with lithium perchlorate as a source of charge carriers at room temperature using electrochemical impedance spectroscopy.

5.2. Experimental

The solid polymer electrolytes are synthesized by solution casting technique. Chitosan (0.5 g) is dissolved in 50 ml 1% aqueous acetic acid solution. 44.44 wt.% lithium perchlorate ($LiClO_4$), anionic salt and 20 wt.% ethylene carbonate (EC), a plasticizer are added in the chitosan solution and stirred continuously until complete dissolution at room temperature. The resulting homogeneous solutions are cast on separate polypropylene petri-dishes and allowed to dry at room temperature. This natural and slow drying process yields solid biopolymer electrolyte (SPE) films. Then the solid films are exposed to high energy gamma irradiation with doses ranging from 0-10 kGy at the rate of 2 kGy/hr under normal atmosphere. ^{60}Co was used as the gamma source. The samples are then characterized using computer interfaced impedance analyzer (Agilent 4294A-Precision Impedance Analyzer) in the frequency range between 40 Hz to 2 MHz at room temperature.

5.3. Results and Discussion

The Cole-Cole plots of the γ-irradiated 44.44 wt.% $LiClO_4$@chitosan (henceforth named as Li/CS) and 20 wt.% EC@Li/CS (henceforth named as EC/Li/CS) SPE systems at room temperature with irradiation doses of 0 kGy, 5 kGy and 10 kGy, respectively are shown in Fig. 5.1a. The DC ionic conductivity ($\boldsymbol{\sigma}_{DC}$) of the γ-irradiated SPEs is calculated using the relation, $\boldsymbol{\sigma}_{DC} = L/R_bA$ where, L is the sample thickness, A is the effective contact area of the electrode and the electrolyte surface and R_b is the bulk resistance. R_b is determined from the high frequency intercept on the real Z-axis of the Cole-Cole plot. The variation of DC conductivity for different doses of gamma irradiation in the SPE systems are illustrated in Fig. 5.1b. It is found that the ionic conductivity of Li/CS SPE increases from ~1.3×10^{-5} S/cm to ~1.9×10^{-4} S/cm for 10 kGy dose of gamma irradiation, while EC/Li/CS SPE exhibits the highest conductivity (~2.3×10^{-4} S/cm) at 5 kGy dose of gamma irradiation. So the enhancement of mobility of the free ions and/or the number density of charge carrier is expected since $\sigma_{dc} = ne\mu$, where, symbols have their usual meaning. For Li/CS SPE system, an increase in gamma dose might result in scission of biopolymer chains which lead to an increase in conductivity, while for EC/Li/CS SPE system, an increase in the gamma dose beyond 5 kGy might initiate cross-linking of biopolymer chains resulting a decrease in conductivity.

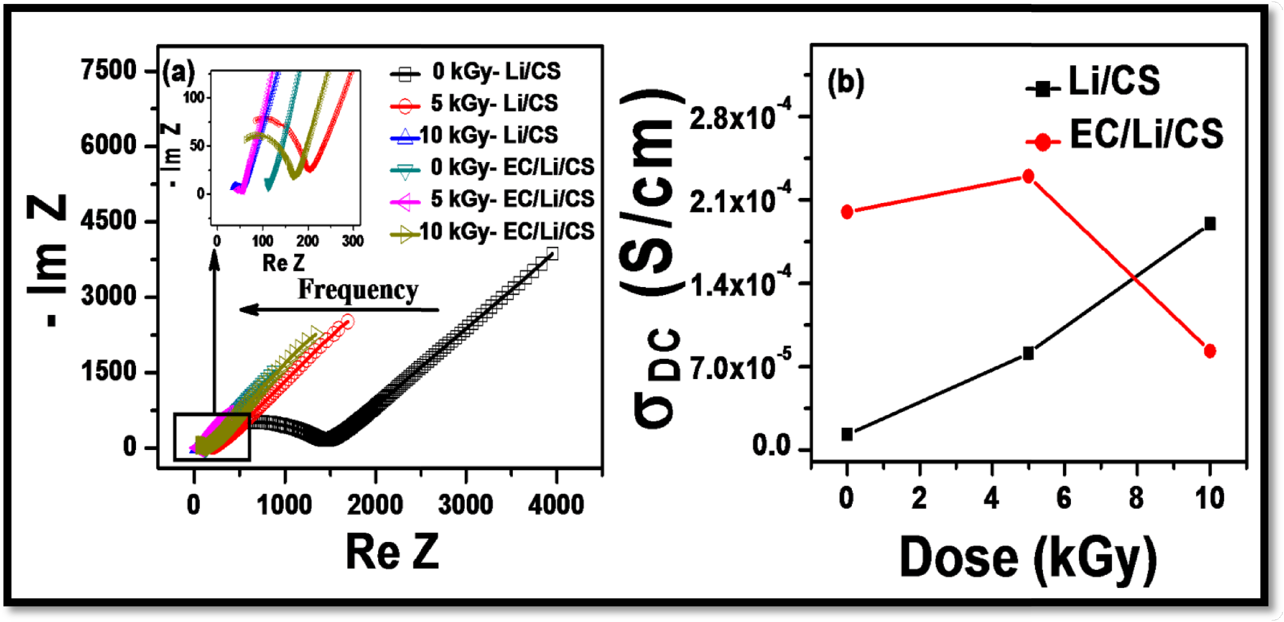

Fig. 5.1. (a) Cole-Cole plots of γ-irradiated Li/CS and EC/Li/CS SPE systems at room temperature having radiation doses of 0 kGy, 5 kGy and 10 kGy, respectively, (b) the variation of DC conductivity with different radiation doses at room temperature. Inset of (a) shows the plots at higher frequencies.

The frequency dependence of real part of complex permittivity (dielectric constant) for the γ-irradiated Li/CS and EC/Li/CSSPE systems are shown in Fig. 5.2a and modeled with modified Cole-Cole model with a DC conductivity correction term [5] as,

$$\varepsilon_r = \varepsilon_\infty + \left[\frac{(\varepsilon_s-\varepsilon_\infty)\left\{1+(\omega\tau)^\beta\cos\left(\frac{\beta\pi}{2}\right)\right\}}{1+2(\omega\tau)^\beta\cos\left(\frac{\beta\pi}{2}\right)+(\omega\tau\ ^{2\beta}}\right] + \frac{\sigma_{sp}}{\varepsilon_0\omega^m} \tag{5.1}$$

where, ε_s and $\varepsilon_\infty$are the low and high frequency dielectric constants, respectively, τ is the relaxation time, **ω** is the angular frequency, β is the parameter, m is the exponent and σ_{sp} is the space charge conductivity. The solid lines in Fig. 5.2a depicts the modeled plots of the frequency dependence of dielectric constant (ε_r) for the SPE systems at different gamma irradiation doses. It shows that ε_r is higher in the low frequency regime which is due to the effect of electrode polarization. This may be due to the charge carrier accumulation at the electrode-electrolyte interface. As frequency increases, ε_r decreases gradually. It may be due to the effect of ionic and electronic polarization. In the high frequency regime, the periodic reversal of the electric field occur very fast giving insufficient time for charge to accumulate at the interface, so the dielectric constant decreases. The best fit of the experimental results with the modified Cole-Cole equation illustrates that the relaxation time decreases on increasing the dose of gamma irradiation for Li/CS SPE system. On the contrary, the relaxation time corresponding to the EC/Li/CS SPE for 5 kGy dose of gamma irradiation is found to be the lowest (~ 1.27×10^{-7} s) as expected from the conductivity results. It is worthwhile to point out that the value of relaxation time obtained from the fitting of the modified Cole-Cole equation is same as that obtained from the tan δ versus frequency plot (Fig. 5.2b) using the relation $\tau = \frac{1}{2\pi f_{peak}}$ where, f_{peak} is the frequency corresponding to the loss peak. For an ideal Debye type relaxation, β= 1 [6]. In our case, all the SPEs exhibit non-Debye relaxation since β≠1 (shown in the inset of Fig. 5.2a). Moreover the large width of the loss peaks (Fig. 5.2b) indicates the non-Debye type relaxations in the SPEs. A reduction in dielectric loss is observed on exposing the EC/Li/CS SPEs with gamma irradiation (shown in Fig. 5.2b) making them potential candidates for electrochemical device applications.

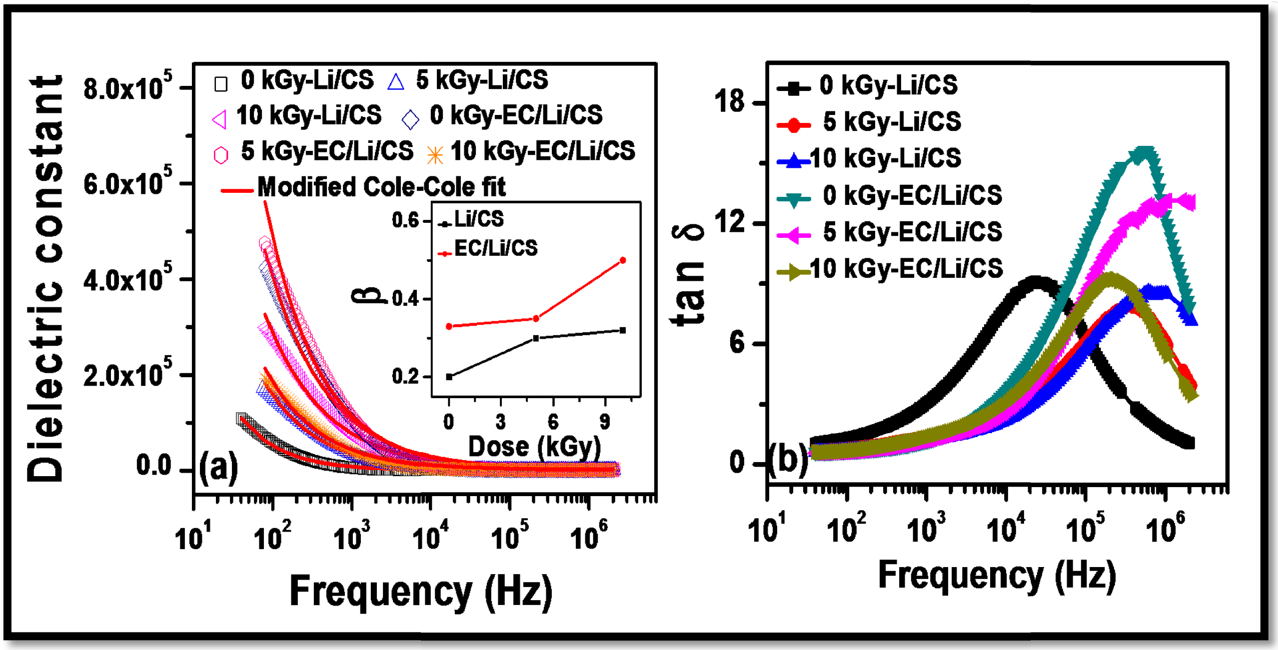

Fig. 5.2. Frequency variation of (a) dielectric constant (ε_r) where the solid lines represent the modified Cole-Cole fits using Equation 5.1 and (b) tan δ of SPEs for different doses of gamma irradiation at room temperature. Inset of (a) shows the variation of β for different radiation doses.

The variation of relaxation time with different doses of gamma irradiation in both the SPE systems is shown in Fig. 5.3a. The space charge conductivity also found to be increased with gamma irradiation doses for Li/CS SPE system and attains a maximum value of ~2.5× 10^{-6} S/cm for EC/Li/CS SPE system at 5 kGy dose of gamma irradiation (shown in Fig. 5.3a).Electric modulus spectra is studied to acquire an idea about the dielectric relaxation by suppressing the electrode effect in the SPEs. The frequency dependence of the imaginary part of electric modulus (M'')for the γ-irradiated Li/CS and EC/Li/CS SPE systems are shown in Fig. 5.3b and modeled using a modified Kohlrausch-Williams-Watts (KWW) function having two independent shape parameters of low and high frequency sides and a smoothing parameter [5] as,

$$M''(f) = \frac{M''_{max}}{\left(\frac{1-c}{a+b}\right)\left[b\left(\frac{f}{f_{max}}\right)^{-a} + a\left(\frac{f}{f_{max}}\right)^{b}\right] + c} \qquad (5.2)$$

where, ‘a’ and ‘b’ are two independent shape parameters of low and high-frequency sides of M''spectra and ‘c’ is the smoothing parameter. The values of the shape parameters and smoothing parameter for the highest conducting sample EC/Li/CS at 5 kGy dose of gamma irradiation are a = 0.93, b = 0.79 and c = 0.02 indicating non-Debye type relaxations.

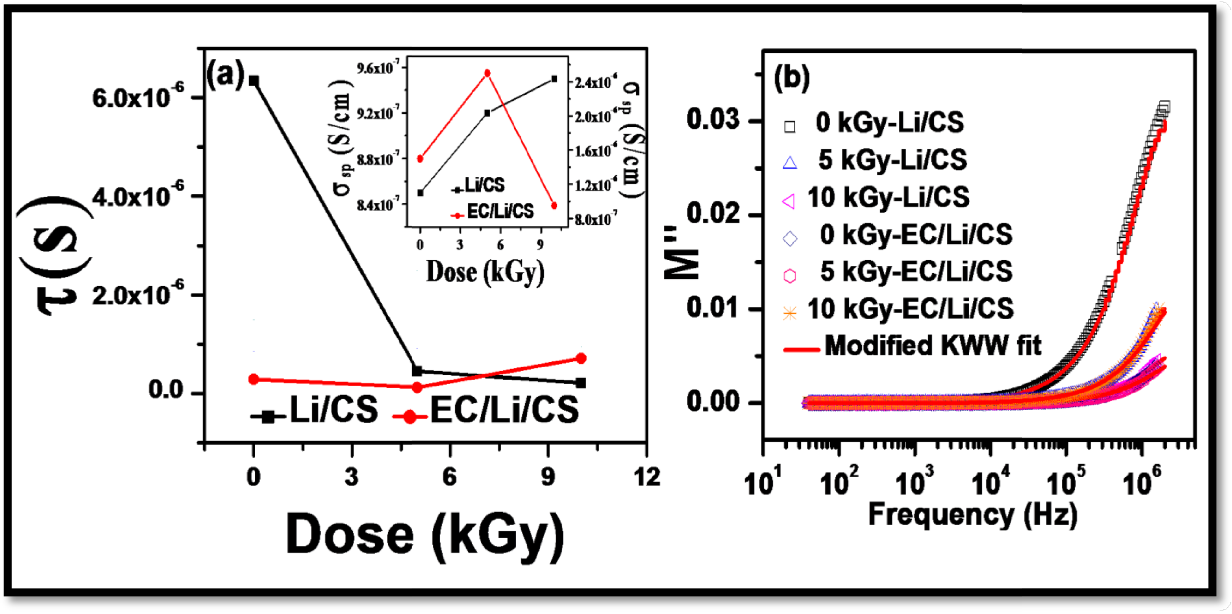

Fig. 5.3. (a) Variation of τ with different gamma radiation doses, (b) frequency variation of imaginary part of electric modulus (M'') of SPEs for different irradiation doses in SPEs at room temperature (solid lines represent the modified KWW fits using Equation 5.2). Inset of (a) shows the variation of σ_{sp} with different gamma radiation doses.

Mobility (μ) of the free charge carriers in the γ-irradiated Li/CS and EC/Li/CS SPE systems is calculated using MacDonald-Trukhan model along with the Nernst-Einstein relation [7] given as,

$$\mu = \frac{eL^2}{32\tau K_B T(\tan\delta_{max})^3} \qquad (5.3)$$

where, e is the electron charge, L is the sample thickness, K_B is the Boltzmann constant, τ is the dielectric relaxation time, T is the absolute temperature and tan δ_{max} is the maxima of loss tangent. The variations of mobility and number density of charge carriers for different gamma irradiation doses in the SPEs are shown in Fig. 5.4. Although Li/CS SPE exhibits maximum conductivity along with the maximum free charge carrier density (~2.14×10^{15} /cm^3) for 10 kGy dose of radiation but it acquires maximum mobility (~ 0.92 $cm^2V^{-1}s^{-1}$) for 5 kGy dose of radiation. On contrary, in EC/Li/CS SPE, both the transport parameters e.g., mobility and number density are in exact synchronization with the variation of conductivity vs radiation dose. Both the transport parameters of EC/Li/CS SPE decrease with an increase in the gamma dose beyond 5 kGy which might be due to biopolymer cross-linking. This may lead to an increase in localized crystallinity which is hindering the mobility of the free charge carrier, thereby resulting a decrease in conductivity.

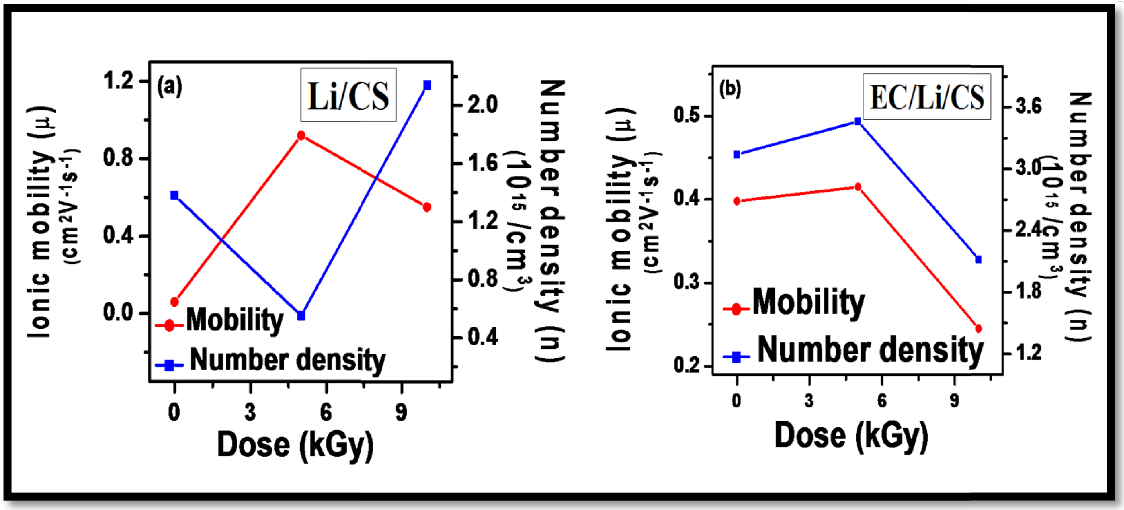

Fig, 5.4. Variation of ionic mobility and number density of free charge carriers with different gamma irradiation doses in (a) Li/CS, (b) EC/Li/CS SPE systems.

5.4. Conclusions

The chitosan based solid biopolymer electrolyte film containing 44.44 wt.% $LiClO_4$ salt and 20 wt.% EC as plasticizer are synthesized by solution casting technique and are subjected to high energy gamma irradiation having doses ranging from 0-10 kGy. The effect of gamma irradiation on the dielectric and transport properties of the chitosan based solid biopolymer electrolytes at room temperature have been reported. For plasticizer (EC)-free system, the ionic conductivity increases with increase in γ-irradiation doses. The maximum ionic conductivity is observed for EC/Li/CS SPE system at 5 kGy dose of gamma irradiation having minimum dielectric relaxation time. The modeling of the dielectric constant and electric modulus spectra indicates non-Debye type relaxations in the SPEs. The mobility of the Li/CS SPE system at 5 kGy irradiation dose has been increased by 15 times compared to the un-irradiated sample. Also the loss factor is reduced for γ-irradiated EC/Li/CS SPE system making it a potential candidate for electrochemical device applications.

Chapter 6

Dielectric and transport studies of graphene oxide@chitosan based solid biopolymer nanocomposite electrolytes

6.1. Introduction

Solid polymer electrolytes (SPE) have attracted much attention in recent years owing to their potential applications in different energy storage and energy conversion devices. The increasing demand of renewable energy sources lead to the development of SPE using natural polymers due of their easy availability, low cost, principal bio-degradation properties and their ease technique of fabrication as thin films unlike in liquid electrolytes which have harmful leakage problems [1,2]. Chitosan is one of the natural biodegradable polymers which are mechanically more stable but with comparatively low conductivity than other biopolymers. Incorporating with ionic salts and suitable plasticizers into the host polymer, the ionic conductivity increases. Their electrical and dielectric properties are optimized with appropriate nanofillers without compromising their mechanical properties, thus making solid polymer nanocomposite electrolytes (SPNE) very attractive for energy storage applications. Graphene oxide (GO) has multiple oxygen-containing functional groups (carboxyl, epoxy and hydroxyl) on its basal planes and edges which enables it to be well dispersed in water compared to other nanofillers. This makes GO able to get homogenously distributed in the polymer electrolyte matrix [2]. Few studies have been investigated on the incorporation of GO as a nanofiller into SPE and thus demands extensive works to explore their potential applications. In this work, the effect of graphene oxide as a nanofiller into chitosan based solid biopolymer electrolytes are studied using electrochemical impedance spectroscopy (EIS) analysis at room temperature.

6.2. Experimental

Graphene oxide is chemically prepared from pure graphite powder following modified Hummers's method [3]. The solid polymer electrolytes are synthesized by solution blending and evaporation casting technique. Chitosan (0.5 g) is dissolved in 50 ml dilute acetic acid. 44.44 wt% lithium perchlorate ($LiClO_4$), an ionic salt and 20 wt% ethylene carbonate (EC), a plasticizer are added in the chitosan solution and stirred continuously until complete dissolution at room temperature. Various weight percentages of GO (2.17, 3.85, 5.06, 6.25 wt%) are dispersed in deionised water and ultrasonicated for about 5 minutes. Then both the solutions are blended and stirred for 10 minutes, followed by ultrasonication for about 30 minutes to get a homogenous mixture. Resulting homogeneous solutions are cast on polypropylene petri dishes and allowed to dry at room temperature. This natural and slow drying process yields solid biopolymer nanocomposite films. The samples are characterized using computer interfaced impedance analyzer (Agilent 4294A-Precision Impedance Analyzer) in the frequency range between 40 Hz to 2 MHz at room temperature.

6.3. Results and Discussion

The Cole-Cole plots of the chitosan/GO solid biopolymer nanocomposite electrolytes for different wt% of GO at room temperature are shown in Fig. 6.1a. Results are analyzed using an equivalent circuit consisting of combinations of resistor and constant phase element (CPE) as shown in inset of Fig. 6.1b and the bulk resistance (R_b) of the nanocomposite is calculated. The impedance of the CPE is given by $Z_{CPE} = k\,(j\omega)^{-p}$ where, k is the CPE coefficient and p is some fractional parameter having its values lying between 0 and 1. The dc ionic conductivity (σ_{dc}) of the SPNE is calculated using the equation, $\sigma_{dc} = \frac{L}{R_b A}$ where, L is the sample thickness, A is the effective contact area of the electrode and the electrolyte surface. The variation of dc conductivity for different wt % of GO in the nanocomposite is illustrated in Fig. 6.2a.

The impedance of the equivalent circuit as shown in inset of Fig. 6.1b is given as,

$$Z^* = \text{Re } Z + j\,(\text{-Im } Z) \;= \frac{R_b}{1+R_b k_1^{-1}(j\omega^{\;p_1}} + k_2(j\omega^{\;-p_2} \qquad (6.1)$$

Simplifying Equation 6.1 and then equating its real and imaginary parts, we get the final expressions for Re Z (resistance) and Im Z (reactance) [4] as,

$$\text{Re } Z = \frac{R_b + R_b^2 k_1^{-1}\omega^{p_1}\cos\left(\frac{\pi p_1}{2}\right)}{1+R_b^2 k_1^{-2}\omega^{2p_1}+2R_b k_1^{-1}\,\omega^{p_1}\cos\,\frac{\pi p_1}{2}\Big)} + \frac{\cos\left(\frac{\pi p_2}{2}\right)}{k_2^{-1}\omega^{p_2}} \qquad (6.2)$$

$$\text{Im } Z = \frac{R_b^2 k_1^{-1}\omega^{p_1}\sin\left(\frac{\pi p_1}{2}\right)}{1+R_b^2 k_1^{-2}\omega^{2p_1}+2R_b k_1^{-1}\,\omega^{p_1}\cos\,\frac{\pi p_1}{2}\Big)} + \frac{\sin\left(\frac{\pi p_2}{2}\right)}{k_2^{-1}\omega^{p_2}} \qquad (6.3)$$

Equations 6.2 and 6.3 are used to calculate the bulk resistance R_b of the nanocomposite material and the Cole-Cole plot fitting is shown in Fig. 6.1b for the highest ion-conducting nanocomposite with 2.17 wt% GO. The values of the independent parameters used to fit the plot for the SPNE with 2.17 wt% GO are R_b = 84 Ω, $k_1 = 6\times10^{7}$ F^{-1}, p_1 = 0.9, $k_2 = 1.3\text{x}10^{4}$ F^{-1} and p_2 = 0.53.

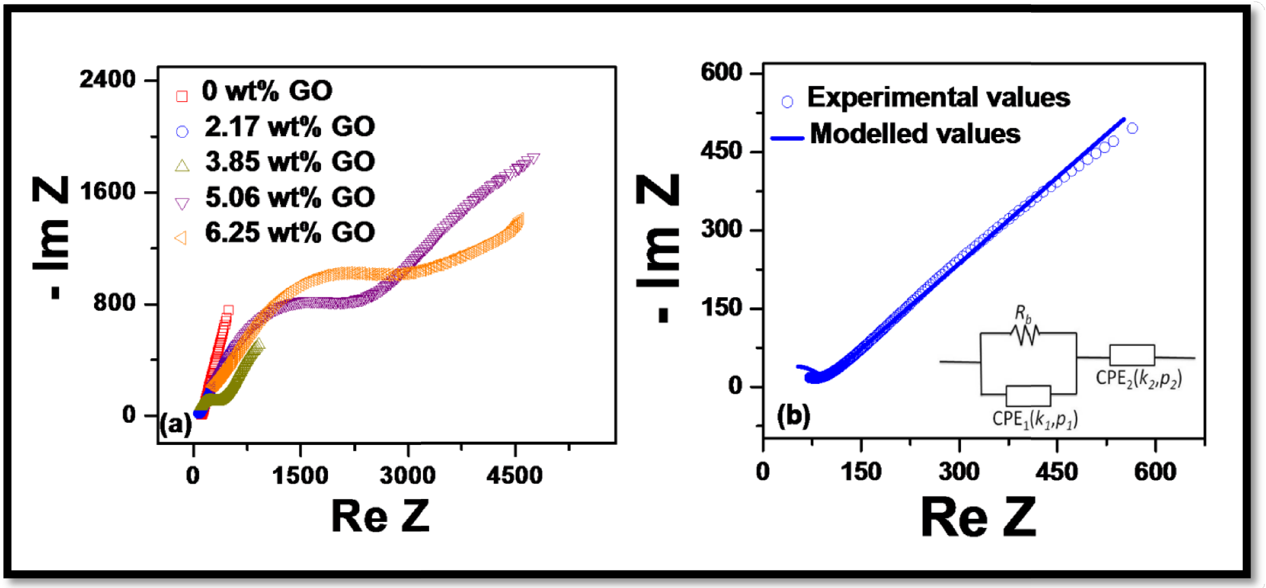

Fig. 6.1. (a) Cole-Cole plots of SPNE based on chitosan, 44.44 wt% LiClO$_4$, 20 wt% EC with different wt % of graphene oxide, (b) the modeled Cole-Cole plot for the SPNE with 2.17 wt% GO. Inset of (b) shows the equivalent circuit used to fit the plots.

The ionic conductivity attains maximum value of 5.47 × 10^{-4} Scm^{-1} for 2.17 wt % GO in the polymer electrolyte as shown in Fig. 6.2a. It infers the improvement of mobility of the free ions and/or the number density of charge carrier ions as, $\sigma_{dc} = ne\mu$, where, symbols have their usual meaning. The variation of ac conductivity (σ_{ac}) of the composite with frequency for different wt % GO is shown in Fig. 6.2b. The variation of σ_{ac} in the low frequency region corresponds to the electrode polarization effects. As frequency decreases, more charge accumulation occurs at the electrode/SPNE interface and thus the conductivity decreases.

The frequency dependence of the real part of complex permittivity (ε_r) and the loss tangent (tan δ) for SPNE system are shown in Fig. 6.3. It shows that ε_r decreases rapidly with increase in frequency in the low frequency regime indicating the charge carrier accumulation at the electrode-electrolyte interface. At high frequencies, the periodic reversal of the electric field occur very fast giving insufficient time for charge to accumulate at the interface, leading to almost frequency independent ε_r. Inset of Fig. 6.3a shows how the presence of GO in the SPNE tune the dielectric constant (ε_r) with the different wt % at the high frequency regime. Dielectric constant corresponding to 3.85 wt % GO is maximum at 2 MHz and is 9 times enhanced compared that of the parent system.

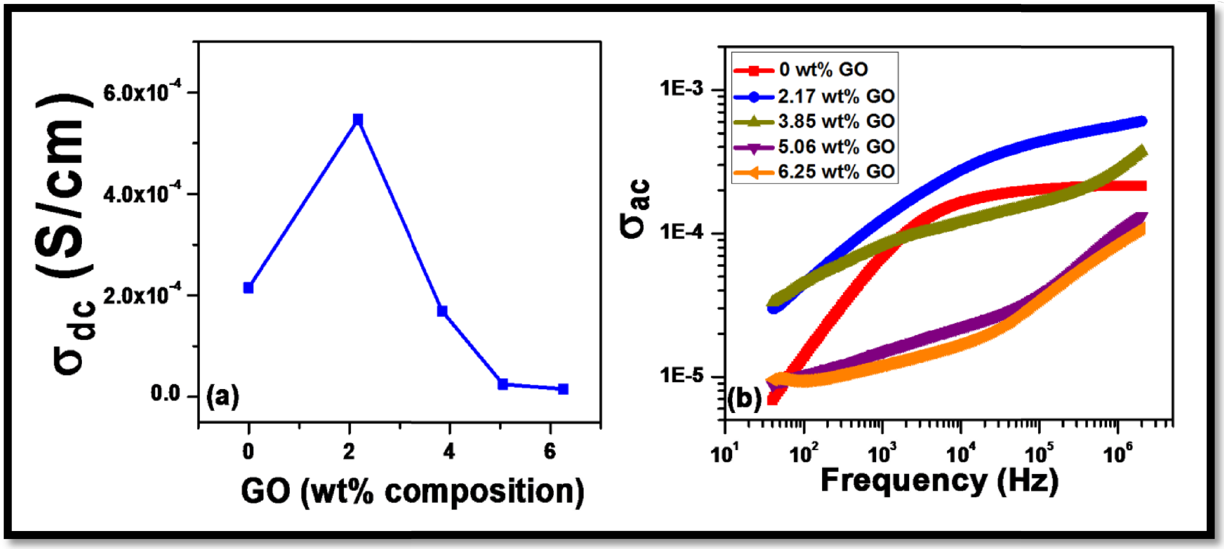

Fig. 6.2. (a) The variation of dc conductivity with different wt% of GO at room temperature, (b) σ_{ac}vs frequency for different GO compositions at room temperature.

Variation of dielectric loss, tan δ = $\varepsilon_i/\varepsilon_r$ with frequency for different wt % of GO is shown in Fig. 6.3b. This depicts the significant reduction of loss on incorporation of GO into SPNE making them potential candidates for electrochemical device applications. The relaxation time (τ) is obtained from tan δ versus frequency plot (shown in Fig. 6.3b) using the relation, $\tau = \frac{1}{2\pi f_{peak}}$, where, f_{peak} is the frequency corresponding to the relaxation peak. The variation of relaxation time with different wt % GO is shown in the inset of Fig. 6.3b. The relaxation time corresponding to the SPNE containing 2.17 wt % GO is the lowest (~ 2.6 x 10^{-7} s) as expected.

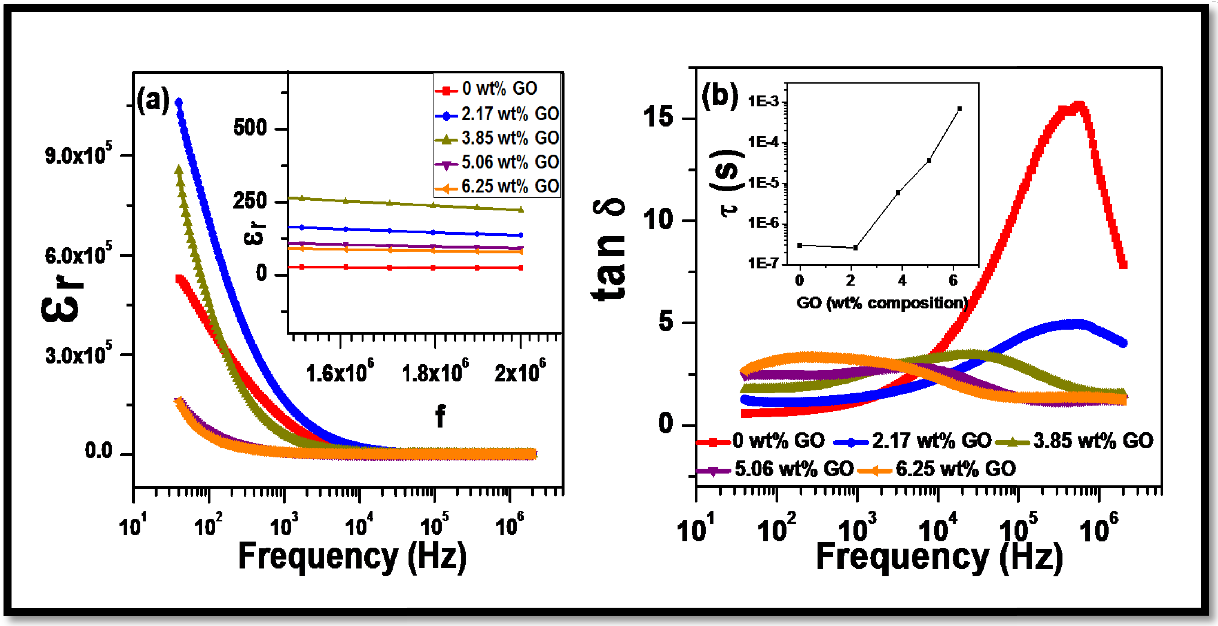

Fig. 6.3. Frequency variation of (a) ε_r and (b) tan δ of SPNE containing different wt % of GO at room temperature. Inset of (a) shows the variation of ε_r at high frequencies. Inset of (b) shows the variation of dielectric relaxation time with different wt% of GO.

Mobility (μ) of the free charge carrier ions in the nanocomposite is calculated using MacDonald-Trukhan model along with the Nernst-Einstein relation [5,6] given as,

$$\mu = \frac{eL^2}{32\tau K_B T(\tan\delta_{max})^3} \qquad (6.4)$$

where, e is the electron charge, L is the sample thickness, K_B is the Boltzmann constant, τ is the dielectric relaxation time, T is the absolute temperature and tan δ_{max} is the maxima of loss tangent. The variation of mobility with different wt % of GO in the SPNE is shown in Fig. 6.4a which depicts maximum mobility (~3.06 x 10^{-4} $m^2V^{-1}s^{-1}$) for 2.17 wt % of GO. The thickness of the diffuse part of the electrical double layer (EDL) formed at the electrode/SPNE interface is represented by the Debye length (λ_D). The Debye length [6 - 8] depends on the number density of free ions (n) as $\lambda_D = \sqrt{\frac{\epsilon_r \epsilon_0 K_B T}{2ne^2}}$. This length represents the distance up to the point where the effect of the surface is felt by the charge carrier ions in the SPNE. The variation of number density and Debye length with different wt% of GO in the SPNE is shown in Fig. 6.4b illustrating the maximum λ_D corresponding to 3.85 wt % of GO.

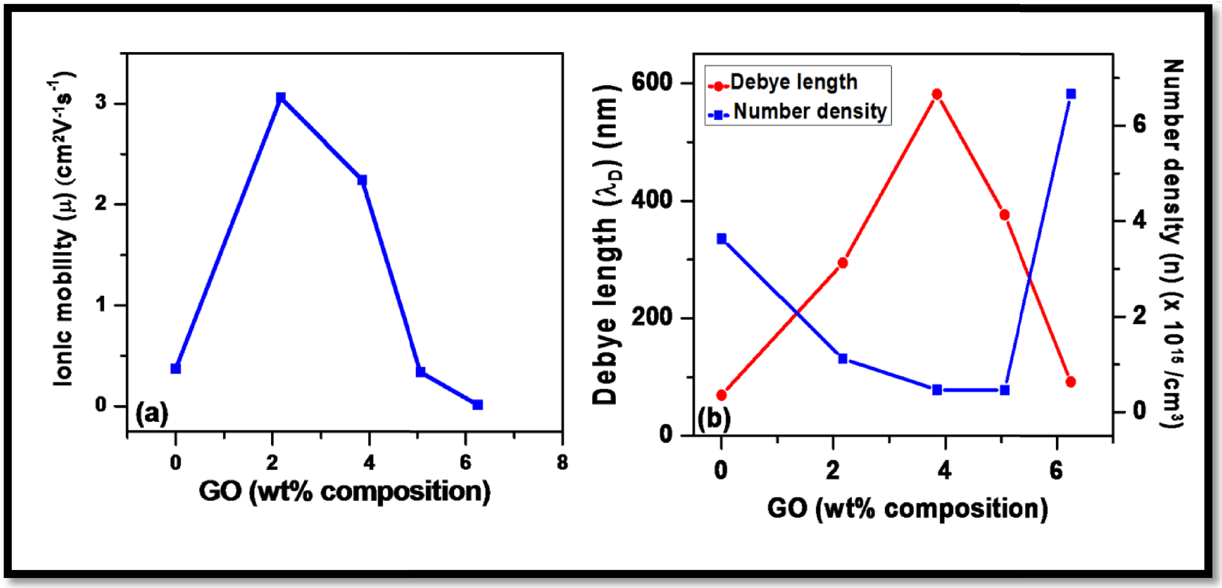

Fig. 6.4. (a) Variation of ionic mobility and (b) Debye length and number density of free charge carrier ions with different GO content in the SPE at room temperature.

6.4. Conclusions

The chitosan based solid biopolymer electrolyte film containing 44.44 wt % $LiClO_4$ salt and 20 wt% EC as plasticizer with varying wt% of graphene oxide (GO) in the range (0-7 wt %) are synthesized by solution blending and evaporation casting technique. Dielectric and transport properties of this graphene oxide@chitosan based biopolymer nanocomposite at room temperature have been reported. The maximum ionic conductivity is observed for 2.17 wt% GO incorporation in SPNE having minimum dielectric relaxation time. Moreover, the dielectric constant is found to be considerably increased on incorporation with GO. It becomes maximum for 3.85 wt % of GO which is associated with significantly reduced loss factor making it a potential candidate for electrochemical device applications.

Chapter 7

Anomalous intra diffusive behavior of chitosan/PVDF solid polymer electrolytes and the enhancement of effective specific capacitance with nanostructured spinel $MnCoFeO_4$ electrode in solid-state supercapacitors

7.1. Introduction

The excessive consumption of fossil fuels and the undesirable consequences of environmental pollution are the major concerning factors in the present scenario. Many researchers have focused on developing cost effective and environment friendly efficient energy storage devices [1,2]. Batteries and supercapacitors are the typical energy storage devices which can store electrical energy through electrochemical processes. Supercapacitors have attracted huge attention due to its higher power density than batteries and conventional capacitors, thereby offering a promising approach to meet the demand of global energy crises [3-5]. Supercapacitors have good thermal and chemical stability and have longer cycling stability [6]. Recently due to the increasing demand of renewable energy sources, intense efforts have been made to develop solid polymer electrolytes (SPE) using natural resources (such as starch, chitosan, cellulose, gelatin, etc.) as they are biodegradable, cost effective and ease of fabrication as thin films unlike liquid electrolytes suffering from major leakage problem [7-9]. But the poor ionic conductivity of the SPE raise the question of their feasibility in the field of energy storage systems. Several techniques have been developed in order to improve the conductivity of the SPE systems. Polymer blending is one such technique which is being adopted to enhance the conductivity by incorporating new complexation sites for ion migration [10,11]. The commercial chitosan (CS), derivable from the shell of shrimps and crabs, have amine and hydroxyl groups on its backbone through which its electrical properties can be improved by blending with other polymers. Various polymers especially starch, poly(ethylene) glycol (PEG), poly(vinyl) alcohol (PVA) have been used to blend with chitosan [12-14]. Among all the alternatives, polyvinylidene fluoride (PVDF) attracts much attention in preparing SPE due to its semi-crystalline nature having strong electron withdrawing functional group (–C–F) [15-17]. The fluorine atoms in –C–F possess very high electronegativity which may improve the transport properties of SPE [16,18]. Thus, PVDF has been considered to blend with CS in the present investigation. Both the polymers have individually very low value of conductivity, which can be tailored by using suitable plasticizers and ionic salts as dopant materials. The most common salt used for introducing the charge carriers in the blended polymer host is lithium perchlorate ($LiClO_4$) [12]. Polymer electrolytes are comprised of fractal structures in macroscopic as well as in microscopic scales, where anomalous diffusion of the charge carriers mainly governs the conductivity of the SPE systems. Anomalous diffusion is a diffusion process with scaling different to that of normal diffusion, where mean squared displacement $(\boldsymbol{r})$ of the diffusing ions grows in time as $\langle \boldsymbol{r}^2(\boldsymbol{t}) \rangle \sim t^{\gamma}$ [19]. The parameter γ is the anomalous exponent. $\gamma = 1$ indicates normal Fickian diffusion, $0 < \gamma < 1$ indicates the diffusion is sub-diffusive and $\gamma > 1$ indicates super-diffusive process. Solid polymer electrolytes are generally sub-diffusive systems having a complex microstructure with dynamic disorder which leads to non-Debye relaxation phenomenon in these materials. Conductivity behavior of solid polymer electrolytes is correlated to the diffusivity of the mobile ions in the electrolyte.

Supercapacitors are divided into two broad categories depending on the mechanism of energy storage at the electrode: electrical double layer capacitors (EDLC) which store energy by ion adsorption at the electrode-electrolyte interface and pseudocapacitors (PC) which store energy by faradaic redox processes at the electrode-electrolyte interface [20-22]. The active material in the EDLCs is composed of carbon-based materials, such as activated carbon, graphite and graphene whereas for PCs, the active material is mainly composed of transition metal (TM) oxides, conducting polymers, spinel ferrites etc. [20,23]. Sudhakar et. al. [12] reports a solid-state EDLC with chitosan-starch blended solid biopolymer electrolytes having a high specific capacitance value of 133 Fg^{-1}. The spinel has the general chemical formula of AB_2O_4, where A refers to a divalent cation and B refers to a trivalent cation. The divalent cations occupy the tetrahedral sites and the trivalent cations occupy the octahedral sites in a normal spinel structure [20]. Spinel ferrites, $\boldsymbol{M}Fe_2O_4$ or $\boldsymbol{M\acute{M}}FeO_4$ (where $\boldsymbol{M}$ or $\boldsymbol{\acute{M}}$= Mn, Ni, Zn, Co, etc.), are fascinating electrode materials for supercapacitors owing to their ability to exhibit different redox states, impressive electrical properties and good electrochemical stability. Numerous binary and ternary TM ferrites have been investigated for supercapacitor applications [20,24,25]. Among all the alternatives, $MnCoFeO_4$ has been chosen as the electrode material in the present investigation owing to their high specific capacitance and power density [20].

In the present work, impedance spectroscopy at higher frequency (~ 100 KHz) have been carried out to evaluate the conductivity, dielectric and transport properties of the CS/PVDF blended solid polymer electrolytes (SPE) containing different weight fractions of salt ($LiClO_4$) and plasticizer (glycerol). Anomalous intra diffusive behavior of the charge carriers in the blended solid polymer electrolytes has been investigated. Fourier transform infrared spectroscopy (FTIR) studies have also been explored in light of transport properties. Finally, a hybrid supercapacitor has been developed with CS/PVDF polymer as SPE and manganese cobalt ferrite ($MnCoFeO_4$) as electrode material. Oxidation states of the different elements of ($MnCoFeO_4$) have been ascertained by X-ray photoelectron spectroscopy (XPS). To the best of our knowledge, the electrochemical performance of this hybrid supercapacitor and the inter-diffusion mechanism of the charge carriers in order to evaluate the effective specific capacitance, were investigated for the first time. The inter ion transport properties between electrode and blended polymer electrolytes have been determined by electrochemical impedance spectroscopy (EIS) specifically at very low frequency regime. Enormous enhancement of effective specific capacitance (C_E ~ 750 Fg^{-1}) (compared with the specific capacitance values of those reported in the literature as listed in Table 7.1) has been reported.

Table 7.1. Supercapacitive performance of CS/PVDF blended solid polymer electrolytes compared with other polymer electrolyte materials.

Polymer electrolytes with electrode materials	Capacitance	References
Chitosan/PEG/$LiClO_4$/EC/PC with carbon	47 Fg^{-1}	[13]
Epoxy resin/LiTFSI/BMIM-TFSI/Al_2O_3 with activated carbon	90 Fg^{-1}	[26]
PVA/CH_3COONH_4/BmImCl with activated carbon	28.36 Fg^{-1}	[27]
PVA/$NaCF_3SO_3$/BmImBr with carbon	16.32 Fg^{-1}	[28]
Chitosan/Methyl cellulose/NH_4I with carbon	1.76 Fg^{-1}	[29]
PMMA/MgTr/EC/DEC with carbon	23 Fg^{-1}	[30]
PVA/$LiClO_4$/TiO_2 with carbon	12.5 Fg^{-1}	[31]
PVP/ $LiClO_4$ with glass/ITO/PEDOT	15 Fg^{-1}	[32]
Chitosan/PVDF/ $LiClO_4$/Glycerol with $MnCoFeO_4$	750 Fg^{-1} (effective specific capacitance)	Present work

7.2. Experimental

7.2.1. Synthesis of the CS/PVDF based blended solid polymer electrolyte (SPE)

The solid polymer electrolytes were synthesized by solution blending and evaporation casting technique [33]. Various weight ratios of chitosan (CS) and polyvinylidene fluoride (PVDF) were dissolved in 50 ml of 1 % aqueous acetic acid solution and 30 ml DMF respectively. CS/PVDF blend solutions were prepared by mixing both of the solutions followed by stirring for 10 minutes at room temperature. Then different weight percentages of $LiClO_4$ (15-80 wt. %) as ionic salt and glycerol (15-60 wt. %) as a plasticizer, were added in the CS/PVDF blended solutions and stirred continuously until a homogenous viscous solution was obtained, followed by ultrasonication for 30 minutes. Finally, the homogenous solutions were casted separately on polypropylene petri dishes and allowed to dry in a vacuum oven at 40℃ for 24 hours for the thin polymer films to form (thickness of the order of ~ 250 μm). The films were characterized by computer interfaced impedance analyzer (Agilent 4294A-Precision Impedance Analyzer) in the frequency range between 40 Hz and 100 KHz at room temperature. The impedance of the films were measured several times after repeatedly drying in vacuum oven. The reproducibility of the conductivity results confirms the absence of residual water which may contribute towards conductivity enhancement. Fourier transform infrared spectroscopy (FTIR) was performed using Perkin Elmer FT-IR Spectrum 2 spectrometer having resolution of 4 cm^{-1}.

7.2.2. Synthesis of $MnCoFeO_4$

$MnCl_2.4H_2O$, $CoCl_2.6H_2O$ and anhydrous $FeCl_3$ taken in stoichiometric ratio were dissolved in deionised water. 100 ml of 0.8 M NaOH solution was added dropwise to the mixed solution with continuous stirring and a black precipitate was formed. The precipitate was washed several times with deionised water and ethanol via centrifugation and dried at 100℃. Finally, the product was calcined at 600℃ for 3 hours. The nanoparticles were characterized by X-ray diffraction (XRD), High resolution transmission electron microcopy (HR-TEM) and X-ray photo electron spectroscopy (XPS). XRD was done by a X-ray diffractometer (model: Bruker D8 Advance) using the CuKα radiation of wavelength 1.5406Å.The morphology and size of the nanoparticles were studied by HR-TEM images using the microscope, JEOL (model: JEM, 2100F). XPS was studied using OMICRON-0571 system.

7.2.3. Development of the symmetric supercapacitor

The electrodes of the symmetric supercapacitor were fabricated by using a paste of a homogeneous mixture made of $MnCoFeO_4$ nanoparticles, acetylene black (AB) and polytetrafluoroethylene (PTFE) taken in the wt. % ratio of 50:45:5. The paste was then compacted into a thin sheet using mortar and pestle and compressed on a stainless steel mesh having the surface area of 1 cm^2. The prepared electrode was heated at 60 ℃ for 6 h under vacuum to evaporate the solvent completely. The total weight of the active material in the electrode is usually ~10 mg. Electrochemical behavior of the samples through cyclic voltammetry (CV) measurement was investigated with AUTOLAB-30 potentiostat/galvanostat.

7.3. Results and Discussion

7.3.1. Structural Characterization: X-ray Diffraction (XRD) studies

$MnCoFeO_4$ nanoparticles are characterized by XRD. Figure 7.1a illustrates the diffraction peaks of $MnCoFeO_4$ nanoparticles which exhibit a spinel structure (cubic, space group $Fd\bar{3}m$, JCPDS #22-1086) having general formula AB_2O_4, where A refers to a divalent metal ion and B refers to a trivalent metal ion. The crystallite size (D) and microstrain (ε) of $MnCoFeO_4$ nanoparticles are estimated by using Williamson and Hall's modified Scherrer's formula given by [34],

$$\beta\cos\theta = \frac{0.89\lambda}{D} + 2\varepsilon\sin\theta \tag{7.1}$$

The inset of the Fig. 7.1a shows the $\beta\cos\theta$ vs $\sin\theta$ plot revealing the average size of the $MnCoFeO_4$ nanoparticles as 34 nm.

7.3.2. High Resolution Transmission Electron Microscopy (HR-TEM)

The morphology and size of the $MnCoFeO_4$ nanoparticles have been studied using HR-TEM images as shown in Fig. 7.1b. Distribution of the particle size of $MnCoFeO_4$ is in the range 27-67 nm (Fig. 7.1b). The selected area diffraction (SAD) pattern of the $MnCoFeO_4$ nanoparticles is shown in Fig. 7.1c. It consists of four well resolved concentric rings representing four crystallographic planes (i.e. 220, 311, 422, 440) of the $MnCoFeO_4$ nanoparticles.

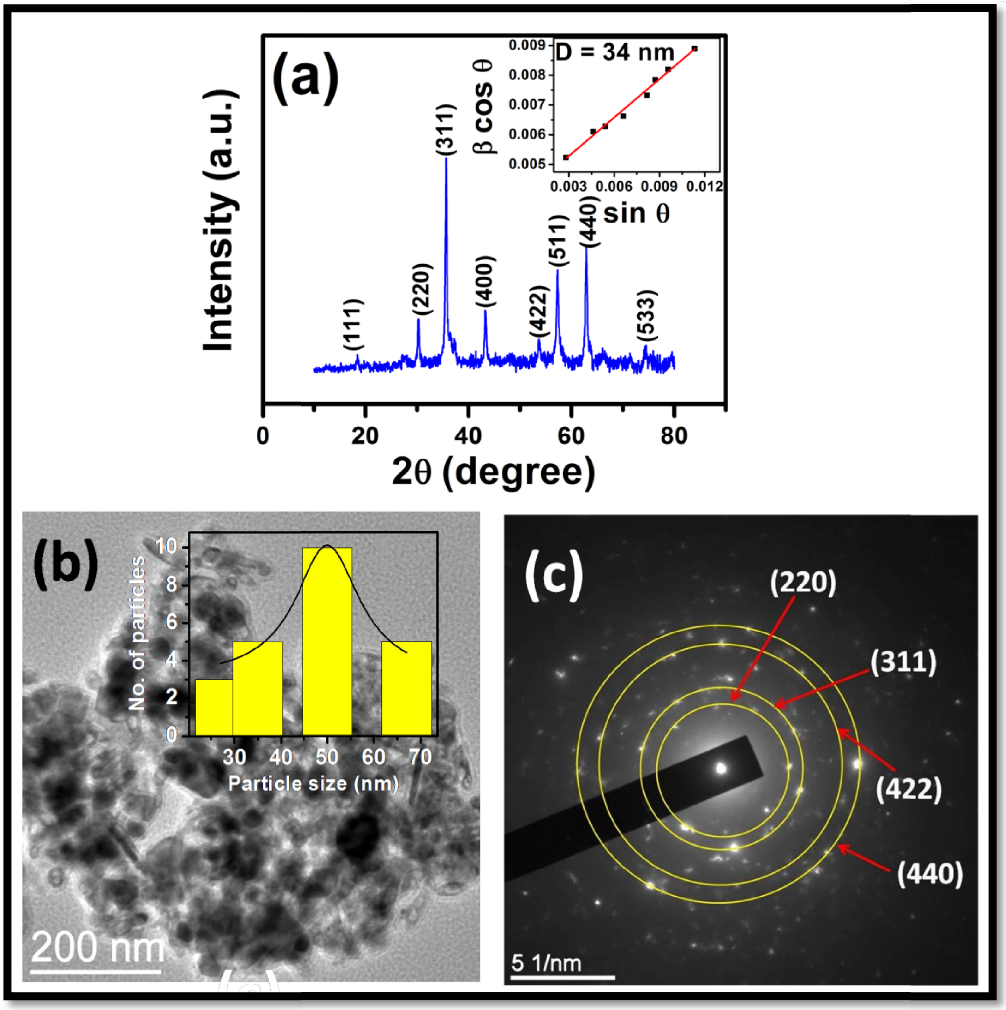

Fig. 7.1. (a) XRD spectrum of $MnCoFeO_4$ and the inset figure shows the Williamson–Hall plot, (b) HR-TEM images of $MnCoFeO_4$ and the inset figure shows the distribution of the particle size and (c) Selected area diffraction (SAD) pattern of the $MnCoFeO_4$ nanoparticles showing different planes.

7.3.3. Spectroscopic Characterization: X-ray photoelectron spectroscopy (XPS) studies

Spinel ferrites exhibit multiple oxidation states which enable fast and reversible faradaic redox reactions. XPS, an useful surface analysis tool, is used to characterize the oxidation state of each constituting elements of $MnCoFeO_4$. A typical XPS spectrum of $MnCoFeO_4$ (shown in Figure 7.2) depicts the spectroscopic signature of manganese, cobalt, iron and oxygen.

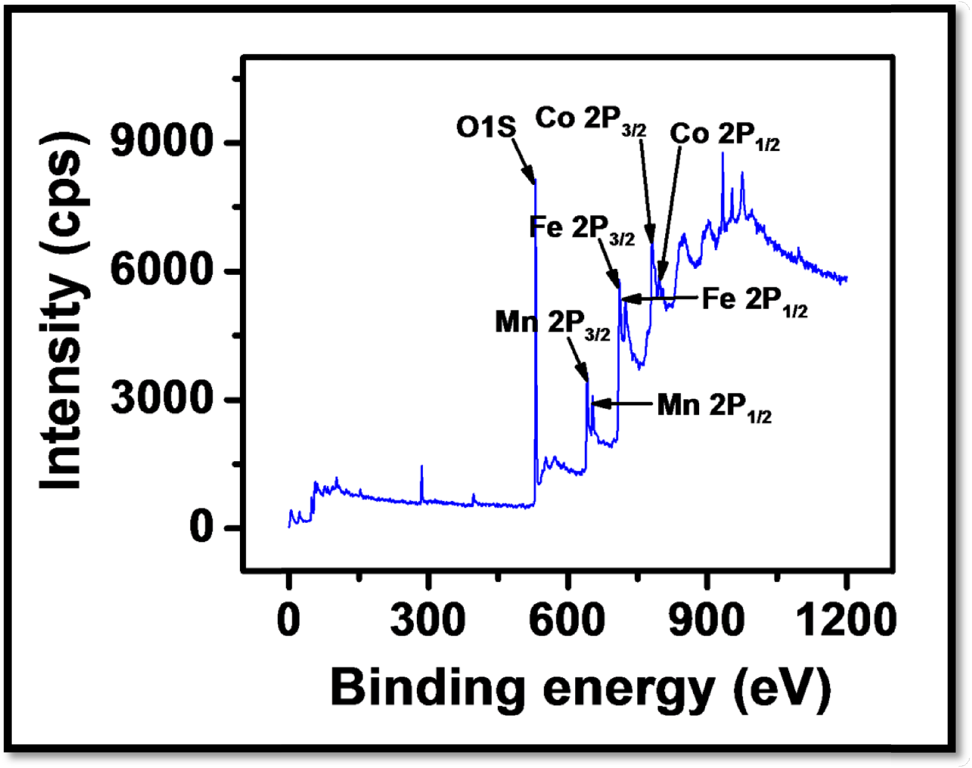

Fig. 7.2. High resolution XPS spectrum of survey scan of $MnCoFeO_4$ nanoparticles.

The peaks centered at 641.4 eV and 653.2 eV are assigned to $Mn2p_{3/2}$ and $Mn2p_{1/2}$ (Fig. 7.3a), respectively [35]. The $Mn2p_{3/2}$ peak is deconvoluted into two peaks positioned at 640.4 eV and 641.8 eV (Fig. 7.3b) which are assigned to $Mn^{2+}$and Mn^{3+}, respectively [36]. The ratio of Mn^{2+} and Mn^{3+} present in $MnCoFeO_4$ can be obtained from the ratio of the area under the corresponding peak of XPS spectra and it is found as 25.8 : 74.2. The $Fe2p_{3/2}$ and $Fe2p_{1/2}$ peaks centered at 711 eV and 724.2 eV are confirming the presence of +3 oxidation state of iron at octahedral sites (Fig. 7.3c) [37]. The Co 2p signal has been deconvoluted into four peaks (Fig. 7.3d). The first two peaks with binding energies (BE) around 780.8 eV and 786.2 eV are assigned to Co2p$_{3/2}$ and its shakeup satellites, while the higher BE peaks around 796.5 eV and 803.3 eV correspond to Co2p$_{1/2}$ and its shakeup satellites respectively. This concludes that the oxidation state of the cobalt is +2 [38].

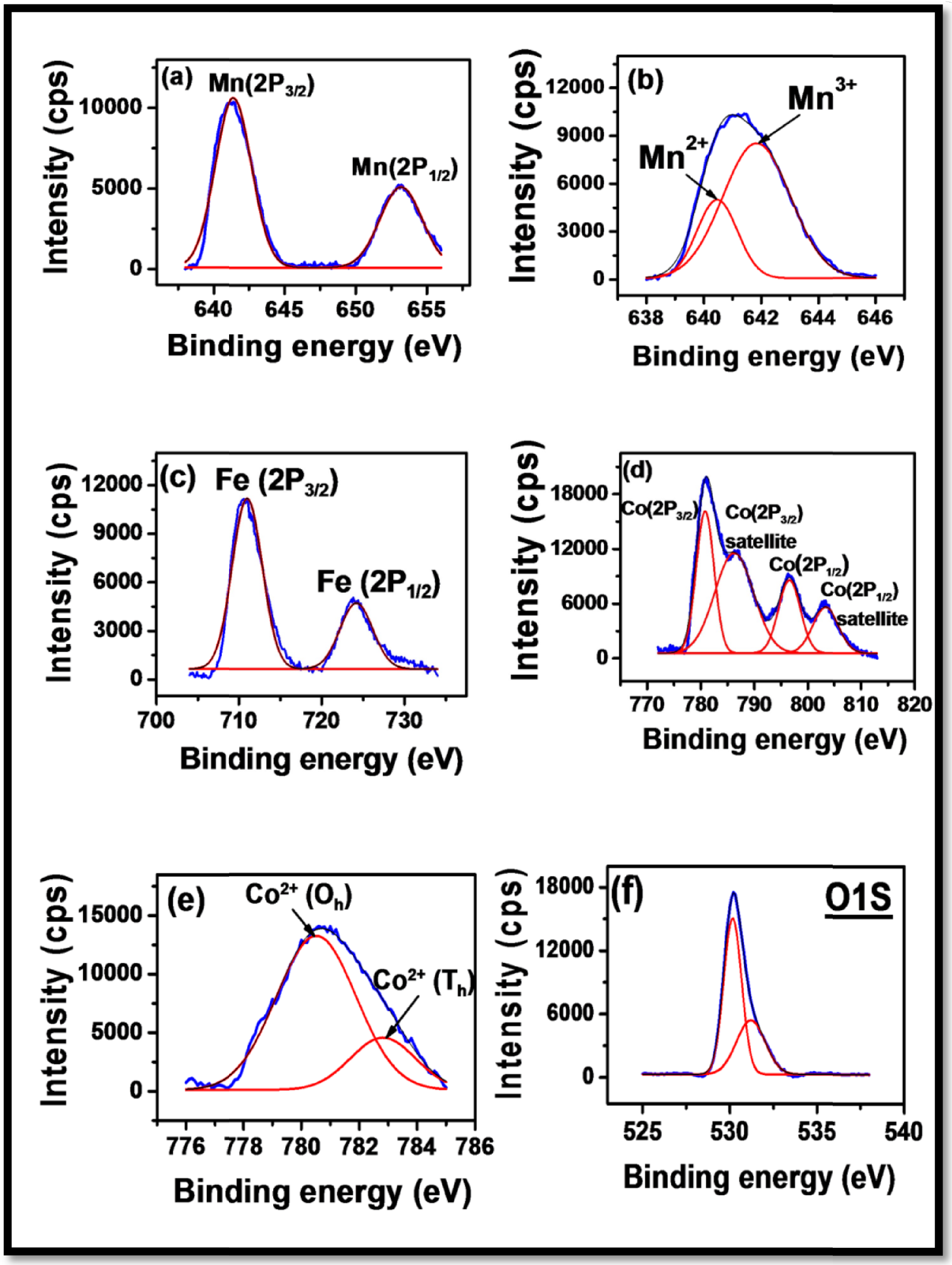

Fig. 7.3. (a) High-resolution XPS spectrum of survey scan of (a,b) Mn2P, (c) Fe2P, (d,e) Co2P, (f) O1S. The red solid lines are the deconvoluted XPS spectra based on Gaussian fitting function.

Moreover, the decovoluted peak of Co^{2+} ions at 780.5 eV and 782.8 eV (Fig. 7.3e) [39] reveals the distribution of the Co^{2+} ions at octahedral sites (78.36 %) and tetrahedral sites (21.64 %) respectively and thereby supporting a partial inverse spinel structure as $[MnCo_{1-x}]_{Tet}[Co_xFe]_{Oct}O_{4-\delta}$. The oxygen non-stoichiometry or deficiency (δ) can be accounted for the divalent Mn present in $MnCoFeO_4$. The oxygen O1s peak has been decovoluted into two peaks located at 530.1 eV and 531.2 eV (Fig. 7.3f), which corresponds to the typical metal-oxygen bonds with oxygen deficiency [40]. Typical oxidation states of the transition metal ions in the $MnCoFeO_4$ can play a critical role in the enhancement of capacitance.

7.3.4. Impedance Spectroscopy

7.3.4.1. Ionic conductivity studies of the blended composites

A solid polymer electrolyte (SPE) intended to use in solid-state supercapacitors must have sufficient ionic conductivity. Ionic conductivity of the blending SPE depends upon the charge of the carrier ions and its concentration. Charge carrier concentration may be changed by doping the polymers with salt. AC impedance spectroscopy is used to characterize the electrical properties of the CS/PVDF blended SPE material in a broad range of frequencies at an applied AC potential of amplitude 500 mV.

The Nyquist plots of different blended compositions of chitosan (CS) and polyvinylidene difluoride (PVDF) polymers are shown in Fig. 7.4a at 300K. All the results are analyzed based on equivalent circuit consisting of contact resistance (R_s), bulk resistance (R_b) and constant phase element (CPE) [41]. The DC ionic conductivity ($\boldsymbol{\sigma}_{DC}$) of the blended polymers is calculated based on the relation, $\boldsymbol{\sigma}_{DC} = L/R_bA$ where, L is the sample thickness, A is the effective contact area of the electrode and the electrolyte interface. The bulk resistance (R_b) can be determined from the intersection of the tilted straight lines to the real axis (Re Z) at lower frequencies. The variation of the DC conductivity for different percentage of blended composition of CS in the blended polymer matrix is illustrated in the inset of Fig. 7.4a. No significant improvement of the conductivity (~ 10^{-9} S/cm) is observed in the blending compositions. But, on increasing the percentage of CS in the blended polymer matrix, the film becomes more brittle. As a consequence, the blending composition of CS/PVDF has been optimized to the blending ratio of as 20:80 [CS/PF(20:80)].

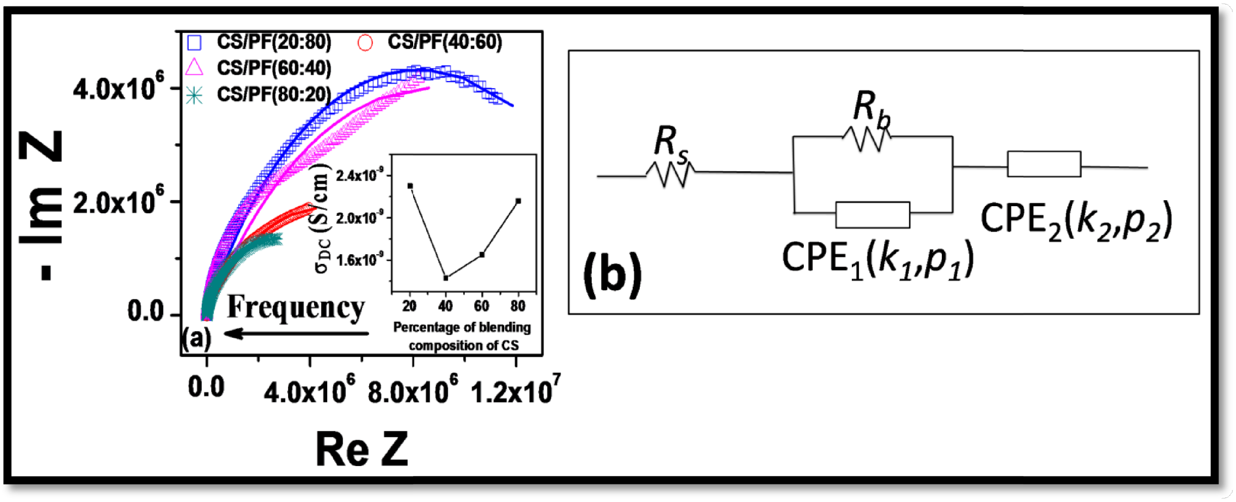

Fig. 7.4. (a) Nyquist plots of different blending compositions of CS/PVDF, solid lines represent the modeled plots based on equivalent circuit fitting and the inset figure shows the DC conductivity variation with the percentage blending composition of chitosan (CS), (b) Equivalent circuit used to model the Nyquist plots of the blended SPEs.

The Nyquist plots of the CS/PF(20:80) blended solid polymer electrolytes with different concentration of $LiClO_4$ salt (hence forth denoted as CPL_x, where $x = 15$, 50, 70 and 80 weight percentages of the blended polymer) are shown in Fig. 7.5a. The DC conductivity of different CPL_x are shown in Fig. 7.5b. In real systems, there is always some energy dissipation and thus the experimental results can only be explained by an equivalent circuit involving “constant phase element (CPE)” instead of ideal capacitors. The impedance of the CPE is given by, $Z_{CPE} = k\ (j\omega)^{-p}$, where k is the CPE coefficient and p is some exponent fractional parameter ($0 < p < 1$). It is important to note here that the value of the exponent (p) of the CPE for CS/PF(20:80) is 0.62, while for CPL_x (15 to 80) materials, $p \sim 0.3$ which infers that the salt ($LiClO_4$) creates stronger disorder in the blended polymer structure. Moreover, the ionic conductivity of the CPL_x increases from $\sim 4.25\times10^{-4}$ to $\sim2.7\times10^{-2}$ S/cm with the increment of salt concentration x from 15% to 80%. It is quite interesting that the room temperature ionic conductivity of the blended polymer has increased by seven orders in magnitude (from $\sim 10^{-9}$ to $\sim10^{-2}$ S/cm) on the incorporation of salt in the CPL_x (for $x = 80$), where the mobile carrier Li^+ ions plays a significant role for the enhancement of conductivity [42,43]. This is discussed in details in the subsequent text. In order to enhance the mobility of the charge carrier further, different concentrations of the glycerol as plasticizer, have also been added in the matrix of the blended polymer CPL_{80} and the products are denoted as $CPL_{80}Gl_y$ where, y = 15, 45 and 60 weight percentages of the blending polymer (Figs. 7.5c & 7.5d). It is observed that the film quality further improves on treating with glycerol which makes the SPE more soft, sticky in nature and provides a good contact with the electrode surface essential for the fabrication of the high performance solid state supercapacitor.

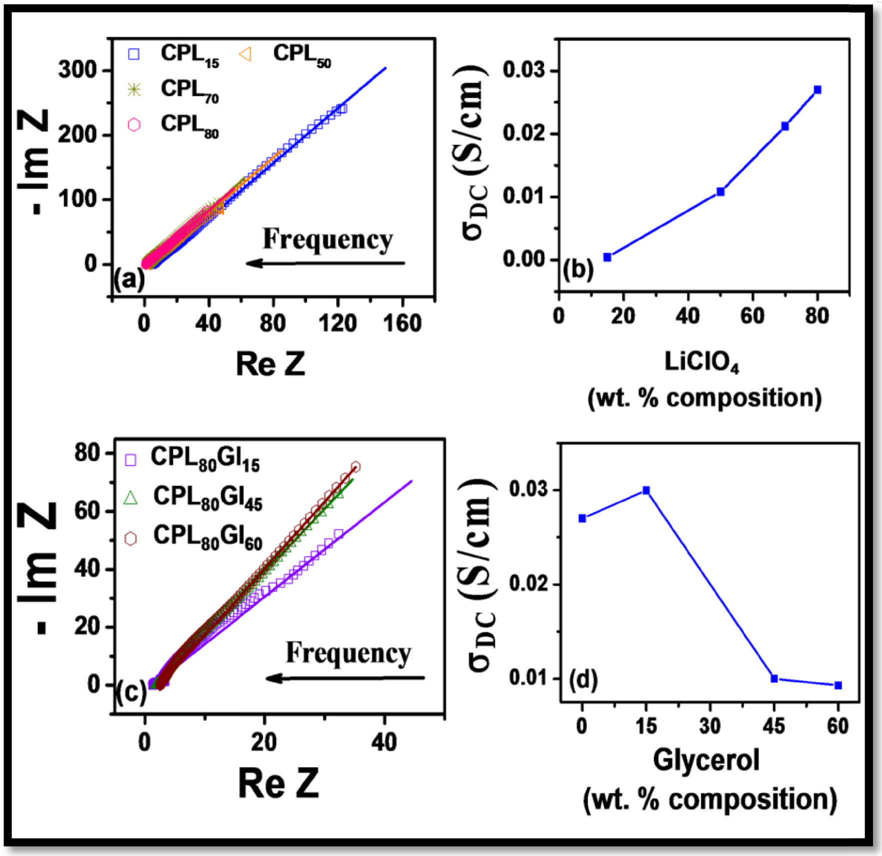

Fig. 7.5. (a) The Nyquist plots of the CPL_x blended solid polymer electrolytes with different concentration of $LiClO_4$ salt (x = 15, 50, 70 and 80 weight percentages of the blended polymer), (b) Variation of DC conductivity of the CPL_x blended SPE as a function of salt composition, (c) The Nyquist plots of the $CPL_{80}Gl_y$ (y = 15, 45 and 60 weight percentages of the blending polymer) blended SPE, (d) Variation of DC conductivity of the $CPL_{80}Gl_y$ blended SPE as a function of glycerol composition. The solid lines in (a) and (c) represent the modeled plots based on equivalent circuit fitting.

There is a nominal increase in conductivity of the SPE followed by a significant decrease with the increase in glycerol concentration as shown in Fig. 7.5d. The initial increase of the conductivity may be attributed to the slight increase of salt dissociation in presence of glycerol. On the contrary, further increase of the glycerol may help in the salt recrystallization and that way decrease the conductivity by inhibiting the fast transport of carrier ions [44].

7.3.4.2. Dielectric Studies

Real and imaginary parts of the permittivity are estimated from the real and imaginary part of the complex impedance. The frequency dependent complex dielectric permittivity (ε^*) is given by, $\varepsilon^*(\omega) = \boldsymbol{\varepsilon}_{\mathbf{r}}(\omega) - j\boldsymbol{\varepsilon}_{\mathbf{i}}(\omega)$ where $\boldsymbol{\varepsilon}_{\mathbf{r}}$ and $\boldsymbol{\varepsilon}_{\mathbf{i}}$ are the real and imaginary parts of the complex dielectric permittivity. Real part of the permittivity ($\boldsymbol{\varepsilon}_{\mathbf{r}}$) corresponds to ordinary dielectric constant of the material which measure the amount of elastic energy stored in the material during every cycle of the applied AC field. As a consequence, higher value of $\boldsymbol{\varepsilon}_{\mathbf{r}}$ advocates better conductivity. On the other hand**,** imaginary part of the permittivity ($\boldsymbol{\varepsilon}_{\mathbf{i}}$) corresponds to the energy dissipation due to motion of ions especially at lower frequency. The frequency dependence of the dielectric constant ($\boldsymbol{\varepsilon}_{\mathbf{r}}$) for the composites, CPL$_x$ (x = 15, 50, 70 and 80) and CPL$_{80}$Gl$_y$ (y = 15, 45 and 60) are shown Figs. 7.6a & 7.6b, respectively. In both cases, the dielectric constant **(**$\boldsymbol{\varepsilon}_{\mathbf{r}}$) decreases rapidly with increase in frequency. At low frequency regime, the dipoles of the charge carriers are getting enough time to align themselves according to the direction of the electric field and hence contribute large polarization responsible for high value of dielectric constant **(**$\boldsymbol{\varepsilon}_{\mathbf{r}}$). At high frequency, the change in the electric field becomes too fast for the charges to follow and thus their contribution towards polarization approaches a small value. At 100 KHz, $\boldsymbol{\varepsilon}_{\mathbf{r}}$ enormously increases from ~ 10^3 to ~ 10^5 with increase in $LiClO_4$ doping as illustrated in the inset of Fig. 7.6a. On contrary, reverse behavior of $\boldsymbol{\varepsilon}_{\mathbf{r}}$ is observed in CPL$_{80}$Gl$_y$ at 100 KHz with increase of plasticizer loading as shown in the inset of Fig. 7.6b. The frequency dependence of the dielectric loss ($\boldsymbol{\varepsilon}_{\mathbf{i}}$) for the composites, CPL$_x$ (x = 15, 50, 70 and 80) and CPL$_{80}$Gl$_y$ (y = 15, 45 and 60) as shown in Figs. 7.6c & 7.6d, respectively, do not exhibit any relaxation peak in the frequency range of investigation.

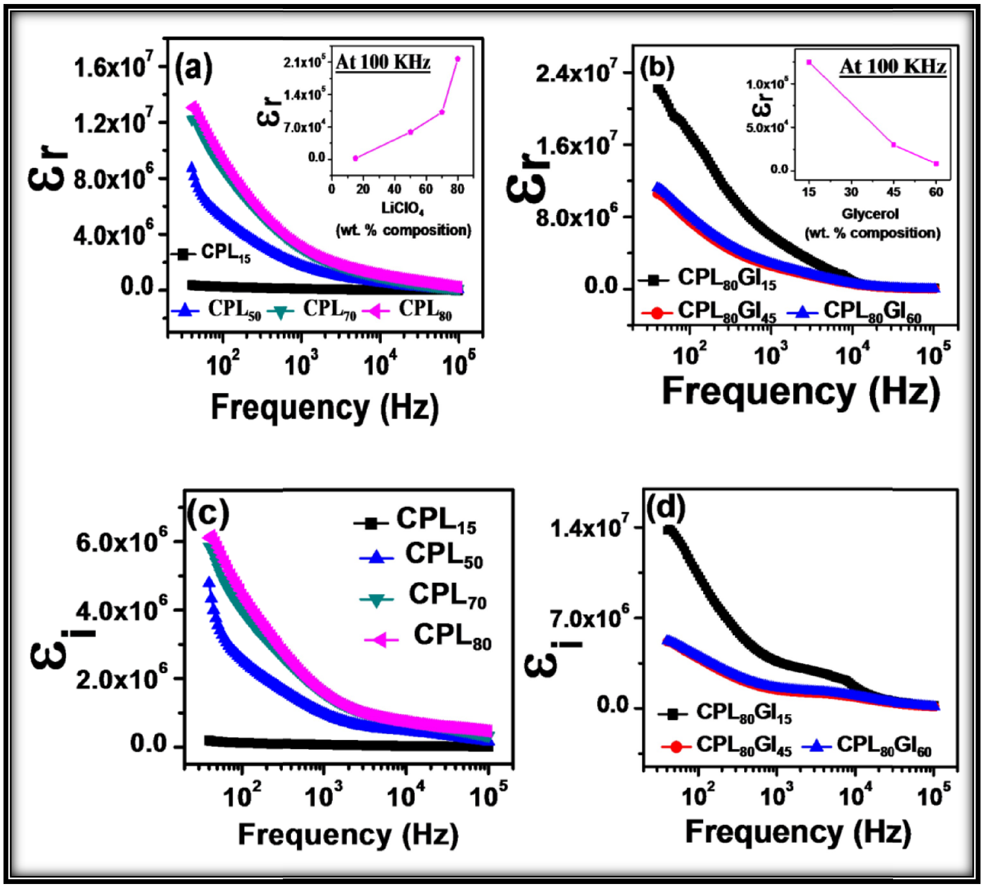

Fig. 7.6. (a) Frequency dependence of the dielectric constant of (a) CPL$_x$ (x = 15, 50, 70 and 80), (b) CPL$_{80}$Gl$_y$ (y = 15, 45 and 60) blended SPE. Frequency dependence of the dielectric loss of (c) CPL$_x$ (x = 15, 50, 70 and 80), (d) CPL$_{80}$Gl$_y$ (y = 15, 45 and 60) blended SPE.

The loss tangent (tan δ) is defined as the ratio of energy loss to energy stored (**$\varepsilon_i/\varepsilon_r$**) in a periodical field and is also called as dissipation factor. The tan δ gives the idea of relaxation. A maximum in tan δ vs frequency can be obtained for a particular frequency (ω_{max}) satisfying the equation $\omega_{max}\tau = 1$, where τ is the dielectric relaxation time. It is observed that there are no significant relaxation peak in the frequency range of investigation except for the highest conducting composite, CPL$_{80}$Gl$_{15}$ (shown in the inset of Fig. 7.7b). The relaxation time (τ) calculated for CPL$_{80}$Gl$_{15}$ composite is ~ 6.59 μs. Asymmetric nature of the tan δ peak suggests non-Debye relaxation indicating short range movement of ions. It is also depicted in the Fig. 7.7b that the loss factor increases with increase in glycerol loading in the blended SPE system. The conduction path may get perturbed on addition of plasticizer due to more amorphisation of the polymer matrix [45,46].

7.3.4.3. Electric Modulus Study

The modulus study is extensively useful to investigate the conductivity relaxation by suppressing the electrode polarization effect especially at low frequency. On plotting against frequencies, the imaginary part of the electric modulus (M″) exhibits a characteristic relaxation peak where the frequency region to the left of this relaxation peak is associated with the hopping conduction due to mobile charge carriers over long distances and the region to the right of this peak corresponds to the short range or localized motion of charge carriers as they are spatially confined to the potential wells. Thus, the frequency range where the relaxation peak occurs suggests the transition region from long-range to short-range mobility of charge carriers.

The frequency dependence of the imaginary part of electric modulus (M″) for the composites, CPL$_x$ (x = 15, 50, 70 and 80) and CPL$_{80}$Gl$_y$ (y = 15, 45 and 60) are shown in Figs. 7.7c & 7.7d, respectively. In both the cases the M″show an increase at the higher frequency end and exhibit a long tail feature at low frequency regime. These indicate that the materials are capacitive in nature [13].

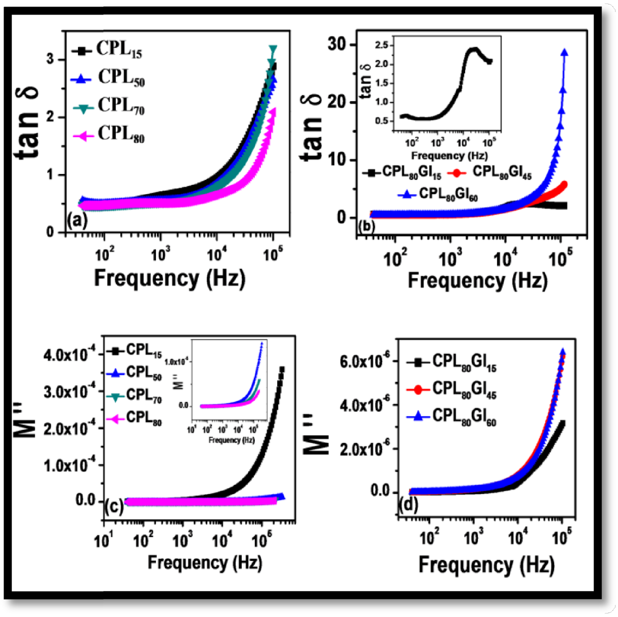

Fig. 7.7. (a) Frequency dependence of tan δ of (a) CPL$_x$ (x = 15, 50, 70 and 80), (b) CPL$_{80}$Gl$_y$ (y = 15, 45 and 60) blended SPE. Frequency dependence of the imaginary part of electric modulus of (c) CPL$_x$ (x = 15, 50, 70 and 80), (d) CPL$_{80}$Gl$_y$ (y = 15, 45 and 60) blended SPE.

On increasing the salt concentration, M″ of CPL$_x$ at high frequency gradually diminishes which corroborates with the dielectric results. On the other hand, M″ of CPL$_{80}$Gl$_y$ increases with increasing glycerol loading (y) at higher frequency. It may be due to the enhancement of amorphization of the polymer matrix resulting a non-ideal perturbed system which is responsible for the multi frequency non-Debye type relaxation process.

7.3.4.4. Intra diffusion process

The conductivity of the solid polymer electrolytes (SPE) depends on the number density (n) and mobility (μ) of the free carrier ions as, $\sigma_{\mathrm{DC}} = ne\mu$. Hence, it is dependent on the intra diffusion coefficient or diffusion rate of the mobile ions within the electrolyte matrix. It is important to study the intra diffusion processes of the mobile ions in the SPE system. The ion diffusion mechanism in the non-crystalline solid polymer electrolytes is quite similar to that of liquid electrolytes. Polymer electrolytes are considered to be composed of fractal structures in macroscopic as well as in microscopic scales [47]. In order to explore the ion conduction mechanism inside solid polymer electrolytes, impedance results have been analyzed based on a model proposed by Lenzi et al, where anomalous diffusion through a fractional order parameter γ has been incorporated as [48,49],

$$Z = \frac{2}{i\mathrm{A}\omega\boldsymbol{\varepsilon}_{\mathbf{r}}\boldsymbol{\varepsilon}_{\mathbf{0}}\beta^2}\left[\frac{1}{\beta\lambda_D^2}\tanh\left(\frac{\beta \mathrm{L}}{2}\right) + h\,\frac{(i\omega)^{\gamma}\mathrm{L}}{2\mathrm{D}_{\gamma}} + (1-\ h)\,\frac{i\omega \mathrm{L}}{2\mathrm{D}}\right] \qquad (7.2)$$

where, λ_D is the Debye screening length, $\boldsymbol{\varepsilon}_{\mathbf{r}}$ is the dielectric constant of the electrolyte material, D_{γ} and D are the anomalous and normal diffusion coefficients, respectively, L is the sample thickness, A is the effective contact area of the electrode and the electrolyte surface, $\beta = \sqrt{\frac{1}{\lambda_D^2} + h\frac{(i\omega)^{\gamma}}{\mathrm{D}_{\gamma}} + (1-h)\frac{i\omega}{\mathrm{D}}}$ is the characteristic exponent of the model, h is the fraction of anomalous diffusion and $(1-h)$ is the fraction of normal diffusion. Equation 7.2 is used to analyze the diffusive behavior of the ions in the blended CS/PVDF system by fitting the Nyquist plots based on this theoretical model as shown by best fit in Fig. 7.8. The model parameters are listed in Table 7.2. It is found that the value of γ decreases with increase in both LiClO$_4$ and glycerol concentrations in the CPL$_x$ ($15 \le x \le 80$) and CPL$_{80}$Gl$_y$ ($15 \le y \le 60$) composites, respectively. The values of γ changes from 0.425 to 0.335 for different x and y values studied. It is evident from the modeling results that the contribution of anomalous diffusion in the blended SPE is much higher compared to that of normal diffusion as the value of *h* is close towards 1. The fractal structure of the polymers leads to this anomalous diffusive behavior of ions in the blended solid polymer electrolytes [50]. The anomalous diffusion coefficient for the blended composites obtained through this modeling approach corroborate with the intra diffusion coefficient values obtained through FTIR results as discussed in the subsequent section. The maximum value of D_γ (3.25×10^{-10} m^2/s) and λ_D (0.97 μm) supports the highest conductivity of $CPL_{80}Gl_{15}$.

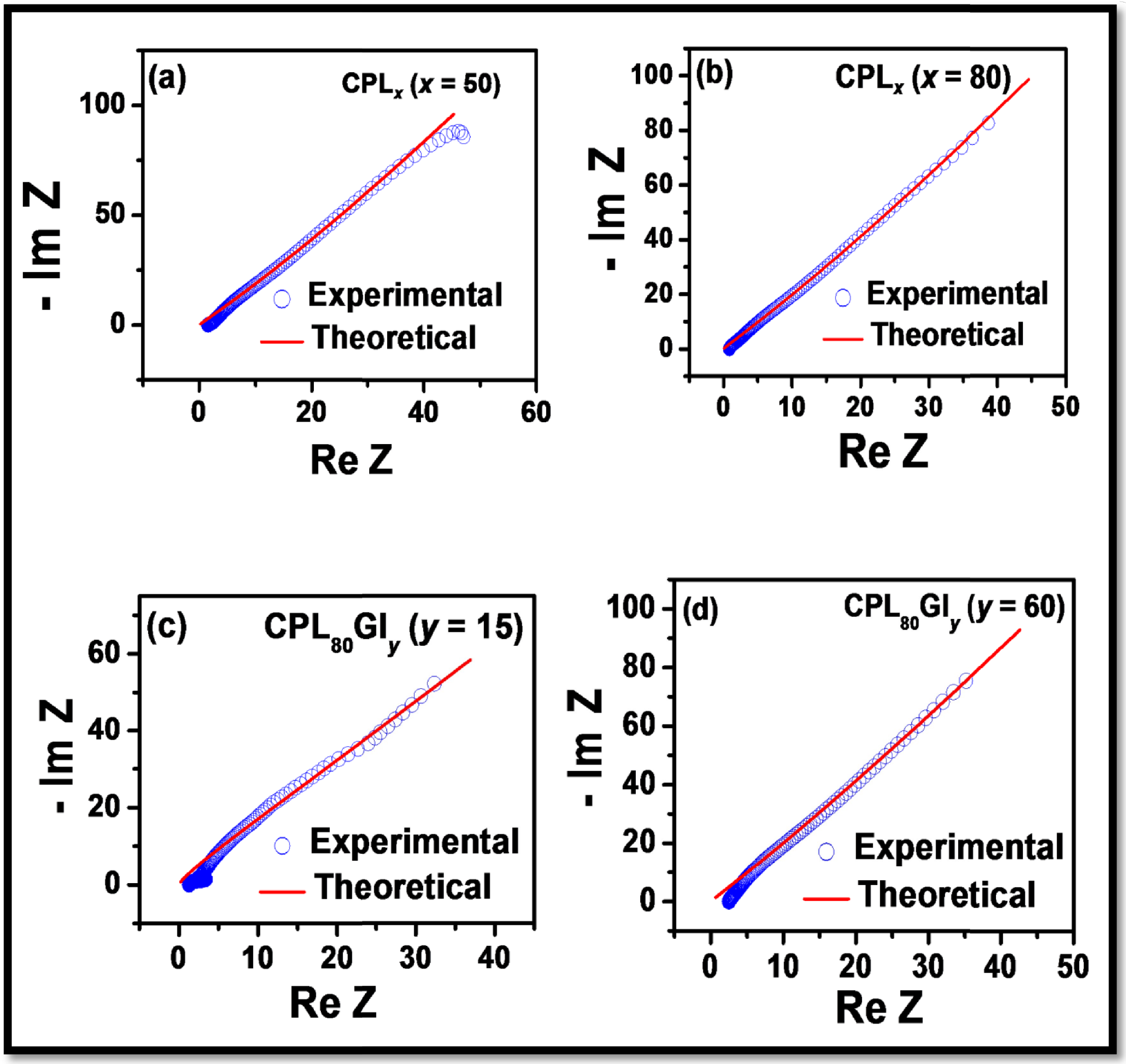

Fig. 7.8. Modeling of Nyquist plots based on fractional diffusion model (Eq. 7.2) for the blended SPE: CPL_x (a) $x = 50$, (b) $x = 80$ and $CPL_{80}Gl_y$ (c) $y = 15$, (d) $y = 60$.

Table 7.2. Best fit model parameters to analyze diffusion processes in the blended SPEs.

SPE	D (× 10^{-3} m^2s^{-1})	D_γ(× 10^{-10} m^2s^{-1})	γ	h	λ_D (μm)
$CPL_x(x = 15)$	1	0.17	0.425	0.99	0.139
$CPL_x(x = 50)$	7	1.45	0.365	0.99	0.50
$CPL_x(x = 70)$	9	2.35	0.357	0.98	0.58
$CPL_x(x = 80)$	13	2.72	0.356	0.97	0.95
$CPL_{80}Gl_y(y = 15)$	15	3.25	0.420	0.96	0.97
$CPL_{80}Gl_y(y = 45)$	10	1.15	0.349	0.97	0.505
$CPL_{80}Gl_y(y = 60)$	5	1.11	0.335	0.98	0.33

7.3.5. Fourier Transform Infrared spectroscopy (FTIR)

The FTIR transmission spectra over the range of 400 cm^{-1} to 2000 cm^{-1} for the blended SPEs with varying salt and plasticizer content are shown in Figs. 7.9a and 7.9b, respectively. FTIR spectra analysis has been carried out to study the interactions between the polymer matrix comprised of CS, PVDF with $LiClO_4$ salt in order to determine the transport properties of SPE.

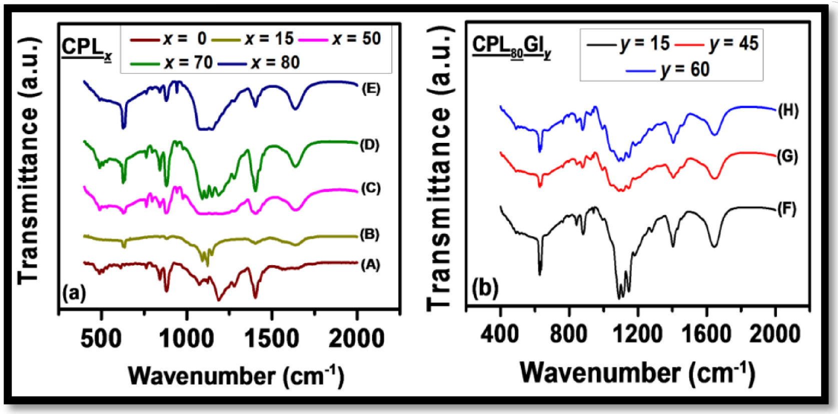

Fig. 7.9. FTIR Transmission spectra of (a) CPL_x blended SPE with (A) $x = 0$, (B) $x = 15$, (C) $x = 50$, (D) $x = 70$, (E) $x = 80$ and (b) $CPL_{80}Gl_y$ blended SPE with (F) $y = 15$, (G) $y = 45$, (H) $y = 60$.

The deconvolution technique of the absorption spectrum has been adopted to estimate the ion transport parameters. The number density of free charge carrier (n), the ionic mobility (μ) and the diffusion coefficient (D_{intra}) of the ions are calculated using the Eqs. 7.3, 7.4 and 7.5 respectively,

$$n = \frac{M \times N_A}{V_{total}} \times P_f \tag{7.3}$$

$$\mu = \frac{\sigma_{DC}}{ne} \tag{7.4}$$

$$D_{intra} = \frac{\mu K_B T}{e} \tag{7.5}$$

The peak close to 628 cm^{-1} and 637 cm^{-1} are assigned as free and contact ions pairs respectively in the blended SPE system [33,51]. The FTIR spectra are deconvoluted over the range of 620 cm^{-1} to 640 cm^{-1} for CPL$_x$ SPE (x = 50 and 80) and CPL$_{80}$Gl$_y$ SPE (y = 15 and 60) as shown in Fig. 7.10.

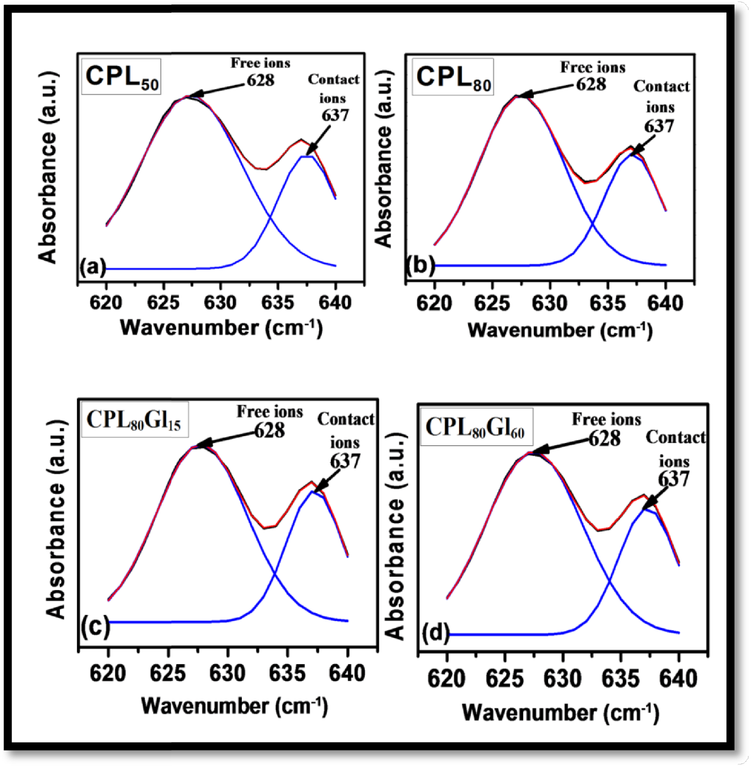

Fig. 7.10. Deconvolution of the FTIR absorption spectra in the region of 620-640 cm^{-1} based on Gaussian fitting function for the blended SPE: CPL$_x$ (a) x = 50, (b) x = 80 and CPL$_{80}$Gl$_y$ (c) y = 15, (d) y = 60.

The percentage of free ions (P_f) in Eq. 7.3 is estimated as,

$$P_f = \frac{A_f}{A_f + A_c} \times 100\ \% \tag{7.6}$$

where, A_f is the area under the peak representing the free ions and A_c is the area under the peak representing the contact ion pairs [33,52]. M is the number of moles of $LiClO_4$ salt in each sample, N_A is the Avogadro's number, V_{total} is the total volume of the blended SPE, σ_{DC} is the DC conductivity obtained from impedance spectroscopy. The transport parameters n, μ and D_{intra} of the blended SPE system containing different concentrations of $LiClO_4$ and glycerol are shown in Fig. 7.11. Number of free charge carriers (n) increases with increase of salt concentrations as shown in Fig. 7.11c. The mobility of the free charge carriers has been remarkably improved by two orders (from ~ 7×10^{-10} to ~ 1×10^{-8} $m^2V^{-1}s^{-1}$) with increasing salt concentration~~s~~. It is known that the motion of the charge carrier (i.e. the ionic mobility) in polymer chains plays an important role in conductivity. Any segmental motion in polymer results in lowering of ionic conductivity [53]. With increasing the salt concentrations in the blending composite, more ion-coordination sites become available for ion migration, resulting in the enhancement of charge carrier mobility.

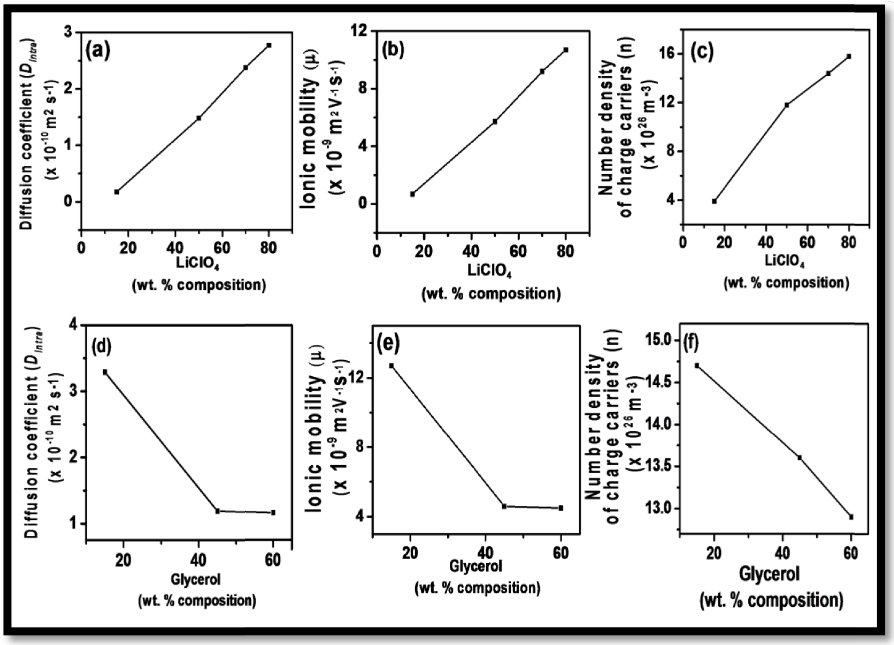

Fig. 7.11. Transport parameters as a function of salt and glycerol compositions respectively for CPL_x blended SPE (a-c) and $CPL_{80}Gl_y$ blended SPE (d-f).

The maximum ionic mobility of the charge carriers (1.27×10^{-8} m^2 V^{-1} s^{-1}) and their corresponding intra diffusion coefficient (3.29×10^{-10} m^2 s^{-1}) have been obtained in the blended $CPL_{80}Gl_{15}$ electrolyte. These transport parameters are corroborated with the results (Table 7.2) obtained from the impedance analysis considering anomalous diffusion mechanism as discussed in section 7.3.4.4 (Intra diffusion process). The conduction path is getting disturbed on addition of plasticizer due to increase of the amorphization of the polymer matrix [45,46]. As a consequence, the transport parameters decrease with increase in glycerol concentrations as illustrated in Figs. 7.11d, 7.11e and 7.11f.

Significant red shift [33,54,55] of the absorption peaks corresponding to amine ($R\text{-}NH_2$) and secondary amide ($R\text{-}CONH_2$) of chitosan (CS) in the blended composites is observed from 1595 cm^{-1} to ~ 1575 cm^{-1} and 1658 cm^{-1} to ~ 1645 cm^{-1} respectively, as shown in Fig. 7.12. This shift remains same and found to be independent of the salt and plasticizer concentrations in the CS/PF(20:80) blended composites.

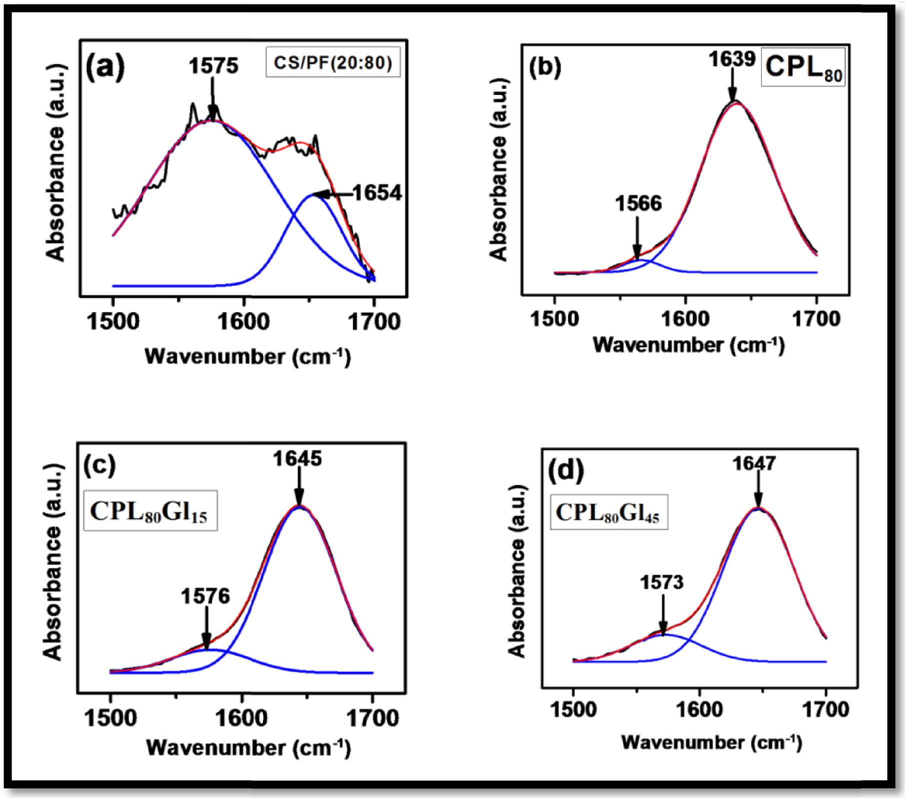

Fig. 7.12. Deconvolution of the FTIR absorption spectra in the region of 1500-1700 cm^{-1} based on Gaussian fitting function for the blended SPE: CPL_x (a) $x = 0$ [CS/PF(20:80)], (b) $x = 80$ and $CPL_{80}Gl_y$ (c) $y = 15$, (d) $y = 45$.

The deconvolution of these characteristic peaks are displayed in Fig. 7.12 for CPL_{80} and $CPL_{80}Gl_y$ $(y = 15, 45)$ SPE. The ratio of the area under the absorption peak corresponding to R-$CONH_2$ to R-NH_2 in CPL_x is found to be increased with salt loading i.e. with increase in x. Figure 7.12 depicts the same for CPL_{80}. This attributes to the interaction of charge carrier (i.e. Li^+ ion) with the secondary amide (R-$CONH_2$) in greater extent compared to primary amine (Fig. 7.13a). There is a slight change in peak area under amide curve on further addition of plasticizer. Thus in conduction mechanism, the role of amide will dominate over amine.

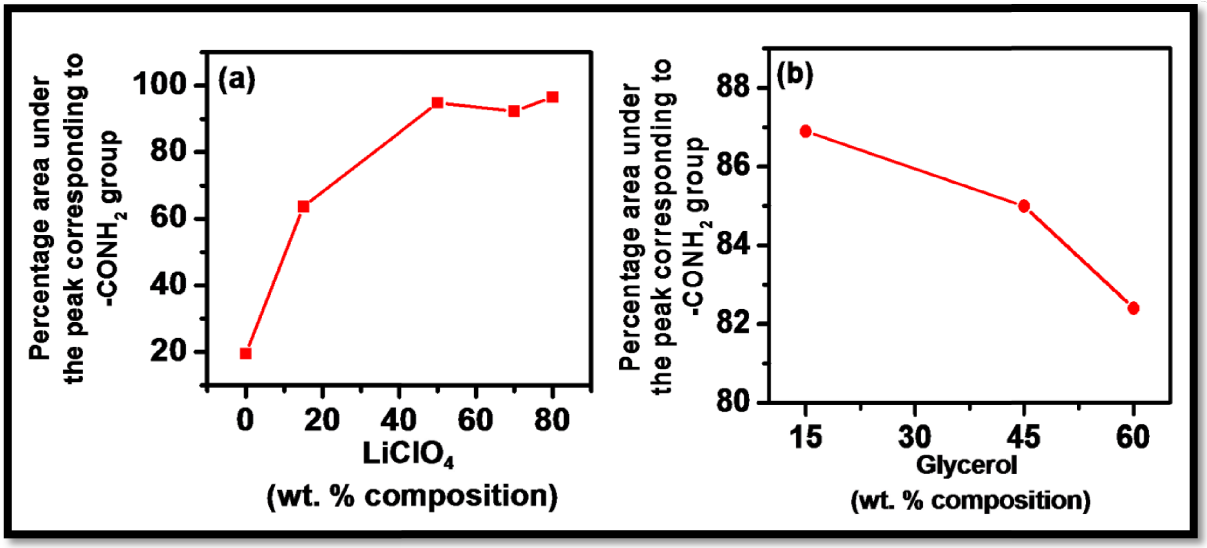

Fig. 7.13. Percentage area under the peak corresponding to amide group as a function of (a) $LiClO_4$ and (b) Glycerol wt. %.

7.3.6. Electrochemical characterization

In order to evaluate the electrochemical performance of the CS/PVDF as solid state polymer electrolyte, a coin type unique symmetric super capacitor has been developed with active carbon and $MnCoFeO_4$ as electrode materials designated as EL-1 and EL-2 respectively. The active mass of the electrode material is ~ 10 mg. $MnCoFeO_4$ has been considered as the second electrode material owing to its nanoporous structure responsible for high specific capacitance and power density [20].

7.3.6.1. Cyclic Voltammetry analysis

Cyclic voltammetry (CV) is one of the simplest techniques to evaluate the accumulation of charge on the electrode materials. The typical cyclic voltammograms (for the cell constructed with EL-1 and $CPL_{80}Gl_{15}$ SPE) at different scan rates from 20 to 250 mV/s over the voltage range from –0.1 to +1.1 V. are shown in Fig. 7.14a. A semi-rectangular shaped CV curve is obtained at slower scan rates**,** indicating a good capacitive characteristics of the electrode materials [56]. The nature of the curves remains almost semi-rectangular shape at faster scan rates, inferring good capacitive behavior. Figure 7.14b shows the CV responses for the cell constructed with EL-2 and $CPL_{80}Gl_{15}$ SPE at different scan rates from 20 to 250 mV/s over the voltage range from -0.1 to +1.1 V. The larger area under the curve of the CV measurement demands higher capacitance value corresponding to EL-2 as compared to EL-1. The mechanisms of the storage capacity of the different electrode materials with respect to the blended SPE are discussed later.

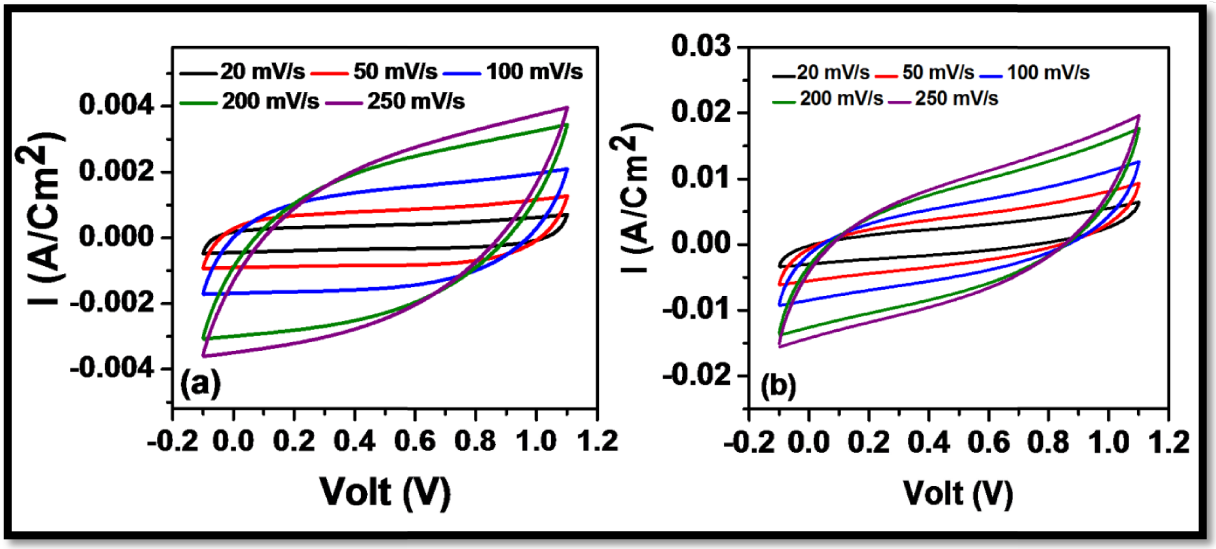

Fig. 7.14. (a) Cyclic voltammograms at different scan rates from 20 to 250 mV/s over the voltage range from –0.1 to +1.1 V for the cell constructed with (a) EL-1 and $CPL_{80}Gl_{15}$ SPE and (b) EL-2 and $CPL_{80}Gl_{15}$ SPE.

7.3.6.2. Galvanostatic charge-discharge studies

Galvanostatic charge-discharge (GCD) is an accurate technique for evaluating the applicability of the supercapacitor. In this method, the supercapacitor is charged and discharged at a constant current within a potential range of -0.6 V to +0.6 V. The GCD for the cell constructed with EL-1 and $CPL_{80}Gl_{15}$ SPE is performed at different current densities such as 100 μA/cm^2, 200 μA/cm^2 and 1 mA/cm^2 (Fig. 7.15a).

The specific capacitance (C_{sp}) and Coulombic efficiency (η) of the cell are calculated by GCD using equations as follows,

$$C_{sp} = \frac{2I}{\frac{\Delta V}{\Delta t} \times m} \tag{7.7}$$

$$\eta\ (\%) = \frac{t_d}{t_c} \times 100 \tag{7.8}$$

where, ΔV is the potential window (V), m is the mass of the active material per electrode (g), I is the charging current (A), Δt or t_d is the discharging time (s) and t_c is the charging time (s) [20]. The specific capacitance value (C_{sp}) for the cell constructed with EL-1 and $CPL_{80}Gl_{15}$ SPE at current densities of 100 μA/cm^2, 200 μA/cm^2 and 1 mA/cm^2 are 11.97 Fg^{-1}, 10.10 Fg^{-1} and 5.83 Fg^{-1}, respectively. Generally, the specific capacitance decreases with increase in current density due to the increase in IR drop across the electrodes. Furthermore, the coulumbic efficiency (η) increases with the increase in current density which comes around 95.34 %, 97.11 % and 97.22 % at the current densities of 100 μA/cm^2, 200 μA/cm^2 and 1 mA/cm^2, respectively. Figure 7.15b shows the GCD for the cell constructed with EL-2 and $CPL_{80}Gl_{15}$ SPE at current density of 1 mA/cm^2. The maximum apparent specific capacitance obtained is 125.31 Fg^{-1}. The specific capacitance of EL-2 at lower current density cannot be measured due to its high capacitance value as compared to EL-1.

The $MnCoFeO_4$ demonstrates much higher charging and discharging times at a current density of 1 mA/cm^2, indicating higher values of specific capacitance compared to that of AC electrodes (Figs. 7.15a and 7.15b). This is happened due to the nanoporous structure of the $MnCoFeO_4$ which allow the electrolyte ions to easily diffuse into the electrode nanopores and access their internal surface. Moreover, different redox states of the manganese play an important role in the significant enhancement of the specific capacitance of the $MnCoFeO_4$.

In the application point of view, energy density (E_D) and power density (P_D) are also important parameters for the evaluation of the electrochemical performance of the supercapacitors. E_D and P_D can be estimated from the relation [57] as follows,

$$E_D = \frac{1}{2}\left[\frac{C_{sp}\Delta V^2}{3.6}\right] \text{Wh/kg} \qquad (7.9)$$

$$P_D = \left[\frac{E_D}{t_d}\right] \times 3600 \text{ W/kg} \qquad (7.10)$$

Achievement of highest energy density 25.06 Whkg^{-1} at a power density 60.06 Wkg^{-1} of EL-2 as compared to highest energy density 2.39 Whkg^{-1} at a power density 12.26 Wkg^{-1} of EL-1, suggest that EL-2 / SPE system as promising combination for future hybrid supercapacitor.

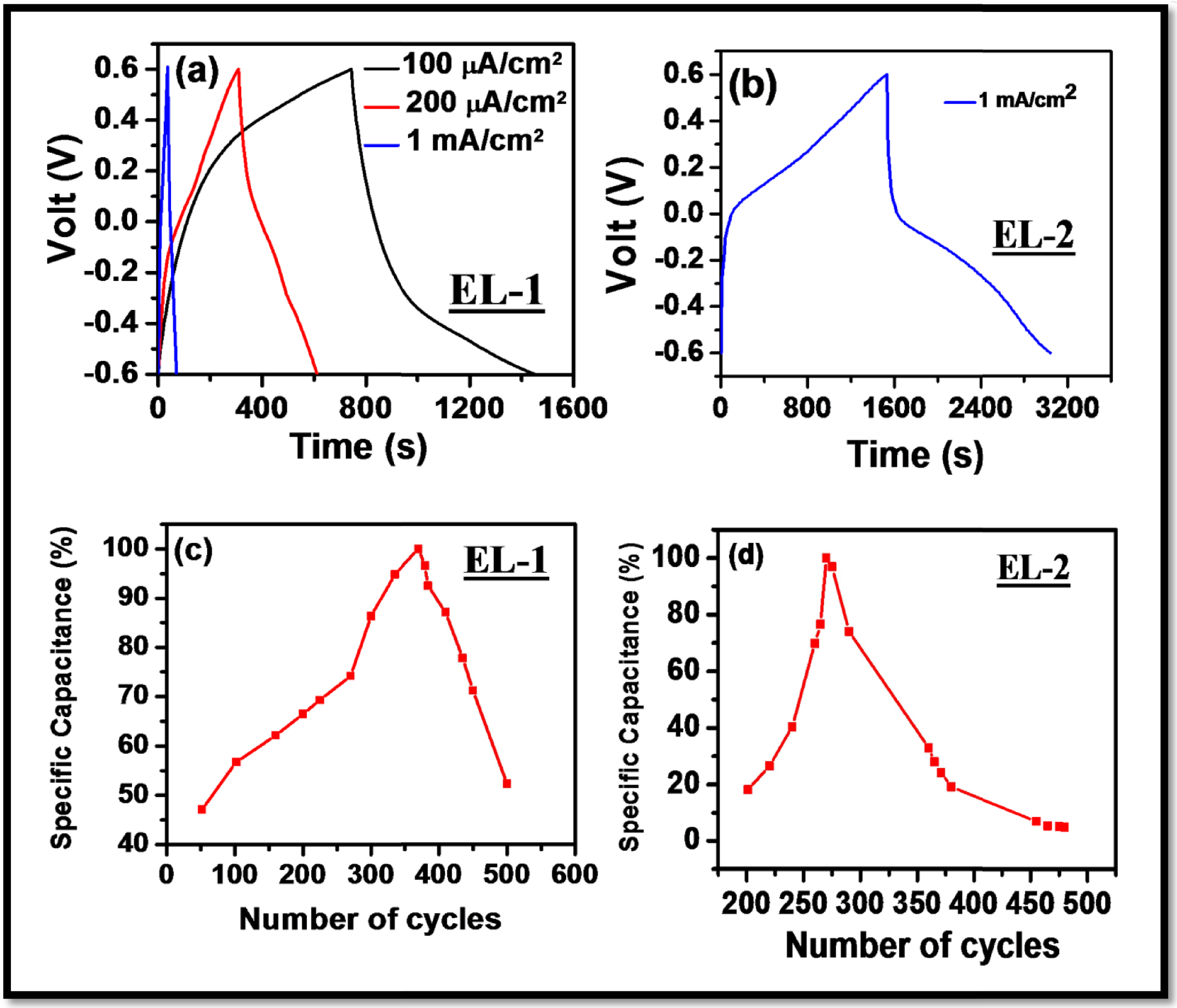

Fig. 7.15. Galvanostatic charge-discharge for the cell constructed with (a) EL-1 and CPL$_{80}$Gl$_{15}$ SPE and (b) EL-2 and CPL$_{80}$Gl$_{15}$ SPE. Cycling stability for the cell constructed with (c) EL-1 and CPL$_{80}$Gl$_{15}$ SPE and (d) EL-2 and CPL$_{80}$Gl$_{15}$ SPE.

Cycling stability is another important factor from the commercial point of view. Figure 7.15c shows the retention of the specific capacitance of the cell constructed with EL-1 as electrode material and $CPL_{80}Gl_{15}$ as SPE over 500 continuous GCD cycles at a current density of 200 μA/cm^2. It is quite interesting that the specific capacitance slowly increases up to 370 cycles and then starts to decrease, which is different from liquid electrolyte based supercapacitor where the specific capacitance remains constant over a period of long cycle with initial minor loss after few cycles. The slow kinetics of the ion in SPE may be responsible for the appearance of this type of peak in the cycle stability measurements (Fig. 7.15c). Figure 7.15d shows the retention of the specific capacitance of the cell constructed with EL-2 and $CPL_{80}Gl_{15}$ SPE at current density of 1 mA/cm^2 over 500 continuous GCD cycles. In this case, peak appears at lower number of the cycle (~ 270) indicating faster kinetics of ion movement between electrode and electrolyte essential for high performance supercapacitor.

7.3.6.3. Electrochemical impedance analysis

Electrochemical impedance spectroscopy (EIS) has been carried out to study the kinetics of the electrolyte ion responsible for charge accumulation. Figure 7.16a demonstrates the typical Nyquist plots for EL-1 and EL-2 with $CPL_{80}Gl_{15}$ as SPE, respectively over a low frequency range of 100 KHz – 10 mHz. The impedance spectra were analyzed using semi-quantitative fittings program supplied by the instrument (AUTOLAB-30) on the basis of the Randles equivalent circuit comprised of R_s, R_{ct}, W, C_{dl} and C_{FS} as shown in the inset of Fig. 7.16a. R_s represents the contact resistance between the current collector and electrode and that with the electrode and electrolyte. R_{ct} represents the charge transfer resistance and W represents the Warburg impedance. C_{dl} and C_{FS} represent the electric double layer capacitance and the pseudocapacitance which accounts for the faradaic reactions inside the electrode. The very low R_s and R_{ct} values reveal the intimate contact between electrode-electrolyte and better ion diffusion at the interfacial region of the electrode and electrolyte, respectively. The Warburg impedance (W) is related to the diffusion of ions in the electrode pores [58].

All the electrolyte ions in SPE are not diffusing completely inside the electrode materials, as happened in case of liquid electrolytes. Hence the effective specific capacitance of the electrode material cannot be determined based on total mass of the electrode materials.

Therefore, it is utmost important to know the approximate length of diffusion, which depends upon inter diffusion coefficient of the electrolyte ions (D_{inter}) between SPE and electrode. The inter diffusion coefficient (D_{inter}) of the lithium ions can be estimated using the following relation [59],

$$D_{inter} = \frac{R^2T^2}{2n^4F^4A^2C^2\sigma^2} \tag{7.11}$$

where, R is the gas constant (8.314 J mol^{-1} K^{-1}), T is absolute temperature, A is the electrode area (1 cm^2), n is the number of electrons transferred which is considered as 1 for EL-1 system, F is Faraday constant (96500 C mol^{-1}), C is lithium concentration and σ is the Warburg factor. The Warburg factor (σ) can be calculated based on the linear Randles relation [56],

$$Z_{re} = R_D + R_L + \sigma\omega^{-\frac{1}{2}} \tag{7.12}$$

The slope of the linear relationship between the real impedance (Z_{re}) and the inverse square root of frequency ω at low-frequency range (10 mHz to 20 mHz) gives the Warburg factor (σ) as shown in Fig. 7.16c. It is found that the value of σ which comes out as 107 for EL-1 system is decreased to 38 for EL-2 system. The lower value of Warburg factor in the EL-2 electrode is attributed to more mass transfer of ions in the porous electrode structure at lower frequencies, resulting high capacitance value of EL-2.

The inter diffusion coefficient, D_{inter} obtained for EL-1 electrodes is 8.74 × 10^{-17} m^2s^{-1}. The inter diffusion length of the electrolyte ions (L) within the electrodes can be determined using the following equation, in order to estimate the effective specific capacitance (C_E) of the electrode materials,

$$L = \sqrt{D_{inter} \,.\, t} \tag{7.13}$$

where, t is the time constant of the supercapacitor which is the reciprocal of the relaxation peak frequency. The relaxation peak frequency ~ 1.38 Hz was obtained for EL-1/SPE/EL-1 system from the variation of C_{im} with frequency (Fig. 7.16b). The reciprocal of this relaxation frequency gives the response time or time contant (t) of the system which comes out as 0.725 s for EL-1 electrode.

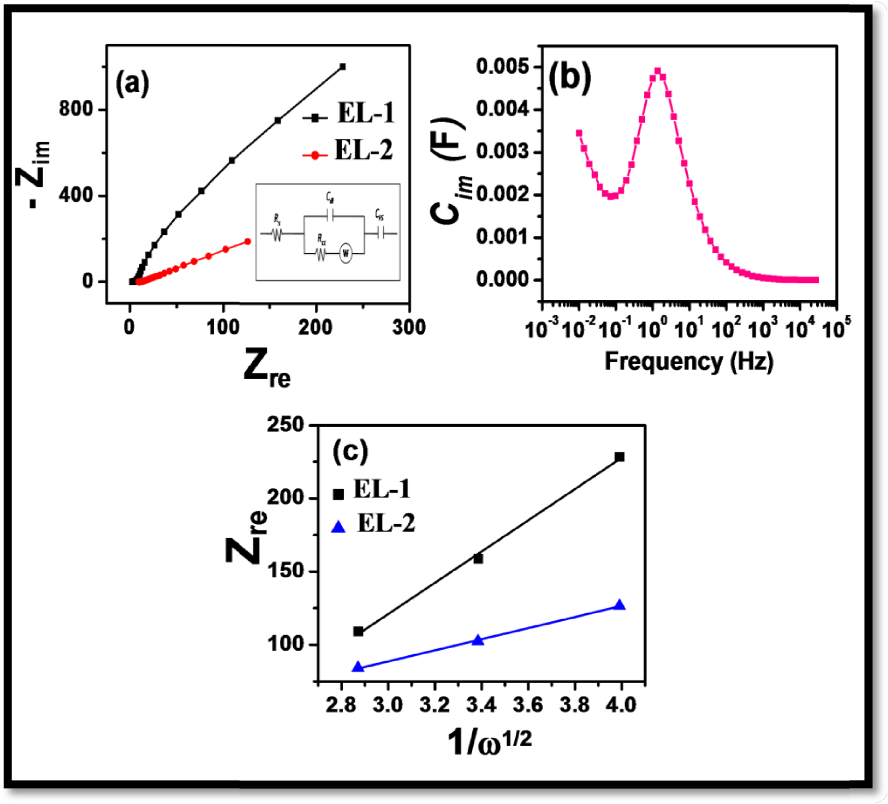

Fig. 7.16. (a) Nyquist plots for EL-1 and EL-2 with $CPL_{80}Gl_{15}$ as SPE, respectively over a low frequency range of 100 KHz – 10 mHz, the inset figure shows the Randles equivalent circuit used to analyze the impedance spectra, (b) the variation of C_{im} with frequency, (c) the variation of the real impedance (Z_{re}) and the inverse square root of frequency ω at low-frequency range (10 mHz to 20 mHz).

The diffusion length (L) has been obtained for EL-1 electrodes is ~ 8 nm. A realistic approach of maximum 10,000 diffusion length (i.e. 80 micron) inside the electrode material has been considered for the estimation of the effective specific capacitance (C_E) of the electrode with respect to solid polymer electrolyte, as the inter diffusion coefficient between electrode EL-1 and solid polymer electrolyte (D_{inter} ~ 8.74×10^{-17} m^2s^{-1}) is significantly less compared to that of intra diffusion coefficient within the electrolyte material (D_{intra} ~ 3.25×10^{-10} m^2s^{-1}). The effective specific capacitance (C_E) of $MnCoFeO_4$ has been achieved as high as ~ 750 Fg^{-1}, which can thus demand a suitable candidate for $CPL_{80}Gl_{15}$ SPE based solid state supercapacitor.

7.4. Conclusions

Solid biopolymer blend electrolytes (SPE) based on chitosan (CS) and polyvinylidene difluoride (PVDF) with $LiClO_4$ as a charge carriers and glycerol as a plasticizer are prepared using solution blending and evaporation casting technique. Optimization of salt and plasticizer helps to tune the ionic conductivity of the blended polymers from ~ 10^{-9} S/cm to ~ 10^{-2} S/cm at room temperature. The maximum ionic mobility of the charge carriers (1.27×10^{-8} m^2 V^{-1} s^{-1}) and their corresponding intra diffusion coefficient (3.29×10^{-10} m^2 s^{-1}) have been obtained in the blended $CPL_{80}Gl_{15}$ electrolyte. In the conduction mechanism, the role of amide dominates over amine as revealed from FTIR spectra. The increasing trend in imaginary electric modulus (M'') results in a non-ideal perturbed system responsible for multi frequency non-Debye type relaxation process. The dielectric constant is increased enormously (from ~ 10^3 to ~ 10^5) with increase in $LiClO_4$ concentration in the blended SPE system. The ion-diffusion processes inside the blended SPE system is entirely analyzed in light of anomalous fractional diffusion model. FTIR studies support the transport results obtained through this modeling approach. A solid-state supercapacitor is developed with manganese cobalt ferrite ($MnCoFeO_4$) as electrode material and CS/PVDF as solid polymer electrolyte. HRTEM reveals the size of $MnCoFeO_4$ nanoparticles (27-67 nm). The XRD results confirmed the spinel cubic structure of the fabricated $MnCoFeO_4$ nanoparticles. XPS analysis of $MnCoFeO_4$ reveals a partially inverse spinel structure as $[MnCo_{1-x}]_{Tet}[Co_xFe]_{Oct}O_{4-\delta}$. In order to evaluate the effective specific capacitance of the $MnCoFeO_4$ electrodes, an unique inter-diffusion model has been adopted. Significant enhancement of effective specific capacitance (750 Fg^{-1}) suggests that the $MnCoFeO_4$ electrode/$CPL_{80}Gl_{15}$ electrolyte system can be a promising candidate for future development of safe and cost effective electrochemical solid state supercapacitors.

Chapter 8

CNT assisted anomalous Li^+ transport in CS/CMC solid biopolymer nanocomposite: An electrolyte in hybrid solid-state supercapacitors

8.1. Introduction

Solid biopolymer electrolytes (SBE) are emerging class of materials for replacing liquid electrolytes in solid-state supercapacitors [1-3]. SBE materials are flexible and have the ability to improve the safety and stability of supercapacitors owing to their non-leakage and non-reactive characteristics. However, SBE suffers from poor conductivity at room temperature. To tackle these issues, several techniques have been attempted and one such is polymer blending through which overall crystallinity of the solid polymer electrolyte (SPE) can be usually reduced.[4]Chitosan (CS) and carboxymethyl cellulose (CMC) are two naturally abundant biopolymers whose complexation and miscibility are confirmed by several researchers [5-7], but their conductivities are very low. Incorporation of suitable plasticizers and ionic salts helps in tuning the conductivity of the blended host polymers. But the conductivity value of the solid polymer electrolyte is still low for their usage in energy-storage device applications. Incorporation of nanofillers in the solid polymer electrolytes has been emerging as a very useful technique for the significant enhancement of conductivity. The nanofiller incorporation creates disorder in the SPE and hence enhances the amorphous phase of the system which facilitates fast ion transport. Researchers have reported that the incorporation of various inorganic nanofillers (SiO_2, TiO_2, Al_2O_3) into the SPE enhances both the ionic conductivity and mechanical strength of the SPE films[8-10].Since the breakthrough invention of carbon nanotubes (CNT) in 1991, it has garnered much attention for their excellent electrical and mechanical properties[11].Thus among the different inorganic fillers, carbon nanotubes (CNT) has been considered as a promising nanofiller material in SPE due to their high aspect ratio, low electrical resistance and extremely high strength [12]. These outstanding properties of CNT encourages us to improve the performance of the blended CS/CMC SBE through the incorporation of carbon nanotube (CNT) filler and thus use it in solid-state supercapacitor. Spinel ferrites, $M\mathrm{Fe_2O_4}$ or $MM'\mathrm{FeO_4}$ (where M or M'= Mn, Ni, Zn, Co, etc.), are fascinating electrode materials for supercapacitors owing to their impressive electrical properties, good electrochemical stability andmultiple redox states which can enhance the specific capacitance [13,14]. Among various alternatives, $MnCoFeO_4$ has been chosen as the electrode material in the present investigation owing to its high specific capacitance and power density [1].

The present paper reports the effect of a conducting nanofiller CNT in the blended biodegradable polymer system by optimizing the nanofiller concentration for the better performance of the solid electrolyte. The ionic conductivity, dynamics and relaxation in solid biopolymer blend CS/CMC electrolytes incorporated with CNT nanofiller has been studied in details. The morphology of the solid nanocomposite electrolytes are investigated from FE-SEM images. Transference number measurement has been done in order to estimate the contribution towards the conductivity due to the movement of the ionic species inside the CNT incorporated solid nanocomposite electrolyte. The ion diffusion processes in the nanocomposite solid electrolytes has been analyzed in light of anomalous fractional diffusion model. The interactions between the host biopolymer and the dopant in the nanocomposite were studied by FTIR spectroscopy. Finally, a hybrid solid-state symmetric supercapacitor has been fabricated with active carbon along with manganese cobalt ferrite ($MnCoFeO_4$) nanoparticles as electrode materials and carbon nanotube (CNT) incorporated CS/CMC blended solid biopolymer nanocomposite as electrolytes. A fairly good effective specific capacitance (C_E~ $94 Fg^{-1}$) has been reported.

8.2. Experimental

8.2.1. Material synthesis

8.2.1.1. Synthesis of CS/CMC blend solid biopolymer electrolytes (SBE)

Chitosan/Carboxymethyl Cellulose (CS/CMC) are blended in the ratio of 90:10.Chitosan (CS) and Carboxymethyl Cellulose (CMC) were dissolved individually in 50 ml of 1% aqueous acetic acid solutions and stirred respectively at 50℃ and 70℃ for 20 minutes. CS/CMC blend solutions were prepared by adding the CMC solution dropwise in CS solution followed by stirring for 10 minutes at room temperature. Then different weight percentages of glycerol (15-60 wt. %) as a plasticizer and $LiClO_4$ (80 wt. %) as an ionic salt were added in the CS/CMC blend solutions and stirred continuously until a homogenous viscous solution was obtained. Finally, the homogenous solutions were cast separately on polypropylene petri dishes and allowed to dry in a vacuum oven at 40℃.

8.2.1.2. Synthesis of CNT@CS/CMC solid biopolymer nanocomposite electrolytes (SBNE)

Various weight percentages of carbon nanotubes, CNT (0.25, 0.50, 1.00 wt. %) were dispersed individually in 50 ml of 1% aqueous acetic acid solutions and probe sonicated in an ultrasonic processor UP400S (400 Watts, Hielscher) for about 2.5 hours. Then CS is added in the sonicated CNT solution, followed by stirring and heating at 50 ℃ for 20 minutes. CMC solution obtained by dissolving in 50 ml of 1% aqueous acetic acid solution followed by continuous stirring and heating at 70℃is added dropwise in the CS/CNT solution. Then 80 wt. % $LiClO_4$ and 30 wt. % glycerol were added in the CS/CMC/CNT blended solutions and stirred continuously until a homogenous viscous solution was obtained. Finally, the resulting homogenous solutions were cast on polypropylene petri dishes and allowed to dry in a vacuum oven at 40℃ to form free-standing thin films.

8.2.2. Development of the symmetric hybrid supercapacitor

The electrodes of the symmetric supercapacitor were fabricated by using a paste of a homogeneous mixture made of $MnCoFeO_4$ nanoparticles (synthesis, XRD and XPS characterizations of $MnCoFeO_4$ nanoparticles are reported elsewhere [1] by Majumdar *et al*), acetylene black (AB) and polytetrafluoroethylene (PTFE) taken in the wt. % ratio of 50:45:5. The paste was then compacted into a thin sheet using mortar and pestle and compressed on a stainless steel mesh having the surface area of 1 cm^2. The prepared electrode was heated at 60℃ for 6 h under vacuum to evaporate the solvent completely. The total weight of the active material in the electrode is usually ~20 mg.

8.2.3. Characterization

Conductivity and dielectric studies of the solid nanocomposite electrolyte materials were carried out using computer interfaced impedance analyzer (Solartron SI 1260 Impedance Analyzer) in the frequency range between 40 Hz and 100 KHz at 300 K by sandwiching the material between two gold electrodes. Ionic interactions with the biopolymers were studied by Fourier transform infrared (FTIR) spectroscopy which was performed using Perkin Elmer FT-IR Spectrum 2 spectrometer having resolution of 4 cm^{-1}. The surface morphology of the solid electrolytes were characterized by field emission scanning electron microscopy (FE-SEM) (model: JSM-7610F, JEOL). Total ionic transference number of the CNT@CS/CMC SBNE material was measured by dc polarization method using Keithley 2450 source meter. The leakage current characteristics of the capacitor cell(Gold Electrode | CNT@CS/CMC SBNE | Gold Electrode) were measured with Keithley 2450 source meter at 300 K. Electrochemical behavior of the developed hybrid supercapacitor was investigated with AUTOLAB-30 potentiostat/galvanostat.

8.3. Results and Discussion

8.3.1. Field Emission Scanning Electron Microscopy (FE-SEM)

The surface morphology of CNT-free and CNT-incorporated CS/CMC blended solid biopolymer electrolytes are investigated from FE-SEM micrographs and are shown in Figs. 8.1a and 8.1b, respectively. It is evident from the FE-SEM images that the morphology of the blended CS/CMC biopolymer matrix is significantly affected by the incorporation of CNT. The FE-SEM micrograph image reveals that the carbon nanotubes (CNT) are finely distributed and embedded within the CS/CMC blended biopolymer matrix (Fig. 8.1b).

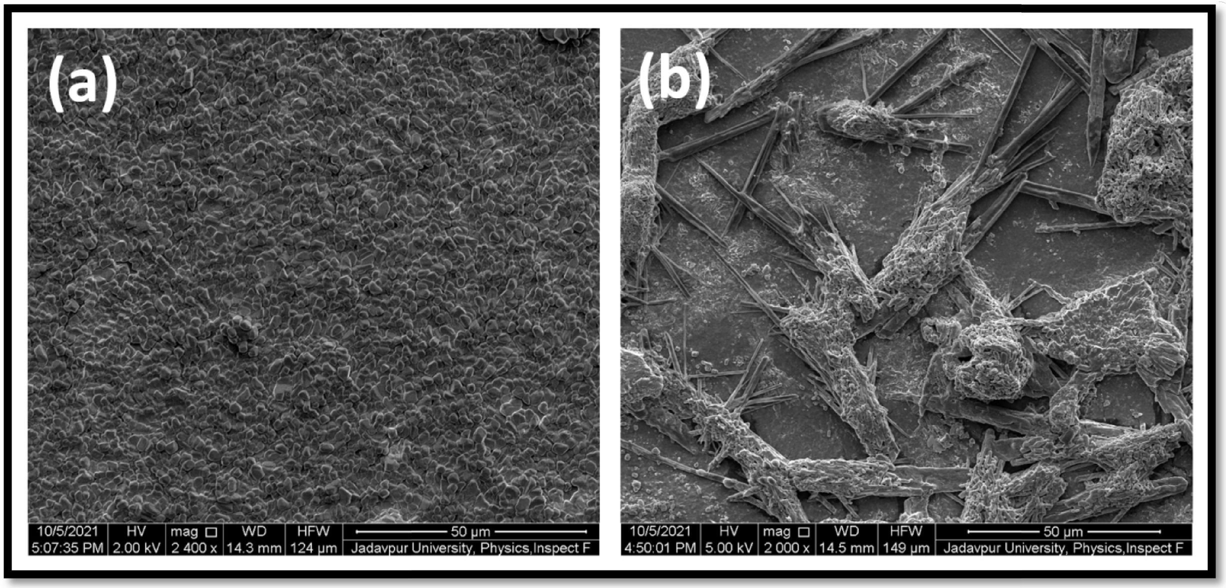

Fig. 8.1. FE-SEM images of (a) CNT-free and (b) CNT-incorporated CS/CMC blended solid biopolymer electrolytes.

8.3.2. Transference number

Ionic transference number is a crucial parameter for solid nanocomposite electrolytes since it gives estimation of the fraction of conductivity due to the movement of the ionic species inside the solid electrolytes. Total ionic transference number of the CNT-incorporated CS/CMC blended solid biopolymer nanocomposite electrolyte (CNT@CS/CMC SBNE) has been measured by DC polarization method. A fixed DC voltage (1 V) was applied to the material and the current was measured as a function of time. The normalized polarization current against time for CNT@CS/CMC SBNE material is shown in Fig. 8.2a. It is observed that the DC current decreases with time and becomes almost constant as polarization develops. The ionic transference number can be calculated from the polarization graph using the following equation:

$$t_{ion} = \frac{I_{initial} - I_{final}}{I_{initial}} \tag{8.1}$$

The calculated ionic transference number in CNT@CS/CMC SBNE material is 0.95 which indicates predominant ionic conduction in the CNT-incorporated solid biopolymer nanocomposite electrolytes.

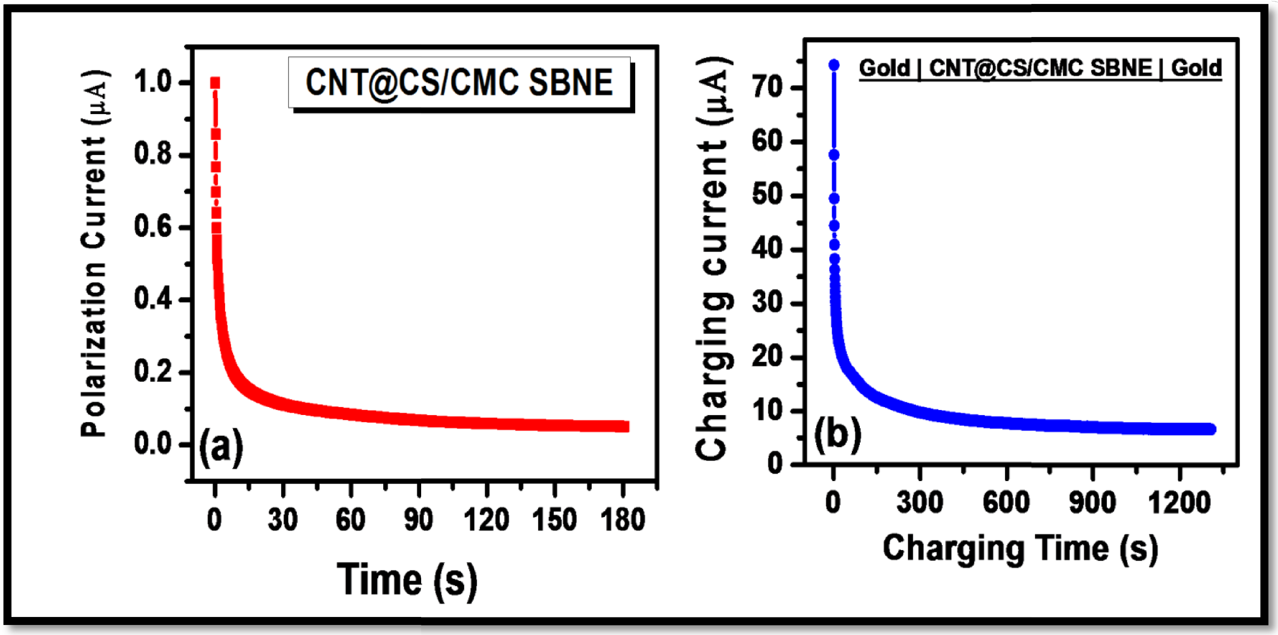

Fig. 8.2. (a) Normalized polarization current versus time for CNT@CS/CMC SBNE material,(b) Leakage current characteristics of "Gold | CNT@CS/CMC SBNE | Gold" cell at 300 K.

8.3.3. Leakage current

The dielectric material generally used between two conducting plates of a capacitor is an imperfect insulator that allows a very small amount of current leaking through it. The DC leakage current refers to this small current that flows between the two conducting plates when a fixed dc voltage is applied and it depends on the characteristics of the dielectric material. The value of this leakage current is dependent on the charging period. A fixed DC voltage (1 V) is applied across "Gold | CNT@CS/CMC SBNE | Gold" cell at 300 K and the leakage current characteristics of the cell is shown in Fig. 8.2b.The maximum current is ~ 74 µA at the instant when dc voltage is just applied. This charging current drops and becomes nearly constant and stable over time (as shown in Fig. 8.2b). This stable current is called the leakage currentwhich is found to be quite small (~ 6 µA) for the cell under study and this makes it attractive for energy storage applications.

8.3.4. Impedance spectroscopy

8.3.4.1. Ionic conductivity studies

Figure 8.3a represents the Nyquist plots for different plasticizer (glycerol) concentrations in CS/CMC blended SBE ($CML_{80}Gl_y$, where y = 0, 15, 30, 45 and 60 wt. percentages of the blended biopolymers) at 300 K. The DC ionic conductivity (σ_{DC}) of the blended SBE is calculated based on the relation, $\sigma_{DC} = L/R_bA$ where, L is the thickness of the SBE, A is the effective contact area of the electrode and SBE interface and R_b is the bulk resistance of the SBE which has been determined from the equivalent circuit fitting [1] as shown in the inset of Fig. 8.4a.The ionic conductivity (σ_{DC}) of different $CML_{80}Gl_y$are shown in Fig. 4b where,σ_{DC} of the blended SBE has been increased by an order of magnitude (from ~ 10^{-5} to ~ 5.7×10^{-4} S/cm) due to the incorporation of glycerol (Fig. 8.4b) in the $CML_{80}Gl_y$ (with y = 30).This enhancement of the conductivity of SBE suggests that the dissociation of the salt is favored in the presence of optimum value (y = 30) of glycerol in the blended biopolymer matrix. Further increment in glycerol content beyond y= 30 lowers the conductivity which may be attributed to the recrystallization of salt.

To enhance the conductivity of the electrolyte more, which is essential for the fabrication of high performance solid-state supercapacitor, CNT, a conducting nanofiller has been incorporated in the matrix of $CML_{80}Gl_{30}$ in different volume fraction. The resultant products are denoted as $CML_{80}Gl_{30}CNT_z$,where z = 0.25, 0.50 and 1.00 wt. percentages of the blended biopolymers. The Nyquist plots of $CML_{80}Gl_{30}CNT_z$ ($0.25 \le z \le 1.00$) blended solid biopolymer nanocomposite electrolytes (SBNE) are shown in Fig. 8.3b at 300 K. The equivalent circuit used for fitting of the Nyquist plot of $CML_{80}Gl_{30}CNT_{1.00}$ SBNE is shown in Fig. 8.4a.The variation of σ_{DC} as a function of CNT content in the blended SBNE is shown in Fig. 8.4c. The ionic conductivity is found to be increased by an order in magnitude (from ~ 10^{-4} to~ 3 × 10^{-3} S/cm) on addition of CNT in the $CML_{80}Gl_{30}$. It is observed that σ_{DC} is almost independent of CNT content beyond z = 0.25 in the blended SBNE. The Li^+ ions exhibit strong affinity to the electron cloud at the outer surface of CNT, which subsequently favors the dissociation of $LiClO_4$ [12]. Moreover, the large aspect ratio of CNT increases the amorphous phase by preventing the recrystallization of the blended biopolymer chains. As a result, more free volume is obtained which facilitates the faster migration of Li^+ ion through the least resistant pathways in the blended SBNE.

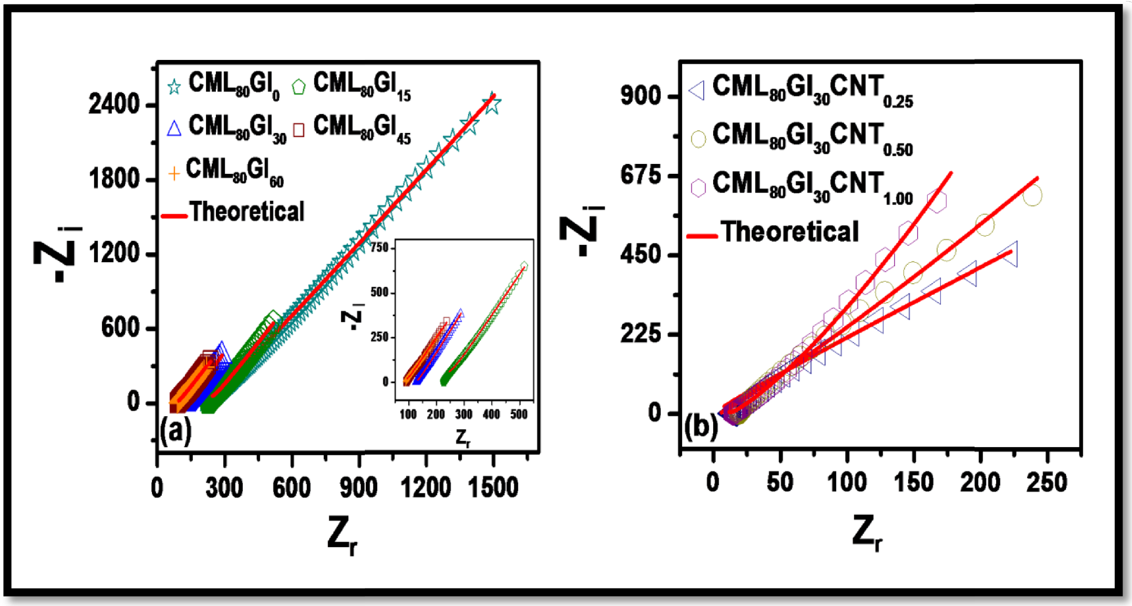

Fig. 8.3. Nyquist plots at 300 K for (a) $CML_{80}Gl_y$($0 \le y \le 60$) and (b) $CML_{80}Gl_{30}CNT_z$($0.25 \le z \le 1.00$) blended solid biopolymer electrolyte materials. The solid lines in (a) and (b) represent the modeled plots based on fractional diffusion model (Eq. 8.2) for the blended solid polymer electrolytes.

8.3.4.2. Fractional diffusion analysis

The mechanism of ion diffusion inside the non-crystalline solid biopolymer electrolytes is very similar to that of liquid electrolytes. The intra diffusion processes of the mobile ions in $CML_{80}Gl_y$ ($0 \le y \le 60$) and $CML_{80}Gl_{30}CNT_z$ ($0.25 \le z \le 1.00$) blended solid electrolytes are investigated based on a fractional calculus approach since the conductivity of the materials are dependent on the intra diffusion rate of the mobile charge carriers within the blended CS/CMC solid biopolymer electrolyte matrix. Solid polymer electrolytes exhibit fractal morphology in both macroscopic and microscopic scales [15]. Contribution of the anomalous diffusion has been thus taken into account since the ions are moving in a highly disordered fractal-like space. Fractional calculus approach has been adopted in order to model this anomalous diffusion inside the solid electrolytes. The impedance results are thus analyzed on the basis of a model as suggested by Lenzi *et al* [16]. Here, in order to examine the ion conduction mechanism through the solid biopolymer electrolyte, the contribution of anomalous diffusion has been introduced through a fractional order parameter ‘γ’as,

$$Z = \frac{2}{i\mathrm{A}\omega\boldsymbol{\varepsilon}_{\mathbf{r}}\boldsymbol{\varepsilon}_{\mathbf{0}}\beta^2}\left[\frac{1}{\beta\lambda_D^2}\tanh\left(\frac{\beta\mathrm{L}}{2}\right) + h\frac{(i\omega)^{\gamma}\mathrm{L}}{2\mathrm{D}_{\gamma}} + (1-h)\frac{i\omega}{2\mathrm{D}}\right] \tag{8.2}$$

where,D_γ and D are the anomalous and normal diffusion coefficients, respectively, h is the fraction of anomalous diffusion, $(1-h)$is the fraction of normal diffusion, $\boldsymbol{\varepsilon}_{\mathbf{r}}$ is the dielectric constant of the SBNE material,λ_D is the Debye screening length, L is the thickness of the solid electrolyte, A is the effective contact area of the electrode and the solid electrolyte surface, $\beta = \sqrt{\frac{1}{{\lambda_D}^2} + h\frac{(i\omega)^{\gamma}}{\mathrm{D}_{\gamma}} + (1-h)\frac{i\omega}{\mathrm{D}}}$is the characteristic exponent of the model.

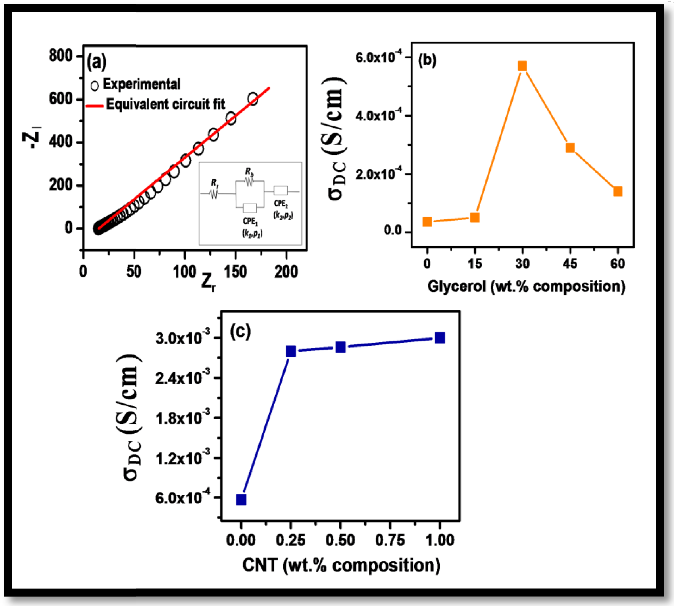

Fig. 8.4. (a) Nyquist plot for $\mathrm{CML}_{80}\mathrm{Gl}_{30}\mathrm{CNT}_{1.00}$ SBNE and its corresponding equivalent circuit (inset figure) fitting represented by solid lines, DC conductivity (σ_{DC}) shown as a function of (b) glycerol and (c) CNT concentrations at room temperature.

The best fit of the Nyquist plots based on this fractional diffusion model as given by Eq. (8.2) are illustrated in Figs. 8.3a and 8.3b for $CML_{80}Gl_y$ ($0 \leq y \leq 60$) and $CML_{80}Gl_{30}CNT_z$($0.25 \leq z \leq 1.00$), respectively. The best fit parameters are listed in Table 8.1.

Table 8.1. Best fit model parameters i.e. normal diffusion coefficient (D), anomalous diffusion coefficient (D_γ), fraction of anomalous diffusion (*h*), Debye screening length (λ_D) and anomalous diffusion fractional order parameter 'γ', to analyze diffusion processes in $CML_{80}Gl_y$($0 \leq y \leq 60$) and $CML_{80}Gl_{30}CNT_z$ ($0.25 \leq z \leq 1.00$) blended solid biopolymer electrolyte materials.

Solid biopolymer electrolytes	D ($\times 10^{-9}$ m^2s^{-1})	D_γ($\times 10^{-10}$ m^2s^{-1})	γ	*h*	λ_D (μm)
$CML_{80}Gl_0$	0.06	0.0011	0.31	0.89	0.010
$CML_{80}Gl_{15}$	1.13	0.013	0.287	0.89	0.0175
$CML_{80}Gl_{30}$	2.60	0.07	0.27	0.89	0.024
$CML_{80}Gl_{45}$	1.45	0.02	0.28	0.89	0.0175
$CML_{80}Gl_{60}$	1.35	0.015	0.285	0.89	0.0175
$CML_{80}Gl_{30}CNT_{0.25}$	240	0.10	0.33	0.90	0.23
$CML_{80}Gl_{30}CNT_{0.50}$	520	1.80	0.29	0.91	0.30
$CML_{80}Gl_{30}CNT_{1.00}$	800	20.1	0.34	0.89	0.90

The modeling results suggest that the relative contribution of anomalous diffusion (*h*) in the blended CS/CMC biopolymer electrolyte material is much higher compared to that of normal diffusion since the value of $h \sim 0.89$. Moreover, the value of γ changes from 0.36 to 0.27 for different *y* and *z* values studied. Thus, anomalous intra diffusive behavior predominates in the blended CS/CMC materials irrespective of dopant (viz. plasticizer and nanofiller) concentrations and is successfully modeled through this fractional calculus approach. This is mainly due to the fractal structure of the biopolymers. The anomalous intra diffusion coefficient (D_γ) is found to be increased by two orders in magnitude (from ~ 10^{-12} to ~ 10^{-10} m^2/s) on the incorporation of CNT in $CML_{80}Gl_{30}CNT_z$. The solid nanocomposite electrolyte, $CML_{80}Gl_{30}CNT_{1.00}$ possesses the highest D_γ (20.1×10^{-10} m^2/s) and λ_D (0.90 μm) that infers the highest conductivity (σ_{DC}), which is in accordance with the impedance results.

8.3.4.3. AC Conductivity and scaling

The frequency dependence of the conductivity are studied in order to explore the ion dynamics in $CML_{80}Gl_y$ ($0 \leq y \leq 60$) and $CML_{80}Gl_{30}CNT_z$ ($0.25 \leq z \leq 1.00$) blended solid biopolymer electrolyte materials. The AC conductivity is calculated following relation, $\sigma(\omega) = \omega\varepsilon_0\varepsilon_{im}$ where, ε_0 is the vacuum permittivity (8.854×10^{-14} F/cm) and ε_{im} is the dielectric loss. Figures 8.5a and 8.5b represent the frequency dependent AC conductivity spectra at 300 K for $CML_{80}Gl_y$ ($0 \leq y \leq 60$) and $CML_{80}Gl_{30}CNT_z$ ($0 \leq z \leq 1.00$), respectively.It is observed that the AC conductivity spectra for all the samples show a dispersive region at lower frequencies which is due to the accumulation of charge carriers at the electrode-electrolyte interface followed by an almost frequency independent plateau region corresponding to the DC conductivity. The frequency dependent complex AC conductivity has been analyzed considering the fractal nature of the electrode-electrolyte interface which is given as [17,18],

$$\sigma(\omega) = \sigma_0 + \frac{\sigma_{DC} - \sigma_0}{1 + (i\omega\tau_j)^{-\alpha}} + i\omega\ {}_0[\varepsilon_{relax}(\omega) - \varepsilon_\infty] \quad (8.3)$$

where, σ_{DC} is the DC conductivity of the electrolyte material, σ_0 is the conductivity at constant electric field, ε_0 is the vacuum permittivity (8.854×10^{-14} F/cm), $\varepsilon_{relax}(\omega)$ determines the contribution of the dielectric relaxation part, ε_∞ is the high frequency limiting value of dielectric permittivity, τ_j is the characteristic relaxation time and α is a constant determining the fractal dimension of the space-time ensemble in the space-charge region having its value lies between 0 and 1. The real part of the frequency dependent AC conductivity spectra for $CML_{80}Gl_y$ ($0 \leq y \leq 60$) and $CML_{80}Gl_{30}CNT_z$ ($0 \leq z \leq 1.00$) solid biopolymer electrolyte materials are fitted using Eq. 8.3 and are shown in Figs. 8.5a and 8.5b, respectively. The best fit parameters are tabulated in Table 8.2. It is to note here that the values of σ_{DC} and σ_0 does not coincide due to the effects of electrode polarization and the value of σ_0 is much less than the value of σ_{DC}.The values of α are less than unity, indicating the fractal dimension of the electrode-electrolyte interface. It is to note here that the relaxation time (τ_j) corresponding to the highest conducting sample, $\mathrm{CML_{80}Gl_{30}CNT_{1.00}}$ is the lowest (~ 3.8×10^{-5} s).

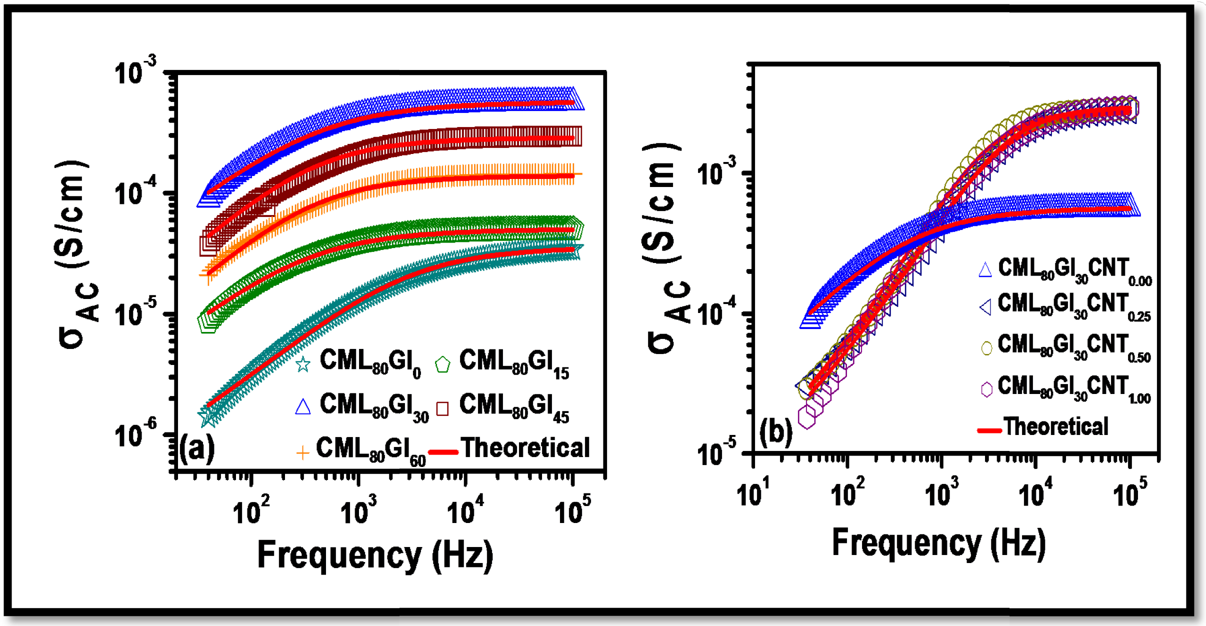

Fig. 8.5. (a) AC conductivity spectra for (a) $\mathrm{CML_{80}Gl}_y(0 \le y \le 60)$and (b) $\mathrm{CML_{80}Gl_{30}CNT}_z(0\le z \le 1.00)$ blended solid biopolymer electrolyte materials. Solid lines are the fits of the experimental data to Eq. 8.3.

In order to understand the composition induced charge carrier relaxation dynamics, the scaling behavior of the AC conductivity spectra has been studied systematically. The AC conductivity has been scaled by the DC ionic conductivity (σ_{DC}) and the ion-hopping frequency (ω_p) with an appropriate choice for the scaling factor [19,20], $\omega_p = \frac{\sigma_{\mathrm{DC}}}{\varepsilon_0 \Delta\varepsilon_r}$ where, $\Delta\varepsilon_r = [\varepsilon_r(\omega \to 0) - \varepsilon_r(\omega \to \infty)]$ which is exclusively dependent on the hopping motion of the mobile charge carriers. This leads to the following scaling law for the real part of the AC conductivity [19],

$$\frac{\sigma(\omega)}{\sigma_{\mathrm{DC}}} = F\left(\frac{\omega}{\omega_p}\right) \tag{8.4}$$

Figures 8.6a and 8.6b show the scaled AC conductivity curve for $\mathrm{CML_{80}Gl}_y$ $(15 \le y \le 60)$ and $\mathrm{CML_{80}Gl_{30}CNT}_z$ $(0.25 \le z \le 1.00)$, respectively, at 300 K using Eq. 8.4. It is observed that the scaled AC conductivity results of $CML_{80}Gl_y$ ($15 \leq y \leq 60$) and $CML_{80}Gl_{30}CNT_z$($0.25 \leq z \leq 1.00$) follow a common master curve which are independent of glycerol and CNT contents, as shown in Figs. 8.6a and 8.6b, respectively. Therefore, the relaxation dynamics of charge carriers can be characterized by a universal function which is independent of dopant compositions, i.e. incorporation of different concentrations of glycerol or CNT in the blended biopolymer matrix affects only the intra diffusion rate and/or number density of free mobile ions without influencing the conduction mechanism. On the other hand, Fig. 8.6c clearly illustrates that the conductivity data of $CML_{80}Gl_0$, $CML_{80}Gl_{30}$ and $CML_{80}Gl_{30}CNT_{1.00}$ cannot be scaled on a common master curve. This infers that the charge carrier relaxation dynamics is dependent on the nature of dopants i.e. $LiClO_4$ (salt), glycerol (plasticizer) and CNT (nanofiller) in the blended CS/CMC solid biopolymer electrolytes.

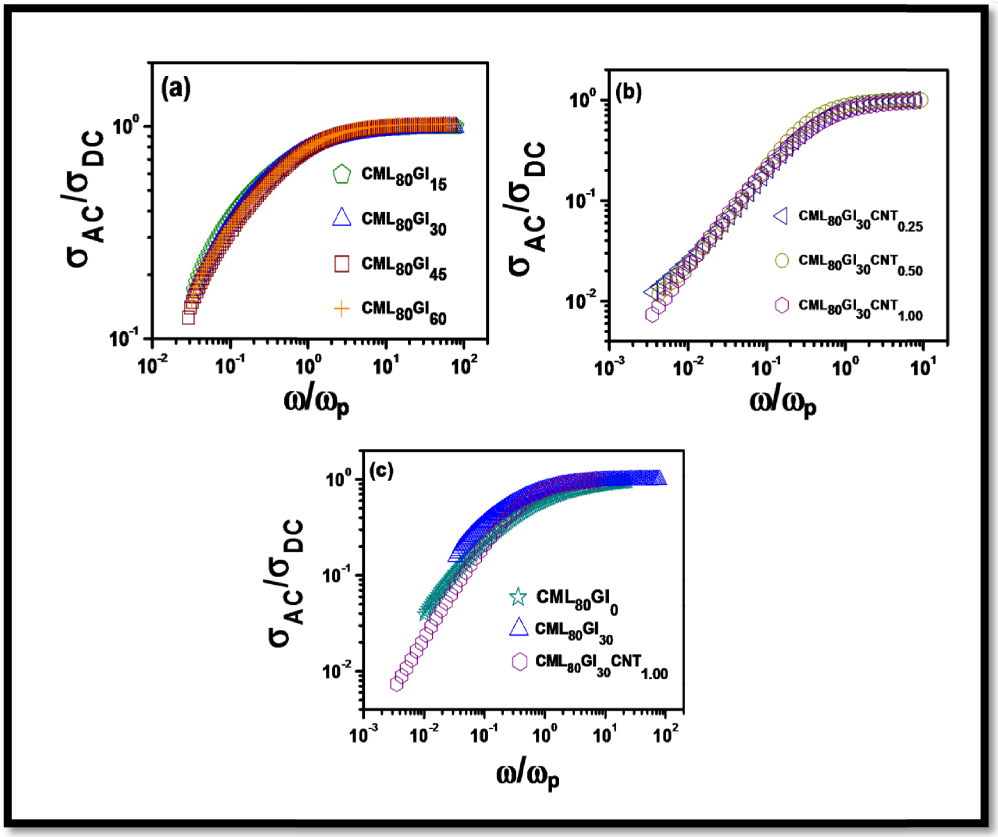

Fig. 8.6. Scaling behavior of AC conductivity spectra for (a) $CML_{80}Gl_y$($15 \leq y \leq 60$) and (b) $CML_{80}Gl_{30}CNT_z$($0.25 \leq z \leq 1.00$) blended solid biopolymer electrolyte materials, (d) Scaling of conductivity spectra for different dopants in the blended electrolytes.

8.3.4.4. Dielectric permittivity and scaling

The dielectric relaxation is studied in terms of frequency dependent complex dielectric permittivity (ε^*) given by, $\varepsilon^*(\omega) = \varepsilon_r(\omega) - j\varepsilon_i(\omega)$ where, ε_r and ε_i are the real and imaginary parts of the complex dielectric permittivity known as dielectric constant and dielectric loss, respectively. The frequency dependence of the dielectric constant for $CML_{80}Gl_y$ ($0 \leq y \leq 60$) and $CML_{80}Gl_{30}CNT_z$ ($0.25 \leq z \leq 1.00$) at 300 K are shown in Figs. 8.7a and 8.7b, respectively. Significant dispersion is visible in the low frequency region which arises due to the effects of electrode polarization (EP). The dielectric constant (ε_r) exhibits a leveling-off at high frequencies due to the effects of ionic and electronic polarization processes. Insets of Figs. 8.7a and 8.7b represent the variations of dielectric constant (ε_r) measured at 100 KHzas a function of glycerol and CNT contents in $CML_{80}Gl_y$ ($15 \leq y \leq 60$) and $CML_{80}Gl_{30}CNT_z$ ($0.25 \leq z \leq 1.00$), respectively. It is observed that the trend of dielectric constant variation is somewhat similar to that of DC conductivity. A maximum value of $\varepsilon_r \sim 4259$ is obtained for $CML_{80}Gl_{30}CNT_{1.00}$ SBNE material which is almost 28 times enhanced compared to that of the CNT free system (i.e. $CML_{80}Gl_{30}$) and 68 times enhanced compared to that of the plasticizer free system (i.e. $CML_{80}\ Gl_0$) as illustrated in Fig. 8.7c.

The scaling behavior of the real part of complex permittivity i.e. dielectric constant has been studied in order to gain an insight into the dopant composition dependence of the ion dynamics. The scaling of the dielectric constant has been done as suggested by Sidebottom *et al* [19,20] which is given as,

$$\frac{\varepsilon_r(\omega) - \varepsilon_r(\omega \to \infty)}{\Delta\varepsilon_r} = G\left(\frac{\omega}{\omega_p}\right) \tag{8.5}$$

where, $\Delta\varepsilon_r = [\varepsilon_r(\omega \to 0) - \varepsilon_r(\omega \to \infty)]$ is a direct consequence of the relaxation of hopping charge carriers and $\omega_p = \frac{\sigma_{DC}}{\varepsilon_0 \Delta\varepsilon_r}$ is the scaling factor. It is important to note here that $\varepsilon_r(\omega \to \infty)$ is not directly related to the hopping dynamics of the mobile ions [19]. Figures 8.8a and 8.8b represent the scaled dielectric constant curve for $CML_{80}Gl_y$ ($15 \leq y \leq 60$) and $CML_{80}Gl_{30}CNT_z$ ($0.25 \leq z \leq 1.00$), respectively at 300 K according to Eq. 8.5. It is observed that the dielectric constant corresponding to $CML_{80}Gl_y$ ($15 \leq y \leq 60$) and $CML_{80}Gl_{30}CNT_z$ ($0.25 \leq z \leq 1.00$) superpose on two different master curves respectively after scaling. On the contrary, the dielectric constant spectra of $CML_{80}Gl_0$, $CML_{80}Gl_{30}$ and $CML_{80}Gl_{30}CNT_{1.00}$, a representative member of each family, cannot be scaled on a single master curve as illustrated in Fig. 8.8c. This suggests that the relaxation phenomenon depends on the nature of dopants [i.e. $LiClO_4$ (salt), glycerol (plasticizer) and CNT (nanofiller)] in these blended CS/CMC solid biopolymer electrolytes.

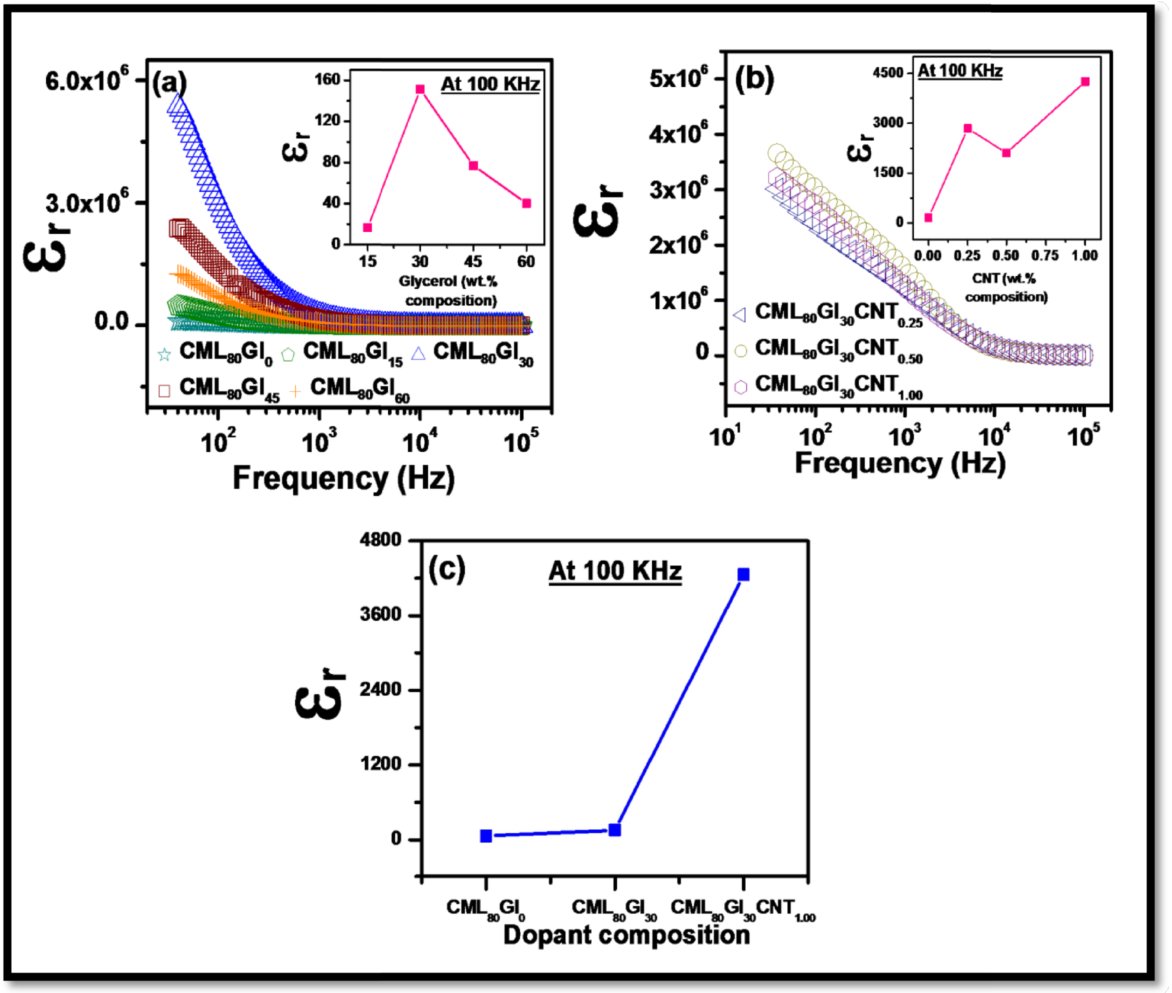

Fig. 8.7. Frequency dependence of dielectric constant (ε_r) for (a) $CML_{80}Gl_y$ ($0 \leq y \leq 60$) and (b) $CML_{80}Gl_{30}CNT_z$ ($0.25 \leq z \leq 1.00$) blended solid biopolymer electrolyte materials. Insets of (a) and (b) show the variation of ε_r as a function of glycerol and CNT concentrations, respectively at 100 KHz. (c) Variation of ε_r for $CML_{80}Gl_0$, $CML_{80}Gl_{30}$ and $CML_{80}Gl_{30}CNT_{1.00}$ solid electrolytes at 100 KHz.

Study of the dielectric relaxation over a broad frequency range is useful for the investigation of dipole relaxations in the material. The loss tangent or the loss factor (tan δ) is defined as the ratio of energy loss to energy stored ($\varepsilon_i/\varepsilon_r$) in an applied AC electric field. The frequency dependence of the loss tangent appears maximum at a certain frequency (ω_{peak}) corresponding to the characteristic dielectric relaxation time (τ), satisfying the equation, $\omega_{peak}\tau = 1$. Figures 8.9a and 8.9b show the variation of tan δ at 300 K, with frequency for $CML_{80}Gl_y$ ($0 \leq y \leq 60$) and $CML_{80}Gl_{30}CNT_z$ ($0 \leq z \leq 1.00$) blended solid biopolymer electrolyte, respectively. No significant relaxation peak is observed in the frequency range of investigation for all the blended CS/CMC solid biopolymer electrolytes. It is worthwhile to point out that the loss factor is significantly reduced on CNT incorporation in the blended CS/CMC SBNE material as demonstrated in the inset of Fig. 8.9b along with significant enhancement in dielectric constant, making them potential candidates for electrochemical device applications.

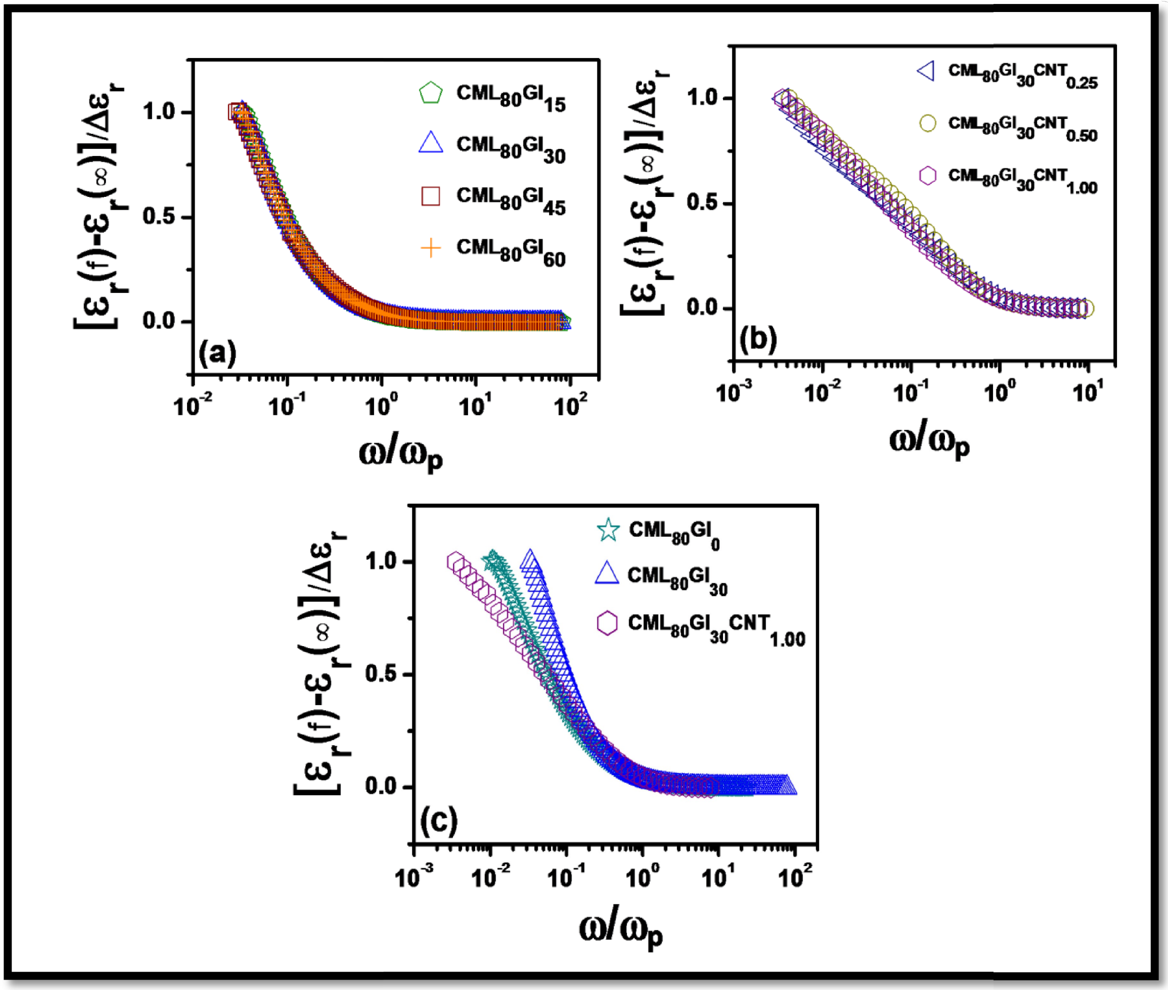

Fig. 8.8. Scaling behavior of the real part of complex permittivity spectra for (a) $CML_{80}Gl_y$($15 \leq y \leq 60$) and (b) $CML_{80}Gl_{30}CNT_z$($0.25 \leq z \leq 1.00$) blended solid biopolymer electrolyte materials, (c) Scaling of conductivity spectra for different dopants in the blended electrolytes.

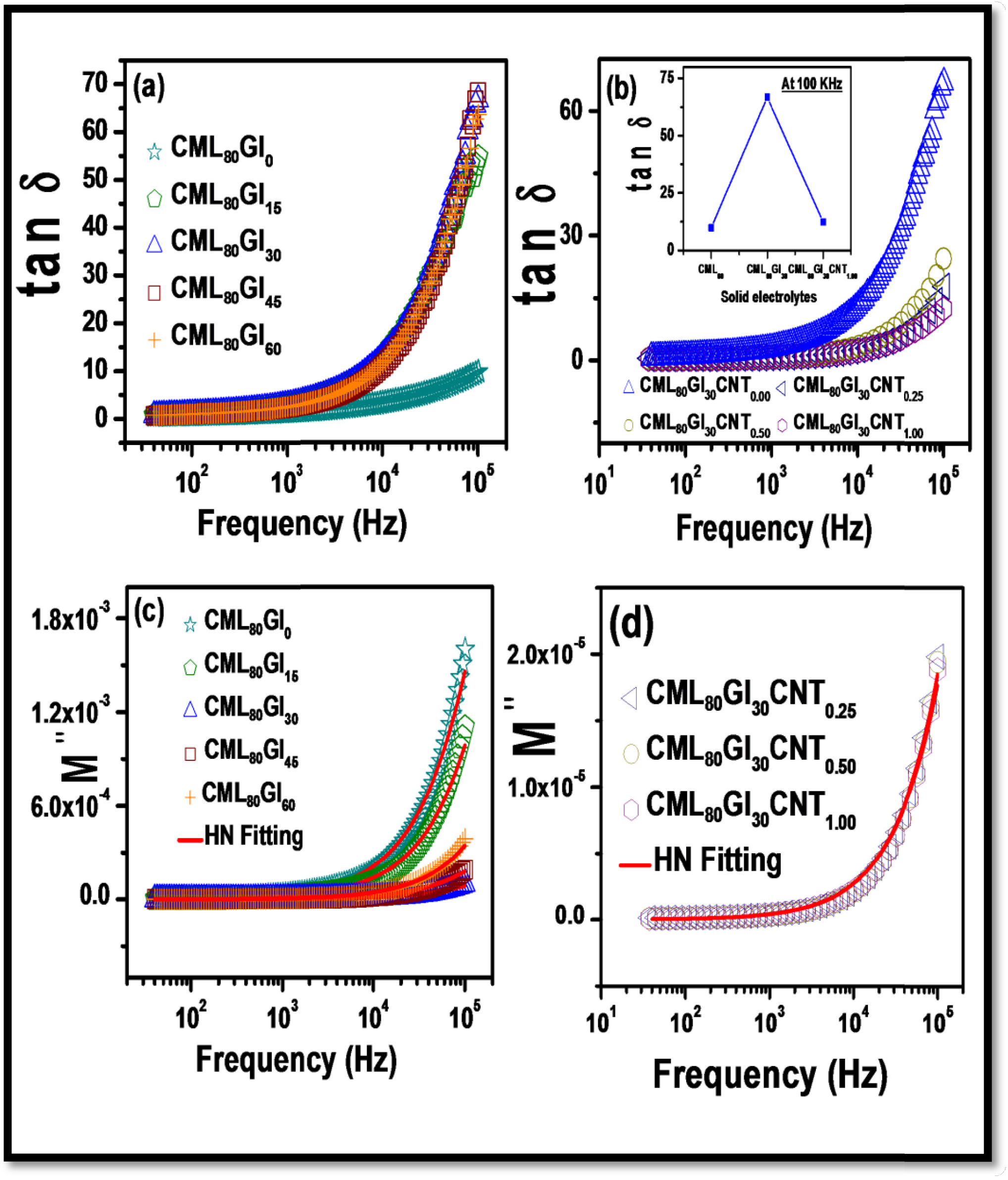

Fig. 8.9. (a-b) Variation of tan δ with frequency at room temperature for $CML_{80}Gl_y(0 \leq y \leq 60)$ and $CML_{80}Gl_{30}CNT_z(0.25 \leq z \leq 1.00)$ blended solid biopolymer electrolyte materials, respectively. Inset of (b) shows the variation of tan δ for $CML_{80}Gl_0$, $CML_{80}Gl_{30}$ and $CML_{80}Gl_{30}CNT_{1.00}$ solid electrolytes at 100 KHz, (c-d)Frequency dependence of imaginary part (M″) of electric modulus for $CML_{80}Gl_y(0 \leq y \leq 60)$ and $CML_{80}Gl_{30}CNT_z(0.25 \leq z \leq 1.00)$ blended solid biopolymer electrolyte materials, respectively. The solid lines in (c) and (d) are fits of the experimental data to Eq. 8.7.

8.3.4.5. Electric Modulus

To get further insights into the ion dynamics as a function of frequency, electric modulus spectra has been studied which suppresses the electrode polarization effects in the low frequency regime. The frequency dependent complex electric modulus (M^*) is as follows,

$$M^*(\omega) = \frac{1}{\varepsilon^*(\omega)} = M' + j\,M'' = \frac{\varepsilon_r}{\varepsilon_r^2+\varepsilon_{im}^2} + j\,\frac{\varepsilon_{im}}{\varepsilon_r^2+\varepsilon_{im}^2} \qquad (8.6)$$

where, M' and M'' are real and imaginary parts of complex electric modulus, respectively.

The frequency dependence of the imaginary part of the electric modulus (M'') at 300 K for $CML_{80}Gl_y$ ($0 \leq y \leq 60$) and $CML_{80}Gl_{30}CNT_z$ ($0.25 \leq z \leq 1.00$) blended solid biopolymer electrolyte materials are shown in Figs. 8.9c and 8.9d, respectively. M'' significantly increases with frequency at the higher frequencies along with a long tail at low frequencies suggesting a capacitive nature of the material [1,3].The complex electric modulus spectra are analyzed based on Havriliak - Negami (HN) function given by [18,21],

$$M^* = M_\infty + \frac{M_s - M_\infty}{[1+(j\omega\tau_c)^{\alpha_{HN}}]^{\gamma_{HN}}} \qquad (8.7)$$

where, M_∞ and M_s are the high frequency and low frequency limiting values of the electric modulus spectra, respectively,τ_c is the conductivity relaxation time, α_{HN} and γ_{HN} are the shape parameters with $0 < \alpha_{HN} \leq 1$ and $0 < \gamma_{HN} \leq 1$. For Debye relaxation, both the shape parameter values should be unity. Figures 8.9c and 8.9d represent the HN best fits of the experimental M''spectra of $CML_{80}Gl_y$ ($0 \leq y \leq 60$) and $CML_{80}Gl_{30}CNT_z$ ($0.25 \leq z \leq 1.00$) blended solid biopolymer electrolyte materials according to Eq. 8.7. The shape parameters as obtained from the best fits are listed in Table 2. It is observed that the values are found to be less than unity, indicating the nature of the relaxation phenomenon is of non-Debye type.

For a quantitative analysis of the modulus data in the time domain, the decay function, $\varphi\,(t)$ giving the time evolution of the electric field [$E(t) = E(0)\varphi\,(t)$] within the blended CS/CMC solid biopolymer electrolyte materials has been studied. The complex electric modulus, $M^*(\omega)$ is expressed in terms of Fourier transform of the decay function $\varphi\,(t)$ given as [18,22],

$$\mathrm{M}^*(\omega) = \mathrm{M}_\infty\left[1 - \int_0^\infty e^{-j\omega t}\left(-\frac{\partial\varphi(t)}{\partial t}\right)dt\right] \tag{8.8}$$

where, M_∞ is the high frequency limiting value of the electric modulus.

The electric field decay function in the time domain can be calculated using the inverse transform of Eq. 8.8 and is given by [18,23],

$$\varphi(t) = \frac{2}{\pi}\int_0^\infty \frac{\mathrm{M}''}{\omega \mathrm{M}_\infty}\cos(\omega t)d\omega \tag{8.9}$$

The inverse transform is carried out for CML$_{80}$Gl$_y$ ($0 \le y \le 60$) and CML$_{80}$Gl$_{30}$CNT$_z$ ($0.25 \le z \le 1.00$) blended solid biopolymer electrolyte materials respectively using the modulus HN equation (Eq. 8.7) keeping the parameters same as obtained from the fitting of the experimental M''spectra. The time dependence of $\varphi(t)$ for CML$_{80}$Gl$_y$ ($0 \le y \le 60$) and CML$_{80}$Gl$_{30}$CNT$_z$($0.25 \le z \le 1.00$) materials as obtained from Eq. 8.9 are shown in Figs. 8.10a and 8.10b, respectively. For non-Debye type relaxations, the decay function can be well approximated by the KWW or stretched exponential decay function given by [18,24],

$$\varphi(t) \approx exp\left[-\left(\frac{t}{\tau_{KWW}}\right)^{\beta_{KWW}}\right] \tag{8.10}$$

where, β_{KWW} is the stretched exponent lying between 0 and 1. The $\varphi(t)$ curves for the materials are fitted to Eq. 8.10 and the resulting curves are shown in Figs. 8.10a and 8.10b. The best fit values of β_{KWW} for CML$_{80}$Gl$_y$ ($0 \le y \le 60$) and CML$_{80}$Gl$_{30}$CNT$_z$($0.25 \le z \le 1.00$) materials are listed in Table 8.2.The small values of β_{KWW} (< 1) suggests that the relaxation is highly non-exponential for the blended CS/CMC solid biopolymer electrolyte material, suggesting non-Debye type relaxations in the materials.

The average relaxation time, $< \tau_a >$ associated with the stretched exponential KWW decay function is given as [18],

$$< \tau_a > = \frac{\tau_{KWW}}{\beta_{KWW}}\left[\boldsymbol{\Gamma}\left(\frac{1}{\beta_{KWW}}\right)\right] \tag{8.11}$$

where, $\boldsymbol{\Gamma}$ is the gamma function. The variation of $< \tau_a >$ as a function of glycerol and CNT contents in CML$_{80}$Gl$_y$ ($0 \le y \le 60$) and CML$_{80}$Gl$_{30}$CNT$_z$ ($0.25 \le z \le 1.00$) blended solid biopolymer electrolyte materials are shown in Figs. 8.10c and 8.10d, respectively. It is to note here that $< \tau_a >$ corresponding to the highest conducting sample, $CML_{80}Gl_{30}CNT_{1.00}$ is the lowest (~ 4.52 × 10^{-8} s). This may be due to the increase in long range hopping motion of the Li^+ ions through the CS/CMC blended solid biopolymer electrolyte matrix on incorporation with CNT.

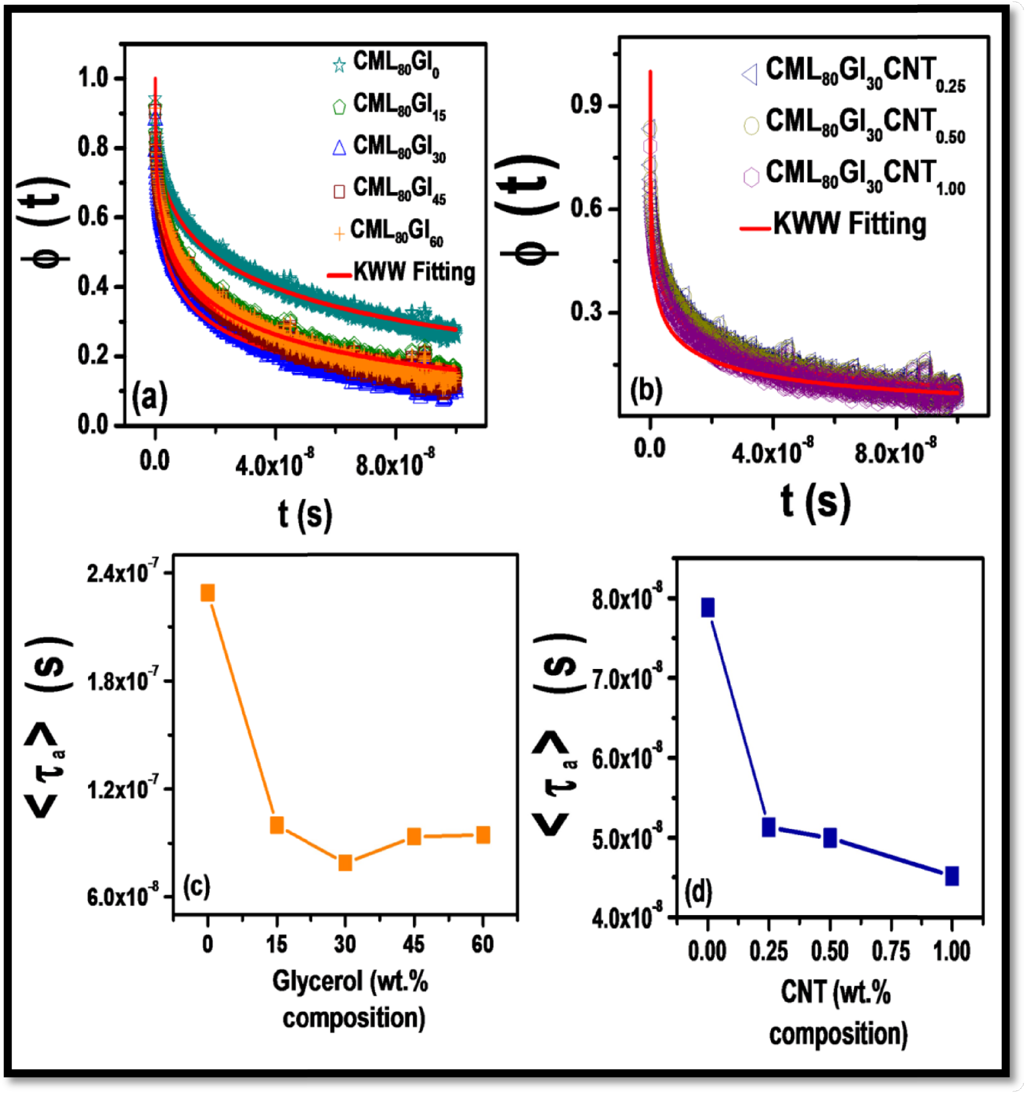

Fig. 8.10. Relaxation function, $\varphi(t)$ shown as a function of time in (a) $CML_{80}Gl_y$ $(0 \le y \le 60)$ and (b) $CML_{80}Gl_{30}CNT_z (0.25 \le z \le 1.00)$ blended solid biopolymer electrolyte materials. The solid lines are fits of the calculated HN relaxation function with the stretched exponential KWW decay function (Eq. 8.10), (c-d) Variation of average relaxation time $(< \tau_a >)$ of charge carriers as a function of glycerol and CNT concentrations in $CML_{80}Gl_y (0 \le y \le 60)$ and $CML_{80}Gl_{30}CNT_z (0.25 \le z \le 1.00)$ blended solid biopolymer electrolyte materials, respectively.

Table 8.2. Values of the fitting parameters, i.e. DC conductivity (σ_{DC}), conductivity at constant electric field (σ_0), characteristic relaxation time (τ_j), constant (α), the shape parameters (α_{HN} and γ_{HN})and thestretched KWW exponent(β_{KWW}) for CML$_{80}$Gl$_y$($0 \leq y \leq 60$) and CML$_{80}$Gl$_{30}$CNT$_z$($0.25 \leq z \leq 1.00$) blended solid biopolymer electrolyte materials.

Solid biopolymer electrolytes	σ_{DC} (S/cm)	σ_0 (S/cm)	τ_j (s)	α	α_{HN}	γ_{HN}	β_{KWW}
CML$_{80}$Gl$_0$	3.62×10^{-5}	6×10^{-8}	7.5×10^{-5}	0.63	0.87	0.33	0.36
CML$_{80}$Gl$_{15}$	5.07×10^{-5}	1×10^{-7}	6.7×10^{-4}	0.62	0.87	0.31	0.34
CML$_{80}$Gl$_{30}$	5.7×10^{-4}	5×10^{-7}	5.2×10^{-4}	0.61	0.85	0.28	0.311
CML$_{80}$Gl$_{45}$	2.9×10^{-4}	3×10^{-7}	5.5×10^{-4}	0.67	0.89	0.29	0.33
CML$_{80}$Gl$_{60}$	1.4×10^{-4}	2×10^{-7}	5.6×10^{-4}	0.67	0.90	0.30	0.34
CML$_{80}$Gl$_{30}$CNT$_{0.25}$	2.8×10^{-3}	2×10^{-6}	4×10^{-5}	0.78	0.84	0.25	0.28
CML$_{80}$Gl$_{30}$CNT$_{0.50}$	2.86×10^{-3}	2.3×10^{-6}	5.5×10^{-5}	0.81	0.84	0.25	0.28
CML$_{80}$Gl$_{30}$CNT$_{1.00}$	3×10^{-3}	3×10^{-6}	3.8×10^{-5}	0.80	0.82	0.22	0.248

8.3.5. Fourier Transform Infrared spectroscopy (FTIR)

FTIR spectroscopy is done to inspect the interactions between the plasticized blended biopolymer matrices comprised of CS and CMC with CNTnanofiller and LiClO$_4$ salt which can induce changes in the vibrational modes of the blended biopolymer molecules. The FTIR absorption spectra of CML$_{80}$Gl$_y$ ($0 \leq y \leq 60$) and CML$_{80}$Gl$_{30}$CNT$_z$($0.25 \leq z \leq 1.00$) blended solid biopolymer electrolyte materials are studied in order to analyze the interactions of LiClO$_4$ salt and CNT nanofiller with plasticized blended CS/CMC biopolymer matrix. Figures 8.11a and

8.11b show the FTIR absorption spectra in the region of 1500-1700 cm^{-1} for CML$_{80}$Gl$_y$ ($0 \leq y \leq 60$) and CML$_{80}$Gl$_{30}$CNT$_z$($0.25 \leq z \leq 1.00$) blended solid biopolymer electrolyte materials.A quantitative analysis is done by deconvolution of the FTIR absorption spectra based on Gaussian function in the region of 1500-1700 cm^{-1} for these materials (Figs. 8.11a-b) in order to examine the interactions of Li$^+$ with amine (R-NH$_2$) and amide (O=C-NHR) functional groups of CS.

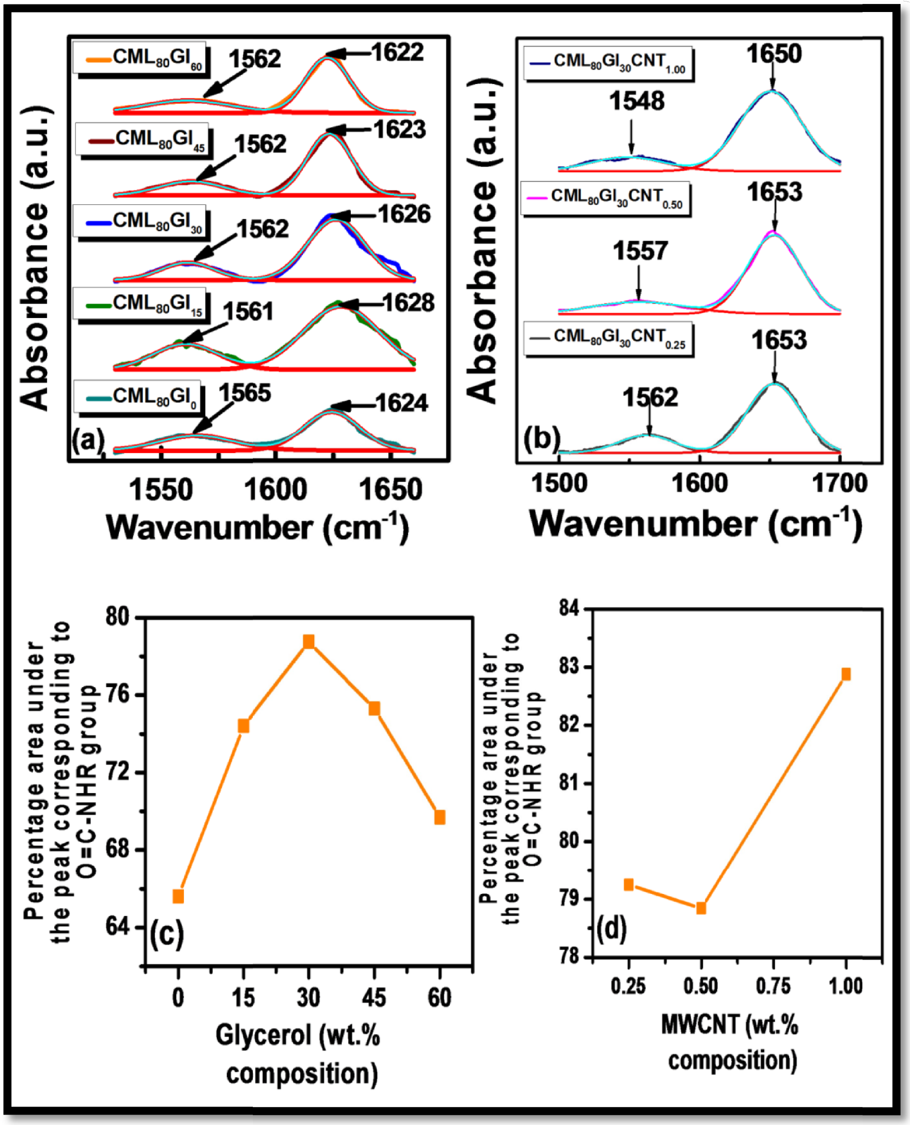

Fig. 8.11.(a-b) Deconvoluted FTIR absorption spectra in the region, 1500 cm^{-1} to 1700 cm^{-1} for CML$_{80}$Gl$_y$($0 \leq y \leq 60$) and CML$_{80}$Gl$_{30}$CNT$_z$($0.25 \leq z \leq 1.00$) blended solid biopolymer electrolyte materials, respectively based on Gaussian fitting function, (c-d)Percentage areas under the peaks corresponding to O=C-NHR are shown as a function of glycerol and CNT concentrations in CML$_{80}$Gl$_y$($0 \leq y \leq 60$) and CML$_{80}$Gl$_{30}$CNT$_z$($0.25 \leq z \leq 1.00$) blended solid biopolymer electrolyte materials, respectively.

A significant red shift of the absorption peak corresponding to amine (R-NH_2) of chitosan (CS) [1,18] is observed on glycerol loading in $CML_{80}Gl_y$ from ~ 1565 cm^{-1} (y= 0) to ~ 1561 cm^{-1}(y= 15) as shown in Fig. 8.11a. But on increasing the glycerol loading in $CML_{80}Gl_y$, there is a slight blue shift of the absorption peaks corresponding to amine (R-NH_2) of CS observed from ~ 1561 cm^{-1} (y = 15) to ~ 1562 cm^{-1} (y = 30-60) as shown in Fig. 8.11a. There is a significant blue shift of the absorption peaks corresponding to secondary amide (O=C-NHR) of CS [1,18] is observed from ~ 1624 cm^{-1} (y= 0) to ~ 1628 (y= 15) (shown in Fig. 8.11a) on incorporation of glycerol (plasticizer).There is a significant and gradual red shift of the absorption peaks corresponding to secondary amide (O=C-NHR) of CS with increase in glycerol content is observed from ~ 1628 cm^{-1} (y = 15) to ~ 1622 (y = 60) (shown in Fig. 8.11a).The area under the absorption peak corresponding to O=C-NHR in $CML_{80}Gl_y$ ($0 \leq y \leq 60$) material is plotted as a function of glycerol content (y) as shown in Fig. 8.11c, where the peak area becomes maximum at y = 30.Further on incrorporation of CNT in $CML_{80}Gl_{30}CNT_z$($0.25 \leq z \leq 1.00$), there is a significant red shift of the absorption peaks corresponding to amine (R-NH_2) and secondary amide (O=C-NHR) of CS observed from ~ 1562 cm^{-1} (z = 0.25) to ~ 1548 cm^{-1} (z = 1.00) and ~ 1653 cm^{-1}(z = 0.25)to ~ 1650 (z = 1.00), respectively as shown in Fig. 8.11b. The area under the absorption peak corresponding to O=C-NHR in $CML_{80}Gl_{30}CNT_z$ ($0.25 \leq z \leq 1.00$)SBNE material is plotted as a function of CNT content (z) as shown in Fig. 11d, where the peak area becomes maximum at z = 1.00. Thus, the role of secondary amide (O=C-NHR) will dominate over the amine (R-NH_2) in aiding the Li^+ transport in the blended CS/CMC solid biopolymer electrolytes.

8.3.6. Supercapacitor studies

A coin-type symmetric supercapacitor cell was constructed with the highest conducting electrolyte i.e. $CML_{80}Gl_{30}CNT_{1.00}$ SBNE material and electrode material comprised of active carbon and $MnCoFeO_4$ (henceforth represented as AC/MCF electrode). $MnCoFeO_4$ has been chosen as the electrode material owing to its nanoporous structure responsible for high specific capacitance and power density compared to AC electrode alone, as reported by Majumdar *et al* [1]. The active mass of the electrode material is ~ 20 mg. Typical cyclic voltammograms for the cell constructed with AC/MCF electrode and $CML_{80}Gl_{30}CNT_{1.00}$ SBNE material at different scan rates of 5-200 mV/s over the voltage range from −0.1 to +1.1 V, are shown in Fig. 8.12a.A nearly semi-rectangular shaped CV curve is obtained at slower scan rates, indicating a good capacitive characteristic behavior of the electrode material.

The specific capacitance value of the supercapacitor has been determined through galvanostatic charge-discharge (GCD) technique. The supercapacitor has been charged and discharged at a constant current within a potential range of -0.6 V to +0.6 V. The GCD for the cell constructed with AC/MCF electrode and $CML_{80}Gl_{30}CNT_{1.00}$ SBNE material are performed at current densities of±100 μA/cm^2, ±300 μA/cm^2 and ±1 mA/cm^2 and the corresponding charge-discharge profiles are shown in Fig. 8.12b. The specific capacitance (C_{sp}) of the cell are calculated by GCD using the following equation given as [1],

$$C_{sp} = \frac{2I}{\frac{\Delta V}{\Delta t} \times m} \tag{8.12}$$

where, $\Delta V$is the potential window (V), m is the mass of the active material per electrode (g), I is the charging current (A) and Δt is the discharging time (s). The specific capacitance value (C_{sp}) for the cell constructed with AC/MCF electrode and $CML_{80}Gl_{30}CNT_{1.00}$ SBNE material at current densities of 100 μA/cm^2, 300 μA/cm^2 and 1 mA/cm^2 are 15 Fg^{-1}, 8 Fg^{-1} and 6 Fg^{-1}, respectively. The specific capacitance value decreases with increase in current density due to the increase in IR drop across the electrodes. Energy density (E_D) and power density (P_D) of the supercapacitor has been estimated from the relation given as [1],

$$E_D = \frac{1}{2}\left[\frac{C_{sp}\Delta V^2}{3.6}\right] \text{Wh/kg} \tag{8.13}$$

$$P_D = \left[\frac{E_D}{t_d}\right] \times 3600 \text{ W/kg} \tag{8.14}$$

An energy density of 3 Whkg^{-1} at a power density 6.12 Wkg^{-1}is achieved with (AC/MCF) | $CML_{80}Gl_{30}CNT_{1.00}$| (AC/MCF) solid-state hybrid supercapacitor.

The AC impedance response of the (AC/MCF) | $CML_{80}Gl_{30}CNT_{1.00}$ | (AC/MCF) solid-state hybrid supercapacitor has been shown in Fig. 8.12 cover a low frequency range of 100 KHz – 10 mHz. The impedance spectra were analyzed using semi-quantitative fittings program supplied by the instrument (AUTOLAB-30) on the basis of the Randles equivalent circuit comprised of R_s, R_{ct}, W, C_{dl} and C_{FS} as shown in the inset of Fig. 8.12d. R_s represents the contact resistance between the current collector and electrode and that with the electrode and SBNE, R_{ct} is the charge transfer resistance, W is the Warburg impedance relating to the diffusion of ions in the electrode pores, C_{dl} and C_{FS} represent the electric double layer capacitance and the pseudocapacitance which accounts for the faradaic reactions inside the electrode.

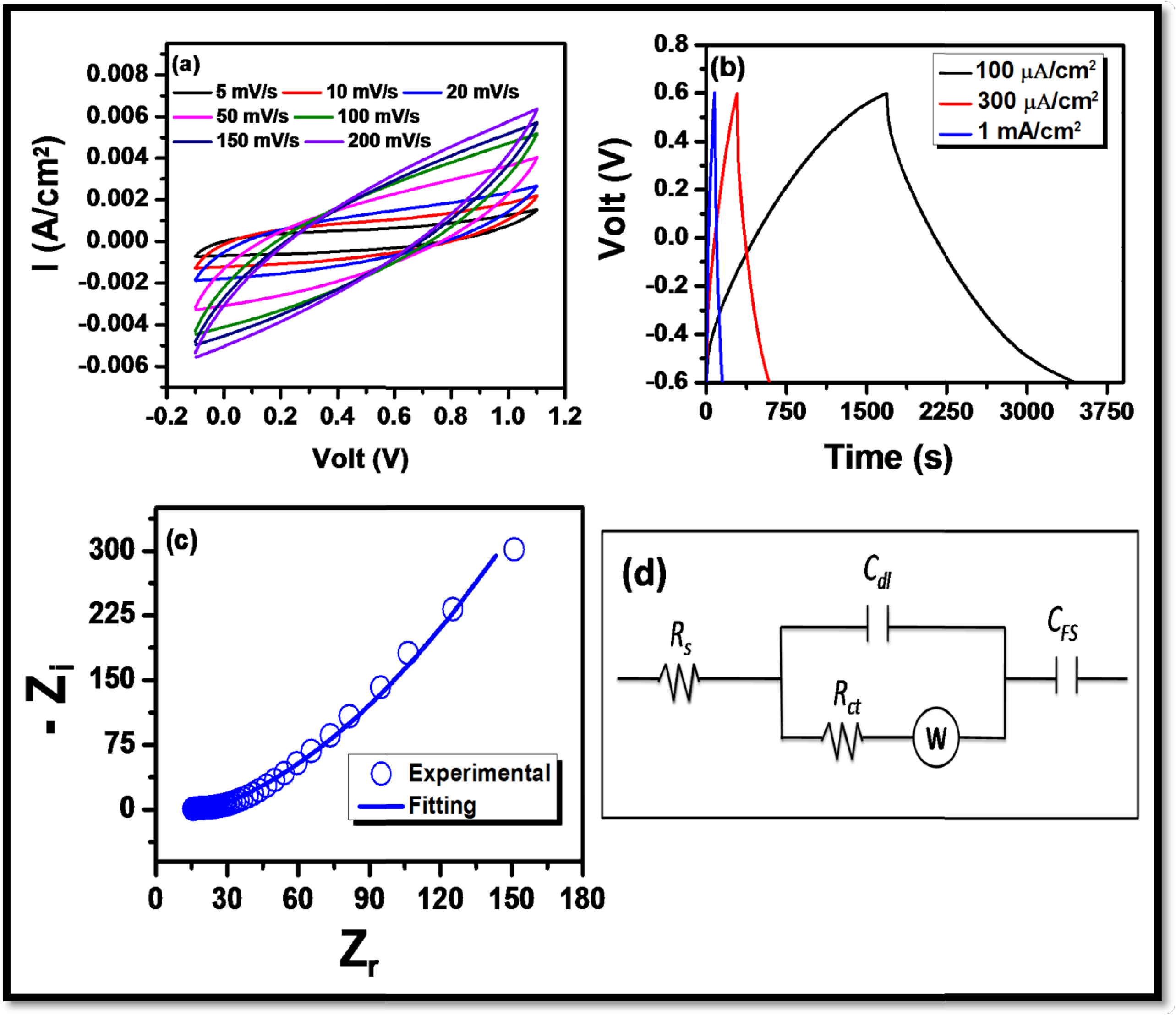

Fig. 8.12. (a) Cyclic voltammograms at different scan rates of 5-200 mV/s over the voltage range from –0.1 to +1.1 V, (b)Galvanostatic charge-discharge at current densities of 100 µA/cm^2, 300µA/cm^{2}and 1 mA/cm^2, (c)Nyquistplotover a low frequency range of 100 KHz – 10 mHz, and (d) shows the Randles equivalent circuit used to analyze the impedance spectrafor (AC/MCF) | $CML_{80}Gl_{30}CNT_{1.00}$ | (AC/MCF) solid-state hybrid supercapacitor. Solid line in (c) represents the modeled impedance spectra based on the equivalent circuit as shown in (d).

The values of R_s, R_{ct}, W, C_{dl} and C_{FS} as obtained from the fittings of the experimental impedance spectra are 16.70 Ω, 6.26 Ω, 0.02341 Ω $s^{-0.5}$, 21.66 μF and 91.4 mF, respectively. The low value of R_{ct} suggest better diffusion of ions at the electrode/SBNE interfacial region. Also it is to note here that the contribution of the pseudocapacitance (C_{FS}) is much large compared to the electrical double layer capacitance (C_{dl}) since $MnCoFeO_4$ behaves as a redox system which increases the kinetics of electron transfer. The nanoporous structure of the $MnCoFeO_4$ allows the ions in the SBNE to easily diffuse into the electrode nanopores and access their internal surface, leading to the enhancement of C_{FS}. The low value of Warburg impedance (W) is attributed to the diffusion of the ions (mass transfer) inside the nanoporous structure of electrode at lower frequencies.

As reported in our previous study [1], a realistic approach of maximum 10,000 diffusion length (i.e. 80 micron) inside the AC/MCF electrode material has been considered for the estimation of the effective specific capacitance (C_E) of the electrode with respect to $CML_{80}Gl_{30}CNT_{1.00}$ SBNE since all the electrolyte ions of the SBNE are not diffusing entirely inside the electrode material, in contrast to liquid electrolytes. The effective specific capacitance (C_E) of the (AC/MCF) | $CML_{80}Gl_{30}CNT_{1.00}$ | (AC/MCF) solid-state hybrid supercapacitor has been achieved as ~ 94 Fg^{-1} at a current density of 100 $\mu A/cm^2$, which makes this combination a promising candidate for future development of a safe, cost-effective and flexible solid state supercapacitor.

8.4. Conclusions

A series of new type of blended biodegradable polymer electrolytes based on chitosan (CS) and carboxymethyl cellulose (CMC) as host biopolymers with varying concentrations of plasticizer (glycerol) and nanofiller (CNT) as dopants have been prepared via solution casting technique. Incorporation of CNT helps to tune the ionic conductivity of the CS/CMC blended electrolytes by an order of magnitude (~ 10^{-3} S/cm) at room temperature (300 K).FE-SEM images reveal the fine distribution of the carbon nanotubes (CNT) inside the CS/CMC blended biopolymer matrix. Transference number measurement analysis confirms the predominant ionic conduction in the CNT incorporated CS/CMC blended solid biopolymer nanocomposite electrolytes. Impedance spectroscopy results are analyzed by considering a fractional diffusion model based on material properties which is physically meaningful instead of the conventional equivalent circuit formalism. The anomalous diffusion of Li^+ ions inside the blended nanocomposite is theoretically modeled based on fractional calculus approach. The electrode polarization effects in the AC conductivity spectra are analyzed considering the fractal nature of the interfacial region of the electrode and SBNE. Using the scaling of the ac conductivity and dielectric constant, it is observed that the relaxation dynamics of charge carriers is independent of the dopant (glycerol/CNT) concentration but dependent on the nature of dopants. Low leakage current obtained with the CNT incorporated solid nanocomposite electrolyte makes it attractive for energy storage applications. A hybrid symmetric solid-state supercapacitor is fabricated with activated carbon and nano-crystallites of manganese cobalt ferrite ($MnCoFeO_4$) as electrode materials and CNT incorporated solid biopolymer blended electrolytes based on CS and CMC, showing a fairly good effective specific capacitance value of ~ 94 Fg^{-1}.

Chapter 9

High-performance graphene oxide grafted chitosan-starch solid biopolymer electrolytes for flexible hybrid supercapacitors

9.1. Introduction

The conventional supercapacitors comprise of liquid electrolytes have potential hazards of leakage which hinder their widespread commercialization. Thus, solid biopolymer electrolytes (SBE) have attracted much attention in recent years in this field of electrochemical energy storage device (supercapacitor) applications [1-3] and are emerging as promising alternatives to liquid electrolytes. However, the very low ionic conductivity of SBE remains a challenge. As an attempt to enhance their conductivities, various techniques have been adopted such as blending with other compatible polymers [2-4] and incorporation with suitable nanofillers [5,6]without compromising their mechanical properties. Polymer blending is a popular technique adopted to tune the ionic conductivity by incorporating new complexation sites for ion migration [4]. Biopolymers such as chitosan (CS) and potato starch (PS) are extremely abundant in nature and their miscibility and complexation are reported earlier [7,8], but they have sufficiently low conductivity. Doping with ionic salts and suitable plasticizers can effectively tune this conductivity. The electrical and dielectric properties of the blended SBE can be improved further on addition of nanofillers in the electrolyte (SBNE). The incorporation of nanofillers is expected to prevent the polymer crystallization and thereby providing abundant conduction paths owing to their high specific surface area [6]. Graphene oxide (GO) has attracted huge attention over other conductive carbons owing to its ultra-large surface area and multiple oxygen rich functional groups (carboxyl, hydroxyl and epoxy) on its basal planes and edges which makes it a promising filler material to enhance the ionic conductivity of the solid biopolymer electrolyte through strong Lewis acid-base interaction with the cationic species of the SBE [5,9,10]. But a very few studies have been done which involve the incorporation of GO in solid polymer electrolytes [9,10]. Hence an extensive study with GO in SBE has become mandatory to explore their potential applications. Spinel ferrites, $M\text{Fe}_2\text{O}_4$ or $MM'\text{FeO}_4$ (where M or M'= Mn, Ni, Zn, Co, etc.), are promising electrode materials for supercapacitor. They have impressive electrical properties, good electrochemical stability and exhibit different redox states [3,11,12]. $MnCoFeO_4$ has been selected as the electrode material in the current investigation as they have quite high specific capacitance and power density [3,13].

In the present work, the ionic conductivity, dielectric and transport properties of CS/PS blended solid biopolymer electrolytes incorporated with GO nanofiller, have been investigated using impedance and FTIR spectroscopy. The frequency dependence conductivity is extensively studied for understanding the ion dynamics in the blended electrolytes. The relaxation dynamics of charge carriers are studied using electric modulus formalism. A fractional diffusive model has been adopted in order to explore the ion conduction mechanism of the mobile ions in GO incorporated CS/PS blended solid biopolymer nanocomposite electrolytes. Further, FTIR spectroscopy analysis is done to understand the interactions between the blended host biopolymers, dopant salt and nanofiller, and finally these transport properties have been compared with the results obtained from fractional diffusion model. In addition, the effect of GO in the CS/PS blended solid biopolymer nanocomposite electrolytes are also been investigated from the molecular point of view. A novel hybrid solid-state symmetric supercapacitor has been fabricated with nano crystallites manganese cobalt ferrite ($MnCoFeO_4$) as electrode material and graphene oxide (GO) grafted CS/PS blended nanocomposite with varying GO compositions (henceforth noted as GO@CS/PS) as solid state electrolytes and their performances are systematically studied. A high effective specific capacitance ($C_E \sim 288Fg^{-1}$) has been reported.

9.2. Experimental

9.2.1. Synthesis of the GO@CS/PS blended solid biopolymer nanocomposite electrolytes (SBNE)

Graphene oxide (GO) was chemically prepared from pure graphite powder following modified Hummers's method [14]. Chitosan/Potato Starch (CS/PS) blended solutions with 30 wt. % of lithium perchlorate ($LiClO_4$) and 25 wt. % of glycerol are prepared based on the method as discussed in our previous work [8]. Various weight percentages of GO (3, 9, 15 wt. %) were dispersed in deionised water and ultrasonicated for about 15 minutes. Then the blending of GO and CS/PS blended solutions were done and stirred for 15 minutes, followed by ultrasonication for about 30 minutes to get a homogenous mixture. Resulting homogeneous solutions were cast on polypropylene petri dishes and allowed to dry in a vacuum oven at 40℃ to form the GO@CS/PS blended SBNE materials (the picture of the free-standing GO grafted SBNE film is shown in Fig. 9.1 having size of 1.5× 1.5 cm and thickness 60 µm).The SBNE materials were characterized by computer interfaced impedance analyzer (Solartron SI 1260 Impedance Analyzer) in the frequency range between 40 Hz and 100 KHz at room temperature (300 K). Fourier transform infrared spectroscopy (FTIR) had been performed using Perkin Elmer FT-IR Spectrum 2 spectrometer having resolution of 4 cm^{-1}.

9.2.2. Synthesis of $MnCoFeO_4$

The $MnCoFeO_4$ nanoparticles were prepared based on the method as reported in our earlier work [3]. The product was calcined at 600^0C for 3 hours. The $MnCoFeO_4$ nanoparticles and graphene oxide were characterized by X-ray diffraction (XRD) which was done by a X-ray diffractometer (model: Bruker D8 Advance) using the CuKα radiation of wavelength 1.5406 Å.

9.2.3. Fabrication of the supercapacitor

The electrodes of the symmetric supercapacitor were fabricated by using a paste of a homogeneous mixture made of $MnCoFeO_4$ nanoparticles, acetylene black (AB) and polytetrafluoroethylene (PTFE) taken in the wt. % ratio of 50:45:5. The paste was then compacted into a thin sheet using mortar and pestle and compressed on a stainless steel mesh having the surface area of 1 cm^2. The prepared electrode was heated at 60°C for 6 h under vacuum to evaporate the solvent completely (henceforth represented as AC/MCF electrode and the schematic illustration of the supercapacitor electrode fabrication is shown in Fig. 9.1). The total weight of the active material in the fabricated electrode is ~20 mg. AC/MCF is a composite electrode (as shown in Fig. 9.1) which is used as both cathode and anode and thus it's a symmetric supercapacitor. Electrochemical behavior of the fabricated cell was investigated with AUTOLAB-30 potentiostat/galvanostat.

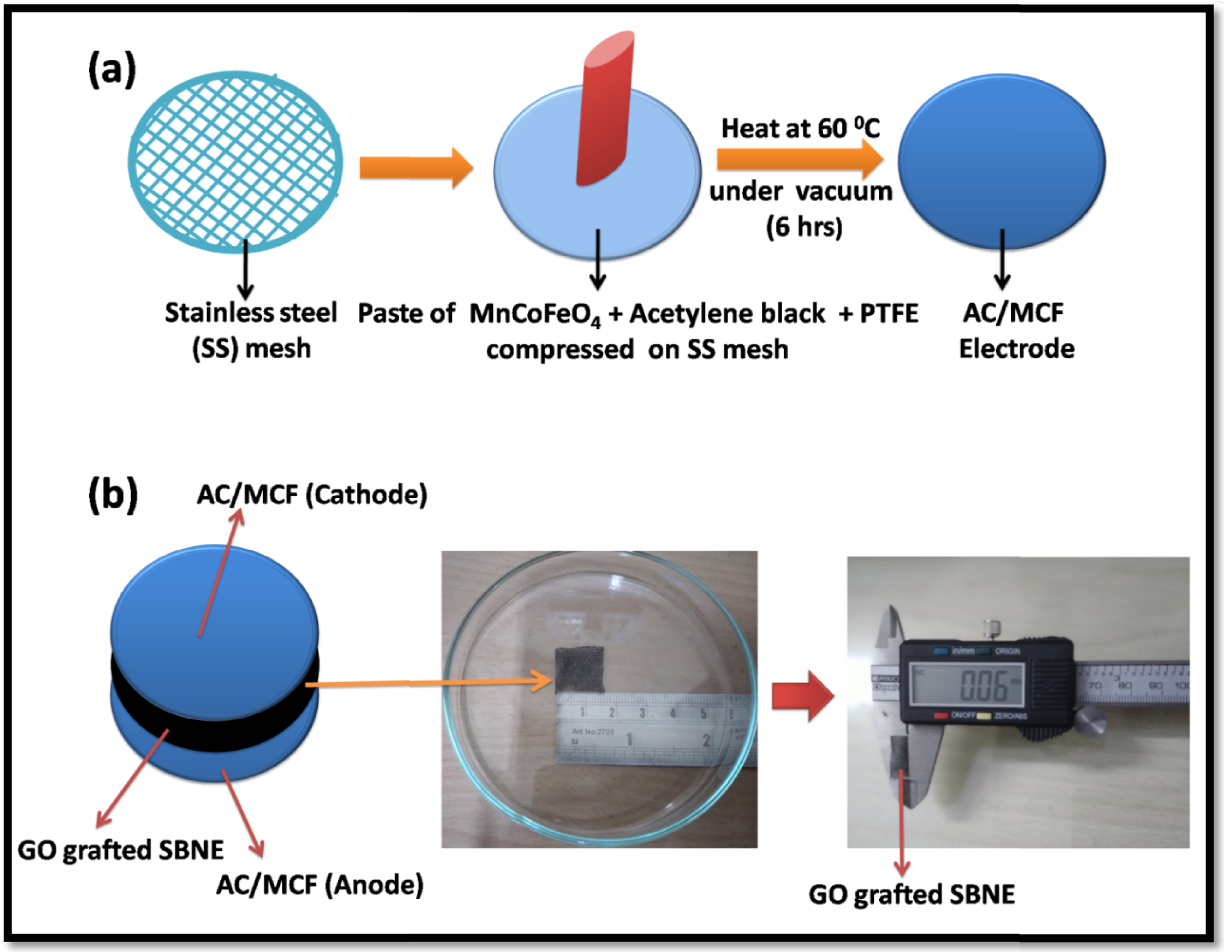

Fig. 9.1. (a) Schematic illustration of the supercapacitor electrode fabrication steps, (b) Schematic diagram of the developed solid-state supercapacitor with synthesized GO grafted SBNE material having size of 1.5 × 1.5 cm and thickness 60 μm.

9.3. Results and Discussion

9.3.1. X-ray Diffraction (XRD)

GO and $MnCoFeO_4$ nanoparticles are characterized by XRD. XRD of graphene oxide (GO) is shown in Fig. 9.2a which shows two peaks around $2\theta = 10.8°$ (d-spacing ~ 8.185Å) and $2\theta = 43.25°$ corresponding to (002) and (100) planes, respectively. Figure 9.2b illustrates the diffraction peaks of $MnCoFeO_4$ nanoparticles which exhibit a spinel structure (cubic, space group $Fd\bar{3}m$, JCPDS #22-1086). The crystallite size (D) of $MnCoFeO_4$ nanoparticles has been calculated by using Williamson and Hall's modified Scherrer's formula which is given as [15],

$$\beta\cos\theta = \frac{0.89\lambda}{D} + 2\varepsilon\sin\theta \qquad (9.1)$$

The inset of the Fig. 9.2b shows the $\beta\cos\theta$ vs $\sin\theta$ plot revealing the average size of the $MnCoFeO_4$ nanoparticles as 46 nm.

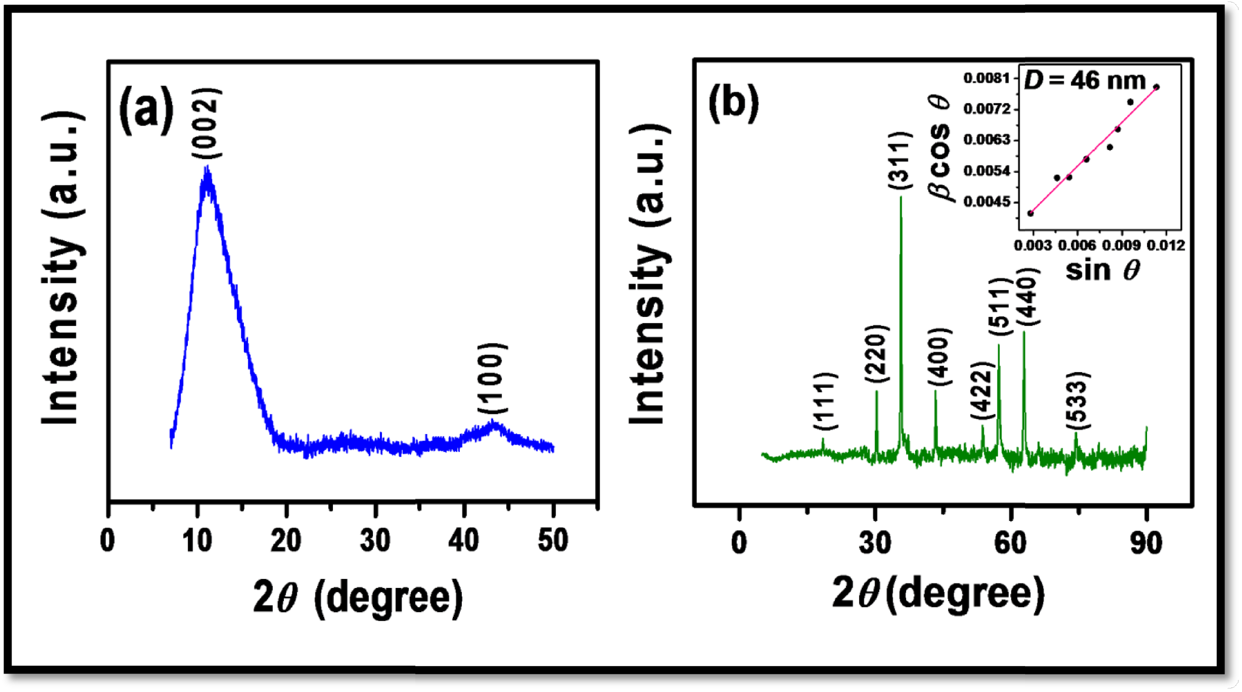

Fig. 9.2. (a) XRD spectrum of Graphene Oxide (GO), (b) XRD spectrum of $MnCoFeO_4$ and the inset figure shows the Williamson–Hall plot.

9.3.2. Surface morphology by Field Emission Scanning Electron Microscopy (FESEM)

The surface morphology of the GO-free and GO-grafted CS/PS blended solid biopolymer electrolytes are characterized by field emission scanning electron microscopy (FE-SEM) (model: JSM-7610F, JEOL) and are shown in Fig. 9.3. As evident from the FESEM micrographs of the solid electrolytes (Fig. 9.3), there are no apparent differences between the GO-free SBE (Fig. 9.3a) and 3 wt. % GO-grafted SBNE (Fig. 9.3b) which clearly suggest that GO is uniformly distributed in the biopolymer matrix. At higher GO doping concentrations (i.e. 9 wt. % GO-grafted SBNE), the surface profile of the matrix changes prominently with the appearance of almost spherical-shaped regions (Fig. 9.3c) which infers that graphene oxide has strong Lewis acid-base interaction with the cationic species of the SBNE [5].

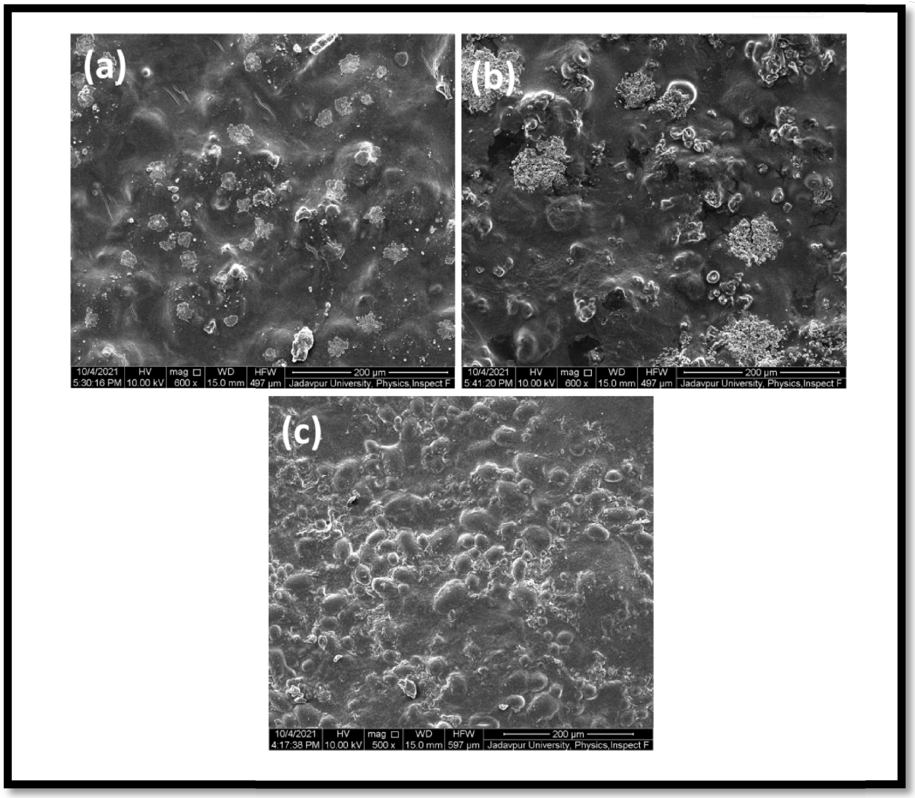

Fig. 9.3. FESEM micrographs for (a) GO-free, (b) 3 wt. % GO-grafted and (c) 9 wt. % GO-grafted CS/PS solid biopolymer electrolytes.

9.3.3. Electrical properties of SBNE by impedance spectroscopy

9.3.3.1. Ionic conductivity

AC impedance spectroscopy studies are done to probe the ionic conductivity and dielectric properties of the GO@CS/PS blended solid biopolymer nanocomposite electrolyte (SBNE) materials. The ionic conductivities of the CS/PS blended solid biopolymer electrolyte (SBE) material having different blended compositions of chitosan (CS) and potato starch (PS) with $LiClO_4$ salt at a concentration of 30 wt.% (weight percentage of the blended polymer) and glycerol as a plasticizer at a concentration of 25 wt.% (weight percentage of the blended polymer) are initially studied using impedance spectroscopy in the range of frequencies from 40 Hz to 100 KHz. Figure 9.4a represents the Nyquist plots for different blended compositions of CS and PS in the SBE material at 300 K. All the results are analyzed based on equivalent circuit (Fig. 9.4d) consisting of contact resistance (R_s), bulk resistance (R_b) and constant phase element (CPE) [9]. There is always some energy dissipation in real systems and thus the experimental results can only be explained by an equivalent circuit involving "constant phase element (CPE)" instead of ideal capacitors [16]. The impedance of the CPE is given by, $Z_{CPE} = k\,(j\omega)^{-p}$, where k is the CPE coefficient and p is some exponent fractional parameter ($0 < p < 1$). The DC ionic conductivity (σ_{DC}) of the blended polymers has been calculated based on the relation, $\sigma_{DC} = L/R_bA$ where, A is the effective contact area of the electrode and the electrolyte interface and L is the thickness of the solid electrolyte. The variation of the DC conductivity for different percentage of blended compositions of CS in the CS/PS blended SBE material is shown in the inset of Fig. 9.4a. It is observed that the room temperature ionic conductivity of the CS/PS blended SBE system increases from ~ 9.89×10^{-6} to ~ 1.97×10^{-4}S/cm with the increment of PS blending concentrations from 20 % to 80 %.The observed enhancement in ionic conductivity in PS-rich blended SBE material [i.e. the blending composition of CS/PS(20:80)] may be attributed to the situation wherein the increment in PS concentrations enhances the amorphicity of the blended biopolymer matrix through which the charge carriers can penetrate quite easily, resulting a higher value of conductivity. Therefore, this particular PS-rich blended SBE material is considered for further studies.

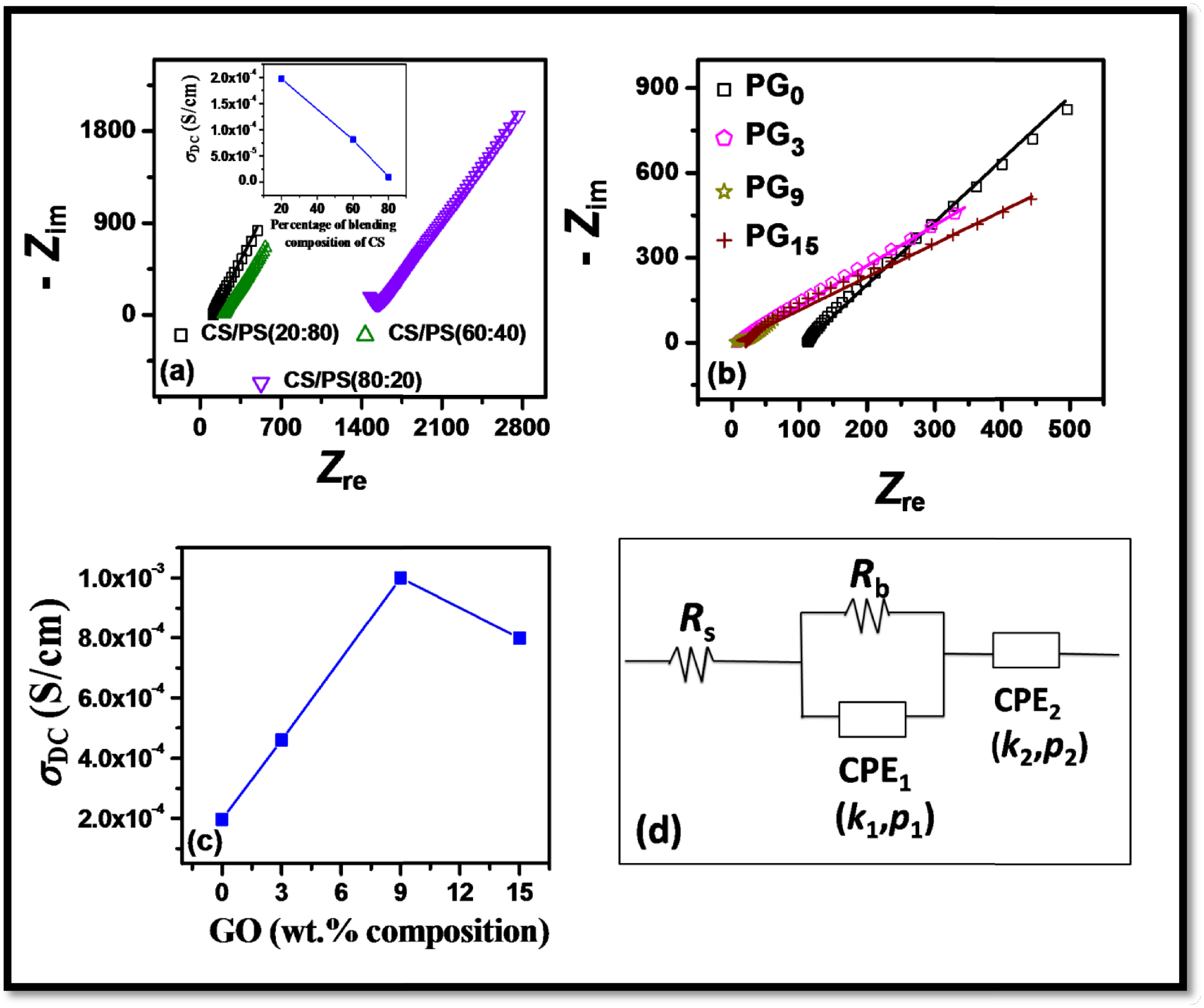

Fig. 9.4. (a) Nyquist plots at 300 K with different CS/PS blending ratios in CS/PS blended solid biopolymer electrolytes and the inset figure shows the DC conductivity (σ_{DC}) as a function of percentage of blending compositions of CS, (b) Nyquist plots of PG_y ($0 \leq y \leq 15$) SBNE material at 300 K, (c) DC conductivity (σ_{DC}) shown as a function of GO concentrations at room temperature, (d) The equivalent circuit used to model the Nyquist plots. The solid lines in (a) and (b) represent the modeled plots based on equivalent circuit fitting.

Since the main objective of this work is to develop a highly ion-conducting solid biopolymer electrolytes for supercapacitor applications, we dope the PS-rich blended composite, CS/PS(20:80) further with different concentrations of graphene oxide (GO)as a nanofiller (3, 9 and 15 weight percentages of the blending polymer). The GO doped PS-rich blended solid biopolymer nanocomposite electrolyte (SBNE) materials are henceforth denoted as PG_y where y = 3, 9 and 15 weight percentages of the blending polymers. The Nyquist plots of PG_y ($0 \leq y \leq 15$) SBNE material is shown in Fig. 9.4b.A systematic investigation on the electrical properties of GO doped CS/PS blended SBNE material reveals that conductivity in PG_9 is an order of magnitude higher than that of PG_0 material (from ~1.97×10^{-4} to ~1×10^{-3} S/cm) at room temperature (as shown in Fig. 9.4c). There are multiple factors involved that affect the ionic conductivity of the blended SBNE material. The most crucial factor behind the conductivity enhancement is the average mobility of the free charge carriers in the blended SBNE. High mobility facilitates fast ionic transport through continuous ion conducting channels [17] created by graphene oxide nanosheets within the SBNE material, resulting an increase in conductivity. The abundant oxygen containing functional groups (carboxyl, hydroxyl and epoxy) on the basal planes and edges of GO reacts with Li^+ ion [5,18] due to Lewis acid-base reaction by weakening the biopolymer-cation interaction, thereby loosing the segmental movement of the CS/PS blended biopolymers which will be discussed later in detail in the subsequent section. The conduction path gets perturbed with excess doping amounts of GO in CS/PS blended composite beyond y = 9 which results in decrease in conductivity. This may be due to the aggregation of GO at a higher loading (y = 15) in the CS/PS blended matrix which partially blocks the fast ion transport channel, thereby reducing the potency of GO [18].

9.3.3.2. AC conductivity spectra

The frequency dependence of the conductivity of SBNE with varying weight percentages of GO, are studied in order to understand the ion dynamics in PG_y ($0 \leq y \leq 15$). The AC conductivity is calculated using the following relation,$\sigma(\omega) = \omega\varepsilon_0\varepsilon_{\text{im}}$ where, ε_0 is the vacuum permittivity (8.854×10^{-14} F/cm) and ε_{im} is the dielectric loss. Figure 9.5a represent the frequency dependent AC conductivity spectra at room temperature (300 K) for PG_y ($0 \leq y \leq 15$) blended SBNE material and the datas are analyzed based on Almond-West (AW) formalism. According to Almond-West (AW) formalism, the conductivity law can be represented in terms of ion-hopping frequency (ω_{p}) which is given as follows [16,19],

$$\sigma(\omega) = \sigma_{\text{DC}}[1 + \left(\frac{\omega}{\omega_{\text{p}}}\right)^n] \tag{9.2}$$

where, n is the power law exponent and σ_{DC} is the DC conductivity of the SBNE material.

The carrier concentration term (K) for the electrolyte material can be calculated fromion-hopping frequency (ω_{p}) which is given as [16,20],

$$K = \frac{\sigma_{\mathrm{DC}} T}{\omega_{\mathrm{p}}} \tag{9.3}$$

where, T is the ambient temperature (300 K). The fittings of the AC conductivity spectra for the blended SBNE material based on Eq. 9.2 are shown in Fig. 9.5a for different doping concentrations of GO ($0 \leq y \leq 15$).

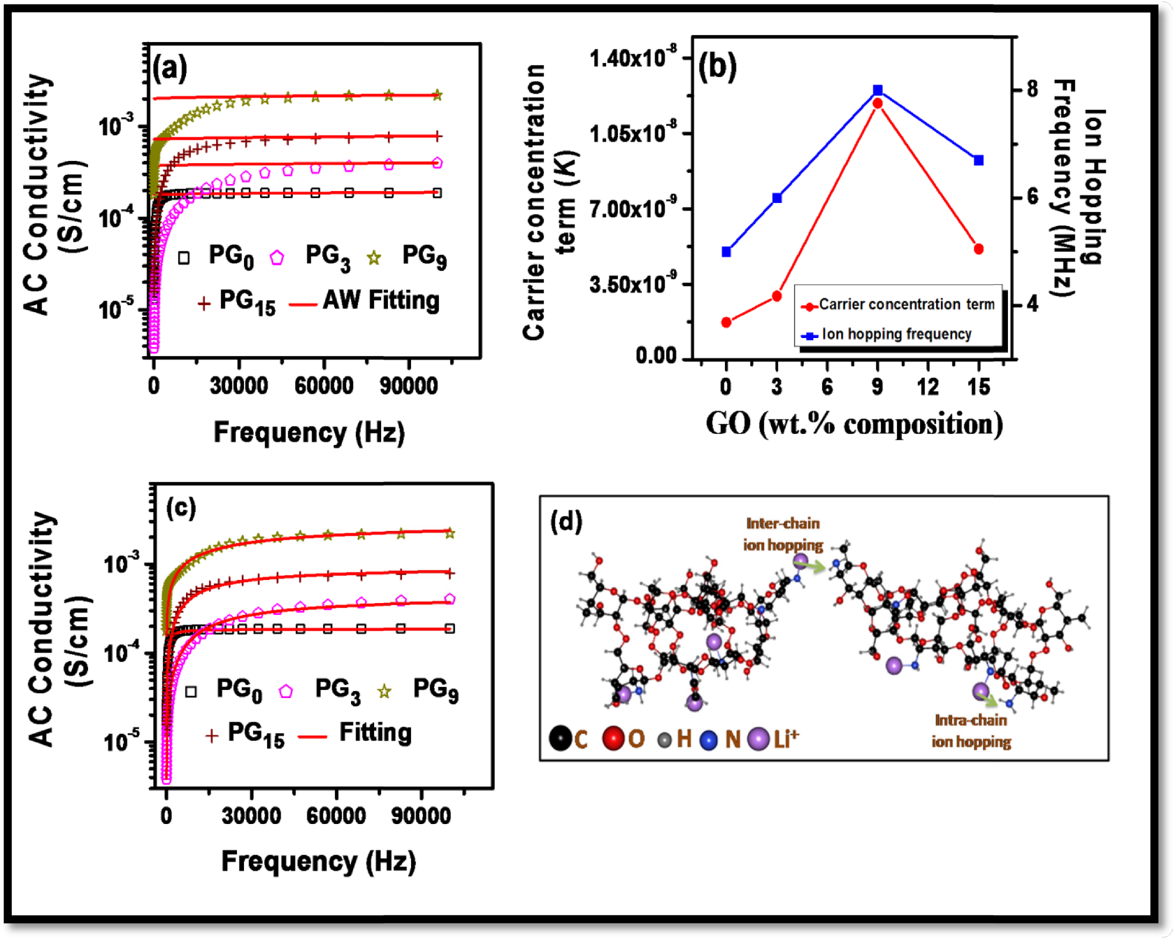

Fig. 9.5. (a) AC conductivity spectra at different GO compositions in PG_y ($0 \leq y \leq 15$) blended SBNE material. Solid lines are the fits of the experimental data to Eq. 9.2, (b) Variation of ion hopping frequency and carrier concentration term with GO compositions, (c) AC conductivity spectra at different GO compositions where solid lines are the fits of the experimental data to Eq. 4, (d) Schematic representation of intra-chain and inter-chain ion-hopping in GO-free material, PG_0.

It is well known that Eq. 9.2 is unable to reproduce the experimental AC conductivity results at lower frequencies [16]. A low frequency dispersive region attributing to the accumulation of charge carriers at the electrode-electrolyte interface followed by an almost frequency independent conductivity region corresponding to the DC conductivity are observed for all the GO doping concentrations. An ion successfully hops from one site to another neighboring vacant ion-coordination site in the blended biopolymer matrix when the frequency is lower than the ion-hopping frequency (ω_p), thus contributing to the DC conductivity. The frequency independent plateau region of the AC conductivity spectra of the SBNE material characterizes the ionic conduction in the material relating to the intra-chain and inter-chain hopping motion of the mobile Li^+ ions during biopolymer segmental motion [16], the schematic representation of which is shown in Fig. 9.5d for PG_0 material. Figure 9.5b indicates that rate of ion hopping along the ion transport channel constructed by GO nanosheets is much faster compared to the ion hopping rate in PG_0 material where the Li^+ transport is strongly coupled to the segmental motion of the blended biopolymers. A maximum value of the carrier concentration term (K) is obtained with PG_9 SBNE material as shown in Fig. 9.5b. The oxygen rich functional groups of GO donate electrons to dissociate Li^+ by Lewis acid-base reaction, thereby resulting an increase in free Li^+ ion dissociation by weakening the bond between the contact ion pairs of the dopant salt (discussed in detail in the subsequent section 9.3.4) with addition of GO in the blended SBNE. This results in a higher transfer rate of Li^+ and finally an enhanced ionic conductivity is obtained.

Since the AW formalism is not valid in the low frequency region where electrode polarization is dominant, we have considered the fractal nature of the electrode-electrolyte interface and therefore, the frequency dependent complex AC conductivity is given as [16,21],

$$\sigma(\omega) = \sigma_0 + \frac{\sigma_{DC} - \sigma_0}{1 + (i\omega\tau_j)^{-\alpha}} + i\omega\varepsilon_0[\varepsilon_{relax}(\omega) - \varepsilon_\infty] \quad (9.4)$$

where, σ_0 is the conductivity at constant electric field, σ_{DC} is the DC conductivity of the solid electrolyte material, τ_j is the characteristic relaxation time, ε_0 is the vacuum permittivity (8.854 × 10^{-14} F/cm), α is a constant determining the fractal dimension of the space-time ensemble in the space-charge region having its value lies between 0 and 1, $\varepsilon_{relax}(\omega)$ determines the contribution of the dielectric relaxation part, ε_∞ is the high frequency limiting value of dielectric permittivity. The real part of the experimental frequency dependent AC conductivity spectra for PG_y $(0 \leq y \leq 15)$ SBNE materials are fitted using Eq. 9.4 and are shown in Fig. 9.5c. The value of the fitting parameters are listed in Table 9.1. It is noted here that the values of σ_{DC} and σ_0 does not coincide due to the effects of electrode polarization and the value of σ_0 is much less than the value of σ_{DC}.The values of α are less than unity, indicating the fractal dimension of the electrode-electrolyte interface. It is to note here that the relaxation time (τ_j) corresponding to the highest conducting sample, PG_y with $y = 9$is the lowest (~0.58×10^{-5} s).

Table 9.1. Values of the fitting parameters σ_{DC}, σ_0, τ_j, α for PG_y $(0 \leq y \leq 15)$ blended SBNE material.

Solid biopolymer electrolytes	σ_{DC} (S/cm)	σ_0 (S/cm)	τ_j (s)	α
PG_0	1.87×10^{-4}	0.9×10^{-6}	3×10^{-4}	0.78
PG_3	4.5×10^{-4}	1.2×10^{-6}	0.8×10^{-5}	0.7
PG_9	3.3×10^{-3}	1.0×10^{-4}	0.58×10^{-5}	0.55
PG_{15}	9.5×10^{-4}	0.5×10^{-5}	1.35×10^{-5}	0.67

9.3.3.3. Dielectric relaxation

The dielectric relaxation is studied in terms of frequency dependent complex dielectric permittivity (ε^*)given by, $\varepsilon^*(\omega) = \varepsilon_r(\omega) - j\varepsilon_i(\omega)$ where,$\varepsilon_r$and ε_i are the real and imaginary parts of the complex dielectric permittivity. The real part of permittivity known as the dielectric constant and imaginary part known as the dielectric loss quantifies the amount of energy stored and energy dissipated in the SBNE material, respectively during each cycle of the applied AC electric field. The frequency dependent dielectric constant for PG_y $(0 \leq y \leq 15)$ blended SBNE material is shown in Fig. 9.6a at 300 K. It shows that the values of ε_r is higher in the low frequency regime due to the effects of electrode polarization. As frequency increases,ε_r decrease graduallydue to the effects of ionic and electronic polarization processes. In the high frequency regime, the rapid periodic reversal of the electric field gives inadequate time for the charge to accumulate at the electrode/solid electrolyte interface, and thus the polarization due to charge accumulation decreases. Inset of Fig. 9.6a represent the variation of dielectric constant (ε_r) with different weight percentages of GO for PG$_y$ ($0 \le y \le 15$) blended SBNE material at 100 KHz. It is important to note here that the value of dielectric constant becomes maximum at y = 9 for PG$_y$ blended SBNE material and it is 50 times enhanced compared to that of the GO free system (i.e. PG$_0$).

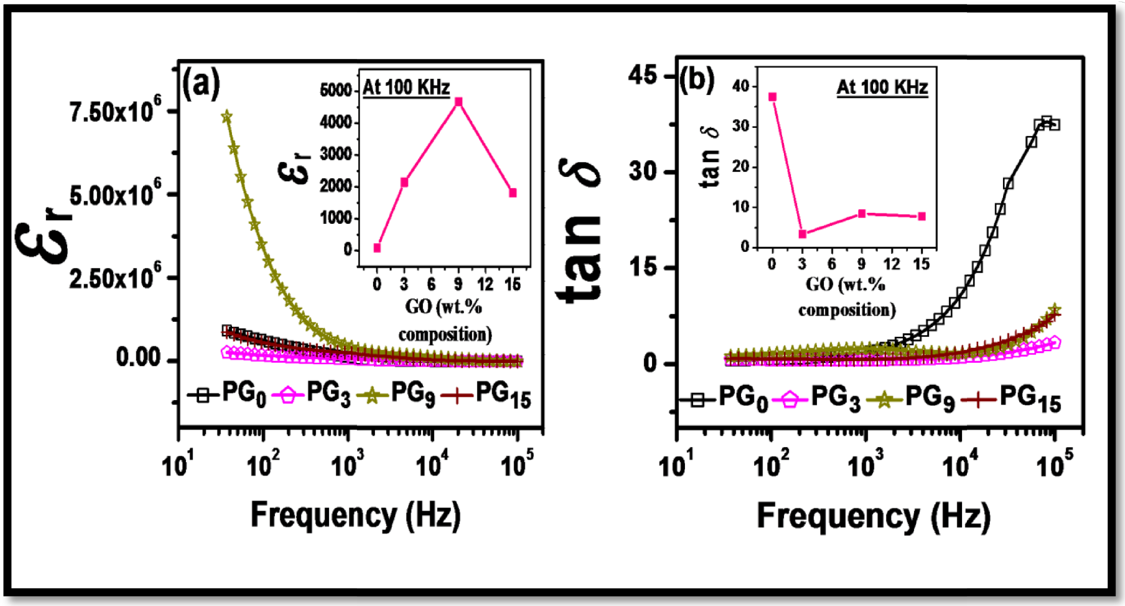

Fig. 9.6. Frequency dependence of (a) dielectric constant (ε_r) for different GO compositions in PG$_y$ ($0 \le y \le 15$) blended SBNE material at room temperature, inset of (a) shows the variation of $\varepsilon_r$as a function of GO compositions at 100 KHz, (b) Variation of tan δ with frequency at room temperature in PG$_y$ ($0 \le y \le 15$) blended SBNE material, inset of (b) shows the variation of tan δ as a function of GO compositions at 100 KHz.

The frequency dependence of the loss tangent defined as the ratio of energy loss to energy stored ($\varepsilon_i/\varepsilon_r$) appears maximum at a certain frequency (ω_{peak}) corresponding to the characteristic dielectric relaxation time (τ), satisfying the equation, $\omega_{\text{peak}}\tau = 1$. Figure 9.6b show the variation of tan δ with frequency for PG$_y$ ($0 \le y \le 15$) at 300 K. Absence of any relaxation peak in the frequency range of investigation for the PG$_y$ SBNE material indicates very small dielectric relaxation time. It is worthwhile to point out that the loss factor is significantly reduced on doping with GO in PG_y SBNEs (shown in inset of Fig. 9.6b) along with significant enhancement in dielectric constant, making them potential candidates for electrochemical device applications.

9.3.3.4. Relaxation study with electric modulus formalism

Electric modulus formalism is extensively used to investigate the ionic relaxation as the electrode polarization (EP) effect is suppressed in this formalism in the low frequency regime. The frequency dependent complex electric modulus (M^*) is given as follows,

$$M^*(\omega) = \frac{1}{\varepsilon^*(\omega)} = M' + j\,M'' = \frac{\varepsilon_{\mathrm{r}}}{\varepsilon_{\mathrm{r}}^2+\varepsilon_{\mathrm{im}}^2} + j\,\frac{\varepsilon_{\mathrm{im}}}{\varepsilon_{\mathrm{r}}^2+\varepsilon_{\mathrm{im}}^2} \qquad (9.5)$$

where, $M'$and M''denotes the real and imaginary parts of M^*, respectively.

The frequency dependence of the imaginary part of the electric modulus (M'') for PG_y ($0 \le y \le 15$) blended SBNE material is shown in Fig. 9.7a at room temperature (300 K). It is observed that M''shows a long tail-like feature at the low frequency region with an increasing trend at the higher frequency regime, indicating the capacitive nature of the SBNE material [2,3]. It is observed that M'' decreases with increasing GO concentrations and becomes minimum for PG_9 SBNE material, which corroborates with the dielectric results.

The complex electric modulus spectra are analyzed using Havriliak - Negami (HN) function given by [22,23],

$$M^* = M_\infty + \frac{M_s - M_\infty}{[1+(j\omega\tau_c)^{\alpha_{\mathrm{HN}}}]^{\gamma_{\mathrm{HN}}}} \qquad (9.6)$$

where, M_∞ and M_s are the high frequency and low frequency limiting values of the electric modulus spectra, respectively,τ_c is the conductivity relaxation time, α_{HN} and γ_{HN} are the shape parameters with $0 < \alpha_{\mathrm{HN}} \le 1$ and $0 < \gamma_{\mathrm{HN}} \le 1$. For Debye relaxation, both the shape parameter values should be unity. Fig. 9.7a represent the HN fits of the experimental M''spectra of PG_y ($0 \le y \le 15$) SBNE material according to Eq. 9.6. The variation of τ_c for varying GO concentrations as obtained from the best fits of M''spectra, is shown in the inset of Fig. 9.7a. It is observed that τ_c is minimum for PG_9 SBNE ($\sim 7\times10^{-9}$s) which indicates the increase in long range hopping motion of the Li^+ ions through the CS/PS blended biopolymer matrix on doping with GO. The variation of the shape parameters obtained from the best fits for different weight percentages of GO in PG$_y$ composite is shown in Fig. 9.7b and their values are found to be less than unity, indicating the nature of the relaxation phenomenon is of non-Debye type. This may be due to the increased dissociation of Li$^+$ ions with the aid of oxygen-rich functional groups in GO in PG$_y$ SBNE material resulting a non-ideal perturbed system which is responsible for the multi frequency non-Debye type relaxation process.

For a quantitative analysis of the modulus data in the time domain, the decay function, $\varphi\ (t)$ giving the time evolution of the electric field within PG$_y$ ($0 \leq y \leq 15$) blended SBNE material is studied. The complex electric modulus, $M^*(\omega)$ is expressed in terms of Fourier transform of the decay function $\varphi\ (t)$ given as [23],

$$M^*(\omega) = M_\infty[1 - \int_0^\infty e^{-j\omega t}\left(-\frac{\partial\varphi(t)}{\partial t}\right)dt] \tag{9.7}$$

The electric field decay function in the time domain can be calculated using the inverse transform of Eq. 9.7 and is given by [24],

$$\varphi(t) = \frac{2}{\pi}\int_0^\infty \frac{M''}{\omega M_\infty}cos(\omega t)d\omega \tag{9.8}$$

The inverse transform is carried out for different weight percentages of GO using the modulus HN equation (Eq. 9.6) keeping the parameters same as obtained from the fitting of the experimental M$''$spectra. The time dependence of $\varphi(t)$obtained from Eq. 9.8 for PG$_y$ ($0 \leq y \leq 15$) blended SBNE material are shown in Fig. 9.7c.

For non-Debye type relaxations, the decay function is approximated by the KWW or stretched exponential decay function given by [25,26],

$$\varphi(t) \approx exp\left[-\left(\frac{t}{\tau_{\text{KWW}}}\right)^{\beta_{\text{KWW}}}\right] \tag{9.9}$$

where, β_{KWW} is the stretched exponent lying between 0 and 1. The $\varphi(t)$ curves for PG$_y$ ($0 \leq y \leq 15$) SBNE material are fitted to Eq. 9.9 in Fig. 9.7c.The variation of β_{KWW} for different weight percentages of GO in PG$_y$ blended SBNE materials, as obtained from the best fits is shown in Fig. 9.7d. The small values of β_{KWW} (<1) are an indication for highly non-exponential relaxation behavior in PG$_y$ ($0 \leq y \leq 15$) blended SBNE material, suggesting non-Debye type relaxations in the material.

The relation between HN shape parameters (α_{HN} and γ_{HN}) and KWW stretched exponent (β_{KWW}) has been given as [16],

$$\beta_{\mathrm{KWW}} = (\alpha_{\mathrm{HN}}\gamma_{\mathrm{HN}})^{\frac{1}{1.23}} \tag{9.10}$$

It is found that the fitting parameters for PG$_y$ ($0 \leq y \leq 15$) blended SBNE material obey Eq. 9.10 successfully. This indicates that both the HN and KWW representations are valid with same physical significance for different doping concentrations of GO in PG$_y$ SBNE material.

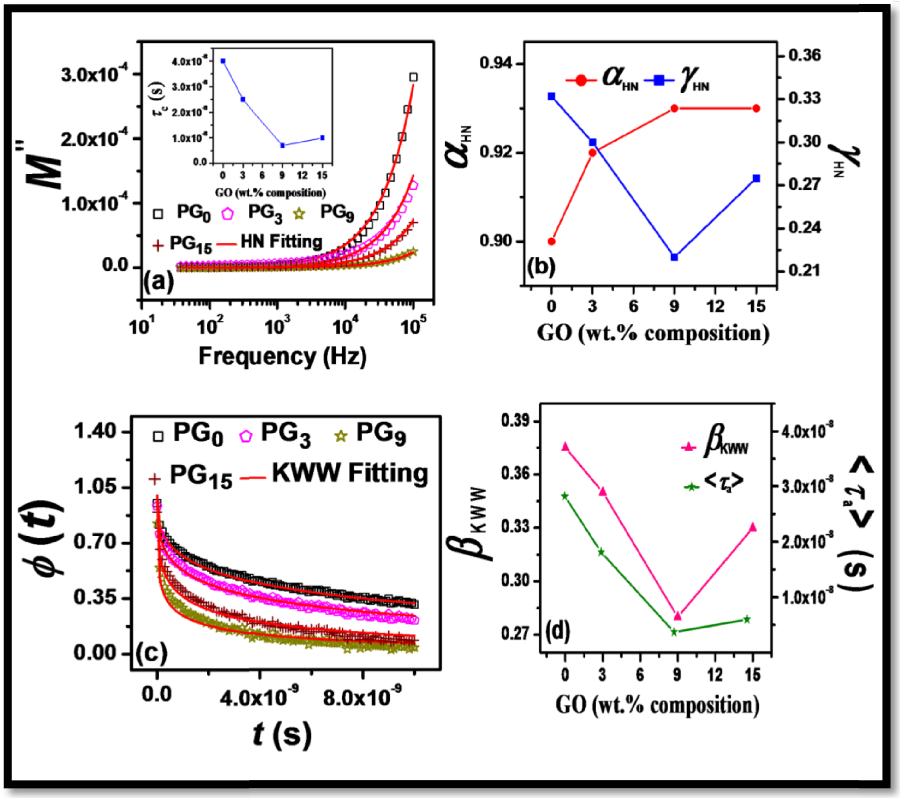

Fig. 9.7. (a) Frequency dependence of imaginary part (M'') of electric modulus in PG$_y$ ($0 \leq y \leq 15$) blended SBNE material at room temperature. The solid lines are fits of the experimental data to Eq. 9.6, (b) Variation of shape parameters α_{HN} and γ_{HN} in PG$_y$ ($0 \leq y \leq 15$) blended SBNE material for varying GO concentrations, (c) Relaxation function, $\varphi(t)$ shown as a function of time in PG$_y$ ($0 \leq y \leq 15$) blended SBNE material. The solid lines are fits of the calculated HN relaxation function with the stretched exponential KWW decay function (Eq. 9.9), (d) Variation of β_{KWW} and average relaxation time ($< \tau_a >$) of charge carriers with different GO compositions in the SBNE material.

The average relaxation time, $< \tau_{\mathrm{a}} >$ associated with the stretched exponential KWW decay function is given as [16,24],

$$< \tau_{\mathrm{a}} > \, = \frac{\tau_{\mathrm{KWW}}}{\beta_{\mathrm{KWW}}} \left[\boldsymbol{\Gamma} \left(\frac{1}{\beta_{\mathrm{KWW}}} \right) \right] \tag{9.11}$$

where, $\boldsymbol{\Gamma}$ is the gamma function. The variation of $< \tau_a >$ for different GO compositions in PG$_y$ $(0 \leq y \leq 15)$ blended SBNE material is shown in Fig. 9.7d, which shows that the highest conducting sample, PG$_9$ exhibits the lowest $< \tau_{\mathrm{a}} >$(~3.72 ×10^{-9}s), as expected.

9.3.3.5. Intra Diffusion

It is of utmost importance to study the intra diffusion processes of the mobile ions in the PG$_y$ $(0 \leq y \leq 15)$ blended SBNE material since the conductivity of the SBNE depends on the intra diffusion coefficient of the mobile ions within the blended biopolymer electrolyte matrix. The mechanism of intra ion diffusion in the non-crystalline solid biopolymer electrolytes is quite similar to that of liquid electrolytes. It is considered that the solid polymer electrolytes are composed of fractal structures in macroscopic as well as in microscopic scales [3].The significance of anomalous diffusion in solid polymer electrolytes arises from the fractal structure of polymers. The ion conduction mechanism inside the PG$_y$ $(0 \leq y \leq 15)$ blended SBNE material is explored on the basis of a model as proposed by Lenzi *et al*, where the contribution of anomalous diffusion has been incorporated through a fractional order parameter ‘γ’as [3,27],

$$Z = \frac{2}{iA\omega\boldsymbol{\varepsilon}_{\mathbf{r}}\boldsymbol{\varepsilon}_{\mathbf{0}}\beta^2} \left[\frac{1}{\beta\lambda_{\mathrm{D}}^2} \tanh\left(\frac{\beta L}{2}\right) + h\frac{(i\omega)^{\gamma}L}{2D_{\gamma}} + (1 - h)\frac{i\omega L}{2D} \right] \tag{9.12}$$

where, λ_{D} is the Debye screening length, ε_{r} is the dielectric constant of the SBNE material,D_{γ} and D are the anomalous and normal diffusion coefficients, respectively, L is the sample thickness, A is the effective contact area of the electrode and the electrolyte surface, $\beta = \sqrt{\frac{1}{\lambda_{\mathrm{D}}^2} + h\frac{(i\omega)^{\gamma}}{D_{\gamma}} + (1 - h)\frac{i\omega}{D}}$ is the characteristic exponent diffusion of the model, h is the fraction of anomalous diffusion and $(1 - h)$ is the fraction of normal diffusion.

Eq. (9.12) is used to analyze the intra diffusive behavior of the mobile ions inside the PG$_y$ $(0 \leq y \leq 15)$ blended SBNE material by fitting the Nyquist plots based on this theoretical model as shown in Fig. 9.8. The best fit parameters are tabulated in Table 9.2. The fractional contribution of the anomalous diffusion (h) in the PG_y ($0 \leq y \leq 15$) blended SBNE material is found to be much greater compared to that of normal diffusion since the 'h' value is very close towards 1. Also the value of γ remains constant at ~ 0.48 for all the SBNE materials, inferring the dominant anomalous intra diffusive behavior of the PG_y ($0 \leq y \leq 15$) blended SBNE material. The fractal structure of the biopolymers in both microscopic and macroscopic scales results in the dominating anomalous diffusive behavior of charge carriers in the blended SBNE material [3,28]. But the noticeable feature is observed for the PG_9 SBNE material where the fractional contribution of anomalous diffusion (h) has been decreased from 0.99 to 0.80, resulting in an increment in the contribution of normal diffusion inside the PG_9 SBNE material. Thus both the normal and anomalous diffusion play a very important role to explain the impedance results of PG_9 SBNE material properly. The value of the anomalous intra diffusion coefficient (D_γ) for the PG_y ($0 \leq y \leq 15$) blended SBNE material obtained through this fractional diffusive model corroborates with the value of intra diffusion coefficient obtained through FTIR method, as discussed in detail in the subsequent section 9.3.4. The highest conducting SBNE material, PG_9 has the maximum value of D_γ (0.18×10^{-6} cm^2/s), as expected.

Table 9.2. Best fit model parameters to analyze diffusion processes in PG_y ($0 \leq y \leq 15$) blended SBNE material.

Solid biopolymer electrolytes	D ($\times 10^{-5}$cm^{2}s^{-1})	D_γ($\times 10^{-6}$cm^{2}s^{-1})	γ	h	λ_D (μm)
PG_0	0.006	0.02	0.48	0.99	0.003
PG_3	1	0.07	0.47	0.99	0.09
PG_9	1.1	0.18	0.48	0.80	0.049
PG_{15}	1.01	0.12	0.48	0.99	0.069

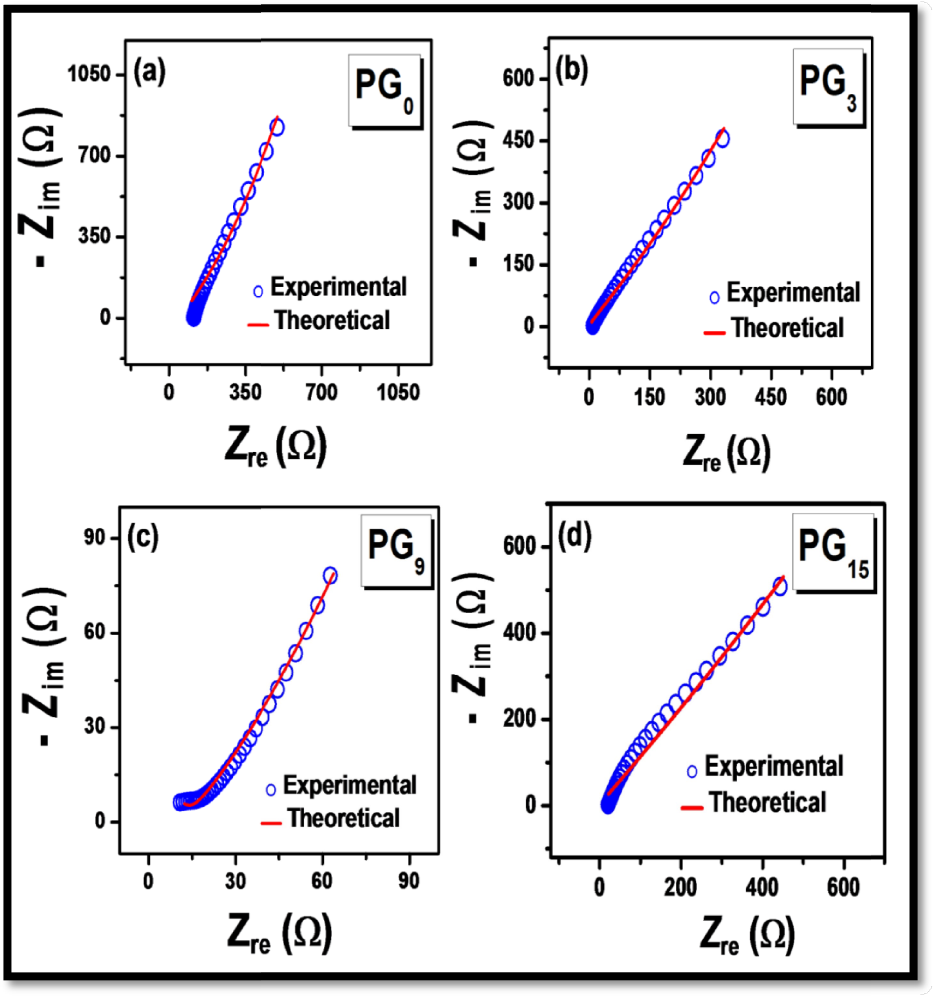

Fig. 9.8. Modeling of Nyquist plots based on fractional diffusion model (Eq. 9.12) for the PG_y($0 \leq y \leq 15$) blended SBNE material, (a) y = 0, (b) y = 3, (c) y = 9, (d) y = 15.

9.3.4. Fourier Transform Infrared spectroscopy (FTIR)

To investigate the mechanism of GO in promoting the transfer of Li^+ in PG_y ($0 \leq y \leq 15$) blended SBNE material, FTIR spectroscopy measurement has been carried out. FTIR spectra analysis helps to inspect the interactions between the blended biopolymer matrices comprised of CS and PS with GO nanofiller and $LiClO_4$ salt and further to determine the transport properties of the SBNE material. The transport parameters viz. number density (n), mobility (μ) and diffusion coefficient (D) of the free charge carriers are calculated using the Eqs. 9.13, 9.14 and 9.15 respectively [3,8],

$$n = \frac{M \times N_A}{V_{\text{total}}} \times P_f \tag{9.13}$$

$$\mu = \frac{\sigma_{\mathrm{DC}}}{ne} \tag{9.14}$$

$$D = \frac{\mu K_{\mathrm{B}} T}{e} \tag{9.15}$$

where, P_{f} represent the percentage of free ions, σ_{DC} denotes the DC conductivity of the SBNE material obtained from impedance spectroscopy analysis, M is the number of moles of $LiClO_4$ salt in each sample, N_{A} is the Avogadro's number and V_{total} is the total volume of the blended SBNE material.

The FTIR absorption spectra are deconvoluted over the range of ~ 610 cm^{-1} to ~ 650 cm^{-1} for PG_y ($0 \leq y \leq 15$) blended SBNE material as shown in Fig. 9.9a in order to estimate the ion transport parameters. The peak close to 627 cm^{-1} and 638 cm^{-1} are assigned as free and contact ions pairs of $LiClO_4$ [8,29] respectively in PG_0 material, which downshifted and upshifted respectively to ~ 624 cm^{-1} and ~ 639 cm^{-1}respectively on doping with GO in PG_y ($3 \leq y \leq 15$) blended SBNE material.

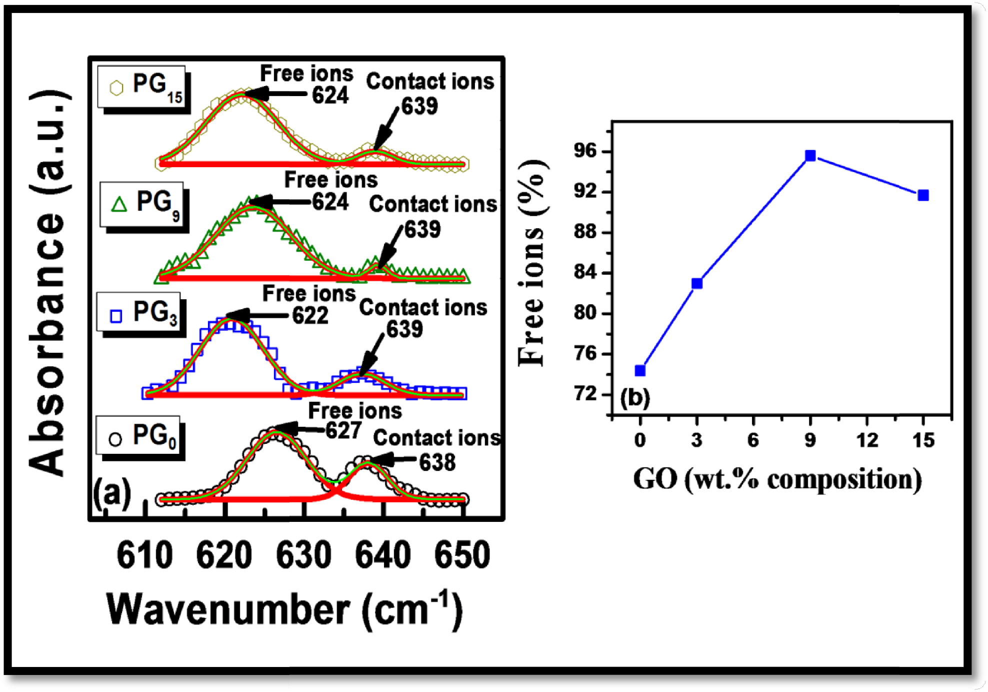

Fig. 9.9. (a) FTIR absorption spectra in the region, 610 cm^{-1} to 650 $cm^{-1}$for PG_y ($0 \leq y \leq 15$) blended SBNE material with different GO compositions. Deconvoluted FTIR absorption spectra based on Gaussian fitting function for the blended SBNE are represented by solid lines, (b) The percentage of free ions as a function of GO compositions in the SBNE.

The percentage of free ions (P_f) is estimated as,

$$P_{\mathrm{f}} = \frac{A_{\mathrm{f}}}{A_{\mathrm{f}}+A_{\mathrm{c}}} \times 100\ \% \qquad (9.16)$$

where, $A_f$is the area under the peak representing the free ions and A_c is the area under the peak representing the contact ion pairs [3,8]. The variation of P_f as a function of GO weight percentages in PG_y ($0 \leq y \leq 15$) blended SBNE material as shown in Fig. 9.9b almost follows the DC conductivity trend of the SBNE material. On doping with GO, P_f is remarkably increased from 74 % (for PG_0) to 96 % (for PG_9) where it reaches the maximum. This attributes to the more dissociation of $LiClO_4$ in the blended CS/PS biopolymer matrix by oxygen-rich functional groups in GO, resulting in an increment in the quantity of free ionic species in PG_y ($0 \leq y \leq 15$) blended SBNE material. Increase in GO beyond $y = 9$ reduces the number of free ions in the blended biopolymer matrix. This may be due to the aggregation of GO which blocks the fast ion-transport network, thereby resulting in a decrease in conductivity beyond the GO doping concentration of $y = 9$.

The transport parameters, D, μ and n of PG_y ($0 \leq y \leq 15$) blended SBNE material containing different GO concentrations as obtained from FTIR deconvolution technique are listed in Table 9.3.These transport parameters are corroborated with the results (Table 9.2) obtained from the impedance analysis considering anomalous diffusion mechanism as discussed in section 9.3.3.5. It is interesting to note here that the highest conducting SBNE material, PG_9exhibits around four fold improved mobility (7.08×10^{-6} $cm^2V^{-1}s^{-1}$) of the free ions, compared to that of the GO free material, PG_0. The increase in mobility of the free charge carriers with GO concentrations is attributed to the fast transport of ions through continuous ion conducting networks formed by GO within the blended SBNE matrix.

A significant red shift of the absorption peaks corresponding to amine ($R\text{-}NH_2$) of chitosan (CS) is observed on increasing the doping concentrations of GO in PG_y ($0 \leq y \leq 15$) SBNE material from ~ 1566 cm^{-1} (for PG_0) to ~ 1524 cm^{-1} (for PG_{15}) as shown in Fig. 9.10a.There is a slight red shift of the absorption peaks corresponding to secondary amide (O=C-NHR) of CS [8,30] is observed from ~ 1645 cm^{-1} (for PG_0)to ~ 1639 (for PG_{15}) (shown in Fig. 9.10a). The deconvolution of these characteristic peaks are displayed in Fig. 9.10a for PG_y ($0 \leq$

$y \leq 15$) SBNE material in order to quantitatively analyze the interactions of Li^+ with amine (R-NH_2) and amide (O=C-NHR) functional groups of CS. The area under the absorption peak corresponding to O=C-NHR in PG_y ($0 \leq y \leq 15$) blended SBNE material is plotted as a function of GO compositions as shown in Fig. 9.10b, where peak area increases with increase in GO content. On the other hand, the area under the absorption peak of R-NH_2decreases significantly with increase in GO content as shown in Fig. 9.10b. This infers that the interaction between the amine (R-NH_2) functional group of CS and Li^+ cation has been significantly weakened on incorporation of GO in PG_y ($3 \leq y \leq 15$) blended SBNE material.

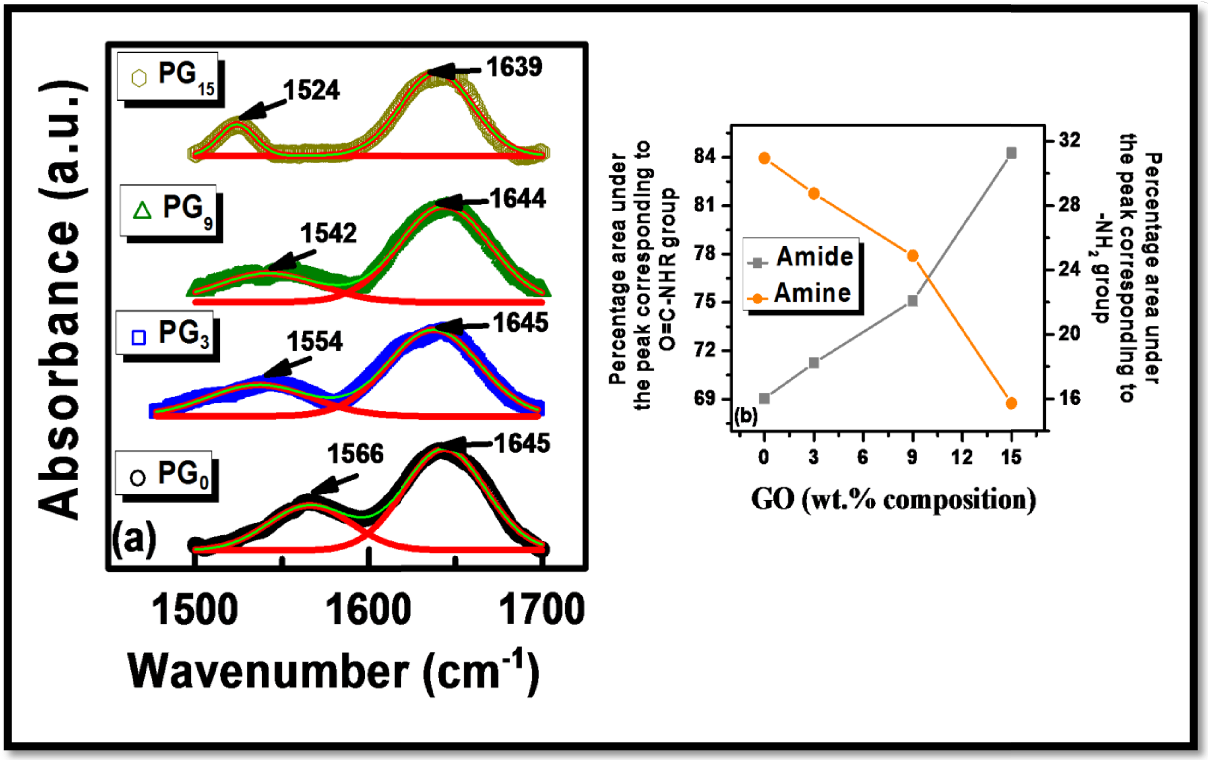

Fig. 9.10. (a) FTIR absorption spectra in the region, 1500-1700 cm^{-1} for PG_y ($0 \leq y \leq 15$) blended SBNE material with different GO compositions. Deconvoluted FTIR absorption spectra in the region of 1500-1700 cm^{-1} based on Gaussian fitting function for the blended SBNE material with different GO compositions are represented by solid lines, (b) Percentage areas under the peaks corresponding to amine and amide groups are shown as a function of GO compositions.

Here, we propose a schematic illustration to explain the effect of GO in PG_y ($0 \leq y \leq 15$) blended SBNE material from the molecular level point of view as shown in Figs. 9.11a and 9.11b. In PG_0 material, Li^+ is tightly coupled to the amine (R-NH_2) and secondary amide (O=C-

NHR) groups of CS as shown in Fig. 9.11a. In this way, the Li^+ transport is directly coupled with the blended biopolymer segmental movement in the PG_0 material. But on incorporation of GO in PG_y ($3 \leq y \leq 15$) blended SBNE material, the strong Lewis acid-base reaction between oxygen containing functional groups of GO and Li^+ ion (as shown in Fig. 9.11b) hugely alleviates the interaction between nitrogen containing functional groups of the blended biopolymer matrix (i.e. $R\text{-}NH_2$ and O=C-NHR) and Li^+, resulting in a faster ion transport rate along the interconnected continuous network created by GO. This results in decoupling of the transport of Li^+ from the blended biopolymer segmental movement [5] and finally enhancing the ionic conductivity in the blended SBNE material.

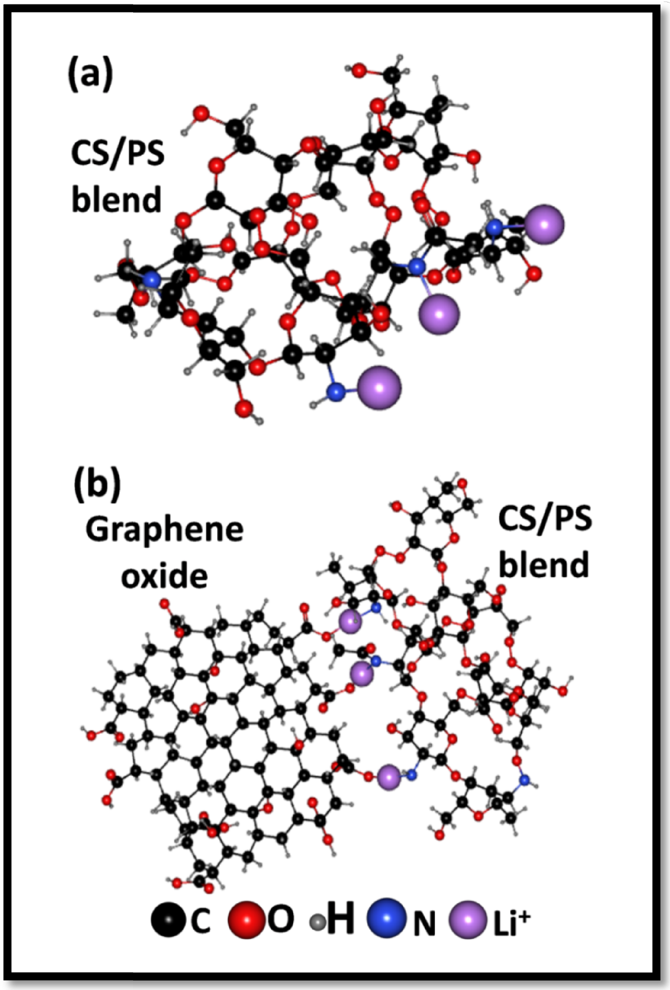

Fig. 9.11. Schematic illustration of Li^+ conduction mechanism in PG_y ($0 \leq y \leq 15$) blended SBNE material (a) GO-free CS/PS blended SBE (PG_0), (b) GO-incorporated CS/PS blended SBNE.

Table 9.3.Values of the transport parameters for PG_y ($0 \leq y \leq 15$) blended SBNE material obtained from FTIR spectroscopy.

Solid biopolymer electrolytes	D (cm^2s^{-1})	μ($cm^2V^{-1}s^{-1}$)	n (cm^{-3})
PG_0	0.04×10^{-6}	1.75×10^{-6}	7.05×10^{20}
PG_3	0.09×10^{-6}	3.68×10^{-6}	7.80×10^{20}
PG_9	0.183×10^{-6}	7.08×10^{-6}	8.83×10^{20}
PG_{15}	0.15×10^{-6}	6×10^{-6}	8.34×10^{20}

9.3.5. Electrochemical characterization

In order to evaluate the electrochemical performance of PG_y ($0 \leq y \leq 15$) SBNE material, a coin type unique symmetric supercapacitor (schematic representation shown in Fig. 9.1) has been developed with active carbon and $MnCoFeO_4$ as electrode materials (represented as AC/MCF electrode). $MnCoFeO_4$ has been chosen as the electrode material owing to its nanoporous structure responsible for high specific capacitance and power density compared to AC electrode alone, as reported in our previous work [3]. The electrode material active mass is ~ 20 mg.

9.3.5.1. Cyclic Voltammetry (CV)

Typical cyclic voltammograms for the cell constructed with AC/MCF electrode and PG_y ($0 \leq y \leq 15$) SBNE material at a scan rate of 5 mV/s over the voltage range from −0.1 to +1.1 V, are shown in Fig. 9.12a.The larger area under the curve of CV indicates higher capacitance value corresponding to PG_9 as compared to other SBNE materials under study. Cyclic voltammograms at different scan rates (2-20 mV/s) with PG_9 SBNE material are shown in Fig.

9.12b. A nearly semi-rectangular shaped CV curve is obtained with all the SBNE materials indicating a good capacitive characteristic behavior of the electrode material.

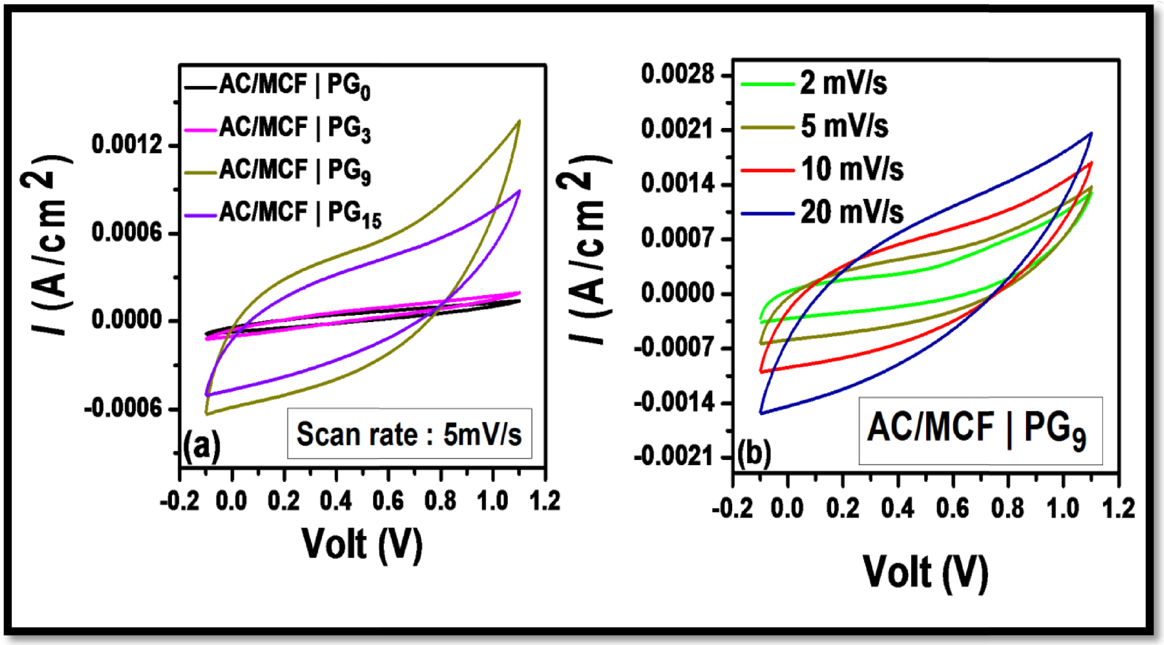

Fig. 9.12.(a) Cyclic voltammograms at a scan rate of 5 mV/s over the voltage range from –0.1 to +1.1 V for the cells constructed with AC/MCF and PG$_y$ ($0 \leq y \leq 15$) SBNE materials, (b) Cyclic voltammograms at different scan rates from 2-20 mV/s over the voltage range from –0.1 to +1.1 V for the cell constructed with AC/MCF | PG$_9$ system.

9.3.5.2. Galvanostatic charge-discharge (GCD)

The applicability of the supercapacitor is evaluated through galvanostatic charge-discharge (GCD) technique. The supercapacitor has been charged and discharged at a constant current within a potential range of -0.6 V to +0.6 V. The GCD for cell constructed with AC/MCF electrode and PG$_y$ ($0 \leq y \leq 15$) SBNE material are performed at a current density of ±300 μA/cm^2. Charge-discharge profiles of the cell with PG$_y$ ($0 \leq y \leq 15$) SBNE material are shown in Fig. 9.13a. The specific capacitance (C_{sp}) of the cell are calculated by GCD using the following equation given as [3],

$$C_{\mathrm{sp}} = \frac{2I}{\frac{\Delta V}{\Delta t} \times m} \tag{9.17}$$

where, $\Delta V$is the potential window (V), m is the mass of the active material per electrode (g), I is the charging current (A) and $\Delta t$is the discharging time (s) [3].The specific capacitance value (C_{sp}) for the cell constructed with AC/MCF electrode and PG_0, PG_3, PG_9 and PG_{15} SBNE materials at a current density of 300 μA/cm^2 are 1.5 Fg^{-1}, 6 Fg^{-1}, 46 Fg^{-1} and 15 Fg^{-1}, respectively.

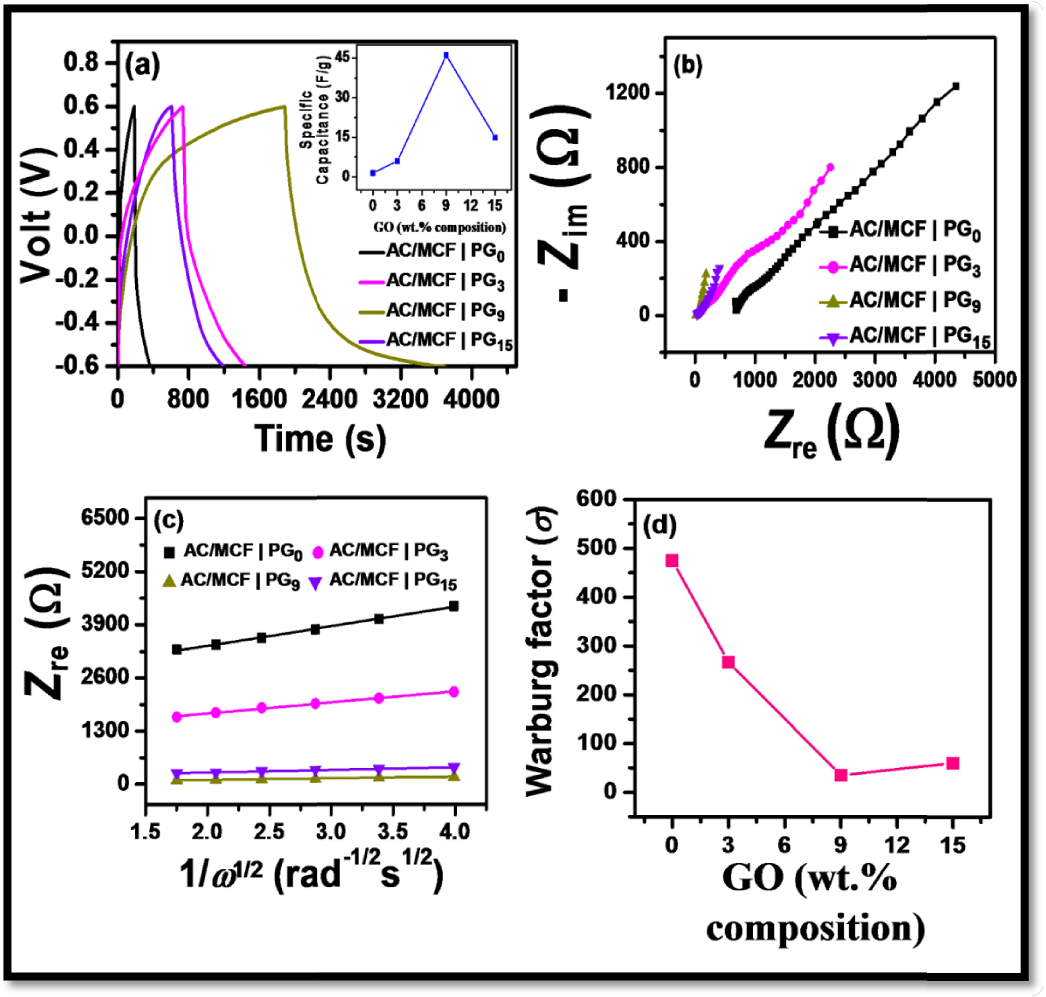

Fig. 9.13. (a) Galvanostatic charge-discharge for the cells constructed with AC/MCF and PG_y ($0 \leq y \leq 15$) SBNE materials. Inset of (a) shows the variation of specific capacitance as a function of GO compositions, (b) Nyquist plots for AC/MCF with PG_y($0 \leq y \leq 15$) SBNE materials over a low frequency range of 100KHz – 10 mHz, (c) the variation of the real impedance (Z_{re}) and the inverse square root of frequency ω at low-frequency range (10 mHz to 50 mHz), (d) Variation of Warburg factor for different GO compositions in the PG_y($0 \leq y \leq 15$) SBNE material with AC/MCF as electrode material.

The variation of specific capacitance as a function of GO concentrations is shown in the inset of Fig. 9.13a.This clearly suggests that the highest ion conducting SBNE material (PG_9) which exhibits highest dielectric constant shows the maximum value of specific capacitance. The Coulomb efficiency (η) comes as ~ 97 % with AC/MCF | PG_y ($0 \leq y \leq 15$) SBNE material. A much higher charging and discharging times at a current density of300 µA/cm^2 is observed with (AC/MCF) | PG_9 system, as compared with (AC/MCF) | PG_0 system (shown in Fig. 9.13a).

Energy density (E_D) and power density (P_D) are important parameters for the evaluation of the electrochemical performance of the supercapacitors, which can be estimated from the relation given as [3,31],

$$E_D = \frac{1}{2}\left[\frac{C_{sp}\Delta V^2}{3.6}\right] \text{Wh/kg} \qquad (9.18)$$

$$P_D = \left[\frac{E_D}{t_d}\right] \times 3600 \text{ W/kg} \qquad (9.19)$$

Achievement of the highest energy density of 9.05 Whkg^{-1} at a power density 18 Wkg^{-1} suggest that (AC/MCF) | PG_9 system as a promising combination for future development of safe and cost-effective solid-state hybrid supercapacitors.

9.3.5.2. Electrochemical impedance spectroscopy (EIS)

Electrochemical impedance spectroscopy (EIS) is a significant technique to explore the kinetics of the electrolyte ions responsible for charge accumulation. Fig. 9.13b demonstrates the typical Nyquist plots for AC/MCF | PG_y ($0 \leq y \leq 15$) SBNE material over a low frequency range of 100 KHz – 10 mHz. It is observed that the contact resistance R_s (between the current collector and electrode and that with the electrode and electrolyte) has been decreased significantly on doping the blended SBE with GO, i.e.PG_y ($3 \leq y \leq 15$)SBNE material, revealing intimate contact between electrode-electrolyte. This indicates that GO helps in the formation of a stable solid SBNE-electrode interface.

An important parameter is Warburg factor (σ) which gives information relating to the diffusion of ions in the electrode pores [32], can be calculated based on the linear Randles relation [33],

$$Z_{\mathrm{re}} = R_{\mathrm{D}} + R_{\mathrm{L}} + \sigma\omega^{-\frac{1}{2}} \tag{9.20}$$

The slope of the linear relationship between the real impedance (Z_{re}) and the inverse square root of frequency ω at low-frequency range (10 mHz to 50 mHz) gives the Warburg factor (σ) as shown in Fig. 9.13c. It is found that the value of σ which comes out as 475 with PG_0 material has been decreased to 35 with PG_9 SBNE material (Fig. 9.13d). The lower value of Warburg factor with GO addition is attributed to more mass transfer of ions in the porous electrode structure at lower frequencies, resulting high capacitance value with AC/MCF | PG_9 system. The probable mechanism associated with the supercapacitive behavior of AC/MCF | PG_9 system can be related to the presence of Mn^{2+}/Mn^{3+} redox system in $MnCoFeO_4$. These redox states of manganese in $MnCoFeO_4$ electrode material play a significant role in exchanging the charge carriers (Li^+) between electrode and solid electrolytes. The nanoporous structure of $MnCoFeO_4$ allow the Li^+ ions to easily diffuse into the electrode nanopores and access their internal surface.

As reported in our previous study [3], a realistic approach of maximum 10,000 diffusion length (i.e.80 micron) inside the AC/MCF electrode material has been considered for the estimation of the effective specific capacitance (C_E) of the electrode with respect to solid biopolymer nanocomposite electrolyte (SBNE).The effective specific capacitance (C_E) of AC/MCF | PG_9 system has been achieved as high as ~ 288Fg^{-1}, which makes this combination a promising candidate for future development of a safe, cost-effective and flexible solid state supercapacitor.

9.4. Conclusion

In summary, a novel hybrid symmetric solid-state supercapacitor are fabricated with nano-crystallites manganese cobalt ferrite ($MnCoFeO_4$) as electrode material and graphene oxide (GO) incorporated solid biopolymer blended electrolytes based on chitosan (CS) and potato starch (PS) with $LiClO_4$ as a charge carriers, glycerol as a plasticizer. Incorporation of GO helps to tune the ionic conductivity of the CS/PS blended nanocomposite electrolytes by an order of magnitude (~ 10^{-3} S/cm) at room temperature (300 K). The transport properties of the blended composites are calculated from FTIR spectroscopy revealing four fold improved mobility of the free ions on the inclusion of GO. The frequency dependent conductivity spectra has been analyzed based on a model which takes into account the effects of electrode polarization by considering the fractal nature of the electrode-SBNE interface. The intra diffusion processes inside the GO incorporated CS/PS blended SBNE material is analyzed based on a fractional diffusion model. The dielectric constant of the blended composite is 50 times enhanced on incorporation of GO in the CS/PS blended SBNE with significant reduction of loss factor. The highly non-exponential behavior of the relaxation function suggests non-Debye relaxation phenomenon within the SBNE material. The percentage of free ions in the blended composites are significantly increased on incorporation of GO. The oxygen rich functional groups of GO results an increase of free Li^+ ion dissociation due to Lewis acid-base reaction in the blended SBNE. Moreover, a maximum effective specific capacitance value of 288 Fg^{-1} is obtained with GO doped PS-rich blended SBNE containing 9 wt. % GO.

Chapter 10

Graphene oxide induced high dielectricity in CS/PMMA solid polymer electrolytes and the enhanced specific capacitance with Ag decorated $MnCoFeO_4$ nanoparticles anchored graphene sheets in hybrid solid-state supercapacitors

10.1. Introduction

Nowadays, global energy demands for all energy sources (viz. coal, natural gas, oil and renewables) have risen rapidly. The increasing consumption of fossil fuels is one of the major reasons behind the global climate change. Though the usage of the renewable energy sources (such as solar energy, wind energy etc.) can effectively reduce the emissions of greenhouse gases but their dependence on the condition of weather is the greatest barrier in using these resources to their full capacity. This leads to the development of green, cost-effective and highly efficient energy storage devices. Nowadays supercapacitors or ultracapacitors are the best energy storage systems which provide high power and energy densities, long cycle life and offers faster charging ability, thereby bridging the gap between batteries and traditional capacitors. They have promising applications in hybrid electric vehicles, backup systems etc. Thus, exploring new electrode and electrolyte materials for supercapacitors are the emerging areas of research.In recent years, major attention has been given to the solid polymer electrolyte (SPE) materials owing to their potential technological applications in both rechargeable lithium ion batteries and solid state supercapacitors [1-3]. Besides being leakage-free, SPE materials possess good thermal and electrochemical properties [4] which make them suitable replacement of liquid electrolytes in charge storage devices. But the major limitation of the SPE materials is their poor ionic conductivities at room temperature. Intensive efforts have been made for several years to improve their ionic conductivity. Polymer blending is a very popular technique which has been performed to improve the electrical as well as thermal properties of the SPE materials. The overall crystallinity of the SPE can be usually reduced by blending two polymers [5].The biodegradability of chitosan (CS) which is easily derivable from the shell of shrimps and crabs and its ability to form mechanically strong thin film makes them promising candidate for SPE materials in supercapacitor applications [2,6,7]. But low ionic conductivity of CS[6] demands blending with other polymers to improve its conductivity[2,7]. Recently polymethyl methacrylate (PMMA) has attracted much attention due to the presence of bulky electron donating ester functional group (O=C-O-CH_3) which is particularly active in coordinating with the alkali metal salt cations [8-9]. Thus, PMMA has been considered to blend with CS in this present investigation. The blended polymers are usually doped with plasticizers and alkali metal salts (as a source of charge carriers)to achieve high ionic conductivity [2,10]. Nowadays, nanofiller incorporation in the solid polymer electrolytes has been considered as a very useful technique for the remarkable enhancement of conductivity. Various research groups have reported the incorporation of different inorganic nanofillers (SiO_2, CeO_2, Al_2O_3) into the SPE which improves both the electrical and mechanical properties of the materials [11-13]. Amongst the various nanofillers of practical interest, graphene oxide (GO) is immensely considered due to the multiple oxygen containing functional groups (carboxyl, hydroxyl and epoxy) on its basal planes and edges and its ultra-large surface area [14-15].

During the last few decades, different nanomaterials have been synthesized and investigated for supercapacitor electrodes such as carbon materials, conducting polymers and transition metal oxides [16-19]. Among various alternatives, manganese cobalt ferrite ($MnCoFeO_4$) is a promising electrode material due to their high specific capacitance and power density [2,20]. The presence of silver nanoparticles (AgNP) can remarkably reduce the electrical resistance of the composite [21]. Also the unique physical and chemical properties of AgNP can significantly enhance the electrochemical performance of a supercapacitor [22]. On the other hand, Graphene sheet has extensively gathered huge attention as electrode materials because of its high surface area and remarkable electrical conductivity [23-24]. Moreover, graphene provides stable mechanical support to the active electrode materials [26] resulting a potential composite for supercapacitor applications.

The present work reports the ionic conduction and dielectric properties of the graphene oxide (GO) grafted CS/PMMA blended solid polymer electrolytes. The thermal properties of the solid nanocomposite electrolytes has been systematically studied for different doping concentrations of GO. The ion diffusion processes in the nanocomposite electrolytes has been investigated with a fractional diffusion model. The ionic interactions with the blended host polymers in the nanocomposites have been examined through FTIR spectroscopy analysis. Finally, a novel hybrid solid-state symmetric supercapacitor has been developed with silver decorated manganese cobalt ferrite ($MnCoFeO_4$) nanoparticles anchored onto the graphene (rGO) sheets as electrode material and GO grafted CS/PMMA blended solid polymer nanocomposite electrolyte with an effective specific capacitance of $C_E \sim 294$ Fg^{-1}, which is ~ 2.5 times enhanced compared to that with $MnCoFeO_4$ electrode.

10.2. Experimental

10.2.1. Synthesis of the GO grafted CS/PMMA solid polymer nanocomposite electrolytes (SPNE)

Graphene oxide (GO) has been chemically prepared from pure graphite powder following modified Hummers's method [27]. Chitosan/Polymethyl methacrylate (CS/PMMA) has been blended in the ratio of 20:80 and 80:20 with $LiClO_4$ salt at a concentration of 80 wt.% (weight percentage of the blended polymer) and glycerol as a plasticizer at a concentration of 30 wt.% (weight percentage of the blended polymer). CS was dissolved in 50 ml of 1% aqueous acetic acid solutions and stirred at 50°C for 20 minutes. PMMA was dissolved in 25 ml DMF and stirred at 90 °C for 15 minutes. The CS/PMMA blended solid polymer electrolytes were prepared by solution casting technique as reported earlier in our previous works [2,10]. To prepare the GO grafted CS/PMMA solid polymer nanocomposite electrolytes (SPNE), various weight percentages of graphene oxide, GO (3, 9, 15 wt. %) were dispersed individually in 50 ml of 1% aqueous acetic acid solutions and probe sonicated in an ultrasonic processor UP400S (400 Watts, Hielscher) until a homogenous solution is obtained. Then CS is added in the sonicated GO solutions, followed by stirring and heating at 50℃ for 20 minutes. Solution of PMMA in DMF at 90 °C is mixed with the CS/GO solution and stirred for 10 minutes. Then 30 wt. % glycerol and 80 wt. % $LiClO_4$ were added subsequently in the CS/PMMA/GO blended solutions and stirred continuously until a homogenous viscous solution was obtained. Finally, the resulting homogenous solutions were cast on polypropylene petri dishes and allowed to dry in a vacuum oven at 40 °C. All the materials were characterized by computer interfaced impedance analyzer (Solartron SI 1260 Impedance Analyzer) in the frequency range between 10 Hz and 100 KHz at room temperature (300 K). Differential Scanning Calorimetry (DSC) measurement was done using DSCQ 2000 TA Instrument (Waters India) in the temperature range from 0 to 200 °C at a constant heating rate of 10 °C/min. Fourier transform infrared (FTIR) spectroscopy was performed using Perkin Elmer FT-IR Spectrum 2 spectrometer having resolution of 4 cm^{-1}.

10.2.2. Synthesis of the Ag-$MnCoFeO_4$@rGO nano-composite

The $MnCoFeO_4$ nanoparticles were synthesized based on the method as reported in our earlier work [2]. $MnCoFeO_4$ nanoparticles decorated with Ag nanoparticles were embedded onto reduced graphene oxide (rGO) sheet by dispersing 16.987 mg of $AgNO_3$, 40 mg of GO and 100 mg of $MnCoFeO_4$ in 150 ml of deionised water and sonicating the mixture in the ultrasonic processor UP400S (400 Watts) for 30 minutes. Then the solution was heated at 100 °C and ~ 7.5 ml of Hydrazine Hydrate solution (99-100 %) was added dropwisefor reduction of both Ag^+ ions and GO. Stirring at 100 °C had been done initially for 4 hours, after which stirring was continued at room temperature for the next 20 hours which is followed by centrifugation and washing by deionised water and ethanol. Then the collected precipitate was dried at 100 °C and the desired Ag-$MnCoFeO_4$@rGO nanocomposite is formed. The yield of rGO by hydrothermal reduction of

GO has been estimated [25,28] to be around 50 %. The weight fraction of rGO in the Ag-MnCoFeO$_4$@rGO nanocomposite has been determined by the following equation,

$$\varphi = \frac{\mathrm{w}_{\mathrm{GO}} \times 0.5}{(\mathrm{w}_{\mathrm{GO}} \times 0.5) + \mathrm{w}_{\mathrm{Ag}} + \mathrm{w}_{\mathrm{MnCoF}\quad{}_4}}$$

where,$\mathrm{w}_{\mathrm{MnCoFeO_4}}$, w_{GO} and w_{Ag} denote the mass of MnCoFeO$_4$, GO and Ag, respectively. The weight fractions of Ag nanoparticles, rGO and MnCoFeO$_4$ in the Ag-MnCoFeO$_4$@rGO nanocomposite are 8 wt. %, 15 wt. % and 77 wt.%. The graphene oxide (GO), MnCoFeO$_4$ nanoparticles and Ag-MnCoFeO$_4$@rGO nanocomposite were characterized by X-ray diffraction (XRD) which was done by X-ray diffractometer (model: Bruker D8 Advance) using the CuKα radiation of wavelength 1.5406Å. Raman spectroscopy measurement for the Ag-MnCoFeO$_4$@rGO nanocomposite was performed in backscattering geometry using LabRAM HR (Jobin Yvon) spectrometer equipped with a Peltier-cooled charge-coupled-device (CCD) detector.

10.2.3. Fabrication of the symmetric hybrid super-capacitor with Ag-MnCoFeO$_4$@rGO nanocomposite as electrode

The electrodes of the symmetric supercapacitor were fabricated by using a paste of a homogeneous mixture made of Ag-MnCoFeO$_4$@rGO, acetylene black (AB) and polytetrafluoroethylene (PTFE) taken in the wt. % ratio of 50:45:5. The paste was then compacted into a thin sheet using mortar and pestle and compressed on a stainless steel mesh having the surface area of 1 cm^2. The prepared electrode was heated at 60°C for 6 h under vacuum to evaporate the solvent completely. The total weight of the active material in the electrode is usually ~20 mg. Electrochemical behavior of the fabricated cell was investigated with AUTOLAB-30 potentiostat/galvanostat.

10.3. Results and Discussion

10.3.1. X-ray Diffraction (XRD)

GO, $MnCoFeO_4$ and Ag-$MnCoFeO_4$@rGO nanocomposite are characterized by XRD. The X-ray diffraction pattern (XRD) measured at room temperature in the 2θ range of 7°-50° for graphene oxide (GO) is shown in Fig. 10.1a. It shows two peaks around $2\theta = 10.8°$ and $2\theta = 43.25°$ corresponding to (002) and (100) planes, respectively. Figure 10.1b illustrates the XRD patterns of $MnCoFeO_4$ nanoparticles and Ag-$MnCoFeO_4$@rGOnanocomposite. The XRD pattern of Ag-$MnCoFeO_4$@rGO nanocomposite reveals peaks of both $MnCoFeO_4$ and silver nanoparticles with no characteristic peak for rGO.

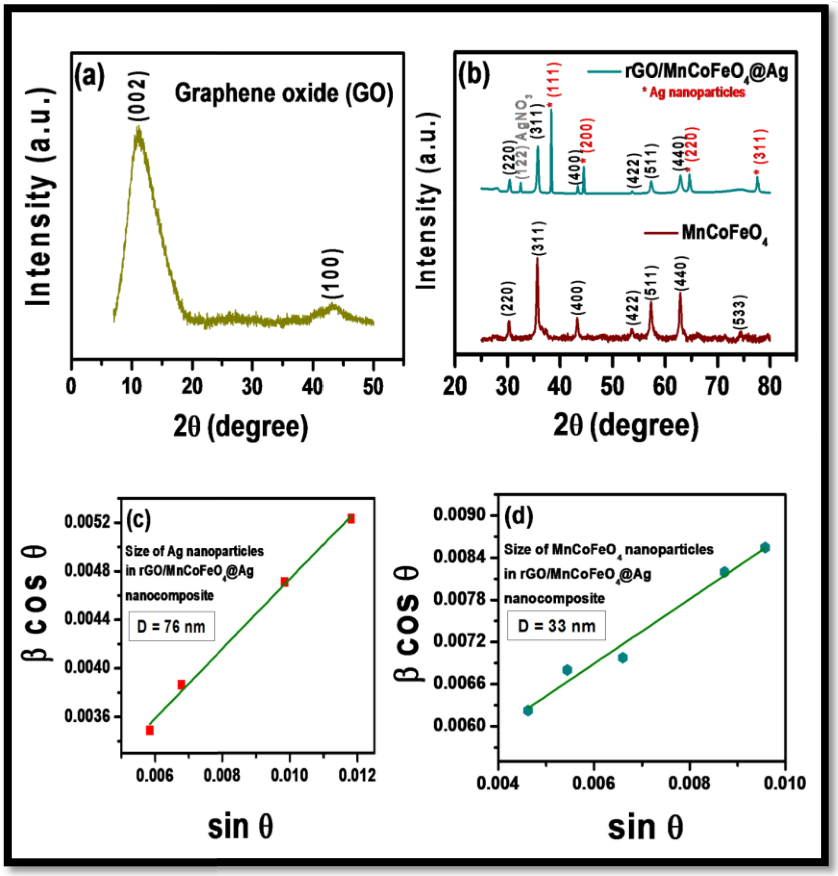

Fig. 10.1. (a) XRD spectrum of Graphene Oxide (GO), (b) XRD spectrum of $MnCoFeO_4$ and Ag-$MnCoFeO_4$@rGO nanocomposite, (c-d) Williamson–Hall plot for Ag and $MnCoFeO_4$ nanoparticles in Ag-$MnCoFeO_4$@rGO nanocomposite, respectively.

The signature of rGO in the nanocomposite has been confirmed from Raman spectroscopy studies which will be discussed in details in the subsection 10.3.2. All the lines in the XRD patterns are unambiguously indexed for different (hkl) planes which corresponds to spinel cubic structured $MnCoFeO_4$ (JCPDS #22-1086) and a face centered cubic structured Ag (JCPDS #04-0783). Trace amount of unreacted silver nitrate salt ($AgNO_3$) is detectable in the XRD pattern of nanocomposite, as reported earlier in the synthesis of Ag nanoparticles [29-30].The crystallite sizes of Ag and $MnCoFeO_4$ nanoparticles in the Ag-$MnCoFeO_4$@rGO nanocomposite are calculated by using Williamson and Hall's modified Scherrer's formula which is given as [31],

$$\beta \cos \theta = \frac{0.89\lambda}{D} + 2\varepsilon \sin \theta \tag{10.1}$$

Figures 10.1c-d show the $\beta \cos \theta$ vs $\sin \theta$ plots revealing the average particle sizes of Ag and $MnCoFeO_4$ nanoparticles in Ag-$MnCoFeO_4$@rGO nanocomposite respectively as 76 nm and 33 nm.

10.3.2. Spectroscopic characterization: Raman spectroscopy

The spectroscopic characterization and the structural properties of the Ag-$MnCoFeO_4$@rGO nanocomposite has been explored by Raman spectroscopy. Figure 10.2a shows the Raman spectra for Ag-$MnCoFeO_4$@rGO nanocomposite in the region of 450-2000 cm^{-1}. The peaks appearing at 466 cm^{-1} corresponds to the T_{2g} phonon mode, while the peak at 616 cm^{-1} is assigned to A_{1g} phonon mode of $MnCoFeO_4$ [32]. Mode A_{1g} represents the symmetric stretching vibration of metal-oxygen bond at tetrahedral site, while T_{2g} mode represents the characteristic vibration in the octahedral site [32]. Figure 10.2b shows the deconvoluted D band (~ 1353 cm^{-1}) and G band (~ 1588 cm^{-1}).The D band emerges due to the local defects and disordered atomic arrangement caused by the sp^3carbon atom, while the G band appears due to the in-plane stretching vibration of the sp^2 carbon of rGO. The ratio of I_D / I_G (= 1.79) which is a measure of disorder present in the rGO composite, is found to be significantly larger compared to that of rGO (~ 1.00) as reported by Sarkar *et al* [25]. This may be due the defects induced in the graphene (rGO) sheet by embedding silver decorated $MnCoFeO_4$ nanoparticles onto it.

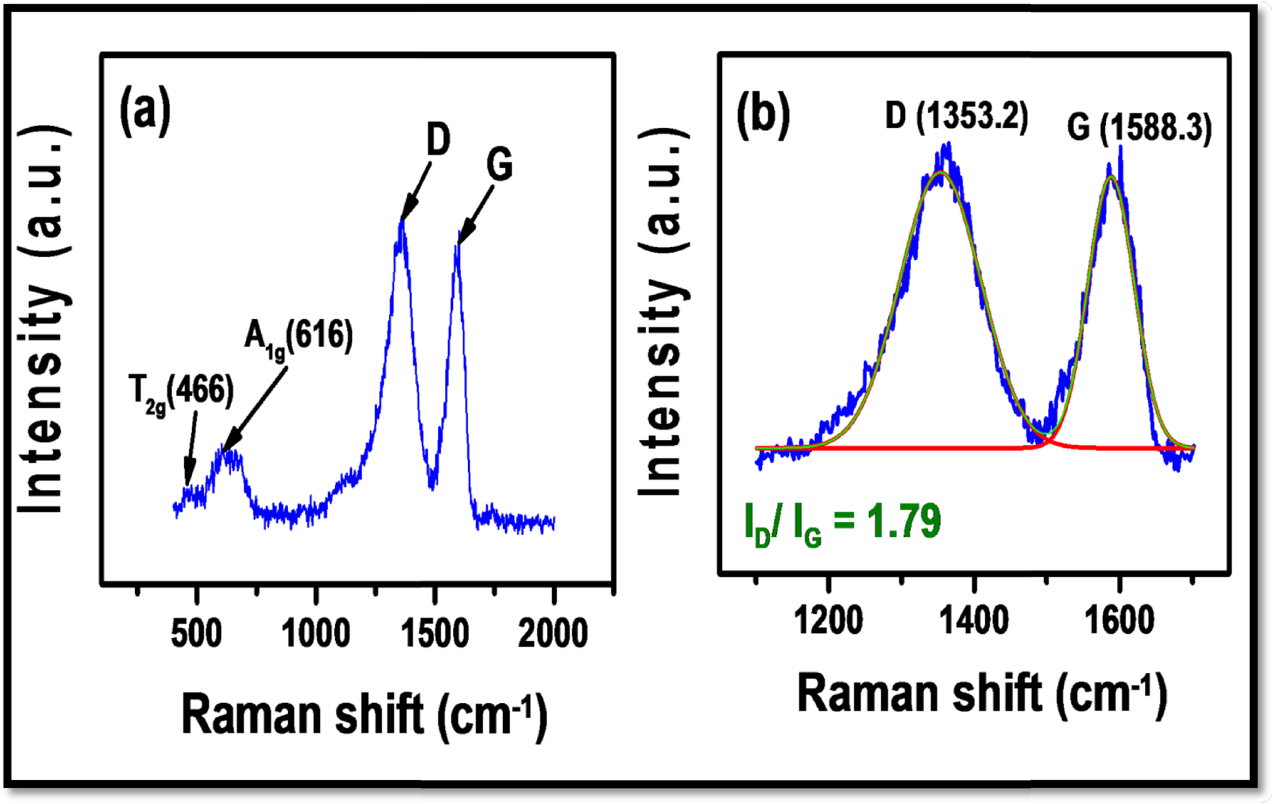

Fig. 10.2. (a) Raman spectra for Ag-$MnCoFeO_4$@rGO nanocomposite, (b) Deconvolution of D and G bands in Ag-$MnCoFeO_4$@rGO nanocomposite using Gaussian fitting function.

10.3.3. Differential Scanning Calorimetry (DSC)

The DSC thermograms of CS/PMMA blended solid polymer electrolyte (SPE) material having different blended compositions of chitosan (CS) and polymethyl methacrylate (PMMA) with $LiClO_4$ salt at a concentration of 80 wt.% and glycerol as a plasticizer at a concentration of 30 wt.% are shown in Fig. 10.3a. A broad endothermic peak is observed for both the CS-rich [CS/PMMA (80:20)] and PMMA-rich [CS/PMMA (20:80)] blended composites (Fig. 10.3a). The area under the endothermic peak which corresponds to the amount of crystalline phase content present in the blended composites [13] has been significantly decreased for PMMA-rich composites as compared with CS-rich material. The endothermic peak has been assessed as the melting temperature (T_m) of the crystalline phase of the polymers. It is to be noted here that T_m decreases slightly from 124℃ to 123℃ due to the increment in PMMA in the blend. Reduction of the crystalline phase favors the ionic conduction in CS/PMMA (20:80) blended SPE as discussed in the section 10.3.4.1.

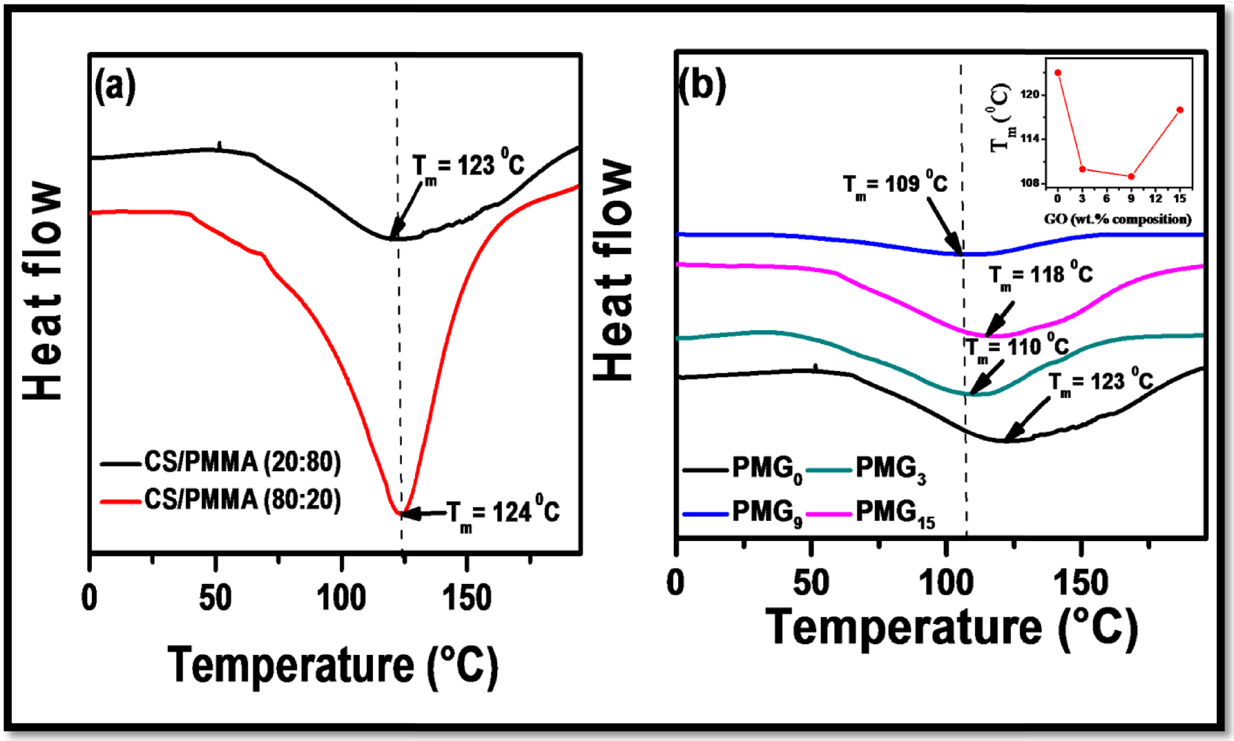

Fig. 10.3. (a) DSC thermograms of CS/PMMA (80:20) and CS/PMMA (20:80) blended solid polymer electrolytes, (b) DSC thermograms of PMG_x ($0 \leq x \leq 15$) SPNE material while its inset shows the variation of melting temperature T_m as a function of GO doping concentrations.

For further enhancement of ionic conductivity of the solid polymer electrolyte, CS/PMMA(20:80) is doped with different concentrations of graphene oxide (GO) as a nanofiller (3, 9 and 15 wt% of the blending polymer). The GO grafted PMMA-rich blended solid polymer nanocomposite electrolyte (SPNE) materials are henceforth denoted as PMG_x where x = 0, 3, 9 and 15. Hence CS/PMMA (20:80) and PMG_0 are synonymous. The DSC thermograms of PMG_x ($0 \leq x \leq 15$) SPNE materials are shown in Fig. 10.3b. A significant drop in T_m is observed on incorporation of GO in the polymer blend. This suggests that the fraction of the amorphous phase content in GO grafted PMMA-rich SPNE materials has been effectively increased[13]. The lowest value of T_m (109°C) is obtained for PMG_9 SPNE. Moreover, the area under the endothermic peak has been remarkably reduced for PMG_9 as illustrated in Fig. 10.3b. These results strongly support the remarkable reduction of crystallinity in PMG_9 which in turn enhances the ionic conductivity of the SPNE material as discussed in the subsequent section 3.4.1. However, further increase in concentrations of GO beyond x = 9 increases the melting temperature (T_m) of the blended composite. This may be due to the overall enhancement of crystallinity of the blended SPNE.

10.3.4. Impedance spectroscopy

10.3.4.1. AC Conductivity and scaling

To probe the ionic conductivity and charge carrier relaxation dynamics in the CS/PMMA blended solid polymer electrolyte (SPE) material, the frequency dependent conductivity spectra has been examined. The AC conductivity has been calculated using the relation given as, $\sigma(\omega) = \omega\varepsilon_0\varepsilon_{im}$ where, ε_0 is the vacuum permittivity (8.854 $\times 10^{-14}$ F/cm) and ε_{im} is the dielectric loss. Figure 10.4a represents the frequency dependent AC conductivity spectra at 300 K for the SPE containing different blending compositions of CS/PMMA, while that for PMG$_x$ ($0 \leq x \leq 15$) SPNE material has been shown in Fig. 10.4b. A large dispersive region at lower frequencies followed by an almost frequency independent plateau region has been observed for all the samples in the frequency range under investigation. The low frequency dispersive region arises due to the charge-carrier accumulation at the interface between electrode and electrolyte, while the plateau region almost independent of frequency corresponds to the DC conductivity.

The frequency dependent complex AC conductivity has been analyzed considering the fractal nature of the electrode-electrolyte interface which is given as [6,33],

$$\sigma(\omega) = \sigma_0 + \frac{\sigma_{DC} - \sigma_0}{1 + (i\omega\tau_j)^{-\alpha}} + i\omega\ {}_0[\varepsilon_{relax}(\omega) - \varepsilon_\infty] \qquad (10.2)$$

where, σ_{DC} is the DC conductivity of the electrolyte material, σ_0 is the conductivity at constant electric field, ε_0 is the vacuum permittivity (8.854 $\times$ 10^{-14} F/cm), $\varepsilon_{relax}(\omega)$ determines the contribution of the dielectric relaxation part, ε_∞ is the high frequency limiting value of dielectric permittivity, τ_j is the characteristic relaxation time and α is a constant determining the fractal dimension of the space-time ensemble in the space-charge region having its value lies between 0 and 1. The real part of the frequency dependent conductivity spectra for the SPE containing different blending compositions of CS/PMMA and PMG$_x$ ($0 \leq x \leq 15$) SPNE material are fitted using Eq. 10.2 and are shown in Figs. 10.4a and 10.4b, respectively. The model parameters are listed in Table 10.1. It is to note here that the values of σ_{DC} and σ_0 does not coincide due to the effects of electrode polarization and the value of σ_0 is much less than σ_{DC}.

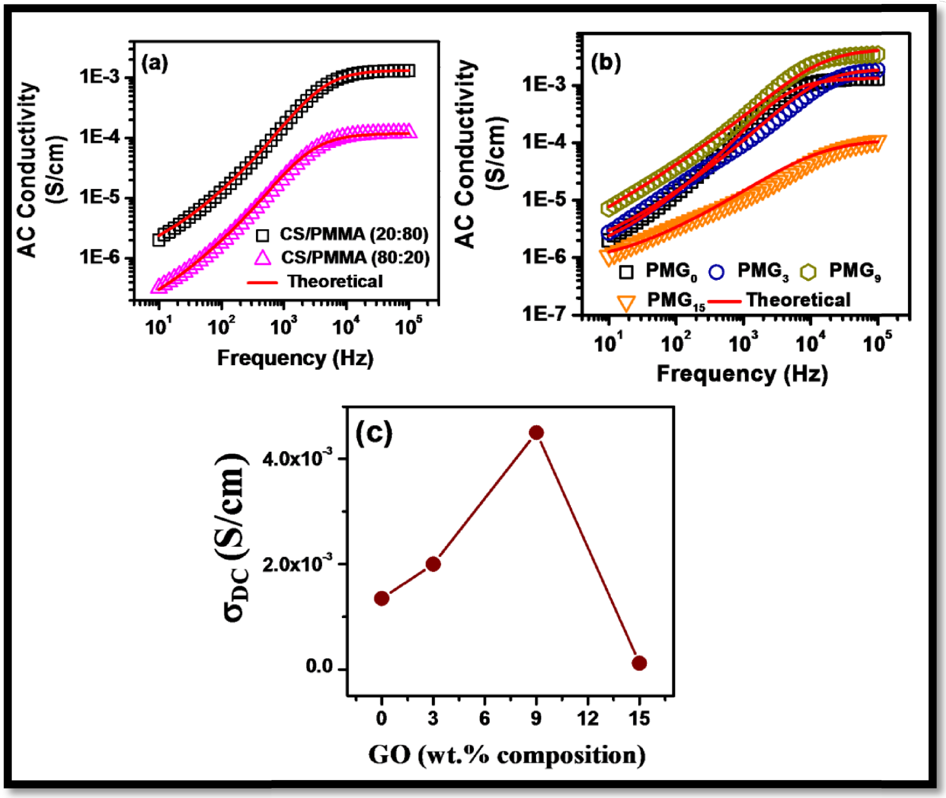

Fig. 10.4. AC conductivity spectra of (a) CS/PMMA (80:20) and CS/PMMA (20:80) blended SPE, (b) PMG_x ($0 \leq x \leq 15$) SPNE material. Solid lines are the fits of the experimental data to Eq. 10.2, (c) Variation of DC conductivity as a function of GO doping concentrations.

It is observed that the ionic conductivity (σ_{DC}) of the blended CS/PMMA SPE material increases from ~ 1.2×10^{-4} to ~ 1.35×10^{-3} S/cm on increasing PMMA blending concentrations from 20 % to 80 %. This conductivity enhancement in PMMA-rich [CS/PMMA(20:80)] blended SPE material is assigned to the reduction of crystallinity in the composite on increasing the PMMA concentrations, as evident from the DSC results. As illustrated in Fig. 10.4c, doping the PMMA-rich composite with GO, the ionic conductivity increases from ~ 1.35×10^{-3} S/cm (for PMG_0) to ~ 4.5×10^{-3} S/cm (for PMG_9) at room temperature. However, further increase of GO beyond $x = 9$ decreases the ionic conductivity. Lewis acid-base reaction between the oxygen containing functional groups of GO (carboxyl, hydroxyl and epoxy) and Li^+ ion at lower GO doping concentrations ($x \leq 9$), weakens the interaction between the polymer and the cation which enhances the segmental movement of the blended CS/PMMA polymers. This increases the ion transport rate through the continuous network formed by GO. Moreover, the overall crystallinity of the polymer blend has been effectively reduced in presence of GO, as inferred from DSC results which supports this conductivity enhancement. Aggregation of GO and inhomogeneity in the composite may occur at higher doping concentrations ($x > 9$) which results in partial blocking of the fast ion transport channel and therefore, conductivity gets decreased. The values of α for all the samples are found to be less than unity which indicates the fractal dimension of the electrode-electrolyte interface. Also the relaxation time (τ_j) corresponding to the highest conducting sample, PMG_9 is the lowest (~ 1.3×10^{-5} s), as expected.

The scaling behavior of the AC conductivity spectra is studied in order to gain an insight into the blending and nanofiller composition dependence of the charge carrier relaxation dynamics. The AC conductivity has been scaled by the DC ionic conductivity (σ_{DC}) and the ion-hopping frequency (ω_p) with an appropriate choice for the scaling factor, $\omega_p = \frac{\sigma_{\mathrm{DC}}}{\varepsilon_0 \Delta\varepsilon_r}$ [34,35] where, $\Delta\varepsilon_r = [\varepsilon_r(\omega \to 0) - \varepsilon_r(\omega \to \infty)]$ which is exclusively dependent on the hopping motion of the mobile ions.This leads to the following scaling law for the real part of the AC conductivity given as [34,35],

$$\frac{\sigma(\omega)}{\sigma_{\mathrm{DC}}} = F\left(\frac{\omega}{\omega_p}\right) \tag{10.3}$$

Figures 10.5a and 10.5b represents the scaled AC conductivity curve for the SPE containing different blending compositions of CS/PMMA and PMG_x ($0 \leq x \leq 15$) SPNE material, respectively at 300 K according to Eq. 10.3. It is evident from Fig. 10.5a that the scaling results for the AC conductivity spectra of the SBE containing different blending compositions of CS/PMMA merges to a common master curve. This near-perfect overlap of the conductivity spectra on a single master curve suggests that the nature of ion relaxation dynamics in CS/PMMA SPE material follows a common mechanism over the entire frequency range under investigation. This infers that the relaxation dynamics of ions can be characterized by a universal function which is independent of blending compositions, i.e. the different blending compositions of CS and PMMA are only affecting the intra diffusion rate and/or number density of free mobile charge carriers without influencing the conduction mechanism. But the scaling results for the AC conductivity spectra of PMG$_x$ ($0 \leq x \leq 15$) SPNE material (as shown in Fig. 10.5b) shows that the curves cannot be scaled on a common master curve. This indicates that the relaxation mechanism depends on the GO doping concentrations in PMG$_x$ ($0 \leq x \leq 15$) SPNE material.

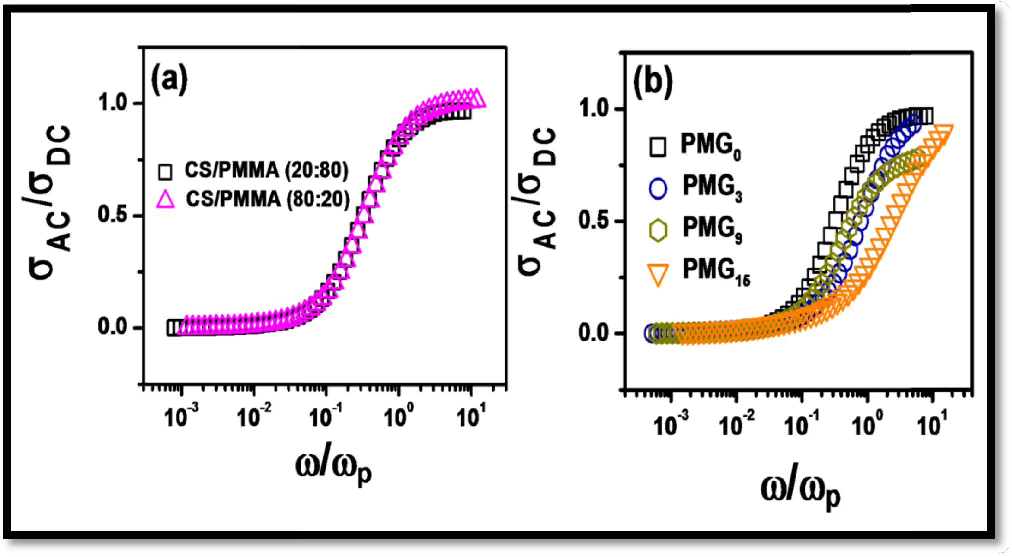

Fig. 10.5. Scaling behavior of AC conductivity spectra for (a) CS/PMMA (80:20) and CS/PMMA (20:80) blended SPE, (b) PMG$_x$ ($0 \leq x \leq 15$) SPNE material.

Table 10.1. Values of the fitting parameters σ_{DC}, σ_0, τ_j, α for CS/PMMA blended SPE and PMG$_x$ ($0 \leq x \leq 15$) SPNE material.

Solid polymer electrolytes	σ_{DC} (S/cm)	σ_0 (S/cm)	τ_j (s)	α
CS/PMMA (80:20)	1.2×10^{-4}	8×10^{-8}	6×10^{-5}	0.86
CS/PMMA (20:80)	1.35×10^{-3}	9×10^{-7}	3.9×10^{-5}	0.87
PMG$_3$	2×10^{-3}	9.8×10^{-7}	1.4×10^{-5}	0.81
PMG$_9$	4.5×10^{-3}	1×10^{-6}	1.3×10^{-5}	0.77
PMG$_{15}$	1.2×10^{-4}	7×10^{-7}	1.5×10^{-5}	0.67

10.3.4.2. Ionic diffusion

The role of the ions on the measured electrochemical impedance values of the SPE containing different blending compositions of CS/PMMA and PMG$_x$ ($0 \leq x \leq 15$) SPNE material specifically in the low frequency regime, is calculated in the framework of a model developed by Lenzi *et al* [36] in which the fractional drift-diffusion equation is taken into account. Though the model was originally developed for liquid electrolytes, it was found to be applicable for SPEs too [2]. The contribution of anomalous diffusion has been introduced by the incorporation of a time derivative of order 'γ'.The importance of anomalous diffusion in SPE originates from the fractal structure of the polymers. The impedance involving contributions of both normal diffusion and anomalous diffusion is given as [2,36],

$$Z = \frac{2}{iA\omega\boldsymbol{\varepsilon_r}\boldsymbol{\varepsilon_0}\beta^2}\left[\frac{1}{\beta\lambda_D^2}\tanh\left(\frac{\beta L}{2}\right) + h\frac{(i\omega)^{\gamma}L}{2D_{\gamma}} + (1-h)\frac{i\omega L}{2D}\right] \tag{10.4}$$

where, λ_D is the Debye screening length, ε_r is the dielectric constant of the solid electrolyte material, D_γ and D are the anomalous and normal diffusion coefficients, respectively, L is the thickness of the solid electrolyte, A is the effective contact area of the electrode and the electrolyte surface, $\beta = \sqrt{\frac{1}{\lambda_D^2} + h\frac{(i\omega)^{\gamma}}{D_{\gamma}} + (1-h)\frac{i\omega}{D}}$ is the characteristic exponent diffusion of the model, h is the fraction of anomalous diffusion and $(1-h)$ is the fraction of normal diffusion. The Nyquist plots of the SPE containing different blending compositions of CS/PMMA and PMG$_x$ ($0 \leq x \leq 15$) SPNE material are successfully fitted using Eq. 10.4 and are shown in Figs. 10.6a and 10.6b, respectively. The best fit parameters are tabulated in Table 10.2. It is found that the fractional contribution of the anomalous diffusion (h) in the materials is very high in comparison with normal diffusion since $h \sim 0.90$. Moreover, the value of γ increases from 0.199 to 0.520 with increment in GO doping concentrations in the PMG$_x$ ($0 \leq x \leq 15$) SPNE material, which is much less than unity. This infers that the anomalous intra diffusive behavior of ions mainly predominates in the blended CS/PMMA solid electrolytes. The fractal structure of the polymers in both microscopic and macroscopic scales results in the anomalous diffusion in the blended solid electrolytes [2].The anomalous intra diffusion coefficient (D_γ) is found to be increased by an order in magnitude (from ~ 10^{-15} to ~ 10^{-14} m^2/s) on increasing the blending compositions of PMMA in the blended CS/PMMA SPE, which has been further improved by an order (~ 10^{-13} m^2/s) on doping with GO at lower concentrations ($x \leq 9$). The maximum conducting material, PMG₉ SPNE exhibits the highest D_γ (4.5×10^{-13} m^2/s) and λ_D (0.014 μm), which is in good correlation with the impedance results.

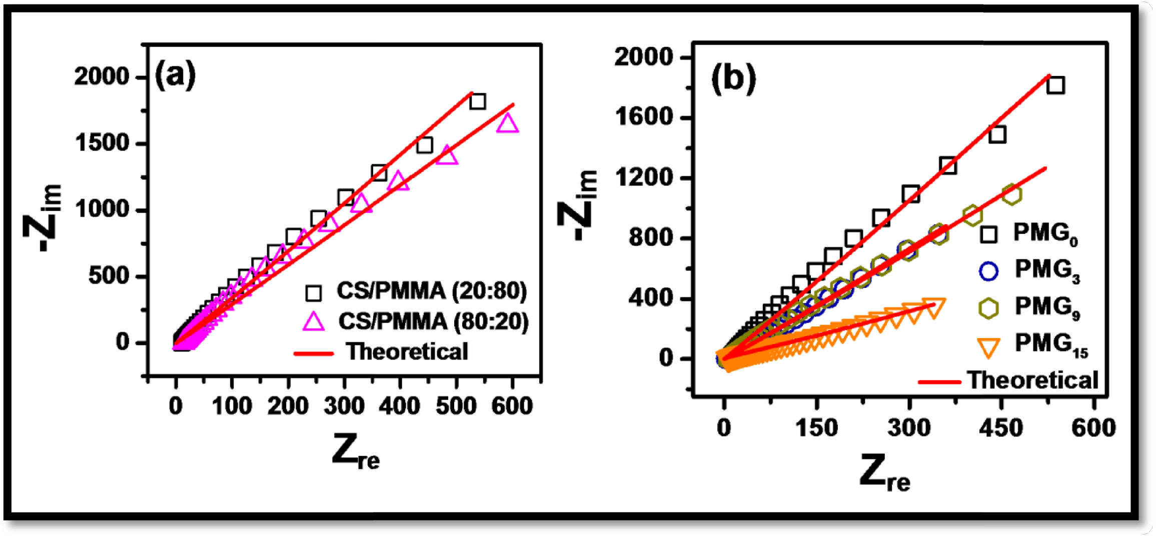

Fig. 10.6. Nyquist plots of (a) CS/PMMA (80:20) and CS/PMMA (20:80) blended SPE, (b) PMG$_x$ ($0 \leq x \leq 15$) SPNE material at 300 K. Solid lines are the fits of the experimental data based on fractional diffusion model according to Eq. 10.4.

Table 10.2. Best fit model parameters to analyze diffusion processes in CS/PMMA blended SPE and PMG$_x$ ($0 \leq x \leq 15$) SPNE material.

Solid polymer electrolytes	D ($\times 10^{-9}$m^{2}s^{-1})	D_γ(m^{2}s^{-1})	γ	h	λ_D (μm)
CS/PMMA (80:20)	1	9.5×10^{-15}	0.22	0.90	0.005
CS/PMMA (20:80)	4	9.6×10^{-14}	0.199	0.90	0.006
PMG₃	5	1×10^{-13}	0.28	0.90	0.01
PMG₉	9	4.5×10^{-13}	0.28	0.90	0.014
PMG₁₅	9	2.5×10^{-14}	0.52	0.90	0.004

10.3.4.3. Dielectric permittivity and scaling

The dielectric relaxation is studied in terms of frequency dependent complex dielectric permittivity (ε^*) given by, $\varepsilon^*(\omega) = \varepsilon_r(\omega) - j\varepsilon_i(\omega)$ where, ε_r denotes the dielectric constant and ε_i denotes the dielectric loss. The frequency dependence of the dielectric constant for the SPE containing different blending compositions of CS/PMMA and PMG$_x$ ($0 \le x \le 15$) SPNE material are shown in Figs. 10.7a and 10.7b, respectively at 300 K.The strong frequency dispersion due the electrode polarization (EP) effects is observed in the low frequency region. Due to the effects of electronic or atomic polarization processes inside the solid electrolyte, the dielectric constant (ε_r) shows a leveling-off at high frequencies. It is to note here that ε_r has been increased significantly [from ~ 59 (for CS-rich) to ~ 1088 (for PMMA-rich)] on increasing the PMMA blending compositions in the SPE.

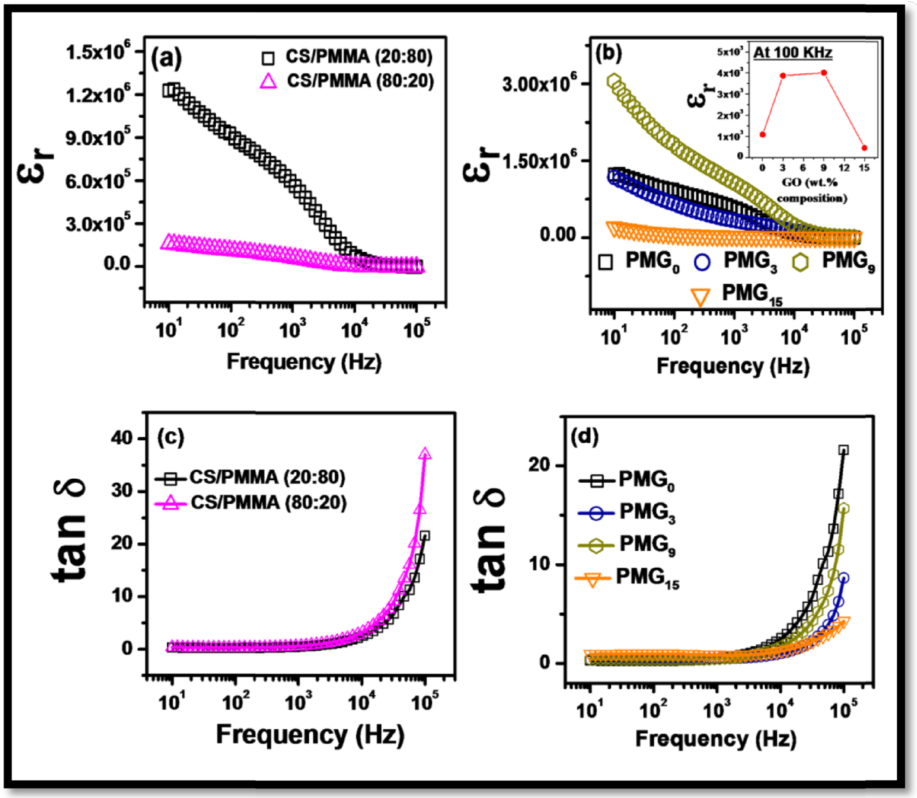

Fig. 10.7. Frequency dependence of dielectric constant (ε_r) for (a) CS/PMMA (80:20) and CS/PMMA (20:80) blended SPE, (b) PMG$_x$ ($0 \le x \le 15$) SPNE material at 300 K. Inset of (b) shows the variation of ε_r as a function of GO compositions at 100 KHz. Variation of tan δ with frequency at room temperature for (c) CS/PMMA (80:20) and CS/PMMA (20:80) blended SPE, (d) PMG$_x$ ($0 \le x \le 15$) SPNE material at 300 K.

The inset of Fig. 10.7b represent the dielectric constant (ε_r) variation as a function of GO doping concentrations in PMG$_x$ ($0 \leq x \leq 15$) SPNE material.The maximum value of ε_r ~ 4018 has been obtained for PMG$_9$ SPNE material which is almost 4times enhanced compared to that of the GO free material (i.e. PMG$_0$). The frequency dependence of the loss tangent which is defined as the ratio of the energy loss to the energy stored ($\varepsilon_i/\varepsilon_r$) in an applied AC field, for the SPE containing different blending compositions of CS/PMMA and PMG$_x$ ($0 \leq x \leq 15$) SPNE materialare shown in Figs. 10.7c and 10.7d, respectively at 300 K. There is no relaxation peaks observed in the frequency range of investigation for all the materials indicating a very small dielectric relaxation time. Moreover, the loss factor is considerably reduced on increasing the PMMA blending compositions and doping with GO in PMG$_x$ ($0 \leq x \leq 15$) SPNE material which makes them suitable for supercapacitor applications.

The scaling behavior of the dielectric constant is studied to examine the blending and nanofiller composition dependence of the ion dynamics. The scaling of the dielectric constant has been done as suggested by Sidebottom *et al* [34,35] which is given as,

$$\frac{\varepsilon_r(\omega)-\varepsilon_r(\omega\rightarrow\infty)}{\Delta\varepsilon_r} = G\left(\frac{\omega}{\omega_p}\right) \tag{10.5}$$

where, $\Delta\varepsilon_r = [\varepsilon_r(\omega \rightarrow 0) - \varepsilon_r(\omega \rightarrow \infty)]$ is a direct consequence of the relaxation of hopping charge carriers and $\omega_p = \frac{\sigma_{DC}}{\varepsilon_0 \Delta\varepsilon_r}$ is the scaling factor. Figures 10.8a and 10.8b represent the scaled dielectric constant curve for the SPE containing different blending compositions of CS/PMMA and PMG$_x$ ($0 \leq x \leq 15$) SPNE material, respectively at 300 K according to Eq. 10.5. It is observed that the dielectric constant spectra as shown in Fig. 10.8a superpose on a common master curve for both CS-rich [CS/PMMA(80:20)] and PMMA-rich [CS/PMMA(20:80)] blended SPE materials which suggests that a single mechanism is governing all the possible ionic motion in the entire frequency range and therefore, independent of both the CS and PMMA blending compositions in the SPE. But, the curves cannot be scaled on a single master curve on doping with GO as evident from Fig. 10.8b. This indicates that the relaxation phenomenon depends on the GO doping compositions in the PMG$_x$ ($0 \leq x \leq 15$) SPNE material.

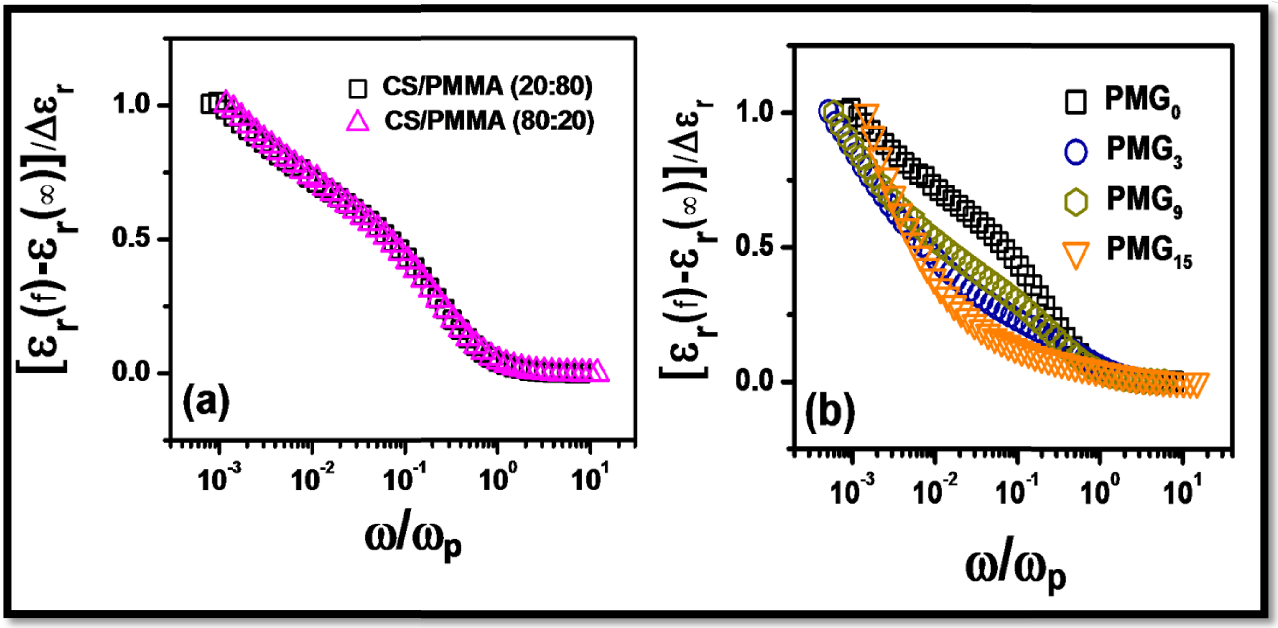

Fig. 10.8. Scaling behavior of the real part of complex permittivity spectra for (a) CS/PMMA (80:20) and CS/PMMA (20:80) blended SPE, (b) PMG_x $(0 \leq x \leq 15)$ SPNE material.

10.3.4.4. Electric Modulus

In ionic conductors, the effect of electrode polarization has been reflected by a prominent increment of the dielectric permittivity in the low frequency regime. The electric modulus study is extensively used to investigate the conductivity relaxation phenomenon by suppressing the electrode polarization effect in the low frequency regime. The frequency dependence of the imaginary part of electric modulus (M'') for the SPE containing different blending compositions of CS/PMMA and PMG_x $(0 \leq x \leq 15)$ SPNE material are shown in Figs. 10.9a and 10.9b, respectively. A long tail behavior of M'' is observed for all the materials in the low frequency regime followed by an increasing trend at the higher frequency regime. The low frequency long tail feature (as shown in Figs. 10.9a and 10.9b) are an indication of capacitive nature of the materials [2]. The value of M'' for PMMA-rich blended SPE at high frequencies is significantly reduced in comparison with that of CS-rich blended SPE which corroborates with the dielectric results.

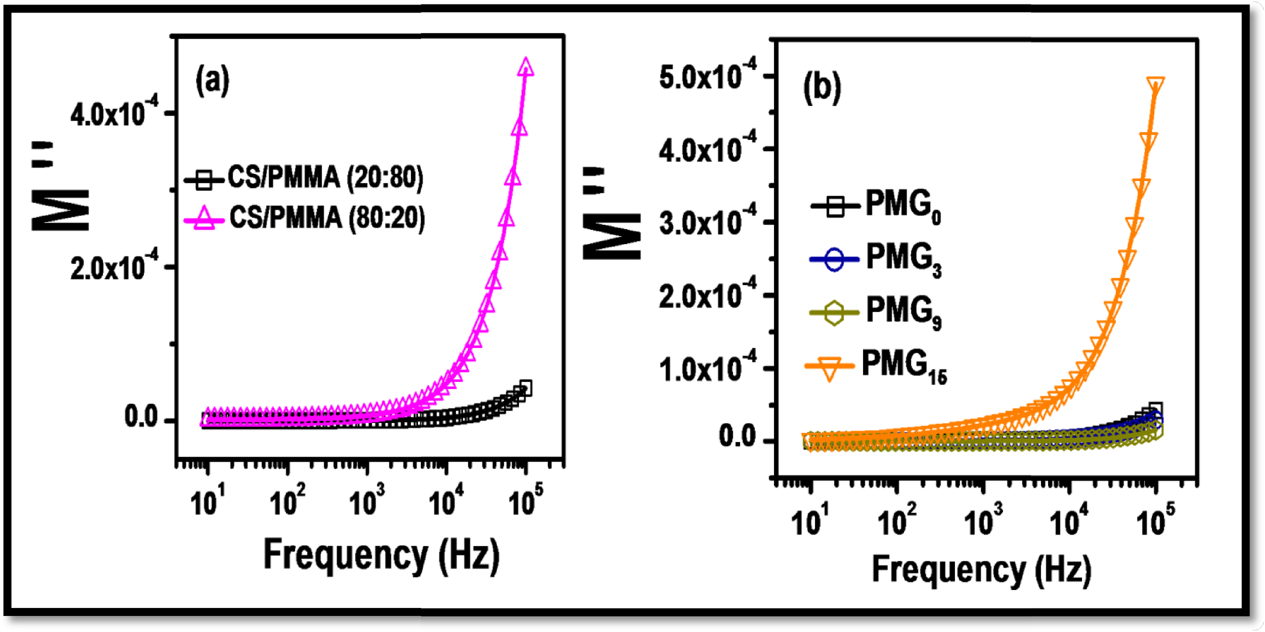

Fig. 10.9. (a) Frequency dependence of imaginary part (M″) of electric modulus for (a) CS/PMMA (80:20) and CS/PMMA (20:80) blended SPE, (b) PMG$_x$ ($0 \leq x \leq 15$) SPNE material.

10.3.5. Fourier Transform Infrared spectroscopy (FTIR)

FTIR spectroscopy is performed to investigate the interactions between the plasticized solid polymer matrices comprised of CS and PMMA with GO nanofiller and $LiClO_4$ salt which can induce changes in the vibrational modes of the blended biopolymer molecules. The FTIR absorption spectra of the SPE containing different blending compositions of CS/PMMA and PMG$_x$ ($3 \leq x \leq 15$) SPNE material has been analyzed for specific vibrational bands in order to analyze the interactions of $LiClO_4$ salt and GO nanofiller with plasticized CS/PMMA blended solid polymer matrix.

Significant blue shifts of the absorption peaks corresponding to amine (R-NH_2) [from ~ 1575 cm^{-1} (for CS-rich SPE) to ~ 1579 cm^{-1} (for PMMA-rich SPE)] and secondary amide (O=C-NHR) [from ~ 1651 cm^{-1} (for CS-rich SPE) to ~ 1654 cm^{-1} (for PMMA-rich SPE)] of chitosan (CS) [2,6,10] are observed on increasing the PMMA concentrations in blended CS/PMMA SPE material, as shown in Fig. 10.10a. A slight blue shift of the absorption peak corresponding to C=O stretching vibrations of ester (O=C-O-CH_3) group [37] of PMMA [from ~ 1724 cm^{-1} (for

CS-rich SPE) to ~ 1726 cm^{-1} (for PMMA-rich SPE)] is observed on increasing the PMMA concentrations in blended CS/PMMA SPE material, as shown in Figs. 10.10a.

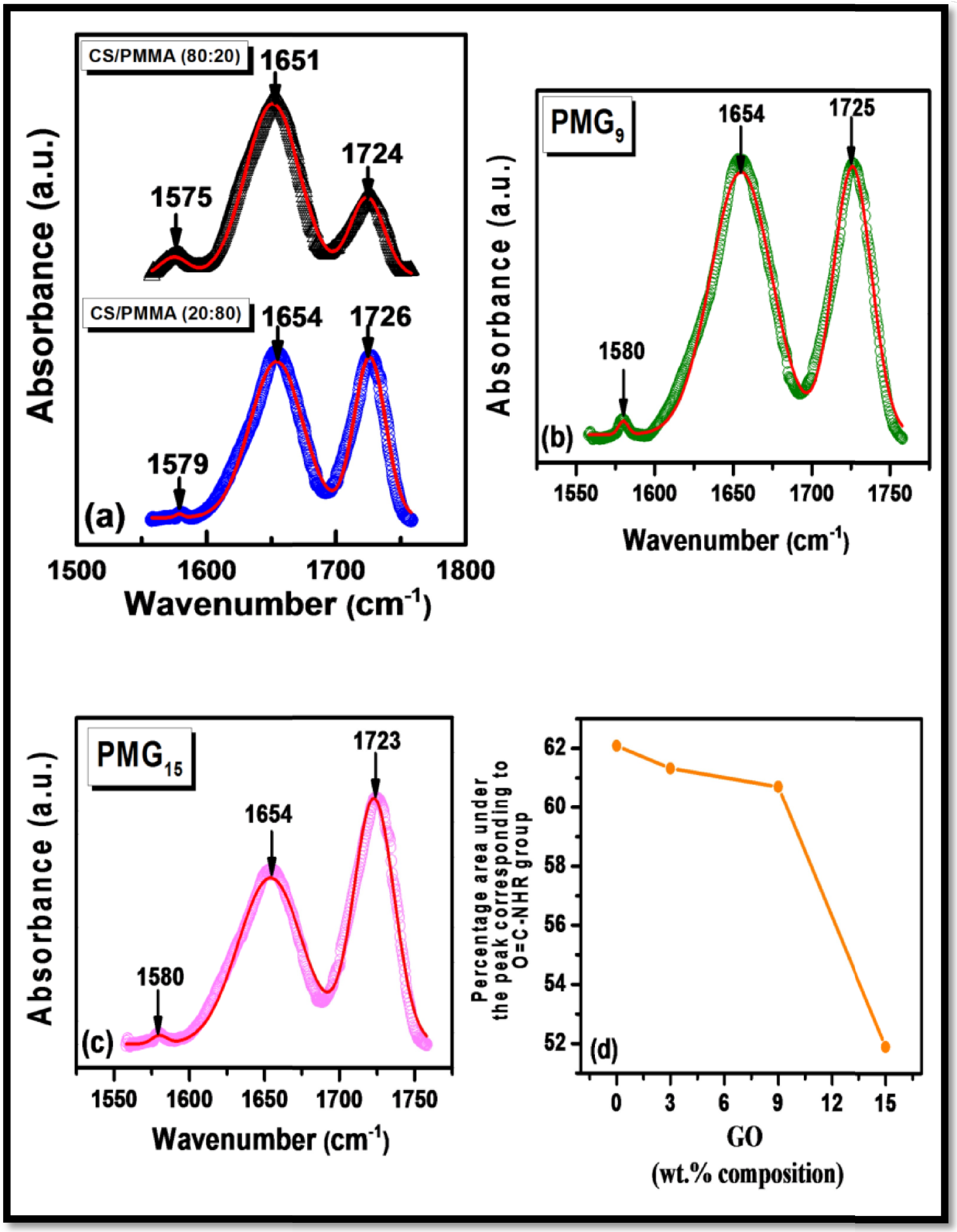

Fig. 10.10. FTIR absorption spectra in the region, 1558 $cm^{-1}$to 1690 cm^{-1} for (a) CS/PMMA (80:20), and CS/PMMA (20:80), (b) PMG_9 and (c) PMG_{15} SPNE materials. Solid lines show the Gaussian fitting of the characteristic absorption peaks. (d) Percentage area under the peak corresponding to secondary amide is shown as a function of GO doping concentrations in PMG_x $(0 \leq x \leq 15)$ SPNE material.

On doping with GO, a slight blue shift of the absorption peak corresponding to amine (R-NH_2) from ~ 1579 cm^{-1} (for PMG_0) to ~ 1580 cm^{-1} has been observed in PMG_x $(3 \leq x \leq 15)$ SPNE material while there is a red shift of the absorption peak corresponding to ester group (O=C-O-CH_3) of PMMA has been observed from ~ 1726 cm^{-1} (for PMG_0) to ~ 1723 cm^{-1} (for PMG_{15}).The Gaussian fitting of these characteristic peaks for the SPE containing different blending compositions of CS/PMMA and PMG_x $(3 \leq x \leq 15)$ SPNE material has been done in order to quantitatively analyze the interactions of Li^+ with amine (R-NH_2), amide (O=C-NHR) and ester (O=C-O-CH_3) functional groups of the blended polymers. Figure 10.10b and 10.10c shows the Gaussian fitting of these characteristic peaks for PMG_9 and PMG_{15} SPNE materials as representatives. The relative area under the absorption peak corresponding to secondary amide for all the materials is shown in Fig. 10.10d. It is interesting to note here that the peak area corresponding to O=C-NHR group of CS decreases with increase in GO doping concentrations in PMG_x $(0 \leq x \leq 15)$ SPNE material. This infers that the interaction between the amide (O=C-NHR) functional group of CS and Li^+ cation has been significantly weakened on incorporation of GO in PMG_x $(0 \leq x \leq 15)$ SPNE material.

A schematic illustration to analyze the effect of GO in the PMG_x $(0 \leq x \leq 15)$ SPNE material has been proposed here from the molecular level point of view (shown in Figs. 10.11a and 10.11b). The Li^+ cation is strongly coupled to the amine (R-NH_2) and secondary amide (O=C-NHR) groups of CS in PMG_0 material as shown in Fig. 10.11a. On grafting the blended polymers with GO, the interaction between nitrogen containing functional group of the blended biopolymer matrix (i.e-O=C-NHR) and Li^+ cation is extensively reduced due to the strong Lewis acid-base reaction between the abundant oxygen containing functional groups of GO and Li^+ (as shown in Fig. 10.11b). This helps in decoupling of the Li^+ transport from the segmental movement of the blended polymers [14]. Thus the interconnected continuous network formed by GO results in a faster transport rate of Li^+, as evident from anomalous modeling results, by acting as a “highway for ions”. This results an enhancement of the ionic conductivity in the blended SPNE PMG_x with $x \leq 9$.

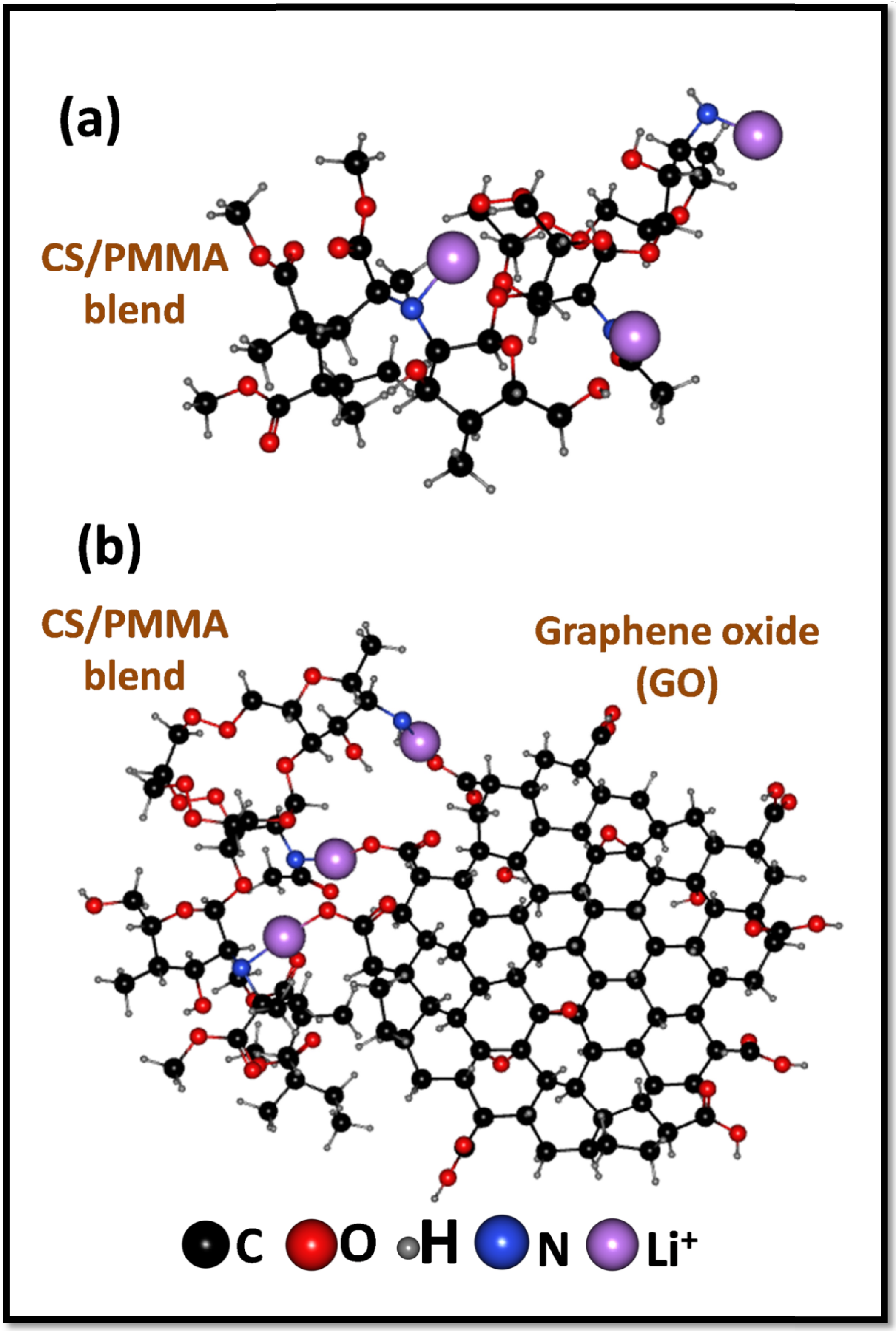

Fig. 10.11. Schematic illustration of Li^+ conduction mechanism in PMG_x ($0 \leq x \leq 15$) SPNE material (a) GO-free CS/PMMA blended SPE (PMG_0), (b) GO grafted CS/PMMA blended SBNE.

10.3.6. Electrochemical characterization

The electrochemical performance of the highest conducting SPNE material, PMG_9 has been investigated using a coin type unique symmetric supercapacitor developed with $MnCoFeO_4$ and Ag-$MnCoFeO_4$@rGO as electrode materials which are designated as EL-1 and EL-2, respectively. Nanoporous $MnCoFeO_4$ has been chosen as the electrode material due to high specific capacitance, as reported in our earlier work [2]. The $MnCoFeO_4$ nanoparticles are decorated with silver nanoparticles as Ag enhances the electrical conductivity and electrochemical charge storage capacity of the nanocomposite [21-22]. Further, Ag-$MnCoFeO_4$ nanocomposite are embedded onto rGO sheet owing to its large surface area and high conductivity [22].

10.3.6.1. Cyclic Voltammetry (CV)

Typical cyclic voltammogram (CV) for the cell constructed with EL-1 electrode and PMG_9 SPNE material over the voltage range from –0.1 to +1.1 V at a scan rate of 20 mV/s, are shown in Fig. 10.12a. It is observed that the CV curve is nearly semi-rectangular shaped obtained which suggests good capacitive characteristics of EL-1. Fig. 10.12a shows the CV curve for the cell constructed with EL-2 electrode over the same window (i.e. -0.1 to +1.1 V) at the same scan rate of 20 mV/s. It exhibits faradaic-type capacitive characteristics having a pair of anodic and cathodic peaks appearing at ~ 0.67 V and ~ 0.06 V corresponding to oxidation and reduction processes, respectively. This suggests the redox charge storage behavior of the Ag-$MnCoFeO_4$@rGO (EL-2) electrode. The larger area of the CV closed curve corresponding to Ag-$MnCoFeO_4$@rGO electrode compared to that of $MnCoFeO_4$ electrode indicate the higher capacitance value of EL-2.

10.3.6.2. Galvanostatic charge-discharge (GCD)

The electrochemical performance of the supercapacitor is evaluated through galvanostatic charge-discharge (GCD) technique. The supercapacitor has been charged and discharged at a constant current within a potential range of -0.6 V to +0.6 V. Figure 10.12b shows the charge-discharge profiles for the cells constructed with $MnCoFeO_4$ electrode | PMG_9 SPNE and Ag-$MnCoFeO_4$@rGO electrode | PMG_9 SPNE at a current density of ±300 $\mu A/cm^2$.

The specific capacitance (C_{sp}) of the cells are calculated by GCD using the following equation given as [2],

$$C_{sp} = \frac{2I}{\frac{\Delta V}{\Delta t} \times m} \tag{10.6}$$

where, I is the charging current (A), ΔV is the potential window (V), m is the mass of the active material per electrode (g), and Δt is the discharging time (s) [2]. It is found to be 19 Fg^{-1} and 47 Fg^{-1} for the cells constructed with $MnCoFeO_4$ electrode and Ag-$MnCoFeO_4$@rGO electrode measured. The high specific capacitance of the cell with the electrode Ag-$MnCoFeO_4$@rGOmay be attributed to the higher conductivity of this composite. Moreover, rGO aids in improving the supercapacitive performance by providing larger surface area and promoting faster electron transport. Additionally, rGO provides a strong mechanical support to the active electrode materials, which helps to keep the electrode structure intact during the electrochemical process [26].

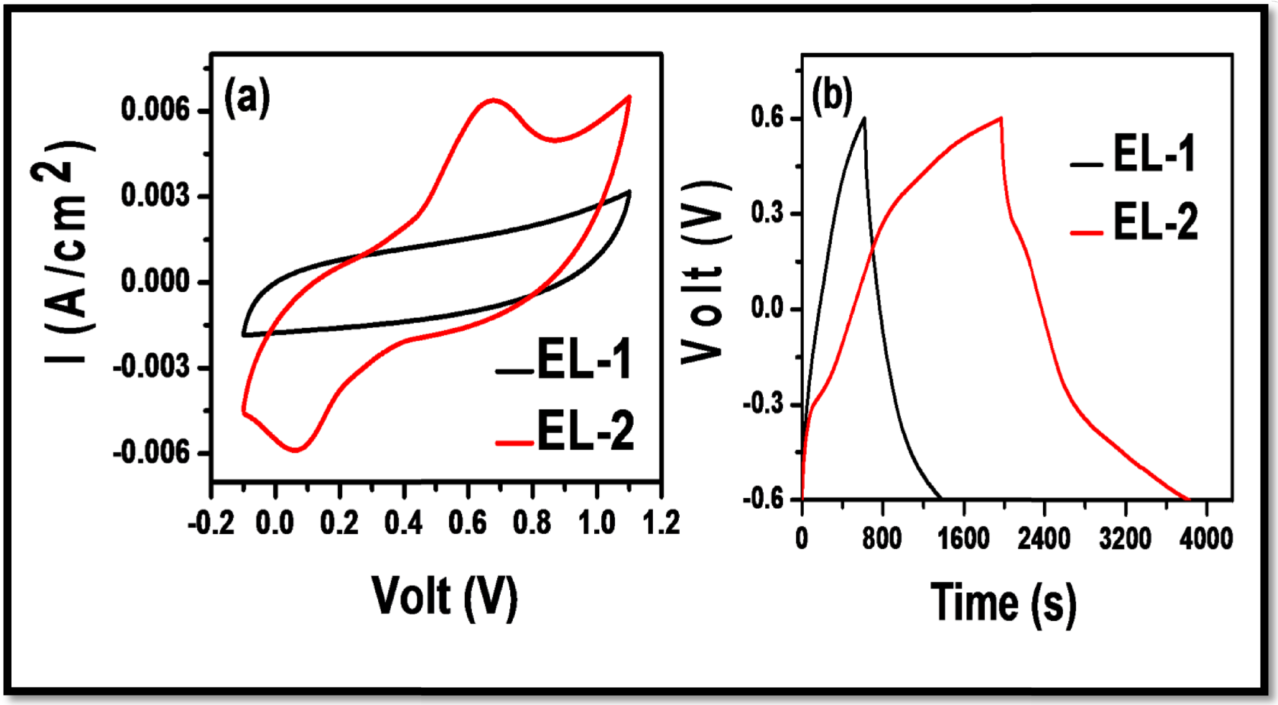

Fig. 10.12. (a) Cyclic voltammograms at a scan rate of 20 mV/s over the voltage range from –0.1 to +1.1 V for the cells constructed with $MnCoFeO_4$ (EL-1) | PMG_9 and Ag-$MnCoFeO_4$@rGO (EL-2)| PMG_9, (b)Galvanostatic charge-discharge for the cells constructed with $MnCoFeO_4$ (EL-1) | PMG_9 and Ag-$MnCoFeO_4$@rGO (EL-2)| PMG_9.

Energy density (E_D) and power density (P_D) are important parameters for the evaluation of the electrochemical performance of the supercapacitors, which can be estimated from the relation given as [2],

$$E_D = \frac{1}{2}\left[\frac{C_{sp}\Delta V^2}{3.6}\right] \text{Wh/kg} \tag{10.7}$$

$$P_D = \left[\frac{E_D}{t_d}\right] \times 3600 \text{ W/kg} \tag{10.8}$$

Achievement of large energy density of 9.28 Whkg^{-1}along with power density 18 Wkg^{-1} of the cell with EL-2 as electrode reveals Ag-$MnCoFeO_4$@rGO electrode | PMG_9 SPNE system as a potential candidate of solid-state hybrid supercapacitors.

10.3.6.3. Electrochemical impedance spectroscopy (EIS)

To explore the kinetics of the ions in the solid electrolyte responsible for charge accumulation, electrochemical impedance spectroscopy (EIS) has been performed. The Nyquist plots for the two cells constructed with EL-1 electrode | PMG_9 SPNE and EL-2 electrode | PMG_9 SPNE, respectively are shown in Fig. 10.13a over the frequency range of 10 mHz-100 KHz. The internal resistance, R_s which denotes the contact resistance between the current collector and electrode and that with the electrode and SPNE can be determined from the high frequency intercept of the real axis (Z_{re}), whereas the charge transfer resistance, R_{ct} can be estimated from the diameter of the semicircle observed in the intermediate frequency range [26]. It is clear from Fig. 10.13a that both R_s and R_{ct} are very low for both the electrodes. Low R_s indicates intimate contact between electrode and SPNE, while low R_{ct} suggests better ion diffusion at the electrode/SPE interface.

To gain information regarding the diffusion of ions inside the electrode pores, Warburg factor (σ) has been calculated based on the linearRandles relation [2],

$$Z_{re} = R_D + R_L + \sigma\omega^{-\frac{1}{2}} \tag{10.9}$$

The slope of the linear relationship between the real impedance (Z_{re}) and the inverse square root of frequency ω at low-frequency range (10 mHz to 50 mHz) gives the Warburg factor (σ) as shown in Fig. 10.13b. The value of $\sigma$is found to be decreased from 70 (for $MnCoFeO_4$ electrode) to 59 (for Ag-MnCoFeO$_4$@rGO electrode). This reduction in the value of Warburg factor with Ag-MnCoFeO$_4$@rGO electrode can be assigned to the increased ionic mass transfer inside the porous electrode structure at lower frequencies, resulting a high specific capacitance with EL-2.

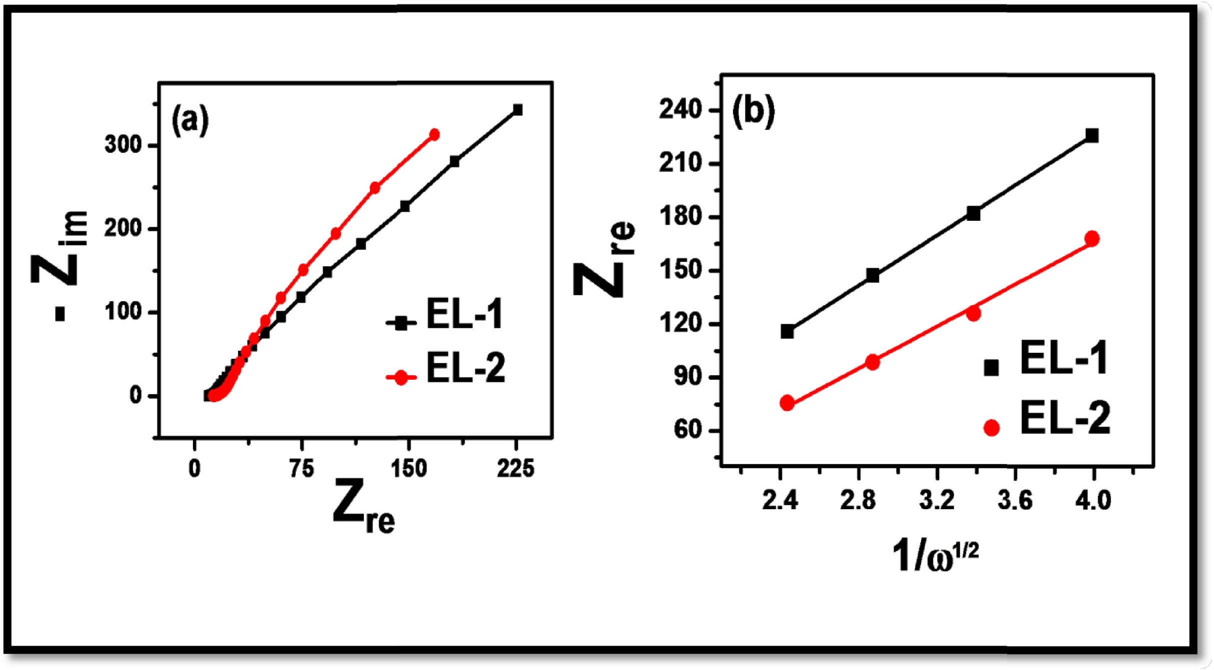

Fig. 10.13. (a) Nyquist plots for the cells constructed with MnCoFeO$_4$ (EL-1) | PMG$_9$ and Ag-MnCoFeO$_4$@rGO (EL-2)| PMG$_9$over a low frequency range of 100 KHz – 10 mHz, (b) the variation of the real impedance (Z_{re}) and the inverse square root of frequency ω at low-frequency range (10 mHz to 50 mHz).

As reported in our earlier study [2], a realistic approach of maximum 10,000 diffusion length (i.e.80 micron) inside the Ag-MnCoFeO$_4$@rGO electrode material has been considered for the estimation of the effective specific capacitance (C$_E$) of the electrode with respect to solid polymer nanocomposite electrolyte (SPNE). The effective specific capacitance (C$_E$) of Ag-MnCoFeO$_4$@rGOelectrode (EL-2) | PMG$_9$ SPNE has been achieved as ~ 294 Fg^{-1}, which makes this combination a potential candidate for future development of solid state supercapacitors.

10.4. Conclusions

We have investigated the ion dynamics and dielectric properties in graphene oxide (GO) grafted CS/PMMA blended solid polymer nanocomposite electrolytes. A maximum ionic conductivity (~ 4.5×10^{-3} S/cm) and dielectric constant (~ 4018) is obtained on doping with GO.

Analysis of the DSC thermograms suggest significant reduction of melting temperature and crystallinity in GO grafted solid electrolytes. The low frequency dispersion in the AC conductivity spectra is analyzed considering the fractal nature of the interfacial region of the electrode and SPNE. The scaling of the ac conductivity and dielectric constant suggests that a single mechanism is governing all the possible ionic motion in the entire frequency range and thus the relaxation phenomenon is independent of the blending compositions but it is found to be dependent on the GO doping compositions in the solid electrolyte material. FTIR spectroscopy results suggest that the interaction between the secondary amide functional group of CS and Li^+ cation has been significantly weakened on grafting the blended CS/PMMA solid electrolytes with GO. The anomalous diffusion rate of Li^+ ions has been increased by an order (~ 10^{-13} m^2/s) on doping with GO. A novel hybrid symmetric solid-state supercapacitor is fabricated with silver decorated manganese cobalt ferrite ($MnCoFeO_4$) nanoparticles anchored onto the graphene (rGO) sheets as electrode material and GO grafted CS/PMMA solid polymer electrolyte, achieving a good effective specific capacitance value of ~ 294 Fg^{-1}.

Chapter 11

General Conclusions

Since the last century, there is an excessive consumption of fossil fuels (such as coal, oil, natural gas) worldwide which are significant contributors of greenhouse gases. This leads to the development of green, sustainable and highly efficient electrochemical energy storage devices. Due to the higher power density, moderate energy density, rapid charge-discharge dynamics and excellent cyclic retention, supercapacitors have attracted huge attention over other energy storage devices. The goal of this study has been the development of light weight and environment friendly solid-state supercapacitors having high specific capacitance and good cycle stability. During this journey in search for the perfect solid-state supercapacitor, this research has explored a large number of alternative solid polymer electrolytes materials based on natural biopolymer host (chitosan) and electrode materials based on spinel ferrites in order to improve the performance of the solid-state supercapacitors and to meet the higher requirements of future energy storage systems.

At the very beginning of our research work, we have discussed the ionic conduction, charge carrier relaxation and transport properties of a cost-effective and environment friendly chitosan acetate (CA) – lithium perchlorate ($LiClO_4$) solid biopolymer electrolytes (SBE). The SBE with 44.44 wt. % salt ($LiClO_4$) concentration exhibits the highest ionic conductivity of 1.33×10^{-5} S/cm at room temperature which is four orders of magnitude higher compared to that without salt. Mobility of the free carrier ions is significantly increased by two orders of magnitude along with enhanced charge carrier hopping rate due to the inclusion of salt. The frequency dependence of the conductivity spectra are analyzed based on a model considering the fractal nature of the electrode-SBE interface. A remarkable improvement in dielectric constant (from ~ 10^2 to ~ 10^5) is observed with increase in salt concentrations. The electric modulus spectra are analyzed using Havriliak–Negami equation, inferring a non-Debye type relaxation process. The relaxation function of the SBE is modeled successfully using non-exponential KWW function. It is observed that the value of the stretched exponent is much less than unity, suggesting that the charge carrier relaxation behavior is highly non-exponential in the SBE. FTIR spectroscopy results confirm more lithium ion coordination with the polar amide groups of biopolymer, resulting in ionic transport through the biopolymer chains.

Next we tried to tune the dielectric and transport properties of chitosan based solid biopolymer electrolytes through gamma irradiation. The chitosan based solid biopolymer electrolyte film containing 44.44 wt.% $LiClO_4$ salt and 20 wt.% EC as plasticizer have been synthesized by solution casting technique. The solid polymer electrolytes are then subjected to gamma irradiation with dose varying from 0 to 10 kGy. Ionic conductivity of these gamma irradiated systems is found to increase with radiation doses and attains maximum value ~ 2.3 $\times10^{-4}$ S/cm at 5 kGy. Moreover, for 5 kGy dose of radiation, it is observed that the mobility of the free carrier ions enhances by 15 times (0.92 $cm^2V^{-1}s^{-1}$). Theoretical analyses of the permittivity and the electric modulus spectra infer that these gamma irradiated samples exhibit non-Debye type relaxations.

To tune the above properties further, we have doped chitosan based biopolymer electrolytes with graphene oxide as a nanofiller. The chitosan based solid biopolymer electrolyte film containing 44.44 wt% $LiClO_4$ salt and 20 wt% EC as plasticizer with varying wt% of graphene oxide (GO) in the range (0-7 wt%) have been synthesized by solution blending and evaporation casting technique. An increase in conductivity, dielectric and transport properties have been obtained with graphene oxide@chitosan based biopolymer nanocomposite at room temperature. The composite containing 2.17 wt% GO exhibits the maximum ionic conductivity of 5.47 $\times10^{-4}$ S/cm along with eight fold improved mobility (3.06 $cm^2V^{-1}s^{-1}$) of the free ions. Enhancement of dielectric constant associated with the reduction of dielectric loss on incorporation with 3.85 wt% GO makes it potential candidate for using in environmental friendly energy storage devices.

Till now, we have achieved a maximum ionic conductivity of the order of ~ 10^{-4} S/cm with chitosan (CS) based solid biopolymer electrolytes. Enhancement of conductivity in solid polymer electrolyte is an essential criterion for the fabrication of high efficient solid-state supercapacitors. Hence we adopted blending technique to increase the conductivity of the electrolytes. The conductivity of the blended polymer matrix composed of Chitosan : PVDF (20 : 80), salt $LiClO_4$ (80 wt. %) and glycerol (15 wt. %) as plasticizer has increased by seven order in magnitude. The imaginary electric modulus (M'') is increased with increasing glycerol loading at higher frequency inferring a non-Debye type relaxation process. The anomalous intra diffusive behavior of the charge carriers inside the blended polymer matrix has been analyzed based on fractional diffusion model. Transport properties have also been studied from FTIR results. A hybrid solid-state supercapacitor has been developed with nano crystallites of manganese cobalt ferrite ($MnCoFeO_4$) as electrode material and CS/PVDF blended polymer as solid state electrolyte. X-ray photoelectron spectroscopy (XPS) analysis of $MnCoFeO_4$ reveals a partially inverse spinel structure with oxygen non-stoichiometry introduced by the mixed oxidation state of Mn ion. A unique model has been approached to evaluate inter ionic transport properties of the charge carriers in order to determine the effective specific capacitance of the electrode materials. A significant enhancement of effective specific capacitance of 750 Fg^{-1} has been achieved which is ~ 24 times enhanced compared to that achieved with the electrical double layer capacitor (EDLC) containing the same solid electrolyte.

. Our next solid-state electrolyte of interest is carbon nanotube (CNT) incorporated chitosan (CS) and carboxymethyl cellulose (CMC) blended solid biopolymer nanocomposite (SBNE) which is based on both natural polymer hosts. Ionic conductivity of the order ~ 10^{-3} S/cm is obtained with the SBNE comprising of the blend of chitosan (CS) and carboxymethyl cellulose (CMC), plasticized with glycerol, lithium perchlorate ($LiClO_4$) as dopant salt and carbon nanotube (CNT) as nanofiller. The ion dynamics and charge carrier relaxation properties in CNT incorporated solid biopolymer nanocomposite electrolytes have been studied. The scaling of the conductivity and permittivity spectra are performed to study the effect of dopant composition on the relaxation mechanism. The anomalous intra diffusive behavior of the charge carriers inside the blended polymer matrix has been investigated based on fractional diffusion model. FTIR spectroscopy results suggest that the secondary amide functional groups of chitosan dominate the conduction mechanism. Transference number analysis confirms the predominant ionic conduction in the CNT incorporated CS/CMC blended solid nanocomposite electrolytes. A very low leakage current of ~ 6 μA has been obtained with the CNT incorporated solid nanocomposite electrolyte which makes it attractive for energy storage applications. A symmetric hybrid solid-state supercapacitor has been fabricated with active carbon and nanocrystallites of manganese cobalt ferrite ($MnCoFeO_4$) as electrode materials and CNT incorporated CS/CMC blended biopolymers as solid state nanocomposite electrolyte, offering an effective specific capacitance value of ~ 94 Fg^{-1}.

As the value of the effective specific capacitance is quite low with CNT incorporated CS/CMC blended SBNE, we have tried to enhance the specific capacitance further with a different solid-state electrolyte based on natural biopolymers. We have synthesized graphene oxide grafted blended chitosan (CS) / potato starch (PS) solid biopolymer nanocomposites for that purpose. Exploring solid biopolymer electrolytes with high ionic conductivity and enhanced dielectric properties is of utmost importance for the development of environment friendly solid-sate supercapacitors. Charge carrier relaxation and transport properties of graphene oxide (GO) grafted blended solid biopolymer electrolytes comprising of chitosan (CS) and potato starch (PS) with $LiClO_4$ as a charge carriers, glycerol as a plasticizer have been reported here. The GO grafted blended CS/PS solid biopolymer nanocomposite electrolyte (SBNE) demonstrates a significant improvement in ionic conductivity and dielectric constant, as compared with that of GO-free solid electrolytes. This improvement is mainly attributed to the distribution of GO as an interconnected network throughout the SBNE which aids in faster ion transport by acting as an "ionic highway". The blended solid biopolymer composite with 9 wt. % GO exhibits the maximum conductivity (~ 10^{-3} S/cm) along with four fold mobility enhancement of the free ions. The ion-diffusion processes in the GO grafted SBNE has been analyzed based on anomalous fractional diffusion model. The relaxation behavior of the charge carriers is highly non-exponential in these blended nanocomposite electrolytes. A hybrid solid-state supercapacitor has been fabricated based on manganese cobalt ferrite ($MnCoFeO_4$) nanocrystallites as electrode and GO grafted CS/PS SBNE which demonstates a high effective specific capacitance of ~ 288 Fg^{-1} with 9 wt. %GO grafted blended nanocomposite electrolyte.

Finally, a hybrid solid-state supercapacitor has been fabricated with silver decorated manganese cobalt ferrite ($MnCoFeO_4$) nanoparticles anchored onto graphene sheets as electrode material and graphene oxide (GO) grafted chitosan (CS)/ polymethyl methacrylate (PMMA) as solid electrolytes which exhibits enhanced specific GO doped CS/PMMA blended solid electrolytes exhibit high ionic conductivity (~ 4.5×10^{-3} S/cm) and dielectric constant (~ 4018) at room temperature. Thermal analysis suggests significant reduction in crystallinity in GO grafted CS/PMMA electrolytes. The scaling of the ac conductivity and dielectric constant suggests that the relaxation phenomenon is independent of the CS/PMMA blending compositions but dependent on the GO doping. The interaction between Li^+ cation and the amide functional group is weakened remarkably on grafting the electrolytes with GO. An effective specific capacitance of ~ 294 F g^{-1} is obtained with Ag decorated $MnCoFeO_4$ nanoparticles anchored onto rGO electrode which is ~2.5 times enhanced compared to that with $MnCoFeO_4$ electrode.

Bibliography

Chapter 2

[1] S. Chandra, "Superionic solids: principles and applications", Amsterdam, North Holland (1981).

[2] R. C. Agrawal, R. K. Gupta, Journal of Materials Science 34 (6), 1131-1162 (1999).

[3] E. Baur, H. Preis, Z. electrochem. 43, 727-32 (1937)

[4] R.J. Cava, F. Reidinger, B.J. Wuench, Solid State Commun. 24, 411-416 (1977).

[5] Y.F.Y. Yao, J.T. Kummer, J. Inorg. Nucl. Chem. 29, 2453-2466 (1967).

[6] D. Kunze, In: Fast ion transport in solids, Van Gool, W. (Eds.), North Holland, Amsterdam, 405 (1973).

[7] C.C. Liang, J. Electrochem. Soc. 120, 1289-1292 (1973).

[8] D.E. Fenton, J.M. Parker, P.V. Wright, Polymer 14, 589 (1973).

[9] I. I. Perepechko, An introduction to polymer physics, Mir Publishers, Moscow (1981).

[10] V. R. Gowriker, N. V. Vishwanathan, J. Sreedhar, Polymer Science, New Age International New Delhi (1996).

[11] V. N. Kulznev, V. A. Shershnev, The Chemistry and Physics of Polymers, Mir Publishers, Moscow (1990).

[12] M.B. Armand, J.M. Chabagno, M.J.K. Duclot, Poly-ethers as solid electrolytes, in Fast Ion Transport in Solids, eds. Vashishta, P.M., Mundy, J.N., and Shenoy, G.K., North-Holland, 131-136 (1979).

[13] G. Feuillade, P.H. Perche, J. Appl. Electrochem. 5, 63-69 (1975).

[14] M. Armand, F. Endres, D.R. MacFarlane, H. Ohno, B. Scrosati, Nature 8, 621-629 (2009).

[15] H. Ohno, Electrochemical aspects of ionic liquids, John Wiley & Sons, Hoboken, New Jersey (2005).

[16] Y. Kumar, G. Pandey, S. Hashmi, The Journal of Physical Chemistry C 116(50), 26118-26127 (2012).

[17] J. Chupp, A. Shellikeri, G. Palui, J. Chatterjee, Journal of Applied Polymer Science 132(26), 42143-42150 (2015).

[18] H. Ericson, C. Svanberg, A. Brodin, A.M. Grillone, S. Panero, B. Scrosati, P.

Jacobsson, Electrochim. Acta 45, 1409-1414 (2000).

[19] B.K. Choi, S.H. Park, S.W. Joo, M.S. Gong, Electrochim. Acta 50, 649-652 (2004).

[20] M. Watanabe, M. Kanba, K. Nagaoka, I. Shinohara, J. Appl. Polym. Sci. 27, 4191-4198 (1982).

[21] G.B. Appetecchi, F. Croce, B. Scrosati, Electrochim. Acta 40, 991-997 (1995).

[22] E. Quartarone, C. Tomasi, P. Mustarelli, G.B. Appetecchi, F. Croce, Electrochim. Acta 43, 1435-1439 (1998).

[23] D. Kumar, S.A. Hashmi, Solid State Ionics 181, 416-423 (2010).

[24] J.J. Xu, H. Ye, J. Huang, Electrochem. Commun. 7, 1309-1317 (2005).

[25] M.A. Navarra, S. Panero, B. Scrosati, Electrochem. Solid-State Lett. 8, A324-A327 (2005).

[26] P. Kurzweil, Encyclopedia of Electrochemical Power Sources (ed. Garche, J.) Elsevier, 565–578 (2009)

[27] J.-M. Tarascon, A.S. Gozdz, C. Schmutz, F. Shokoohi, P.C. Warren, Solid State Ion. 86–88, Part 1, 49–54 (1996).

[28] Y. Wang, J. Travas-Sejdic, R. Steiner, Solid State Ionics 148, 443-449 (2002).

[29] Gray, F.M., Solid Polymer Electrolytes, Royal Society of Chemistry Monographs, Cambridge (1977).

[30] J. R. MacCallum, C. A. Vincent, "Polymer Electrolyte Reviews", Elsevier applied Science, London, Vo1.-I (1987) and Vo1.-II (1989).

[31] F. M. Gray, "Solid Polymer Electrolytes: Fundamentals and Technological Applications" VCH Publishers Inc., USA (1991).

[32] R. G. Linford (ed.), "Electrochemical Science and Technology of Polymers-I", Elsevier Science, London (1987).

[33] P. G. Bruce, (ed.), "Solid State Electrochemistry", Cambridge University Press (1995).

[34] C. A. Vincent, Progress in Solid State Chem. 17, 1485 (1987).

[35] I. Noor, High Perform Polym 32(2), 168–174 (2020).

[36] S.K. Shetty, Ismayil, I.M. Noor, J Polym Res 28, 415 (2021).

[37] T. Sreekanth, M.J. Reddy, S. Ramalingaiah, U.V.S. Rao, J. Power Sources 79, 105-110 (1999).

[38] S.A. Hashmi, A. Kumar, K.K. Maurya, K.K., S. Chandra, J. Phys. D: Appl. Phys. 23, 1307-1314 (1990).

[39] S. Ibrahim, S.M.M. Yasin, R. Ahmad, M.R. Johan, Solid State Sci. 14, 1111-1116 (2012).

[40] N.K. Karan, D.K. Pradhan, R. Thomas, B. Natesan, R.S. Katiyar, Solid State Ionics 179, 689-696 (2008).

[41] S. Nithya, S. Selvasekarapandian, S. Karthikeyan, D. Inbavalli, S. Sikkinthar, C. Sanjeeviraja, Ionics 20, 1391–1398 (2014).

[42] C.Y. Chiang, Y.J. Shen, M.J. Reddy, P.P. Chu, J. Power Sources 123, 222-229 (2003).

[43] M. H. Buraidah, L. P. Teo, S. R. Majid, R. Yahya, R. M. Taha, A. K.Arof, International Journal of Photoenergy 2010, 1 – 7 (2010).

[44] M. H. Khanmirzaei, S. Ramesh, Int. J. Electrochem. Sci. 8, 9977 – 9991 (2013).

[45] M. Kumar, T. Tiwari, N. Srivastava, Carbohydrate Polymers 88, 54–60 (2012).

[46] M. A. Ramlli, M. I. N. Isa, J. Phys. Chem. B 120, 44, 11567–11573 (2016).

[47] K. H. Teoh, C. S. Lim, S. Ramesh, Measurement 48, 87 - 95 (2014).

[48] T. Basu, M.M. Goswami, T.R. Middya, S.Tarafdar, J. Phys. Chem. B 116, 11362−11369 (2012).

[49] A. K. Arof, S. Amirudin, S. Z. Yusof, I. M. Noor, Phys. Chem. Chem. Phys.16, 1856-1867 (2014).

[50] M. I. H. Sohaimy, M. I. N. Isa, Polym. Bull. 74, 1371–1386 (2017).

[51] J.E. Weston and B.C.H. Steele, Solid State Ionics 7(1), 75-79 (1982).

[52] W. Wieczorek, K. Such, J. Plocharski, J. Przyluski, Proc. 2nd Int. Symp. on Polymer Electrolyte (New York) ed B Scrosati (Amsterdam: Elsevier) 339 (1990).

[53] K. Vignarooban, M. A. K. L. Dissanayake, I. Albinsson, B. -E. Mellander, Solid State Ionics 266, 25-28 (2014).

[54] O. Padmaraj, M. Venkateswarlu, N. Satyanarayana, Ionics 19, 1835–1842 (2013).

[55] B. Scrosati, F. Croce, L. Persi, J. Electrochem. Soc.147, 1718- 1721 (2000).

[56] W. Wieczorek, Z. Florjancyk, J. R. Stevens, Electrochim. Acta, 40, 2251 (1995).

[57] J. Przyluski, M. Siekierski, W. Wieczorek, Electrochim. Acta 40, 2101 (1995).

[58] F. Croce, R. Curini, A. Martinelli, L. Persi, F. Ronci, B. Scrosati, R. Caminiti, J. Phys. Chem. B 103, 10632-10638 (1999).

[59] N.S.T. Do , D.M. Schaetzl, B. Dey, A. C. Seabaugh, S. K. Fullerton-Shirey, J. Phys. Chem. C 116, 40, 21216–21223 (2012).

[60] H.- Y.Sun, H.- J.Sohn, O. Yamamoto, Y. Takeda, N. Imanishi, J. Electrochem. Soc. 146 1672 (1999).

[61] H. Y. Sun, Y. Takeda, N. Imanishi, O. Yamamoto, H.-J. Sohn, Journal of The

Electrochemical Society, 147 (7) 2462-2467 (2000)

[62] W. Wieczorek, J.R. Stevens, Z. Florjanczyk, Solid State Ionics 85, 67- 72 (1996).

[63] A. Chandra, P.C. Srivastava, S. Chandra, J. Mater. Sci. 30, 3633-3638 (1995).

[64] D. Golodnitsky, G. Ardel, E. Peled, Solid State Ionics 147, 141- 155 (2002).

[65] D. M. Ivory, G. G. MilIer, 3. M. Sowa, L. W. Schacklette, R. R. Chance, R. H. Boughman, J. Chem. Phys. 71, 1506 (1979).

[66] L. C. Hardy, D. F. Shriver, J. Am. Chem. Soc. 108, 2887 (1986).

[67] J. R. Owens, "Fast Ion-Transport in Solids: Solid State Batteries and Devices", W. Van Gool, (ed.), North Holland, Amsterdam (1973).

[68] C. A. Angell, C. Liu, E. Sanchez, Nature 362, 137 – 139 (1993).

[69] B. Scrosati, C. A. Vincent, MRS Bull. March 28 (2000).

[70] J. K Park, Principles and Applications of Lithium Secondary Batteries, Wiley, Weinheim (2012).

[71] N.A. Rahman, S.A. Hanifah, N.N. Mobarak, A. Ahmad, N.A. Ludin, F. Bella, M.S. Su'ait, Polymer 230, 124092 (2021).

[72] B.K. Roy, I.Tahmid, T.U. Rashid, J. Mater. Chem. A 9, 17592 (2021).

[73] K.S. Ngai, S. Ramesh, K. Ramesh, J. C. Juan, Ionics 22, 1259–1279 (2016).

[74] S.B. Aziz, M.F.Z. Kadir, Z.H.Z. Abidin, Int. J. Electrochem. Sci. 11, 9228 – 9244 (2016).

[75] M. Z. A Yahya, A. K. Arof, Carbohydrate Polymers 55 (1), 95-100 (2004).

[76] J.F. Du, Y. Bai, W.Y. Chu, L.J. Qiao, J. Polym. Sci. B Polym. Phys. 48, 260-266 (2010).

[77] S. B. Aziz, R. T. Abdulwahid, M. H. Hamsan, M. A. Brza, R. M. Abdullah, M. F. Kadir, S. K. Muzakir, Molecules 24, 3508 (2019).

[78] S. B. Aziz, M. Hamsan, W. O. Karim, M. Kadir, M. Brza, O. G. Abdullah, Biomolecules 9, 267 (2019).

[79] M. Kadir, Z. Aspanut, R. Yahya, A. K. Arof, Mater. Res. Innovations 15, s164-s167 (2011).

[80] M. Shukur, M. Kadir, Electrochim. Acta 158, 152–165 (2015).

[81] Y. A. Salman, O. G. Abdullah, R. R. Hanna, S. B. Aziz, Int. J. Electrochem. Sci. 13, 3185–3199 (2018).

[82] N. H. Idris, H. B. Senin, A. K. Arof, Ionics 13, 213–217 (2007).

[83] Y.N. Sudhakar, M. Selvakumar, D.K. Bhat, Ionics 19, 277-285 (2013).

[84] S. Ramesh, C.W. Liew, J Non-Cryst Solids 358, 931–940 (2012).

[85] K.H. Teoh, S. Ramesh, A.K. Arof, J Solid State Electrochem 16, 3165–3170 (2012).

[86] S. B. Aziz, M. H. Hamsan, M. F. Kadir, W. O. Karim, R. M. Abdullah, Int. J. Mol. Sci. 20, 3369 (2019).

[87] A. J. Bhattacharyya, T. R. Middya, S. Tarafdar, Physical Review B 60 (2), 909-915 (1999).

[88] E. K. Lenzi, L. R. Evangelista, G. Barbero, J. Phys. Chem. B 113, 11371−11374 (2009).

[89] T. Basu, S. Tarafdar, Radiation Physics and Chemistry 125, 180 – 198 (2016).

[90] M.H. Buraidah, A.K. Arof, Journal of Non-Crystalline Solids 357(16-17), 3261–3266 (2011).

[91] M. F. Zaki, J. Phys. D: Appl. Phys. 41, 175404 (2008).

[92] M. H. A. Rahaman, M. U. Khandaker, Z. R. Khan, M. Z. Kufian, I. S. M. Noor, A. K. Arof, Phys. Chem. Chem. Phys. 16, 11527–11537 (2014).

[93] N. Ayoub, Y. M. Amin, A. K. Arof, AIP Conf. Proc. 1250, 209 (2010).

[94] J. R. Maccallum, M. J. Smith, C. A. Vincent, Solid State Ionics 11, 307 – 312 (1984).

[95] S.N.F. Yusuf, S.Z. Yusof, M.Z. Kufian, L.P. Teo, Materials Today: Proceedings 17, 446–458 (2019).

[96] P.K. Varshney, S. Gupta, Ionics 17, 479–483 (2011).

[97] M. Shukur, N. Majid, R. Ithnin, M. Kadir, Phys. Scr. 2013, 014051 (2013).

[98] C. Capiglia P. Mustarelli, E. Quartarone, C. Tomasi, A. Magistris, Solid State Ionics 118, 73–79 (1999).

[99] H.G. Xiong, S.W. Tang, H.L. Tang, P. Zou, Carbohydr Polym 71, 263–268 (2008).

[100] T. Mohamed Ali, N. Padmanathan, S. Selladurai, Ionics 19(8), 1115–1123 (2013).

[101] F. Croce, G. B. Appetecchi , L. Persi , B. Scrosati, Nature 394 , 456 (1998).

[102] D. Zhou, X. G. Mei, J. Y. Ouyang, J. Phys. Chem. C 115,16688-16694 (2011).

[103] J. Shim, D-G Kim, H.J. Kim, J.H. Lee, J-H Baik, J-C Lee, J. Mater. Chem. A, 2, 13873-13883 (2014).

[104] M. Yuan, J. Erdman, C. Tang, H. Ardebili, RSC Adv. 4 (103), 59637–59642 (2014).

[105] R. Olive-Monllau, M.J. Esplandiu, J. Bartroli, Sensors Actuators B 146, 353–360 (2010).

[106] S. L. Agrawal, N. Rai, T. S. Natarajan, N. Chand, Ionics 19, 145–154 (2013).

[107] G.B. Appetecchi, S. Passerini, Electrochim Acta 45, 2139–2147 (2000).

[108] T. Ozel, A. Gaur, J.A. Rogers, Nano Lett 5, 905–911 (2005).

[109] S. Ibrahim, S.M.M. Yasin, N.M. Nee, J Non-Cryst Solids 358, 210–216 (2012).

[110] M.S. Akhtar, J.G. Park, H.C. Lee, Electrochem Acta 55, 2418–2423 (2010).

[111] B. Philip, J.K. Abraham, A. Chandrasekhar, Smart Mater Struct 12, 935–939 (2003).

[112] S.N. Banitaba, D. Semnani, E.H. Soureshjani, B. Rezaei, A.A. Ensafi, Polym Int 68, 1787–1794 (2019).

[113] C. Tang, K. Hackenberg, Q. Fu, P. Ajayan, H. Ardebili, Nano Letters 12, 1152-1156 (2012).

[114] P. Simon, Y. Gogotsi, Nature Materials 7, 845-854 (2008).

[115] P. Barrade, S. Pittet, A. Rufer, PCIM Power Conversion Intelligent Motion, Nurnberg, Germany, 2000.

[116] G. Wang, L. Zhang, J. Zhang, Chem. Soc. Rev. 41, 797–828 (2012).

[117] E. Frackowiak, K. Metenier, V. Bertagna, F. Beguin, Appl. Phys. Lett. 77, 2421–2423 (2000).

[118] L. T. Le, M. H. Ervin, H. Qiu, B. E. Fuchs, W. Y. Lee, Electrochem. Commun. 13, 355–358 (2011).

[119] J. Li, X. Wang, Q. Huang, S. Gamboa, P. Sebastian, J. Power Sources 158, 784–788 (2006).

[120] Z. Fan, D. Qi, Y. Xiao, J. Yan, T. Wei, Materials Letters 101, 29-32 (2013).

[121] S. Zhai, W. Jiang, L. Wei, H. Enis Karahan, Y. Yuan, A. Keong Ng, Y. Chen, Mater. Horiz. 2, 598-605 (2015).

[122] L. Zhou, C. Li, X. Liu, Y. Zhu, Y. Wu, T. van Ree, Metal Oxides in Energy Technologies, 169–203 (2018).

[123] S. Trasatti, G. Buzzanca, Journal of Electroanalytical Chemistry and Interfacial Electrochemistry 29(2), A1-A5 (1971).

[124] A. Eftekhari, L. Li, Y. Yang, Journal of Power Sources 347, 86-107 (2017).

[125] Y. Huang, H. Li, Z. Wang, M. Zhu, Z. Pei, Q. Xue, Y. Huang, C. Zhi, Nano Energy 22, 422-438 (2016).

[126] S. Vijayakumar, S. Nagamuthu, G. Muralidharan, ACS Appl. Mater. Interfaces 5, 6, 2188–2196 (2013).

[127] S.K. Meher, G. R. Rao, J. Phys. Chem. C 115, 31, 15646–15654 (2011).

[128] M. Zhang, Y. Chen, D. Yang, J. Li, Journal of Energy Storage 29, 101363 (2020).

[129] R. Ko¨tz, M. Carlen, Electrochim. Acta 45, 2483–2498 (2000).

[130] J. Evans, C. A. Vincent, P. G. Bruce, Polym. 28, 2324-2328 (1987).

[131] R. G. Linford, Electrical and electrochemical properties of ion conducting polymers, Applications of Electroactive

Polymers, Chapman & Hall, London, UK (1993).

[132] L.L. Zhang, X. S. Zhao, Chem. Soc. Rev. 38, 2520–2531 (2009).

[133] X. Zhao, C. Johnston, P.S. Grant, J. Mater. Chem. 19, 8755-8760 (2009).

[134] S. Mondal, U. Rana, S. Malik, J. Phys. Chem. C 121, 14, 7573–7583 (2017).

[135] H-Q. Wang, Z-S. Li, Y-G. Huang, Q-Y. Li, X-Y. Wang, J. Mater. Chem. 20, 3883-3889 (2010).

[136] A. Muzaffar, M.B. Ahamed, K. Deshmukh, J. Thirumalai, Renewable and sustainable energy reviews 101, 123-145 (2019).

[137] S. Das, N. C. Pramanik, BARC Newsletter 339, 5-10 (2014).

[138] Y.N. Sudhakar, M. Selvakumar, Electrochimica Acta 78, 398– 405 (2012).

[139] A.G. Pandolfo, A.F. Hollenkamp, Journal of power sources 157(1), 11-27 (2006).

[140] K.S. Ryu, Y.G. Lee, Y.S. Hong, Y.J. Park, X. Wu, K.M. Kim, M.G. Kang, N.G. Park, S.H. Chang, Electrochimica acta 50 (2-3), 843-847 (2004).

[141] A. Laforgue, P. Simon, C. Sarrazin, J.F. Fauvarque, Journal of power sources 80 (1-2),142-148 (1999).

[142] Y. Shi, L. Pan, B. Liu, Y. Wang, Y. Cui, Z. Bao, G. Yu, J. Mater. Chem. A 2, 6086–6091 (2014).

[143] Y. Wang, Y. Song, Y. Xia, Chem Soc Rev 45, 5925–50 (2016).

[144] C.C. Hu, K.H. Chang, M.C. Lin, Y.T. Wu, Nano Lett 6, 2690–5 (2006).

[145] J. P. Zheng, T. R. Jow, J. Electrochem. Soc. L6, 142–145 (1995).

[146] S. Ardizzone, G. Fregonara, S. Trasatti, Electrochim. Acta 35, 263-267 (1990).

[147] R. Kötz, S. Stucki, J. Appl. Electrochem. 17, 1190-119 (1987).

[148] K. Lee, J. Lee, N. Wu, Electrochim. Acta 54, 6148-6153 (2009).

[149] N. L. Wu., Mater. Chem. & Phy. 75, 6-11 (2002).

[150] S. Wang, K. Ho, S. Kuo, N. Wu, J. Electrochem. Soc. 153, A75-A80 (2006).

[151] K. Malaie, M.R. Ganjali, Journal of Energy Storage 33, 102097 (2021).

[152] H. Wang, Y. Song, X. Ye, H. Wang, W. Liu, L. Yan, ACS Appl. Energy Mater. 1, 3206−3215 (2018).

[153] V.S. Kumbhar, A.D. Jagadale, N.M. Shinde, C.D. Lokhande, Applied Surface Science 259, 39– 43 (2012).

[154] H. Gao, J. Xiang, Y. Cao, Appl. Surf. Sci. 413, 351–359 (2017).

[155] M.L. Aparna, A.N. Grace, P. Sathyanarayanan, N.K. Sahu, J. Alloys Compd. 745, 385–395 (2018).

[156] A. Ghasemi, M. Kheirmand, H. Heli, Russ. J. Electrochem. 55, 206–214 (2019).

[157] B. Bhujun, M. T. T. Tan, A. S. Shanmugam, Ceram. Int. 42, 6457–6466 (2016).

[158] B. Bhujun, M. T. T. Tan, A. S. Shanmugam, Results Phys. 7, 345–353 (2017).

[159] F.M. Ismail, M. Ramadan, A.M. Abdellah, I. Ismail, N.K. Allam, J. Electroanal. Chem. 817, 111–117 (2018).

[160] M.F. El-Kady, M.S. Rahmanifar, M. Hemmati, R.B. Kaner, M.F. Mousavi, A. Noori, Mater. Today Energy 12, 26–36 (2019).

[161] T.V. Thu, T. Van Nguyen, X.D. Le, T.S. Le, V. Van Thuy, T.Q. Huy, Q.D. Truong, Electrochim. Acta 314, 151–160 (2019).

[162] P. Xiong, H. Huang, X. Wang, Journal of Power Sources 245, 937-946 (2014).

Fig. 2.2. : https://chem-is-you.blogspot.com/2015/03/physical-properties-of-polymers.html

Fig. 2.4. : T. Dam, S.S. Jena, D. K. Pradhan, Phys.Chem.Chem.Phys. 18, 19955 (2016).

Fig. 2.6. : G. Vinodha, L. Cindrella, P.D. Shima, Mater. Res. Express 6, 085548 (2019).

Fig. 2.8. : https://www.futurebridge.com/industry/perspectives-mobility/supercapacitors-a-viable-alternative-to-lithium-ion-battery-technology/

Fig. 2.11. : Y. Jiang, A. Sun, X. Huang, J. Wang, Y. Zhang, L.Shao, J Mater Sci: Mater Electron 32, 27882–27898 (2021),

K. Malaie, M.R. Ganjali, Journal of Energy Storage 33, 102097 (2021).

Fig. 2.12. : P.G. Munoz, F. Fresno, V. A. de la Peña O'Shea,Nicolas Keller, Topics in Current Chemistry 378, 6 (2020).

Chapter 3

Fig. 3.2. : https://upload.wikimedia.org/wikipedia/commons/0/0a/X-ray_spectroscopy_Goniometer.jpg

Fig. 3.6. : https://upload.wikimedia.org/wikipedia/commons/f/f2/System2.gif

Fig. 3.7. :

https://image.slidesharecdn.com/Ramanonline-122955380334-phpapp03/95/raman-spectroscopyand-its-applications-5-728.jpg?cb=1229525352

Fig. 3.9.: T.M.W.J. Bandara, B.-E. Mellander, Ionic Liquids: Theory, Properties, New Approaches (2011)
DOI : 10.5772/15183.

Chapter 4

[1] R. Singh, B. Bhattacharya, H.W. Rhee, P.K. Singh, Int. J. Electrochem. Sci. 9, 2620-2630 (2014).

[2] G.J. Liang, Z.C. Zhong, J. Xu, Z.C. Zhang, M.H. Chen, Z.F. Li, Acta Phys. Chim.Sin. 28, 2852-2860(2012).

[3] C. Polo Fonseca, S. Neves, J. Power Sources 159, 712-716 (2006).

[4] A. R. Polu, H-W Rhee, D. K. Kim, Journal of Materials Science: Materials in Electronics 26, 8548–8554 (2015).

[5] Y.N. Sudhakar, M. Selvakumar, Electrochim. Acta 78, 398-405 (2012).

[6] Y.N. Sudhakar, M. Selvakumar, D.K. Bhat, Ionics 19, 277-285 (2013).

[7] T. Tiwari, N. Srivastava, P.C. Srivastava, Ionics 17, 335-360 (2011).

[8] T. Tiwari, K. Pandey, N. Srivastava, P.C. Srivastava, J. Appl. Polym. Sci. 121, 1-7 (2011).

[9] A. A. Azli, N. S. A. Manan, M. F. Z. Kadir, Ionics 23, 411-425 (2017).

[10] M. H. Buraidah, L. P. Teo, S. R. Majid, A. K. Arof, Physica B 404,1373-1379 (2009).

[11] I. A. Fadzallah, S. R. Majid, M. A. Careem, A. K. Arof, Ionics 20, 969–975 (2014).

[12] M.N.V.R. Kumar, React Funct Polym 46, 1-27 (2000).

[13] M.A. García, A. Pinotti, M. Martino, N. Zaritzky, Food Hydrocoll. 23, 722-728 (2009).

[14] J. R. MacCallum, M. J. Smith, C.A. Vincent, Solid State Ionics 11, 307-312 (1984).

[15] O. G. Abdullah, S. B. Aziz, D. R. Saber, R. M. Abdullah, R. R. Hanna, S. R. Saeed, Journal of Materials Science: Materials in Electronics 28, 8928–8936 (2017).

[16] J. Liu, Z. Khanam, R. Muchakayala, S. Song, Journal of Materials Science: Materials in Electronics 31, 6160–6173 (2020).

[17] J.C. Dyre, P. Maass, B. Roling, D.L. Sidebottom, Rep. Prog. Phys. 72, 046501 (2009).

[18] B. Wang, S. Li, S. Wang, Phys. Rev. B. 56, 11503–11507(1997).

[19] F. Kremer, Broadband Dielectric Spectroscopy. Springer, Berlin (2003).

[20] M.H. Buraidah, S. Shah, L.P. Teo, F.I. Chowdhury, M.A. Careem, I. Albinsson, B.-E. Mellander, A.K. Arof, Electrochimica Acta 245, 846-853 (2017).

[21] T. M. W. J. Bandara, M. A. K. L. Dissanayake, I. Albinsson, B.-E. Mellander, Solid State Ionics 189, 63-68 (2011).

[22] A. K. Arof, S. Amirudin, S. Z. Yusof, I. M. Noor, Phys. Chem. Chem. Phys. 16, 1856-1867 (2014).

[23] D. P. Almond, G. K. Duncan, A.R. West, Solid State Ionics 8,159 (1983).

[24] D. P. Almond, A. R. West, Solid State Ionics 11, 57 (1983).

[25] T. Dam, S. S. Jena, D. K. Pradhan, Phys. Chem. Chem. Phys.18, 19955-19965 (2016).

[26] K. Funke, Prog Solid State Chem. 22, 111(1993).

[27] A. A. Khamzin, I. I. Popov, R. R. Nigmatullin, Phys. Rev. E 89, 032303 (2014).

[28] P. Pal, A. Ghosh, Phys. Rev. E 92, 062603 (2015).

[29] J. C. Dyre, J. Appl. Phys. 64, 2456 (1988).

[30] S. Choudhary, R. J. Sengwa, Electrochimica Acta 247, 924-941 (2017).

[31] R. Baskaram, S. Selvasekarapandian, G. Hirankumar, MS. Bhuvaneswari, J Power Source 134, 235 (2004).

[32] J.R. Dygas, Solid State Ionics 176, 2065 (2005).

[33] S. Havriliak, S. Negami, Polymer 8, 161 (1967).

[34] F.S. Howell, R.A. Bose, P. B. Macedo, C.T. Moynihan, J. Phys. Chem. 78, 639 (1974).

[35] P. Jeevanandam, S. Vasudevan, J. Chem. Phys. 109, 8102 (1998) .

[36] R. Kohlrausch, Ann. Phys. (Leipzig) 12, 393 (1847).

[37] G. Williams and D. C. Watts, Trans. Faraday Soc. 66, 80 (1970).

[38] S. N. Tripathy, Z. Wojnarowska, J. Knapik, H. Shirota, R. Biswas, M. Paluch, J. Chem. Phys. 142, 184504(2015).

[39] K. L. Ngai, J. N. Mundy, H. Jain, O. Kanert, G. Balzer-Jollenbeck, Phys. Rev. B 39, 6169 (1989).

[40] D. L. Sidebottom, B. Roling, K. Funke, PHYSICAL REVIEW B 63, 024301 (2000).

[41] T. M. W. J. Bandara, B. -E. Mellander, ed. A. Kokorin. In Tech Janeza Trdine 9, 383 (2011).

[42] P.W.M. Jacobs, J.W. Lorimer, A. Russer, M. Wasiucionek, J. Power Sources 26, 483 (1989).

[43] S.D. Druger, M.A. Ratner, A. Nitzan, Phys. Rev. B 31, 3939 (1985).

[44] Z. Cui, Y. Xiang, J. Si, M. Yang, Q. Zhang, T. Zhang, Carbohydr. Polym. 73, 111–116 (2008).

[45] I. A. Fadzallah, S. R. Majid, M. A. Careem, A. K. Arof, Journal of Membrane Science 463, 65–72 (2014).

[46] E.J. Baran, Carbohydr. Polym. 74, 704–706 (2008).

[47] L.H. Sim, S.N. Gan, C.H. Chan, R. Yahya, Spectrochimica Acta Part A 76, 287–292 (2010).

[48] S. Majumdar, P. Sen, R. Ray, Materials Today: Proceedings 18, 4913–4920 (2019).

[49] Z. Osman, A.K. Arof, Electrochimica Acta 48, 993-999 (2003).

[50] M.F.Z. Kadir, Z. Aspanut, S.R. Majid, A.K. Arof, Spectrochimica Acta Part A 78, 1068–1074 (2011).

Chapter 5

[1] M.H. Buraidah, L.P. Teo, S.R. Majid, A.K. Arof, Physica B 404, 1373-1379 (2009).

[2] M. F. Zaki, J. Phys. D: Appl. Phys. 41, 175404 (2008).

[3] D. Sinha, K. L. Sahoo, U. B. Sinha, T. Swu, A. Chemseddine, D. Fink, Radiat. Eff. Defects Solids 159, 587-595 (2004).

[4] L.Y. Lim, E. Khor, O. Koo, J. Biomed. Mat. Research 43(3), 282-290 (1998).

[5] D. K. Rana, S. K. Singh, S. K. Kundu, S. Roy, S. Angappane, S. Basu, New J. Chem.43, 3128-3138 (2019).

[6] B. S. Kang, S. K. Choi, C. H. Park, J. Appl. Phys. 94 (3), 1904-1911 (2003).

[7] Y. Wang, C. N. Sun, F. Fan, J. R. Sangoro, M. B. Berman, S. G. Greenbaum, T. A. Zawodzinski, A. P. Sokolov, Physical Review E 87, 042308 (2013).

Chapter 6

[1] M. H. Buraidah, L. P. Teo, S. R. Majid, A. K. Arof, Physica B 404, 1373-1379 (2009).

[2] A. A. Azli, N. S. A. Manan, M. F. Z. Kadir, Ionics 23, 411-425(2017).

[3] W. S. JR. Hummers, R. E. Offeman, Journal of American Chem. Soc. 80, 1339 (1958).

[4] A. K. Arof, S. Amirudin, S. Z. Yusof, I. M. Noor, Phys.Chem.Chem.Phys. 16, 1856-1867 (2014).

[5] T. Dam, S. S. Jena, D. K. Pradhan, Phys. Chem. Chem. Phys. 18, 19955-19965 (2016).

[6] Y. Wang, C. N. Sun, F. Fan, J. R. Sangoro, M. B. Berman, S. G. Greenbaum, T. A. Zawodzinski, A. P. Sokolov, Physical Review E 87, 042308 (2013).

[7] R. J. Kortschot, A. P. Philipse, B. H. Erné, J. Phys. Chem. C 118, 11584-11592 (2014).

[8] T. M.W.J. Bandara, M. A. K. L. Dissanayake, I. Albinsson, B. -E. Mellander, Solid State Ionics 189, 63-68 (2011).

Chapter 7

[1] C. Polo Fonseca, S. Neves, J. Power Sources 159, 712-716 (2006).

[2] M. Yadav, M. Kumar, N. Srivastava, Electrochimica Acta 283, 1551-1559 (2018).

[3] A. Burke, Journal of Power Sources 91, 37-50 (2000).

[4] L. L. Zhang, X. S. Zhao, Chemical Society Reviews 38, 2520-2531 (2009).

[5] M. Winter, R. J. Brodd, Chemical Reviews 10, 4245-4270 (2004).

[6] J. R. Miller, R. A. Outlaw, B. C. Holloway, Science 329, 1637-1639 (2010).

[7] T. Tiwari, N. Srivastava, P. C. Srivastava, Ionics 17, 335-360 (2011).

[8] A. A. Azli, N. S. A. Manan, M. F. Z. Kadir, Ionics 23, 411-425 (2017).

[9] M. H. Buraidah, L. P. Teo, S. R. Majid, A. K. Arof, Physica B 404, 1373-1379 (2009).

[10] D. W. Kim, J. K. Park, H. W. Rhee, Solid State Ionics 83, 49–56 (1996).

[11] S. Rajendran, R. S. Babu, M. U. Rani, Bull. Mater. Sci. 34, 1525–1530 (2011).

[12] Y.N. Sudhakar, M. Selvakumar, Electrochim.Acta 78, 398-405 (2012).

[13] Y.N. Sudhakar, M. Selvakumar, D.K. Bhat, Ionics 19, 277-285 (2013).

[14] M.H. Buraidah, A.K. Arof, Journal of Non-Crystalline Solids 357, 3261–3266 (2011).

[15] N. S. Mohamed, A. K. Arof, J. Power Sources 132, 229–234 (2004).

[16] R.A. Senthil, J. Theerthagiri, J. Madhavan, Journal of Physics and Chemistry of Solids 89, 78–83 (2016).

[17] R. A. Senthil, J. Theerthagiri, J. Madhavan, J.Non-Cryst.Solids 406, 133–138 (2014).

[18] Y. Yang, C. H. Zhou, S. Xu, H. Hu, B. L. Chen, J. Zhang, S. J. Wu, W. Liu, X. Z. Zhao, J. Power Sources 185, 1492–1498 (2008).

[19] J. -P. Bouchaud, A. Georges, Physics Reports 195(4-5), 127–293 (1990).

[20] A. E. Elkholy, F. El-Taib Heakal, N. K. Allam, RSC Adv. 7, 51888–51895 (2017).

[21] G. Lee,Y. Cheng, C. V. Varanasi, J. Liu, J. Phys. Chem. C 118, 2281−2286 (2014).

[22] D. M. E. Gendy, N. A. A. Ghany, E. F. E. Sherbini, N. K. Allam, Sci. Rep.7, 43104 (2017).

[23] P. Xiong, H. Huang, X. Wang, J. Power Sources 245, 937–946 (2014).

[24] P. Guo, Z. Li, S. Liu, J.Xue, G. Wu, H. Li, X. S. Zhao, J. Mater. Sci. 52, 5359–5365 (2017).

[25] L. Liu, H. Zhang, Y. Mu, Y. Bai, Y. Wang, J. Power Sources 327, 599–609 (2016).

[26] S.J. Kwon, T. Kim, B. Mun Jung, S. Bok Lee, U. Hyeok Choi, ACS Appl. Mater. Interfaces 10, 41, 35108–35117 (2018).

[27] C-Wen Liew, S. Ramesh, A.K. Arof, International Journal of Hydrogen Energy 39, 2953-2963 (2014).

[28] N. Farah, H.M. Ng, A. Numan, C-Wen Liew, N.A.A. Latip, K. Ramesh, S. Ramesh, Materials Science & Engineering B 251, 114468 (2019).

[29] S. B. Aziz, M. H. Hamsan, R.M. Abdullah, R.T. Abdulwahid, M. A. Brza, A.S. Marif, M. F. Z. Kadir, Ionics 26, 1829–1840 (2020).

[30] S.N. Asmara, M.Z. Kufian, S.R. Majid, A.K. Arof, Electrochimica Acta 57, 91– 97 (2011).

[31] C-Shen Lim, K.H. Teoh, C-Wen Liew, S. Ramesh, Materials Chemistry and Physics 143, 661-667 (2014).

[32] J. Rodríguez, E. Navarrete, E. A. Dalchiele, L. Sánchez, J. Ramón Ramos-Barrado, F. Martín, Journal of Power Sources 237, 270-276 (2013).

[33] S. Majumdar, P. Sen, R. Ray, Materials Today: Proceedings 18, 4913–4920 (2019).

[34] G. K. Williamson, W. H. Hall, Acta Metall. 1, 22–31 (1953).

[35] Z. Zhang, Y. Wang, Q. Tan, Z. Zhong, F. Su, Journal of Colloid and Interface Science 398, 185–192 (2013).

[36] Z. Beji, M. Sun, L. S. Smiri, F. Herbst, C. Mangeney, S.Ammar, **RSC Adv. 5,** 65010-65022 **(**2015**)**.

[37] J. K. Dey, A. Chatterjee, S. Majumdar, A.-C. Dippel, O. Gutowski, M. v. Zimmermann, S. Giri, Phys. Rev. B 99, 144412 (2019).

[38] Z. Zhang, W. Li, R. Zou, W. Kang, Y. San Chui, M. Fung Yuen, C-Sing Lee, W. Zhang, J. Mater. Chem. A 3, 6990–6997 (2015).

[39] R.S. Yadav, I. Kuřitka, J. Vilcakova, J. Havlica, J. Masilko, L. Kalina, J. Tkacz, JiříŠvec, V. Enev, M. Hajdúchová, Adv. Nat. Sci.: Nanosci. Nanotechnol. 8, 045002 (2017).

[40] S-Yu Chen,W. Song, H-Jan Lin, S.Wang, S. Biswas, M. Mollahosseini, C-HaoKuo, P-Xian Gao, L. Suib, ACS Appl. Mater. Interfaces 8, 7834-7842 (2016).

[41] S. Majumdar, S. Sarkar, R. Ray, AIP Conference Proceedings 2115, 030140 (2019).

[42] R. Kido, K. Ueno, K. Iwata, Y. Kitazawa, S. Imaizumi, T. Mandai, K. Dokko, M. Watanabe, Electrochimica Acta 175, 5-12 (2015).

[43] S. Klongkan, J. Pumchusak, Electrochimica Acta 161, 171-176 (2015).

[44] S. A. Suthanthiraraj, D. J. Sheeba, B. J. Paul, Materials Research Bulletin 44, 1534–1539 (2009).

[45] M. S. Michael, M. M. E. Jacob, S. R. S. Prabaharan, S. Radhakrishna, Solid State Ionics 98, 167–174 (1997).

[46] E. Tsuchida, H. Ohno, K. Tsunemi, Electrochim. Acta 28, 591–595 (1983).

[47] A. J. Bhattacharyya, T. R. Middya, S. Tarafdar, Physical Review B 60 (2), 909-915 (1999).

[48] E. K. Lenzi, L. R. Evangelista, G. Barbero, J. Phys. Chem. B 113, 11371−11374 (2009).

[49] T. Basu, M. Maitra Goswami, T. R. Middya, and S. Tarafdar, J. Phys. Chem. B 116, 11362−11369 (2012).

[50] M. Maitra, D. Mal, R. Dasgupta, S. Tarafdar, Physica A 346, 191 – 199 (2005).

[51] L.H. Sim, S.N. Gan, C.H. Chan, R. Yahya, Spectrochimica Acta Part A 76, 287–292 (2010).

[52] A. K. Arof, S. Amirudin, S. Z. Yusof, I. M. Noor, Phys. Chem. Chem. Phys. 16, 1856-1867 (2014).

[53] N. Molinari, J. P. Mailoa, B. Kozinsky, Chem. Mater. 30, 6298−6306 (2018).

[54] A. Zajac, J. Hanuza, M. Wandas, L. Dyminska, Spectrochimica Acta Part A: Molecular and Biomolecular Spectroscopy 134, 114–120 (2015).

[55] M.F.Z. Kadir, Z. Aspanut, S.R. Majid, A.K. Arof, Spectrochimica Acta Part A 78, 1068–1074 (2011).

[56] H. Y. Lee, J. B. Goodenough, J. Solid State Chem. 144, 220-223 (1999).

[57] A. Mishra, G. Bera, P. Mal, G. Padmaja, P. Sen, P. Das, B. Chakraborty, G. R. Turpu, Applied Surface Science 488, 221-227 (2019).

[58] P. Sen, A. De, Electrochimica Acta 55, 4677-4684 (2010).

[59] P-Pan Wang , C-Yan Xu, W-Da Li, L. Wang, L. Zhen, Electrochimica Acta 169, 440–446 (2015).

Chapter 8

[1] S. Majumdar, R. Ray, P. Sen, Electrochimica Acta 385, 138295 (2021).

[2] M. Yadav, M. Kumar, N. Srivastava, Electrochimica Acta 283, 1551-1559 (2018).

[3] Y.N. Sudhakar, M. Selvakumar, D.K. Bhat, Ionics 19, 277-285 (2013).

[4] H. Horibe, Y. Hosokawa, H. Oshiro, Y. Sasaki, S. Takahashi, A. Kono, T. Nishiyama, T. Danno, Polym. J. 45, 1195–1201 (2013).

[5] S.B. Aziz, M.H. Hamsan, R.M. Abdullah, R.T. Abdulwahid, M.A. Brza, A.S. Marif, M.F.Z. Kadir, Ionics 26, 1829–1840 (2020).

[6] M.S.A. Rani, N.S. Mohamed, M.I.N. Isa, Materials Science Forum 846, 539-544 (2016).

[7] M.S.A. Rani, N.S. Mohamed, M.I.N. Isa International Journal of Polymer Anal. Charact. 20, 491–503 (2015).

[8] F. Croce, L. Persi, F. Ronci, B. Scrosati, Solid State Ionics 135, 47–52 (2000).

[9] S.L. Agrawal, M. Singh, M.M. Dwivedi , M. Tripathi, K. Pandey, J Mater Sci 44, 6060–6068 (2009).

[10] M. Tripathi, S. Trivedi, R. Dhar, M. Singh, N.D. Pandey, S.L. Agrawal, Phase Transition 84, 972–980 (2011).

[11] S. Iijima, Nature 354, 56–58 (1991).

[12] C. Tang, K. Hackenberg, Q. Fu, P. Ajayan, H. Ardebili, Nano Letters 12, 1152-1156 (2012).

[13] P. Guo, Z. Li, S. Liu, J. Xue, G. Wu, H. Li, X.S. Zhao, .J. Mater. Sci. 52, 5359–5365 (2017).

[14] L. Liu, H. Zhang, Y. Mu, Y. Bai, Y. Wang, J. Power Sources 327, 599–609 (2016).

[15] A.J. Bhattacharyya, T.R. Middya, S. Tarafdar, Physical Review B60 (2), 909-915 (1999).

[16] E.K. Lenzi, L.R. Evangelista, G. Barbero, J. Phys. Chem. B 113, 11371−11374 (2009).

[17] A.A. Khamzin, I.I. Popov, R.R. Nigmatullin, Phys. Rev. E. 89, 032303 (2014).

[18] S. Majumdar, R. Ray, Journal of Polymer Research 28, 157 (2021).

[19] D.L. Sidebottom, B. Roling, K. Funke PHYSICAL REVIEW B 63, 024301 (2000).

[20] N. Srivastava, M. Kumar, Solid State Ionics 262, 806–810 (2014).

[21] S. Havriliak, S. Negami, Polymer 8, 161 (1967).

[22] F.S. Howell, R.A. Bose, P.B. Macedo, C.T. Moynihan, J. Phys. Chem. 78, 639 (1974).

[23] P. Jeevanandam, S. Vasudevan J. Chem. Phys. 109, 8102 (1998).

[24] G. Williams, D.C. Watts, Trans. Faraday Soc. 66**,** 80 (1970).

Chapter 9

[1] M. Yadav, M. Kumar, N. Srivastava, Electrochimica Acta 283, 1551-1559 (2018).

[2] Y.N. Sudhakar, M. Selvakumar, D.K. Bhat, Ionics 19, 277-285 (2013).

[3] S. Majumdar, R. Ray, P. Sen, Electrochimica Acta 385, 138295 (2021).

[4] M.H. Buraidah, A.K. Arof, Journal of Non-Crystalline Solids 357, 3261–3266 (2011).

[5] B. Wu, L. Wang, Z. Li, M. Zhao, K. Chen, S. Liu, Y. Pu, J. Li, Journal of The Electrochemical Society 163 (10), A2248-A2252 (2016).

[6] F. Croce, G.B. Appetecchi, L. Persi, B. Scrosati, Nature 394 (6692), 456–458 (1998).

[7] Y.N. Sudhakar, M. Selvakumar, Electrochim. Acta 78, 398-405 (2012).

[8] S. Majumdar, P. Sen, R. Ray, Materials Today: Proceedings 18, 4913–4920 (2019).

[9] S. Majumdar, S. Sarkar, R. Ray, AIP Conference Proceedings 2115, 030140 (2019).

[10] A.A. Azli, N.S.A. Manan, M.F.Z. Kadir Ionics 23, 411-425 (2017).

[11] P. Guo, Z. Li, S. Liu, J. Xue, G. Wu, H. Li, X.S. Zhao, J. Mater. Sci. 52, 5359–5365 (2017).

[12] L. Liu, H. Zhang, Y. Mu, Y. Bai, Y. Wang, J. Power Sources 327, 599–609 (2016).

[13] A.E. Elkholy, F.E.T. Heakal, N.K. Allam, RSC Adv. 7, 51888–51895 (2017).

[14] W.S.J.R. Hummers, R.E. Offeman, Journal of American Chem. Soc. 80, 1339 (1958).

[15] G.K. Williamson, W.H. Hall, Acta Metall. 1, 22–31 (1953).

[16] S. Majumdar, R. Ray, Journal of Polymer Research 28, 157 (2021).

[17] M. Yuan, J. Erdman, C. Tang, H. Ardebili, RSC Adv. 4**,** 59637-59642 (2014).

[18] W. Jia, Z. Li, Z. Wu, L. Wang, B. Wu, Y. Wang, Y. Cao, J. Li, Solid State Ionics 315, 7–13 (2018).

[19] D.P. Almond, G.K. Duncan, A.R. West Solid State Ionics 8, 159 (1983).

[20] T. Dam, S.S. Jena, D.K. Pradhan, Phys. Chem. Chem. Phys. 18, 19955—19965 (2016).

[21] A.A. Khamzin, I.I. Popov, R.R. Nigmatullin, Phys. Rev. E. 89, 032303 (2014).

[22] S. Havriliak, S. Negami, Polymer 8, 161 (1967).

[23] F.S. Howell, R.A. Bose, P.B. Macedo, C.T. Moynihan, J. Phys. Chem. 78, 639 (1974).

[24] P. Jeevanandam, S. Vasudevan, J. Chem. Phys. 109, 8102 (1998).

[25] R. Kohlrausch, Pogg Ann Phys (Leipzig) 12, 393 (1847).

[26] G. Williams, D.C. Watts, Trans. Faraday Soc. 66, 80 (1970).

[27] E.K. Lenzi, L.R. Evangelista, G. Barbero, J. Phys. Chem. B 113, 11371−11374 (2009).

[28] M. Maitra, D. Mal, R. Dasgupta, S. Tarafdar, Physica A 346, 191 – 199 (2005).

[29] L.H. Sim, S.N. Gan, C.H. Chan, R. Yahya, Spectrochimica Acta Part A 76, 287–292 (2010).

[30] A. Zajac, J. Hanuza, M. Wandas, L. Dyminska, Spectrochimica Acta Part A: Molecular and Biomolecular Spectroscopy 134, 114–120 (2015).

[31] A. Mishra, G. Bera, P. Mal, G. Padmaja, P. Sen, P. Das, B. Chakraborty, G.R. Turpu, Applied Surface Science 488. 221-227 (2019).

[32] P.P. Wang, C.Y. Xu, W.D. Li, L. Wang, L. Zhen, Electrochimica Acta 169, 440–446 (2015).

[33] H.Y. Lee, J.B. Goodenough, J. Solid State Chem. 144, 220-223 (1999).

Chapter 10

[1] A. Polu, H. Rhee, International Journal Of Hydrogen Energy. 42, 7212-7219 (2017).

[2] S. Majumdar, R. Ray, P. Sen, Electrochimica Acta. 385, 138295 (2021).

[3] C. Liew, S. Ramesh, A. Arof, International Journal Of Hydrogen Energy. 39, 2953-2963 (2014).

[4] W. Lu, Science 297, 983-987 (2002).

[5] H. Horibe, Y. Hosokawa, H. Oshiro, Y. Sasaki, S. Takahashi, A. Kono, Polymer Journal 45, 1195-1201 (2013).

[6] S. Majumdar, R. Ray, Journal Of Polymer Research 28 (2021).

[7] Y. Sudhakar, M. Selvakumar, D. Bhat, Ionics 19, 277-285 (2012).

[8] P. Meneghetti, S. Qutubuddin, A. Webber, Electrochimica Acta 49, 4923-4931 (2004).

[9] P. Pal, A. Ghosh, Physical Review E 92 (2015).

[10] S. Majumdar, P. Sen, R. Ray, Materials Today: Proceedings. 18, 4913-4920 (2019).

[11] F. Croce, Solid State Ionics 135, 47-52 (2000).

[12] S. Agrawal, M. Singh, M. Tripathi, M. Dwivedi, K. Pandey, Journal Of Materials Science 44, 6060-6068 (2009).

[13] A. Dey, S. Karan, A. Dey, S.K. De, Materials Research Bulletin 46, 2009–2015 (2011).

[14] B. Wu, L. Wang, Z. Li, M. Zhao, K. Chen, S. Liu, Journal Of The Electrochemical Society 163, A2248-A2252 (2016).

[15] S. Majumdar, S. Sarkar, R. Ray, AIP Conference Proceedings 2115, 030140 (2019).

[16] M. Mastragostino, C. Arbizzani, F. Soavi, Solid State Ionics 148, 493-498 (2002).

[17] G. Zhang, X. Xiao, B. Li, P. Gu, H. Xue, H. Pang, Journal Of Materials Chemistry A 5, 8155-8186 (2017).

[18] V. Kumbhar, A. Jagadale, N. Shinde, C. Lokhande, Applied Surface Science 259, 39-43 (2012).

[19] E. Frackowiak, Physical Chemistry Chemical Physics 9, 1774 (2007).

[20] A. Elkholy, F. El-TaibHeakal, N. Allam, RSC Advances 7, 51888-51895 (2017).

[21] P. Kalambate, R. Dar, S. Karna, A. Srivastava, Journal Of Power Sources 276, 262-270 (2015).

[22] M. Khan, W. Khan, M. Ahamed, J. Ahmed, M. Al-Gawati, A. Alhazaa, ACS Omega 5, 31076-31084 (2020).

[23] K. S. Novoselov, Rev. Mod. Phys. 83, 837 – 849 (2011).

[24] A. K. Geim, Rev. Mod. Phys. 83, 851 - 862 (2011).

[25] S. Sarkar, A. Mondal, K. Dey, R. Ray, Materials Research Bulletin 74, 465-471 (2016).

[26] M. Chandel, P. Makkar, N. Ghosh, ACS Applied Electronic Materials 1, 1215-1224 (2019).

[27] W. Hummers, R. Offeman, Journal Of The American Chemical Society 80, 1339-1339 (1958).

[28] S. Sarkar, A. Mondal, N. Giri, R. Ray, Physical Chemistry Chemical Physics 21, 260-267 (2019).

[29] P. Garcia, O. Prymak, V. Grasmik, K. Pappert, W. Wlysses, L. Otubo, Nanoscale Advances 2, 225-238 (2020).

[30] S. Ristig, O. Prymak, K. Loza, M. Gocyla, W. Meyer-Zaika, M. Heggen, Journal Of Materials Chemistry B 3, 4654-4662 (2015).

[31] G. Williamson, W. Hall, Acta Metallurgica 1, 22-31 (1953).

[32] X. Zhang, G. Wang, W. Cao, Y. Wei, J. Liang, L. Guo, M. Cao, ACS Applied Materials & Interfaces 6, 7471-7478 (2014).

[33] A. Khamzin, I. Popov, R. Nigmatullin, Physical Review E 89, 032303 (2014).

[34] D.L. Sidebottom, B. Roling, K. Funke, PHYSICAL REVIEW B 63, 024301 (2000).

[35] N. Srivastava, M. Kumar, Solid State Ionics 262, 806–810 (2014).

[36] E. Lenzi, L. Evangelista, G. Barbero, The Journal Of Physical Chemistry B 113, 11371-11374 (2009).

[37] S. Ramesh, K. Leen, K. Kumutha, A. Arof, Spectrochimica Acta Part A: Molecular And Biomolecular Spectroscopy. 66, 1237-1242 (2007).

Simantini Majumdar
31.1.2022